LIQUID CRYSTAL PHASE-ONLY MODULATOR AND OPTICAL BEAM STEERING SYSTEM

XIUZE WANG

Jesus College

University of Oxford

Supervisors: Prof. Stephen Morris and Prof. Steve Elston

A thesis submitted for the degree of

Doctor of Philosophy

Michaelmas term, 2021

Abstract

Liquid Crystal Phase-Only Modulator and Optical Beam Steering System

By Xiuze Wang

This thesis describes the development of a new analogue, phase-only liquid crystal (LC) modulator and an LC-based optical beam steering configuration. To begin with, a new and simple method for the rapid and precise measurement of the flexoelectro-optic performance of large tilt-angle chiral nematic LC is presented. These large tilt-angle LCs are then employed in the development and demonstration of a flexoelectro-optic LC phase modulator with $>2\pi$ phase range and sub-millisecond response. It is shown that the voltage-induced rotation of the optic axis is converted into a phase modulation with the aid of a reflective device configuration incorporating a $\sim 5\ \mu m$ LC cell, a polarizer, two quarter-wave plates, and a mirror. It is then demonstrated that the mirror and quarter-wave plate can be replaced with a chiral reflector, which improves the robustness of the system.

Based on the reflective phase modulator, two different transmissive phase modulators are considered, which consist of either adding a half-wave plate in between two LC layers when the electric field applied to the two layers is the same or by applying electric fields of opposite polarity, avoiding the need for an additional half-wave plate. Even though those phase modulators can generate 2π phase modulation with sub-millisecond response time, a key disadvantage is that numerous optical components are required. In order to solve this, a LC phase modulator that combines a flexoelectro-optic LC layer, a polymerized reactive mesogen layer and a

mirrored substrate is presented, which demonstrates the potential for making next-generation LC on silicon spatial light modulators. In the final part of this thesis, LC phase modulators are combined with LC polarisation gratings to form a novel beam steering for optical communications.

Acknowledgement

Pursuing a PhD is a difficult and sometimes a lonely path. First of all, I would like to extend my gratitude and appreciation to my supervisors. Thank you, Steve M. for inviting me to join the group, what an adventure it has been! Thank you for helping and giving so much useful advice during my PhD study. Thank you for being such a good man and a caring supervisor. Thank you, Steve E., who always asks me questions to let me think harder, and supports me during the difficult times in my research. Thank you for your wisdom, guidance, friendship and brightening some of the darker times in the downstairs lab. Without your help, I could not finish my PhD with so many achievements. I appreciate you all for spending endless hours proofreading my research papers and giving me excellent suggestions, which always resulted in improved versions of documents. Your effort and patience will never be forgotten.

To the people who make my PhD a time to cherish. Julian, thank you for your help with explaining many difficult concepts and setting up the experiment with me. It is such an honour for me to collaborate with you. To Jiade, who is always there to help, thank you for helping me with carrying so much equipment to the downstairs lab, you are always the people that I thought when I needed to carry a heavy staff. To Taimoor, my Pakistan buddy, Thanks for the laughs, an appreciation of ergonomics, and the memories.

To Waqas, Yihan and John, thank you all for your companionship over the years. I wish you all the very best in your PhDs and life beyond. To Bohan, Zimo and

Mengmeng, welcome to this group. I hope you all have an excellent time in this group. To my best friend Ziheng, thank you for making my DPhil in Oxford so enjoyable and memorable.

Finally, I wish to extend my love and gratitude to my dearest support team back home: My mum, my dad and my wife. Although they have no idea what I do, they have given me endless encouragement and support.

Publications

1. Wang, X. et al. Characterization of large tilt-angle flexoelectro-optic switching in chiral nematic liquid crystal devices. *Liquid Crystals* 46, 408-414 (2018).
2. Fells, J. et al. Flexoelectro-optic liquid crystal analog phase-only modulator with a 2π range and 1kHz switching. *Optics Letters* 43, 4362 (2018).
3. Wang, X. et al. Fast and low loss flexoelectro-optic liquid crystal phase modulator with a chiral nematic reflector. *Scientific Reports* 9, (2019).
4. Wang, X. et al. Transmissive flexoelectro-optic liquid crystal optical phase modulator with 2π modulation. *AIP Advances* 10, 055011 (2020).
5. Wang, X. et al. A Compact Full 2π Flexoelectro-Optic Liquid Crystal Phase Modulator. *Advanced Materials Technologies* 5, 2000589 (2020).
6. Ali, T. et al. A Thin-Film Flexible Defect-Mode Laser. *Advanced Optical Materials* 8, 1901891 (2020).

Conference:

1. Xiuze Wang, Julian Fells, Taimoor Ali, Jiade Lin, Chris Welch, Georg Mehl, Martin Booth, Timothy Wilkinson, Stephen Morris, and Steve Elston "Fast flexoelectro-optic liquid-crystal phase-only modulators (Conference Presentation)", Proc. SPIE 11303, Emerging Liquid Crystal Technologies XV, 1130309 (9 March 2020);

List of Abbreviations

Arbitrary Waveform Generator	AWG
Beam Splitter	BS
Charge Coupled Device	CCD
Complementary Metal Oxide Semiconductor	CMOS
Circularly Polarized	CP
Digital Light Processing	DLP
Direct Laser Writing	DLW
Digital Micromirror Devices	DMD
N,N-Dimethyl-N-Octadecyl-3-Aminopropyltrime Hoxysilyl Chloride	DMOAP
Device Under Test	DUT
Ferroelectric Liquid Crystal	FLC
Fast Steering Mirror	FSM
Helical Twisting Power	HTP
Helium-Neon	He-Ne
Indium Tin Oxide	ITO
Linearly Polarized	LP
Liquid Crystal	LC
Liquid Crystal Display	LCD
Liquid Crystal On Silicon	LCOS
Micro-Electromechanical Systems	MEMS
Numerical Aperture	NA
Optical Polarizing Microscope	OPM
Photonic Bandgap	PBG
Polarisation Grating	PG
Pinhole	PH
Polymer Film	PF

Reactive Mesogen	RM
Sulphonic Azo-Benzene Dye	SD1
Spatial Light Modulator	SLM
Stimulated Emission Depletion	STED
Twisted Nematic	TN
Ultra-Violet	UV
Uniform Lying Helix	ULH
Uniform Standing Helix	USH
Vertically Aligned Nematic	VAN
1,7-Bis-4-(4′-Cyanobiphenyl) Heptane	CB7CB
4′-Pentyl-4-Cyanobiphenyl	5CB

List of Symbols

Characteristic Time	τ
Device Thickness	D
Dielectric Permittivity	E
Director	$\hat{\mathbf{n}}$
Elastic Constant	k
Electric Displacement	**D**
Electric Field	**E**
Electric Polarization	**P**
Flexoelectric Coefficient	e
Flexoelectric Tilt/Twist Angle	Φ
Free Energy (Total)	F
Free Energy Density	f
Order Parameter (Scalar)	S
Optic Axis - Polarizer Angle	X
Phase Delay	δ
Pitch	P
Potential Voltage	V
Relative Permeability	M
Phase Velocity	V_{ph}
Refractive Index	n
Rotational Viscosity	γ
Temperature	T
Tilt Angle	θ
Time	T
Torque	**Γ**
Transmission (Electromagnetic)	T

Wavelength	λ
Wavenumber (Liquid Crystal Helix)	q

Contents

List of Figures

Chapter 1 Introduction

Phase modulation devices based on liquid crystals have found widespread application in beam shaping for photolithography [1], adaptive optics for wavefront corrections [2], telecom as a wavelength selective switch [3], and multifocal displays for augmented reality and head-up displays [4-6], because of its unique light modulating properties, high resolution, small size, low driving voltage and low power consumption [6-9]. A large phase modulation depth ($\geqslant 2\pi$) with a fast response time is required for most applications. However, most of these electrically controlled phase modulation devices that employ nematic LCs confront one of the fundamental limits of slow response (several tens of milliseconds) [10]. Although the rise time can be effectively minimized by increasing the voltage amplitude, the fall time cannot be reduced due to the fact that it mainly depends on the viscosity and elastic of LC material, cell gap and anchoring strength [11]. In addition, increasing the voltage amplitude is not a desirable solution as a large voltage is not suitable for many applications [10]. To improve the response time, many researchers proposed different approaches to overcome the limit, such as using dual-frequency liquid crystal materials to develop a liquid crystal phase modulator that can provide 2π phase modulation with 0.5ms response time. However, the driving voltage for this phase modulator is approximately 10V/μm which is out of satisfaction [12]. YH Lin demonstrated a polarisation independent polymer network liquid crystal light modulator by using a double-layered structure. A 2π phase shift is achieved with submillisecond response time, but the driving voltage is about 10V/μm and it can only be used in transmissive configuration [13]. Ferroelectric liquid crystals

can provide sub-millisecond response time with relatively low driving voltage. However, due to their nature, they can only provide binary phase modulation [14-15]. Recently, a low viscosity and negative dielectric anisotropy ($\Delta\varepsilon$) LC mixture has been developed which can achieve 2π phase change with a thin cell gap ($d \approx 2.4$ μm) [16]. However, to achieve 2π phase modulation, its response time would increase by 4 times which is about 4ms. Each technology has its own advantages and disadvantages, and it is still quite challenging to satisfy all the above-mentioned requirements.

Hence, in this thesis, we have described the development of a novel liquid crystal (LC) phase modulator based upon the flexoelectro-optic effect in short-pitch chiral nematic LCs. It is shown that this phase modulator can exhibit analogue modulation with appropriate voltage at frame rates of the order of 1 kHz. The new phase modulator technology is combined with polarisation gratings to create a high efficiency beam steering system for optical communications. The following describes the structure and content of the thesis.

Chapter 2 provides the relevant background on LC materials needed for the experimental and theoretical studies presented in this thesis. In particular, this chapter describes the LC properties such as the dielectric permittivity and the optical anisotropy. In addition, information about LC spatial light modulators and beam steering systems are also briefly introduced and discussed in this chapter.

Chapter 3-6 present results on a novel phase modulator that can provide 2π phase modulation with sub-millisecond response time. In Chapter 3, a new method for characterising the flexoelectro-optic effect in chiral nematic LCs with a large tilt angle is presented. It is shown that this new method is more appropriate for the characterisation of liquid crystalline devices that exhibit a large tilt-angle of the optical axis in flexoelectro-optic switching. In addition, it has been found that the flexoelectro-optic performance of chiral nematic LC devices can be quickly determined by simply recording the electric field amplitude at the point whereby the transmission properties become equivalent. This property is quite useful and will be used in the following chapters to characterize the flexoelectro-optic performance. The work presented in Chapter 3 has been published in *Liquid Crystals* **46**, 408-414 (2018).

In the following Chapter (Chapter 4), a flexoelectro-optic phase modulator is demonstrated in a reflection configuration where it is shown to exhibit full 2π phase modulation with sub-millisecond response time by applying an appropriate electric field at a suitable temperature. In the future, this configuration can be integrated into a compact device design which will be demonstrated in Chapter 6. In addition, in this chapter, it has also been demonstrated that the system can be improved by replacing the mirror and quarter waveplate with a chiral nematic reflector, which will ensure that the system is less sensitive to the nonideality of the LC phase modulation element. The work shown in this chapter has been published in *Optics Letters* **43**, 4362-4365 (2018) and *Scientific Reports* **9**, 7016 (2019).

Chapter 5 presents how the flexoelectro-optic phase modulator can be made to work in a transmission configuration. In this work, three different transmissive modes LC optical phase modulators based on the flexoelectro-optic effect of a chiral nematic LC aligned in the ULH geometry are considered. A basic configuration consisting of a single LC layer between quarter-wave retarders is found to exhibit a phase modulation π corresponding to a $\pm 45°$ switching angle of the flexoelectro-optic effect. The other two configurations can achieve full 2π modulation by introducing an additional LC layer and a half-wave plate in between two LC layers when the electric field applied to the two layers is the same or by applying electric fields of opposite polarity, avoiding the need for an additional half-wave plate. This work has been published in *AIP Advances* **10**, 055011 (2020).

Finally, in Chapter 6 the optical components are combined to form an integrated LC phase modulator based on the flexoelectro-optic effect. The integrated device contains an LC layer consisting of chiral nematic LC and a birefringent polymer film to work as a quarter waveplate and a silver film to function as a mirror. This integrated device has also exhibited a 2π phase range with a frame rate of 1 kHz. The successful development of this phase modulator has led to a paper published in *Adv. Mater. Tech.* **5**, 2000589 (2020).

Chapter 7 illustrates one of the scenarios in which the new phase modulator could

be applied. Here an LC phase modulator is combined with LC polarisation gratings to make a novel, high efficiency beam steering system for optical communications. This work was limited due to the COVID pandemic. As a result, the system has been demonstrated using a nematic pi-cell LC device rather than a chiral nematic flexoelectro-optic phase modulator. Originally, it had been intended that the use of the pi-cell would serve as a proof-of-concept before the implementation of the new flexoelectro-optic LC phase modulator. This is discussed further in Chapter 8, which summarises the work presented in the thesis and provides some examples of possible future work.

Chapter 2 Background on Liquid Crystals and Phase Modulators

2.1 Liquid crystals

A liquid crystal (LC) is a thermodynamically stable mesophase (a mesophase is a state of matter that is in between the isotropic liquid and crystalline solid states, as shown in **Figure 2.1**) which was first discovered by the Austrian botanist Friedrich Reinitzer in 1888 [17]. It possesses some of the properties of a liquid, such as fluidity as well as certain crystalline properties, such as anisotropy in the electrical, magnetic and optical properties and a periodic arrangement of the molecules in certain spatial directions [18]. Many thousands of compounds have been found to exhibit liquid crystalline behaviour, and many of these compounds are rod-like or lath-like, which means that the molecules usually have one axis that is longer than the other [18-20]. The inherently prolate nature of the molecules also gives rise to molecular anisotropy. From a chemical point of view, the anisotropic shape of an LC molecule usually possesses a rigid molecular core that forms the long axis of the molecule. Hence, the LC phase is more likely to occur if there are flat segments in the molecule such as benzene rings [20-22].

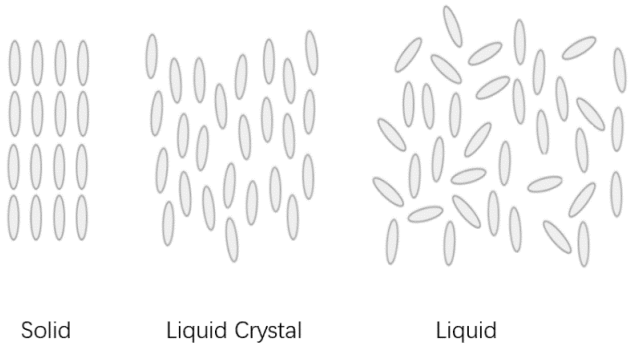

Figure 2.1 Illustration of the solid state, liquid crystal state and isotropic liquid state. Liquid crystals are ordered like a solid, but they flow like a liquid.

Depending on the arrangement of the molecules, LCs can be subdivided into a range of mesophases including nematic, smectics, cholesterics, and columnar mesophases [18,23,24]. The last one (the columnar mesophase) is beyond the scope of this thesis and will not be discussed here. The molecular arrangements for the first three mesophases are presented in **Figure 2.2**.

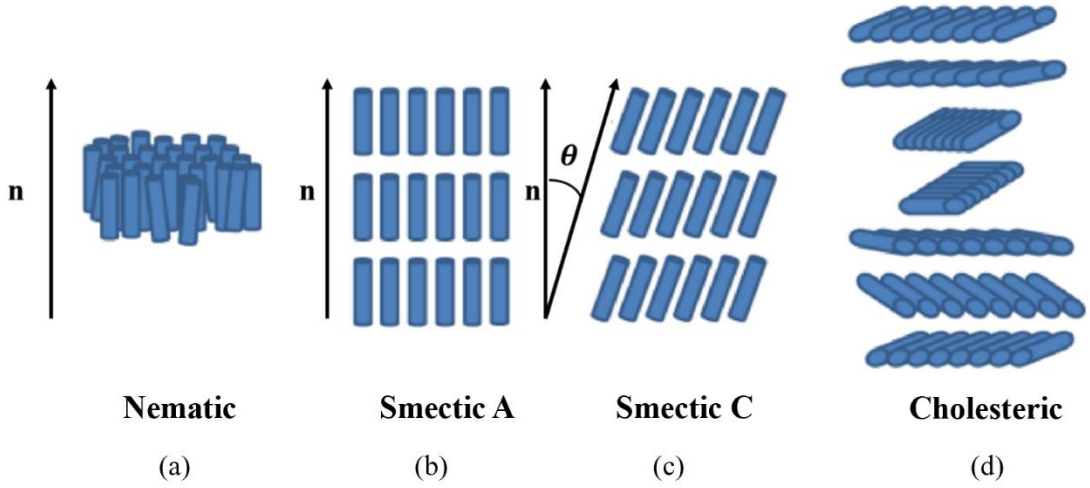

Figure 2.2 Molecular arrangements for different liquid crystalline mesophases.

Nematic LC Phase

Molecules in a nematic mesophase have a high degree of long-range orientational order without any long-range translational order. This is similar to an isotropic liquid, except that all of the molecules are approximately aligned along a preferred direction which is called the director, $\hat{\mathbf{n}}$ [18,24]. The director, shown in **Figure 2.2**, is a unit vector, and its orientation can be represented by a unit vector, **n(r)**. The director and the molecular arrangement in a nematic mesophase are illustrated in Figure 2.2(a), where the anisotropic shape of the molecules is depicted by a cylinder.

An important parameter in considering the orientational order in a nematic LC phase is the scalar order parameter *S*, which is an average of the second Legendre polynomial [25]:

$$S = \langle P_2(\cos\theta)\rangle = \langle \frac{3}{2}\left(\cos^2\theta - \frac{1}{2}\right)\rangle. \qquad (2.1)$$

where θ is the angle between the long axis of a molecule and the director $\hat{\mathbf{n}}$. The average is taken over a large number of molecules. For a perfectly ordered crystalline solid material, $S = 1$, whereas for an isotropic liquid whereby the axes of the molecules are randomly pointing in all directions $S = 0$ [25]. Typically, the value of *S* for a nematic LC is around 0.6. **Figure 2.3** illustrates how the order parameter *S* varies with temperature for a typical nematic LC.

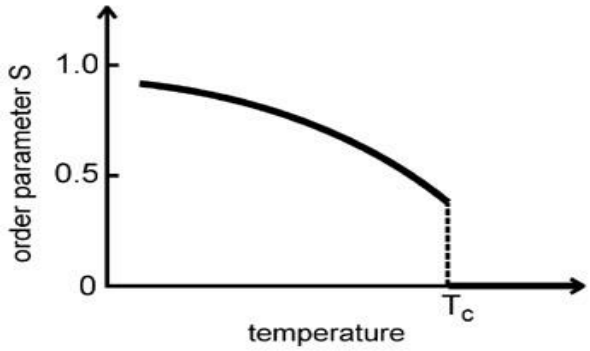

Figure 2.3 The dependence of the scalar order parameter *S* (Equation 2.1) on temperature for a typical nematic LC. The clearing temperature, $T_{C,}$ is the phase transition temperature to the isotropic liquid phase.

Smectic LC Phase

Stratification is the most important feature that distinguishes the smectic LC mesophase from the nematic LC mesophase. Compared with the nematic LC mesophase, the molecules in a smectic LC phase are placed in layers and show some correlation in terms of their positions in addition to the long-range orientational ordering [24,26].

Depending on the arrangement of the molecules in the layers, various smectic mesophases have been observed. This thesis introduces the most common two smectic LC mesophases: the smectic A and smectic C LC phase. In the smectic A phase, the molecules are approximately aligned perpendicular to the layers [27], as shown in Figure 2.2(b). Unlike the smectic A phase, the molecules in the smectic C phase are not perpendicular to the layers but are tilted at an angle, θ, which leads to a biaxial symmetry for the smectic C phase [27]. Many compounds can exhibit both nematic and smectic LC mesophases and the smectic mesophases generally have a greater degree of crystalline order [28]. Hence, for those materials, the nematic mesophase can be obtained by heating the material to above the smectic-nematic transition temperature.

Chiral nematic (Cholesteric) LC Phase

One way that the chiral nematic (Cholesteric) LC phase can be generated is by adding chiral dopant into a nematic LC host, thus breaking the mirror symmetry inherent in the nematic phase. As for the nematic LC phase, the chiral nematic LC phase also exhibits long-range orientational order without any long-range positional order [18]. However, the director in the chiral nematic LC phase varies throughout the medium which differs from nematic phase. In this case, the director distribution is obtained by twisting a nematic aligned along the *y*-axis about the *x*-axis (here the *y*-axis is defined as being perpendicular to the device substrate and the *x*-axis is parallel to the device substrate). The long axes of molecules in each plane are aligned to a single direction which is always perpendicular to the twist axis and rotates uniformly, as illustrated in Figure 2.2

(c). The distance measured along the twist axis over which the director rotates through a full circle is called the pitch of the chiral nematic, *p*. The pitch can be of the order of several hundred nanometers, which is comparable to the wavelength of visible light [18, 26]. The pitch can be measured experimentally or calculated from the helical twisting power (HTP) that controls the concentration of chiral additive required for a desired pitch [29]:

$$P = \frac{1}{\text{HTP}\times\text{concentration}}. \quad (2.2)$$

From the equation, it can be seen that the pitch is not fixed. It can be adjusted by increasing or decreasing the concentration of the chiral dopant. In fact, the pitch is not only sensitive to the concentration of chiral additive but can also be affected by the temperature, external forces and magnetic/electric fields [23, 24].

The pitch is an important property for chiral nematic LCs as it influences the wavelength of the light that it can reflect. A nematic LC can be regarded as a chiral nematic LC with an infinite pitch. As a result, it is not possible to change the nematic phase into a chiral nematic phase by simply heating or cooling the material. Instead, the chiral nematic LC mesophase can be obtained by adding chiral dopants (as discussed) or through the use of inherently chiral molecules. In addition, the helix in the chiral nematic LC mesophase can be either right- or left-handed, which determines the handedness of the polarisation of the light that it can reflect [20, 26].

2.2 Anisotropic Physical Properties

As mentioned in the previous section, the anisotropic shape of the LC molecules causes their anisotropic physical properties. Therefore, each molecule will possess different physical properties depending on the measurement direction e.g., parallel or perpendicular to the director. In this section, we will focus on introducing dielectric anisotropy and optical anisotropy.

2.2.1 Dielectric anisotropy

Due to the anisotropic properties of nematic LCs (the vast majority of LC materials exhibit some dielectric anisotropy because one molecular axis is longer than the other and generally, the molecule possess a permanent dipole), LCs normally possess two different values of the relative dielectric permittivity: $\varepsilon_{\perp}$ for an electric field that is perpendicular to the director and $\varepsilon_{\parallel}$ for the electric field that lies parallel with the director [30,31] (as shown in **Figure 2.4**). The overall relative dielectric permittivity ε_r can take the form of a tensor

$$\varepsilon_r = \begin{bmatrix} \varepsilon_{\perp} & 0 & 0 \\ 0 & \varepsilon_{\perp} & 0 \\ 0 & 0 & \varepsilon_{\parallel} \end{bmatrix} \tag{2.3}$$

and the dielectric anisotropy then is written as [32]

$$\Delta\varepsilon = \varepsilon_{\parallel} - \varepsilon_{\perp} \tag{2.4}$$

Nematic LCs with positive dielectric anisotropy ($\varepsilon_{\parallel} > \varepsilon_{\perp}$) have greater polarisation along the long axis of the molecule, while negative dielectric anisotropy molecules have greater polarisation along the short axis. The sign of the dielectric anisotropy determines the reorientation of the LC director in the presence of an electric field. For

example, whether the LC director lies along the direction of the applied electric field or perpendicular to it (as shown in **Figure 2.5**) [30-32].

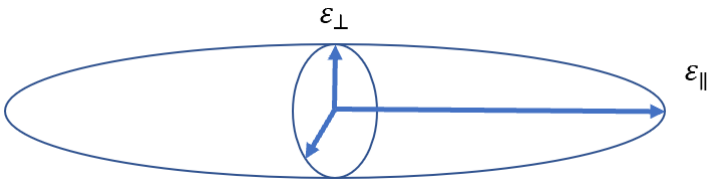

Figure 2.4 Parallel and perpendicular components of the relative dielectric permittivity for anisotropic LC molecules.

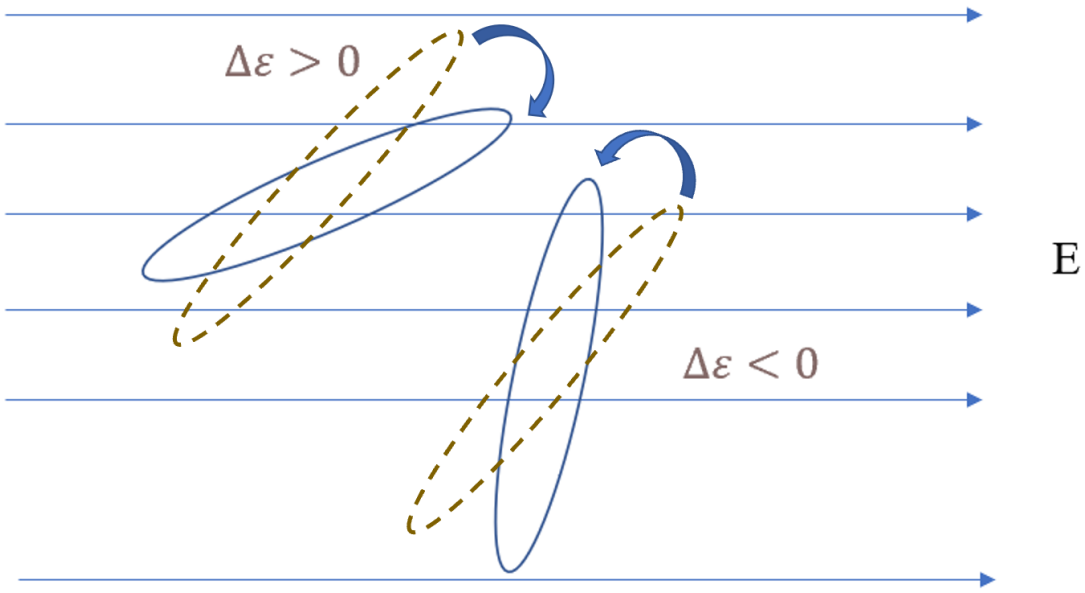

Figure 2.5 Reorientation of the director for positive and negative dielectric anisotropy nematic LCs in response to an applied electric field.

2.2.2 Optical anisotropy

The refractive index is a crucial parameter that defines the phase velocity v_{ph} relative to the speed of light in a vacuum [33]:

$$v_{ph} = \frac{c}{n} \tag{2.5}$$

In addition, the refractive index can also be calculated from the relative permittivity ε and the relative permeability μ of an optical material [32]:

$$n = \sqrt{\mu\varepsilon_r} \tag{2.6}$$

For most materials at optical frequencies [32]

$$n = \sqrt{\varepsilon_r} \tag{2.7}$$

Many phenomena such as refraction, reflection and diffraction are determined by the refractive index. LCs are generally optically birefringent materials due to their anisotropic properties. Polarised components of light propagate through a liquid crystalline material at different speeds as they experience a different refractive index parallel (extraordinary) (n_e) and perpendicular (ordinary) (n_o) to the LC optic axis. The resultant phase delay between the two orthogonal polarisations can be described by the birefringence of the medium as [20, 24, 32]

$$\Delta n = n_e - n_o \tag{2.8}$$

When the incident wave propagates at an angle to the optical axis, the ordinary refractive index remains the same, but the extraordinary refractive index will have a new effective value, n_{eff},

$$n_{eff} = \frac{n_e n_o}{\sqrt{n_e \cos\theta + n_o \sin\theta}} \tag{2.9}$$

where θ is the angle between the optical axis and the direction of the light propagation. In this situation, the birefringence Δn becomes [20, 24, 32]:

$$\Delta n = n_{eff} - n_o \tag{2.10}$$

For nematic LCs, Δn varies in the range between 0.05 and 0.5 [18,26]. When a light beam enters a nematic LC, it splits into two rays which travel at different speeds due to the different refractive indices, resulting in a phase delay between the components. After passing through the material these rays recombine, and the polarisation state of

the light beam is the function of the phase difference. Any polarisation state can be produced with the right control of the birefringence.

As mentioned in the above section, the chiral nematic LC phase is different to the nematic phase because the director rotates around a specific axis to form a helical structure. The distance for the director to rotate through a full circle (the periodicity of the helix) is called the pitch. Depending on the relationship between the pitch and wavelength of the incident light, a chiral nematic LC will interact with the input light in different ways.

For example, when the wavelength of light is $\lambda \ll nP$, the chiral nematic LC acts as a waveguide. The regime under this condition is referred to as the Mauguin regime [34]. A long pitch chiral nematic behaves as a twisted nematic (TN) LC cell when the incident light is polarised along with the director, the transmitted light is still linearly polarised, but the direction of the polarisation is rotated at an angle which is the distance between the director at the two substrates.

If $n_o P < \lambda < n_e P$, selective Bragg reflection takes place (which causes a chiral nematic LC to appear coloured) whereby the light will be reflected within a photonic bandgap (PBG). The PBG, analogous to the electronic bandgaps in semiconductors, forms due to the constructive interference of reflected components of light by the periodicity of the dielectric material. The spectral width of the PBG can be calculated by [34]

$$\Delta\lambda = \Delta n P. \tag{2.11}$$

Figure 2.6 shows the transmission spectrum for white light of a chiral nematic LC obtained using a UV-Visible spectrometer. From the Figure, it can be seen that the short and long edge wavelengths are at ≈530 nm and ≈610 nm, respectively. Hence the sample will appear green in colour (in reflection). If the refractive index of the sample is known, then the pitch of the sample can be estimated. In addition, due to the handedness of chiral nematic LCs, only ~50% of the light can be reflected as only circularly polarised light of the same handedness is transmitted.

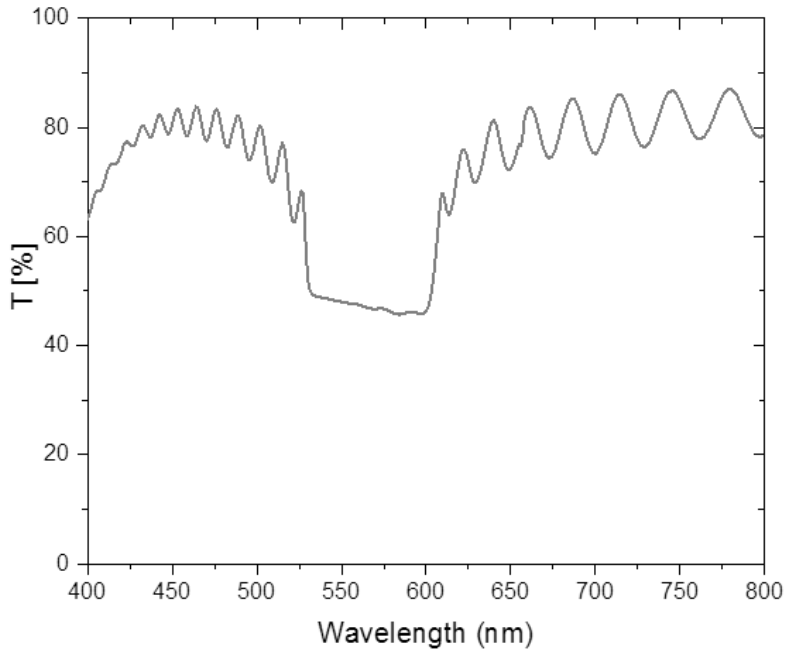

Figure 2.6 The transmission spectrum for the white light of a chiral nematic LC, E7+S811. The thickness of the device is 4.98 μm and the cell is measured at room temperature. The bandgap is between ≈530 nm and ≈610 nm.

Finally, for short pitch chiral nematic LCs $\lambda \gg nP$, the LC behaves as an optically active medium with huge rotatory power. For light polarised perpendicular to the helical axis, the refractive index becomes [32, 34]:

$$n_{\text{eff}} = \sqrt{\varepsilon_{\text{eff}}} = \sqrt{\frac{1}{2}\left(n_{\parallel}^2 + n_{\perp}^2\right)}. \quad (2.12)$$

$$\Delta n = n_{\perp} - \sqrt{\frac{1}{2}\left(n_{\parallel}^2 + n_{\perp}^2\right)}. \quad (2.13)$$

Alternatively, for light polarised parallel to the helical axis, the refractive index is $n = n_{\perp}$.

2.3 Free-energy Characteristics

The free-energy of a nematic LC has attracted lots of interest [18,35]. In Section 2.1, the different LC phases have been introduced. This section gives a brief introduction to the various contributions to the free-energy: elastic, dielectric and flexoelectric. All of which are considered in this thesis.

2.3.1 Dielectric energy

The dielectric properties are related to the response of the LC director to an applied electric field. For non-polar LC molecules, besides the electric polarisation, there also exists an ionic polarisation. For polar LC molecules, in addition to the above two polarisations, there is also an orientation polarisation, owing to the tendency of the permanent dipole moments to orient themselves parallel to the electric field [36]. In this thesis, only electric polarisation is considered. The other two forms of polarisation are outside the scope of this thesis.

When an electric field is applied to a nematic LC, it generates an electric polarisation, **P**, which is proportional to the electric field but not necessarily parallel to it. For a uniaxial material, the resultant electric displacement is defined as [35]:

$$\mathbf{D} = \varepsilon_0 \mathbf{E} + \mathbf{P} = \varepsilon_0 (1 + \chi_e) \mathbf{E} = \varepsilon_0 \varepsilon_r \mathbf{E}, \tag{2.14}$$

where ε_0 is the vacuum permittivity, ε_r the relative dielectric permittivity of the material and the polarizability of a material is defined by the susceptibility, χ_e.

$$\mathbf{D} = \varepsilon_0 \varepsilon_\perp \mathbf{E} + \varepsilon_0 \Delta\varepsilon (\hat{\mathbf{n}} \cdot \mathbf{E}) \hat{\mathbf{n}}. \tag{2.15}$$

The free dielectric energy term can then be derived as [35]:

$$f_{\text{dielectric}}(\hat{\mathbf{n}}) = -\frac{1}{2} \mathbf{D} \cdot \mathbf{E} = -\frac{1}{2} \varepsilon_0 \varepsilon_\perp E^2 - \frac{1}{2} \varepsilon_0 \Delta\varepsilon (\hat{\mathbf{n}} \cdot \mathbf{E})^{\mathbf{2}} \tag{2.16}$$

As mentioned previously, the sign of the dielectric anisotropy can be either positive or negative, depending on the polarizability or permanent dipole orientation of the director. Applying an electric field to a positive dielectric anisotropy LC will reorient the director in the LC layer with the applied electric field. Similarly, the LC director will reorient perpendicular to the externally applied electric field when the dielectric anisotropy is negative [21]

The dielectric energy mainly depends on the angle between the director and the applied electric field due to the LC anisotropy. Thus, any terms independent of the director orientation can be neglected. The free dielectric energy from (2.16) can therefore be reformed to [35]:

$$f_{\text{dielectric}}(\hat{\mathbf{n}}) = -\frac{1}{2} \varepsilon_0 \Delta\varepsilon (\hat{\mathbf{n}} \cdot \mathbf{E})^{\mathbf{2}}. \tag{2.17}$$

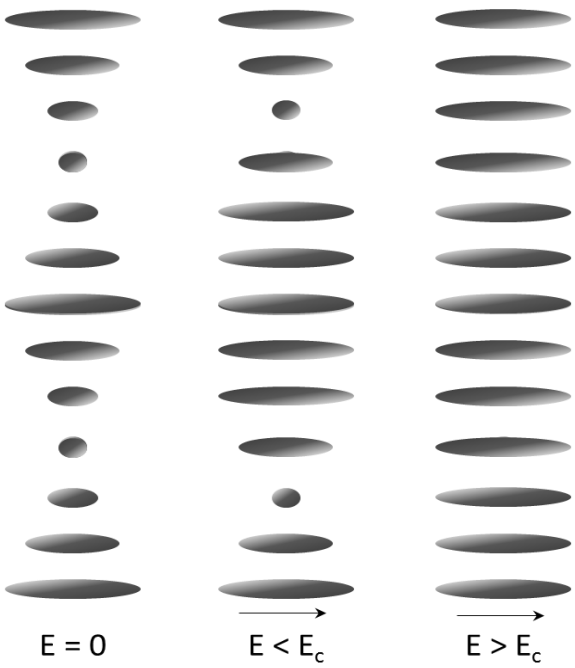

Figure 2.7 Dielectric helix unwinding. The helix distortion in a chiral nematic LC with $\Delta\varepsilon > 0$ when an electric field *E* is applied perpendicular to the helical axis.

From Equation 2.17, it can be found that the dielectric free-energy is negative as it represents the energy the molecules used to change the director profile. For chiral nematic LCs, the helical structure can be unwound if the electric field is sufficiently large to overcome the twist component k_2 of the elastic distortion. This situation can only happen for a positive permittivity material whereby the director in bulk aligns parallel to the applied electric field. **Figure 2.7** shows helix unwinding as the applied electric field tends towards the value of E_c. The helical structure vanishes at $E > E_c$. The critical unwinding field E_c can be obtained according to the approach presented by de Gennes and Prost [37]

$$E_c = \frac{\pi^2}{p}\sqrt{\frac{k_2}{\Delta\varepsilon\varepsilon_0}} \qquad (2.18)$$

2.3.2 Elastic energy

When there are external factors applied to an LC cell (for example, different alignment layers on the cell-substrates, external electric or magnetic fields), the orientation of the LC director will no longer be constant. Instead, the director orientation will continuously change across the LC device. This continuous change is termed as an elastic deformation and causes a deviation of the LC director from the uniform equilibrium state (where the director is almost uniform through the medium and the LC system has the lowest energy). In addition, this change will also lead to an increase in the total energy of the system. There are three fundamental types of elastic distortion: splay, twist, and bend (as shown in **Figure 2.8**); the corresponding elastic constants are denoted by k_1, k_2, and k_3 and are called the Frank elastic constants [35, 37].

Frank elastic constants have been widely used to describe the elastic properties of the medium and, in this case, they have been used to show the stiffness of the LC response to any distortion. Typical magnitudes of the elastic coefficients are ~ 10 pN, although they vary for different liquid crystalline materials. The total frank elastic energy density is given by a splayed elastic distortion (the divergence of the director $(\nabla \cdot \hat{\mathbf{n}})$), a twist elastic distortion (the curl of the director dotted with the director $(\hat{\mathbf{n}} \cdot \nabla \times \hat{\mathbf{n}})$**)** and a bend elastic distortion (a cross-product of the director with the curl of the director field $(\hat{\mathbf{n}} \times \nabla \times \hat{\mathbf{n}})$**)** [35, 38].

$$f_{\text{elastic}}(\hat{\mathbf{n}}) = f_{\text{splay}}(\hat{\mathbf{n}}) + f_{\text{twist}}(\hat{\mathbf{n}}) + f_{\text{bend}}(\hat{\mathbf{n}}) \tag{2.19}$$

$$= \frac{1}{2}\{k_1[\nabla \cdot \hat{\mathbf{n}}]^2 + k_2[\hat{\mathbf{n}} \cdot (\nabla \times \hat{\mathbf{n}})]^2 + k_3[\hat{\mathbf{n}} \times (\nabla \times \hat{\mathbf{n}})]^2\},$$

when the mirror asymmetry is considered, the twist free energy term for the chiral nematic phase has to be slightly modified [35,38].

$$f_{\text{twist}}(\hat{\mathbf{n}}) = \frac{1}{2}k_2[\hat{\mathbf{n}} \cdot (\boldsymbol{\nabla} \times \hat{\mathbf{n}}) + q]^2 \tag{2.20}$$

where $q = \frac{2\pi}{P}$ is the helix wavenumber. The reason why the q term is added into the twist free energy term is that the chiral system has two different handedness. For chiral nematic LCs, the helical axis is set along the *z*-direction. The gradient operator, therefore, acts along the *z*-axis on the director field defined as a function of the tilt angle θ (z) = *qz* which generates energy components in the z-dimension. Through simplifying the term in (2.20), the lowest energy state for the chiral nematic LC system to exist in can be obtained: $f_{\text{twist}}(\hat{\mathbf{n}}) = -q$.

The elastic properties of LCs play an essential role in various applications such as switchable diffraction gratings and LC displays [38]. The Frank elastic energy equation in (2.19) relates different distortions to their elastic potential energy and has proven highly successful in terms of modelling the behaviour of LCs on a macroscopic scale.

$[\boldsymbol{\nabla} \cdot \hat{\mathbf{n}}\,]$ $[\hat{\mathbf{n}} \cdot (\boldsymbol{\nabla} \times \hat{\mathbf{n}})]$ $[\hat{\mathbf{n}} \times (\boldsymbol{\nabla} \times \hat{\mathbf{n}})]$

Figure 2.8 Three different elastic distortions**.** Illustrations of the splay $(\nabla \cdot \hat{\mathbf{n}})$, twist $(\hat{\mathbf{n}} \cdot \nabla \times \hat{\mathbf{n}})$ and bend $(\hat{\mathbf{n}} \times \nabla \times \hat{\mathbf{n}})$ elastic distortions of the nematic director field.

2.4 Jones Matrices

The 2 × 2 Jones matrix is a useful approach to model different polarisations of light propagating through birefringent media. For Jones calculus, the Jones matrix, M, represents the effect each optical component has on the polarisation state and J describes the polarisation state of the light. Therefore, multiplying the optical component M with the polarisation state J yields the polarisation state of the output light [39,40]. For example, let's assume that an LC sample is placed between crossed polarisers in an experiment. Here the first polariser forms an angle θ with respect to the director, as depicted in **Figure 2.9**.

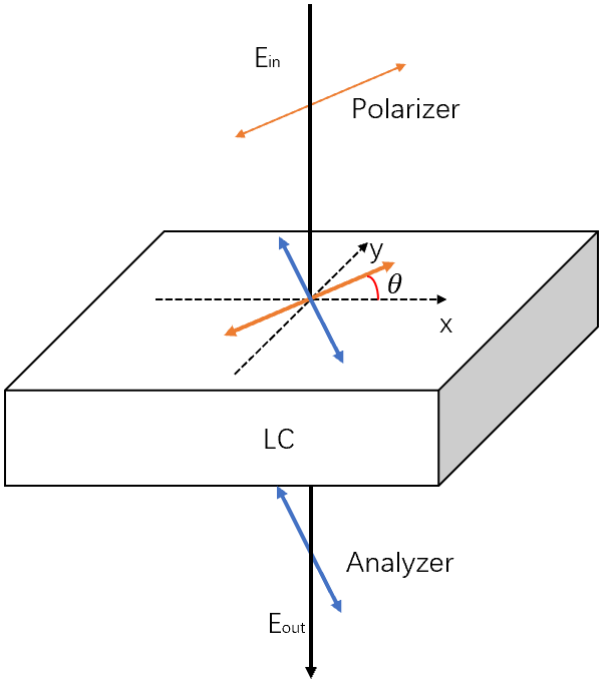

Figure 2.9 Light travelling through an LC layer between crossed polarisers. The LC material will change the polarisation state of the input light and the output polarisation state can be calculated using Jones calculus.

The output light after the polariser takes the form,

$$E_{in} = \begin{pmatrix} E_x \\ E_y \end{pmatrix} = \begin{pmatrix} E_0 \cos\theta \\ E_0 \sin\theta \end{pmatrix} \tag{2.21}$$

Light changes its polarisation after passing through the LC sample,

$$E_{lc} = \begin{pmatrix} E_x e^{jk_1 z} \\ E_y e^{jk_2 z} \end{pmatrix} \tag{2.22}$$

where $k_1 = \frac{2\pi n_e}{\lambda}$ and $k_2 = \frac{2\pi n_0}{\lambda}$. Finally, the output light after transmitting through the second polariser can be written as

$$E_{out} = E_0 \sin(2\theta) \sin\left(\frac{\Delta k d}{2}\right) e^{\frac{i(k_1+k_2)d}{2}} \begin{pmatrix} \sin\theta \\ \cos\theta \end{pmatrix} \tag{2.23}$$

where $\Delta k = k_1 - k_2$. The output light intensity after the analyser

$$|E_{out}|^2 = {E_0}^2 \sin^2(2\theta) \sin^2\left(\frac{\Delta k d}{2}\right) = I \sin^2(2\theta) \sin^2\left(\frac{\pi \Delta n d}{\lambda}\right) \tag{2.24}$$

From equation (2.24), it can be found that the intensity of the output light is dependent upon the phase shift, which is determined by $\frac{\pi \Delta n d}{\lambda}$ where d is the thickness of the LC cell and Δn is the birefringence of the material. For a certain LC between crossed polarisers, if the cell is quite thin, the ordinary and extraordinary components do not become significantly out of phase. However, if the phase difference equals π, then all of the incident light will be blocked by the second polariser. In addition, if equals 0, $\frac{\pi}{2}$ or π, there is also no transmitted component and the cell will appear dark.

2.5 Surface alignment of LCs

Uniform alignment of the LC director is crucial for almost all LC device applications. The permanence of the alignment is necessary for the lifetime of the device. In general, the alignment of the LC director is formed by the substrate surface and the direction of the alignment is determined by the balance between the LC surface tension and the substrate surface tension. If the LC surface tension is bigger than the substrate surface tension, the LC director tends to order themselves perpendicular to the device substrate as the intermolecular forces between the LC molecules dominate. The LC director will reorient parallel to the device substrate if the value of substrate surface tension is bigger

than the LC surface tension. When the LC surface tension is approximately equal to the substrate surface tension, the director tends to adopt a tilted alignment and the tilt angle is determined by the difference between those two forces [41].

According to the orientation of the director, the LC alignment can be classified into three main configurations (**Figure 2.10**): homeotropic (vertical) alignment where the director is approximately perpendicular to the device substrate; homogeneous (planar) alignment where the direction of the director tends to be parallel to the device substrate; and tilted alignment where the angle between the director and device substrate is between 0 and $\frac{\pi}{2}$ [21].

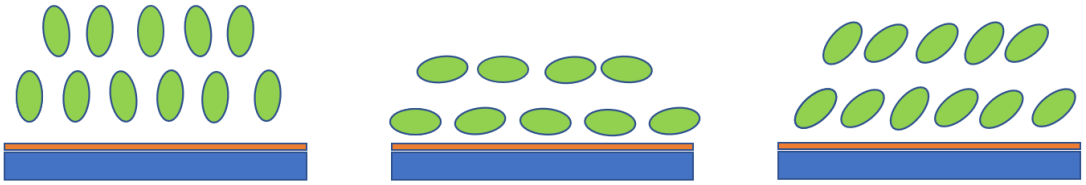

Figure 2.10: Liquid crystal alignments on substrates with different surface alignment conditions: (a) homeotropic, (b) homogeneous, and (c) tilted.

There are various substrate surface treatment methods to generate different alignment conditions to orient the LC director. Each of these methods has its merits and demerits and it is important for all LC applications to have a reliable control on the LC alignment.

Mechanical Rubbing

One of the most commonly used methods for creating alignment of the LC director is mechanical rubbing of the device substrate [42]. In general, the glass substrate is

simply rubbed by a rubbing machine which contains: 1) a roller covered by a cloth; 2) an adjustable platform that can adjust the height of glass substrate; 3) a motor to drive the platform and roller; and 4) a controller to control the speed of the roller and movement of the platform (**Figure 2.11**). Before being exposed to the rubbing process, the glass substrate is first coated with an alignment material such as polyvinyl alcohol or polyimide using a technique such as spin coating.

The treated substrate is then placed on the rubbing machine platform and rubbed by the roller. The speed of the roller and platform needs to be controlled carefully as the alignment layer might be destroyed if the speed is too fast. In addition, it is also important to ensure the distance between the roller and the stage is suitable so that the rubbing strength can be controlled carefully to obtain a fine quality LC alignment layer. The rubbing process causes local heating and stretching of the alignment layer, which results in the alignment of the main chain of the polyimide layer and the generation of grooves in the direction of the rubbing. LC molecules tend to lie into those grooves to reduce surface energy which results in reorienting the director parallel to the rubbing direction. Normally, rubbing is used to obtain planar or tilted alignment depending on the properties of the alignment material [43-45].

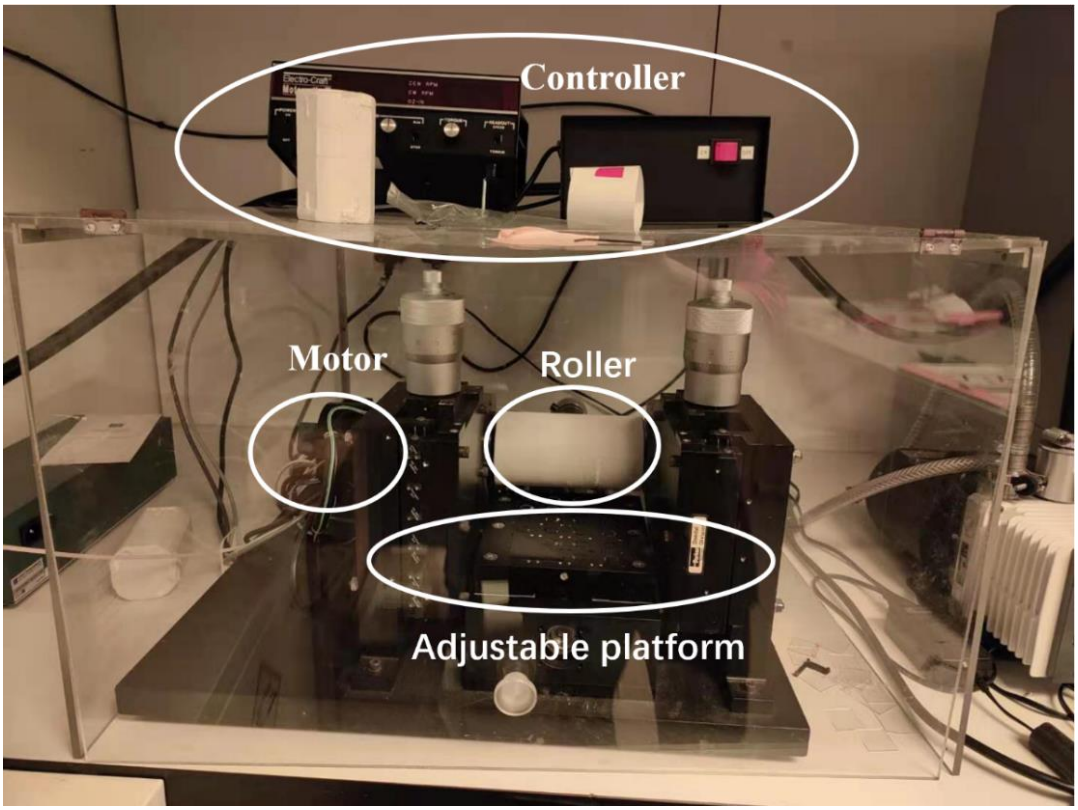

Figure 2.11. A rubbing machine that contains a roller, an adjustable platform, a motor and a controller.

Physico-chemical Technique

Alignment of LCs, especially homeotropic alignment, is often achieved by using a physico-chemical technique. For example, silane surface coupling agents are mostly used which normally contains two or more different kinds of molecular groups. At least one of the groups react with the substrate to form a stable bond, and at least one of the groups must be an orienting group that interacts with the LC molecules in such a way as to produce the desired orientation [46]. Basically, there are two methods to use surface coupling agents, one is to directly deposit them on top of the glass substrate, for instance, depositing N,N-Dimethyl-N-octadecyl-3-aminopropyltrimethoxysilyl chloride (DMOAP) (as shown in **Figure 2.12**) on the glass substrate to create alignment

layer to form planar alignment. Another one is to mix them with the LC material, for example, mixing surfactant lecithin (as shown in **Figure 2.13**) with LC to form homeotropic alignment [47-49].

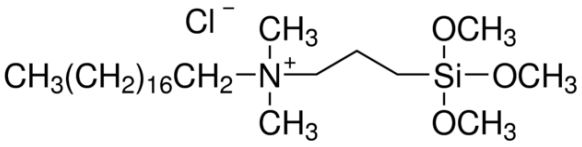

Figure 2.12 Chemical structure of DMOAP.

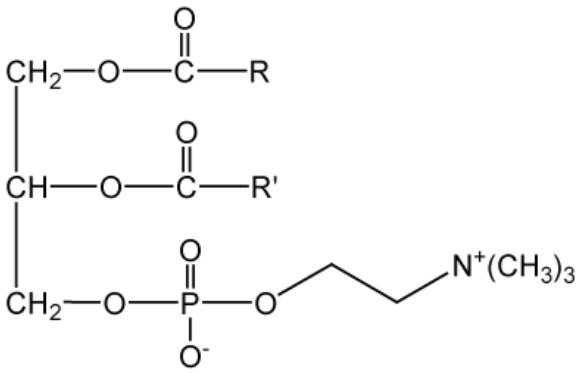

Figure 2.13 Chemical structure of lecithin.

Photoalignment technique

Recently, the photoalignment technique has attracted lots of interest as it is a non-contact process and can achieve high-quality LC alignment [46-51]. For the photoalignment technique, the alignment effect can be realised by illuminating a layer of photoresponsive material with linear polarised UV light [46]. The process of photoalignment is shown in **Figure 2.14**. In general, a thin layer of photoresponsive material is first coated on a clean glass substrate using spin coating. The thickness of the photoalignment layer needs to be carefully controlled by controlling the speed of the spin coater and the concentration of the photoresponsive material solution. After

that, the coated layer is exposed to linear polarised light where the spectrum of the light source lies in the near-ultraviolet or visible range. The linearly polarised UV light induces an anisotropic chemical reaction and hence causes the alignment material's surface orientational ordering. Following that, the processed substrates are combined together to form a cell where the LC material is injected into it.

Due to the ordering of the alignment material and intermolecular interactions, such as dipole-dipole, Van der Waals, hydrogen bonding, π stacking and steric interactions between the alignment material and the LC molecules, the direction of the fast axis of the LC director will be oriented either parallel or perpendicular to the direction of the polarisation of the UV light source, depending on the nature of the photoalignment material (whether the strongest absorption direction of the photoalignment material is along or perpendicular to their long molecular axis) [40, 41]. In work in this thesis, the photoalignment process is carried out using the sulphonic azo-benzene dye (SD1), which is able to orient the LC director perpendicular to the direction of the polarisation of UV light. The chemical structure is shown in **Figure 2.14**.

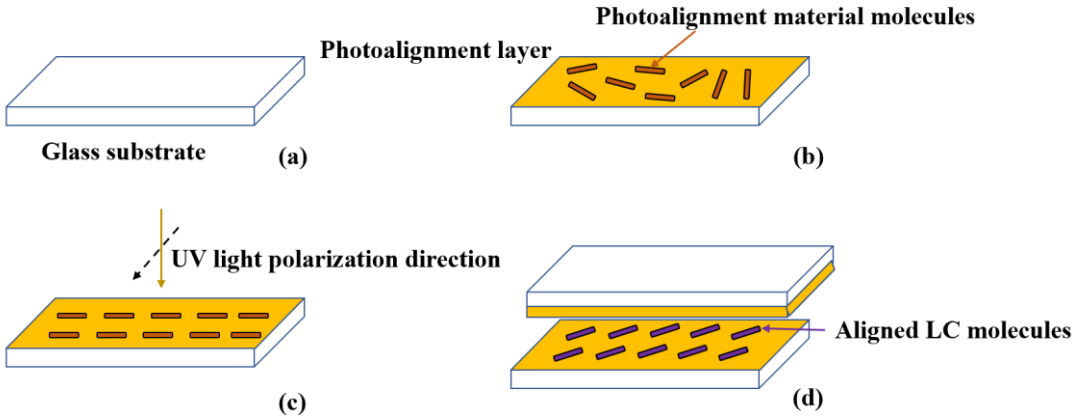

Figure 2.14 The photoalignment process: a) a clean glass substrate is prepared. b) the photoalignment material is coated onto the glass substrate. c) The alignment layer is illuminated by a linear polarised UV light source with a sufficient power density. d) Two substrates with coated alignment layers that orient the LC director perpendicular to the direction of polarisation of the UV light source.

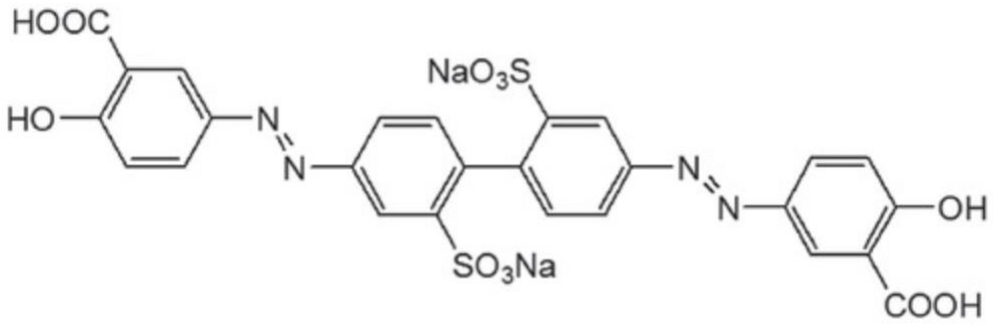

Figure 2.15 Chemical structure of SD1.

2.6 Liquid crystal spatial light modulators (SLMs)

Electrically controllable optical phase modulation is becoming increasingly desirable in a range of applications including holography [52], biomedical imaging [53], aberration correction [54], laser machining [55] and free-space optical communications [56]. Currently, there are a number of technologies available that can be used to modulate the phase of light, this includes optical micro-electromechanical systems (MEMS) and LC-based spatial light modulators (SLMs). Optical MEMS-based phase

modulators contain actuators and micro-mirrors. The most commonly used micro-mirror SLMs are the Texas Instruments' Digital Light Processing (DLP) line of Digital Micromirror Devices (DMDs) which can provide phase modulation and steering a large number of optical beams by driving the micromirrors vertically in a piston motion [57, 58].

Compared with other phase modulation technology, Optical MEMS-based phase modulators have several advantages: 1) the speed of the movement of the mirrors is only limited by the frequency of the micro-mirror, hence, their response can reach tens of kHz. 2) Optical MEMS-based phase modulators will not suffer from crosstalk between adjacent pixels and are polarization-independent which means they do not require control of the polarisation of the input light as is required for LC phase modulators [58]. However, because of the low wavefront quality control and the complexity of the fabrication for a large number of micromirror pixels, MEMS-based phase modulator devices have limited practical use compared with other rival technology [59].

Various incarnations of LC SLMs have been developed over many years combining the merits of high-performance complementary metal oxide semiconductor (CMOS) technology with the unique electro-optical properties of LC materials [60]. In those devices, optical phase modulation is achieved by applying an electric field across a thin LC layer which results in a corresponding change in the refractive index of the material. Such devices are usually called Liquid Crystal on Silicon (LCOS) SLMs. The structure of an LCOS device is similar to conventional LC devices except that a silicon

backplane is added into the system (**Figure 2.16**). The silicon CMOS backplane contains electronic circuitry that is buried underneath pixel arrays to provide a high 'fill factor'. Each pixel is made of aluminium mirrors deposited on top of the silicon backplane. By applying different voltages to each pixel, the phase retardance of each incident wavefront can be altered [60]. Currently, there are two kinds of modulation for LCOS devices: phase modulation and amplitude modulation. As mentioned previously, the output light intensity is proportional to the phase shift which is determined by $\frac{\pi \Delta n d}{\lambda}$ where d is the thickness of the LC layer and Δn is the birefringence of the material. However, amplitude modulation is not the focus of this thesis and hence will not be discussed here. For phase modulation, the phase shift is accomplished by electrically adjusting the optical refractive index along the light path which is possible because of the birefringence of the LC. For phase modulators, it is important to make sure that no amplitude modulation is included in the system.

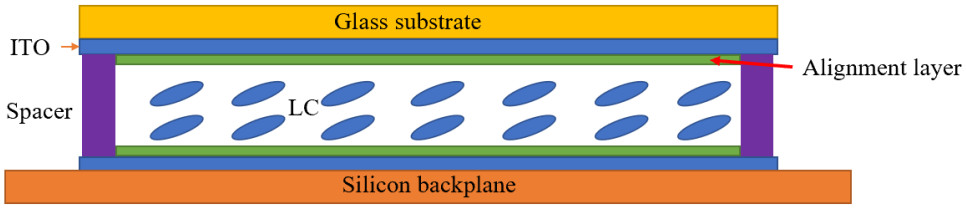

Figure 2.16 The architecture of an LCoS. It involves a glass substrate with transparent indium tin oxide (ITO) electrode, two alignment layers, LC material and a silicon backplane.

Depending on the LC mesophase that is used as the active layer inside of the device, LC-SLMs can be divided into two main categories: nematic LC and ferroelectric LC. Planar aligned nematic LC-SLMs are of interest as they can provide multi-level phase

modulation. However, due to the limited switching speeds available with standard nematic materials their frame rate is restricted to frequencies less than 1 kHz [61]. A fast response time is often highly sought after because it means that the device can transmit more information at relatively short timescales. Since most nematic LC devices consist of a relatively thick LC layer, which is required in order to achieve a 2π phase modulation, this results in an increase in the response time. The conventional approach to reducing the response time is to increase the electric field amplitude applied across the LC layer, but this comes at the expense of a high driving voltage, which is generally not desirable [62-65]. Various types of nematic LC electro-optic structures have been tested and investigated in LCoS devices, such as the twisted nematic and vertically aligned nematic (VAN).

The twisted nematic electro-optic effect has been widely used in various LC applications. In the twisted nematic LC device, the direction of alignment of the two glass substrates are perpendicular to each other so that the LC director completes a $\frac{\pi}{2}$ degree rotation across the LC cell, as shown in **Figure 2.17**. The LC director in the middle of the LC cell can be controlled by the strong interaction between the LC director and the substrate, which is referred to as anchoring. In a twisted nematic LC cell, the device is switched between "on" and "off" states by changing the electric field [66]. When there is no voltage applied between the substrates, the LC director remains in its original state. The polarised light incident on the device undergoes a polarisation transformation where the polarisation of output light changes from linear to elliptic polarisation. In the 'on' state, the LC director is reoriented to align with the electric

field so that there is only one refractive index for all of the incident lights. Therefore, the light will not change its polarisation and be blocked by the analyser after passing through the LC layer. Through controlling the amplitude of applied voltage, the polarisation state of output light can be chosen [67].

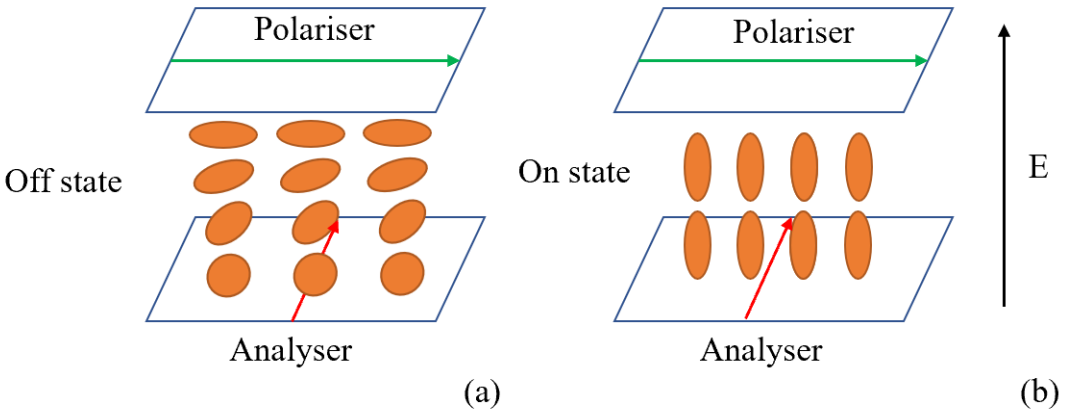

Figure 2.17 A schematic of the twisted nematic LC device in the (a) off state and (b) on state when an external electric field is applied normal to the LC layer. The arrow in red represents the direction of the analyser, whereas the green one represents the direction of the polariser.

Twisted nematic LCs have been considered for phase modulators, however, in order to generate phase modulation, the analyser and polariser must be removed as an incoming linear polarised beam may split into two beams (extraordinary beam and ordinary beam) when entering the LC device. Then each beam will suffer a different phase delay which is not desirable for making a phase modulator. Although this problem can be improved by adding a polarising filter that removes one polarisation state of the output light; however, in general, this process seriously reduces the efficiency. The polarisation crossover leads to the modulation in both the phase and the

polarisation, which makes the twisted nematic electro-optic effect undesirable for a phase-only modulator.

VAN device has also been used in making phase modulators [70]. The direction of the polariser is set to $\frac{\pi}{4}$ degree with respect to the director and is also perpendicular to the analyser. The LC director forms a homeotropic alignment where the LC director is aligned perpendicular to the device substrate as shown in **Figure 2.18**. Different from twisting nematic LC, when no external electric field is applied (off state), the polarisation of the incident light will not be changed and hence be blocked by the analyser. The LC director will reorient when an electric field is applied, and the polarisation of the incident light will be altered. Although VAN has been widely used in displays as the crossed polarisers can block most of the light leading to high contrast ratio, it has many issues when this structure is used for making phase-only LCoS devices since the value of the dielectric anisotropy should be negative, which is usually smaller than that of positive dielectric anisotropy [20]. Hence, a phase-only LCoS device using a VAN configuration normally has a high threshold voltage and long response time.

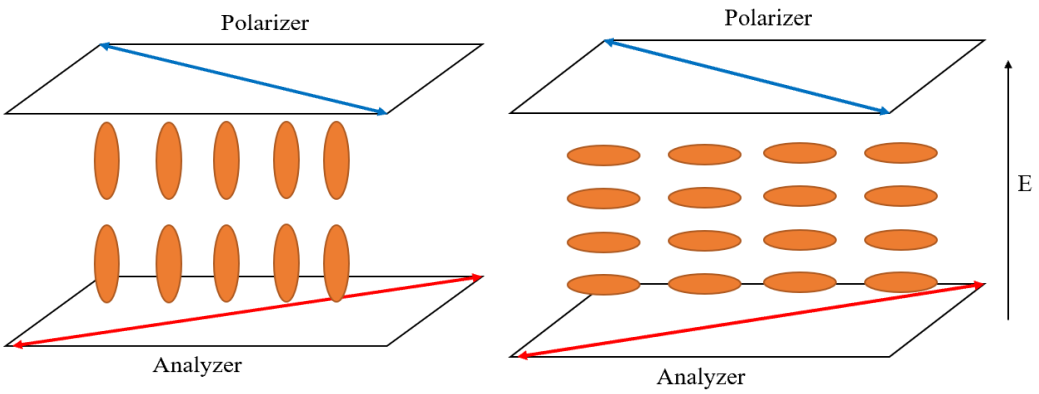

Figure 2.18 A schematic of the LC VAN under (a) off state and (b) on state when an external electric field is applied normal to the LC layer. The arrow in red represents the direction of the analyser, whereas the blue arrow represents the direction of the polariser.

More recently, various incarnations of nematic LC SLMs have been developed. For example, Huang has demonstrated a novel phase modulator with three new LC mixtures which exhibit a relatively high birefringence (Δn) and modest dielectric anisotropy ($\Delta\varepsilon$). The phase modulator can achieve 2π phase change with ~3 ms response time at 40°C. The working electric field for this device is about 3 V/μm [68]. Besides, Lee has designed a multilayer (2 or 3 layers) LC cells by using direct laser writing technology which can achieve 4 times or 7 times faster response time (15 ms or 9 ms) than that of conventional single-layer LC phase modulator of equivalent thickness [69]. Although people have used different methods to develop fast response nematic LC phase modulator, they still cannot achieve sub-millisecond response times, the reason why this happens is because the response time of the nematic LC cell is determined by [70]

$$\tau = \frac{\gamma d^2}{\pi^2 k_1} \tag{2.25}$$

where γ is the rotational viscosity, τ is the response time, k_1 is the splay elastic coefficient of the employed LC and d is the cell thickness. From the equation, it can be found that the response time is proportional to the cell thickness. The thickness of the cell is normally a few micrometres which causes difficulty in reducing the response time to sub-millisecond. As mentioned previously, researchers have tried to use multilayer structures to decrease the response time, but this approach increases the cell thickness which results in a large driving voltage which is also not desirable. In addition, the relationship between driving voltage and phase change is nonlinear which means it is not easy to characterise the phase behaviour of the system.

Ferroelectric LC (FLC) SLMs, on the other hand, can offer much faster frame rates, overcoming the slower switching speeds of nematic LC technology (as shown in **Figure 2.19**). Unfortunately, due to the bi-stable nature of the switching mechanism in standard ferroelectric LC material device configurations, they are commonly only suitable for binary phase modulation and are typically not able to provide analogue phase modulation. Although the subframe sequential technique is used to achieve multi-level modulation, this technique loses at least half of the incident light which results in very low efficiency [71, 72].

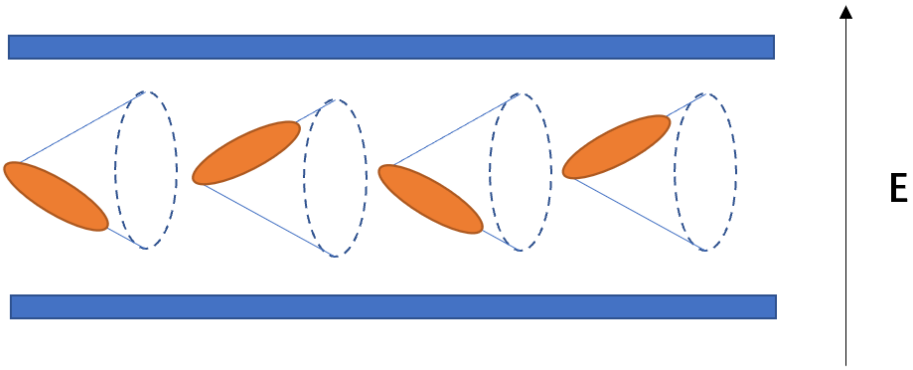

Figure 2.19 Schematic of the ferroelectric liquid crystal (FLC) device for phase modulation.

For nematic LCs and FLC, there are several issues that exist, such as slow response time and binary phase modulation, respectively. Hence, in this thesis, we demonstrate a flexoelectro-optic LC phase-only device that uses a chiral nematic reflector to achieve full 2π phase modulation [73-74]. This configuration is found to be very tolerant to imperfections in the chiral nematic reflector provided that the flexoelectro-optic LC layer fulfils the half-wave condition. Encouragingly, the modulation in the phase, which operates at kHz frame rates, is also accompanied by low amplitude modulation. In addition, we have also successfully combined these optical components into a cell to make an integrated device, which is particularly promising for the development of next-generation LCoS-SLMs.

2.7 Beam steering system

There has been a growing demand for increased data rates while the available radio spectrum has reached its limit. The spectral efficiency of radio frequency communication is saturating. Thus, research has shifted to alternative communication

technology such as visible light communication which is believed to be a potentially disruptive form of wireless communication [75]. Compared with traditional wireless communication, visible light communication takes advantage of the fast-growing light emitting diode technology and has the potential to reach speeds that are around 100 times faster than Wi-Fi implementations [75]. However, due to the much greater attenuation during transmission (the reflected energy is extremely low) and low mobility, visible light communication has not been widely accepted for daily usage [75]. Hence, in order to improve the reception of this technology, an appropriate beam steering system is crucial which can enhance the efficiency and mobility of the system.

Beam steering is crucial for many technological applications, such as optical communications [76], VR/AR displays [77], LiDAR [78], microscopy [79], and laser micro-machining [80]. Currently, there are a number of beam steering methods that have been demonstrated. Generally, these can be divided into two categories: mechanical and non-mechanical methods. Mechanical approaches include rotating prisms, Gimbal, fast steering mirror (FSM), rotating polygon scanning mirror, piezo actuators, lenslet array and micro-electromechanical systems (MEMS) [81, 82] (as shown in **Figure 2.20**). Compared with the non-mechanical approach, mechanical-based approaches are widely adopted due to the fact that they can provide fast, reliable, and inexpensive beam steering, but mechanical approaches generally suffer from problems such as relatively short lifetimes, large power consumption, high cost and their biggest issue is that the size: if they are small, they require magnification after the beam is steered. However, the steering angle is decreased with magnification. Therefore,

in order to obtain a sufficient steering angle, the magnification needs to be small which is not desirable for most applications [83].

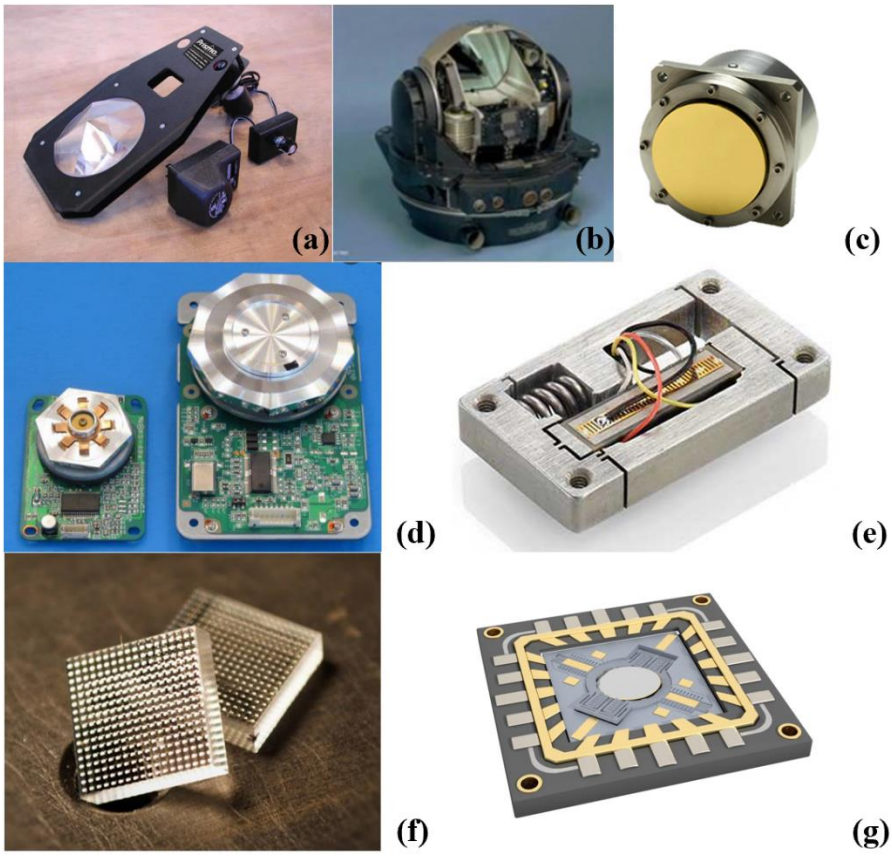

Figure 2.20 Mechanical Approaches to Beam Steering, a) rotating prisms b) Gimbal c) Fast Steering Mirror (FSM) d) Rotating polygon scanning mirror e) piezo actuators f) Lenslet Array and d) MEMs.

On the other hand, non-mechanical beam steering methods have attracted a lot of interest due to the fact that they are lightweight and inexpensive [84, 85]. For example, steering an optical beam with an SLM can be understood from the Huygens principle, where a plane wave can be divided into a series of spherical waves. By considering each pixel of the SLM as an individual wave source, the direction of the wavefront can be changed by adjusting the phase of the individual pixels as shown in **Figure 2.21**. As each pixel's phase has been changed, there is a phase ramp across the SLM (as shown

in the figure). This phase ramp leads to the wavefront being tilted by an angle, θ. In practice, in order to generate enough steering angle, a large phase ramp is required which is beyond the capability of current SLM technology [85]. In fact, most nonmechanical beam steering methods face similar problems such as slow response times, low efficiency and small diffraction angles. In order to solve these issues, many approaches have been proposed, for example, a 'modulo 2π' architecture has been proposed. For any sine wave, 0, 2π, 4π and 2nπ phase shift will not affect the final result. Therefore, as one moves across the width of the prism, one can 2πn of phase every time when phase reaches 2πn, resulting in a saw tooth phase profile [85]. This phase profile can be regarded as propagation from a full prism and steers light in the same manner. Through this method, we can maximise the beam steering angle. However, this method increases the size and cost of the system which is still not desirable [85].

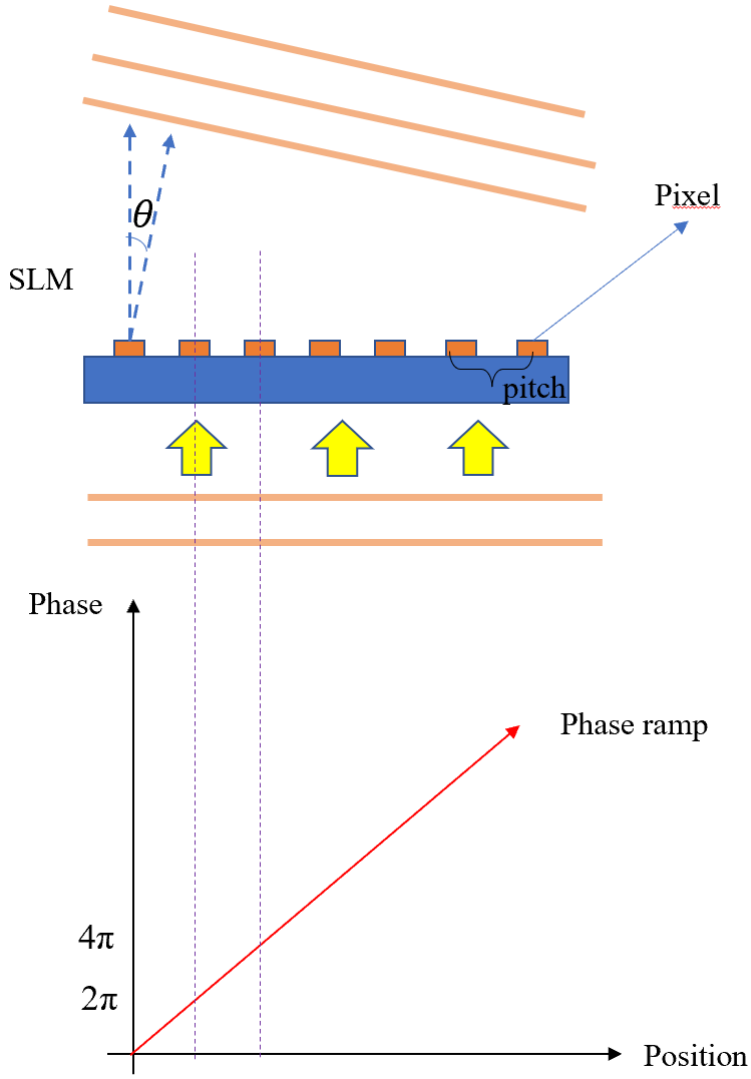

Figure 2.21 Illustration of beamsteering with an SLM.

Recently, there has been considerable interest in the use of polarisation optics (typical elements include lenses, gratings and deflectors) in combination with variable retarders to engineer new photonics technologies [86, 87]. In this thesis, a new optical phase shift technique is presented that combines switchable flexoelectro-optic LC layers, aligned in the so-called uniform lying helix configuration, together with quarter-wave plates to achieve sub-millisecond full 2π phase modulation. This new technology could also potentially be configured as a dynamic switch to control the polarisation

state. By combining commercial off-the-shelf polarisation-gratings with recently developed LC technology, this thesis describes the development of a new type of optical beam-steering device which has substantial potential in Optical Communications and Holographic projection. The details of this device configuration are presented in chapter 7.

2.8 Conclusion

The fundamental concepts of LC materials have been introduced in this chapter. The key principles regarding the free-energy and the physical properties have also been discussed, which will be used later in the thesis when analysing the flexoelectro-optic effect that has been employed in the SLM technology. Besides, the conventional techniques for aligning LCs have also been discussed in this chapter, which is quite important for the application presented in the following chapters. Finally, this chapter also contains information about LC SLM technologies and beam steering devices, which will be considered further in the following chapters. The next chapter presents a new approach to characterising the flexoelectro-optic effect in chiral nematic LCs. The following chapters then employ the use of the flexoelectro-optic effect to develop a new SLM technology.

Chapter 3 Characterisation of large tilt-angle flexoelectro-optic switching in chiral nematic liquid crystal devices

3.1 Introduction

Electro-optic phenomena in liquid crystal (LC) materials are crucial for optoelectronic devices and switchable photonic technologies [88-91]. LCs have been widely used in high-performance light modulators such as spatial light modulators (SLM) and displays [88]. However, traditional electro-optic effects based upon dielectric coupling typically exhibit a slow response time, which cannot satisfy the needs of next-generation SLM technology. Therefore, there is interest in considering alternative fast-switching electro-optic effects such as the flexoelectro-optic effect, which reduces the response time to a sub-millisecond range. This opens up the potential for developing the next-generation of LC on silicon (LCoS) SLMs. In this chapter, a new and straightforward method for characterizing the flexoelecto-optic effect is presented.

3.2 Material Preparation

As mentioned in the previous chapter, LC materials, such as 4′-pentyl-4-cyanobiphenyl (5CB), contain rigid rod-like molecules that normally form the nematic phase with long-range orientational order and no positional order. In this chapter, the LC dimer 1,7-bis-4-(4′-cyanobiphenyl) heptane (CB7CB), is considered which consists of two rigid cyanobiphenyl segments connected by a flexible aliphatic link with seven methyl groups. The chemical structure of CB7CB is shown in **Figure 3.1**. This LC exhibits the

twist-bend nematic phase, whereby the density of the material is uniform but its director rotates helically around a cone to form a spatially modulated director field with an extremely small pitch. In addition to the twist-bend nematic phase, this dimer also exhibits another twist-bend state called the oblique helicoidal phase. This normally occurs when the CB7CB is doped with a small percentage by weight of chiral additive and subjected to an externally applied electric or magnetic field at a specific temperature [89]. This phase is out of the scope of this thesis and will not be discussed here.

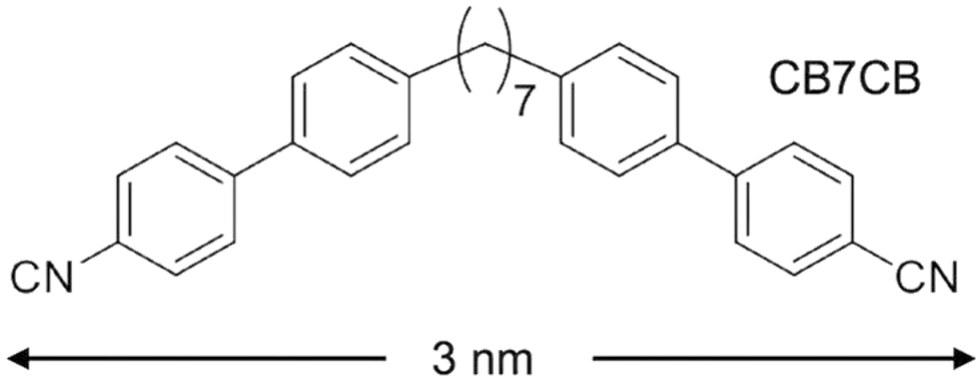

Figure 3.1 The chemical structure of CB7CB.

3.2 Flexoelectricity

Flexoelectricity was first proposed by Meyer in 1969 which is analogous to piezoelectricity in crystalline solids. The phenomenon involves the direct coupling between the electric polarisation and director curvature distortions [90, 91]. Flexoelectricity is attributed to the shape asymmetry and permanent dipole moments of LC molecules. Flexoelectricity is usually discussed with reference to molecules that are either pear shape with a longitudinal dipole or banana-shaped with a transverse dipole.

As shown in **Figure 3.2**, the molecules are arranged in the absence of an external electric field with their long axes and dipoles aligned randomly so that there is no net polarisation. However, when an external electric field is applied, the dipoles of the LC molecules tend to change to the direction parallel to the electric field. For pear-shaped molecules, the field induces a splay deformation in the LC director profile whereas for the banana-shaped molecules, it causes a bend deformation of the director profile [92]. Mathematically, the flexoelectric polarisation can be described in magnitude and direction by the splay (e_1) and bend (e_3) flexoelectric coefficients as

$$\mathbf{P_f} = e_1 \hat{\mathbf{n}} (\nabla \cdot \hat{\mathbf{n}}) + e_3 (\nabla \times \hat{\mathbf{n}}) \times \hat{\mathbf{n}}. \qquad (3.1)$$

where $\hat{\mathbf{n}}$ represents the director, and e_1 and e_3 are the splay and bend flexoelectric coefficients, respectively.

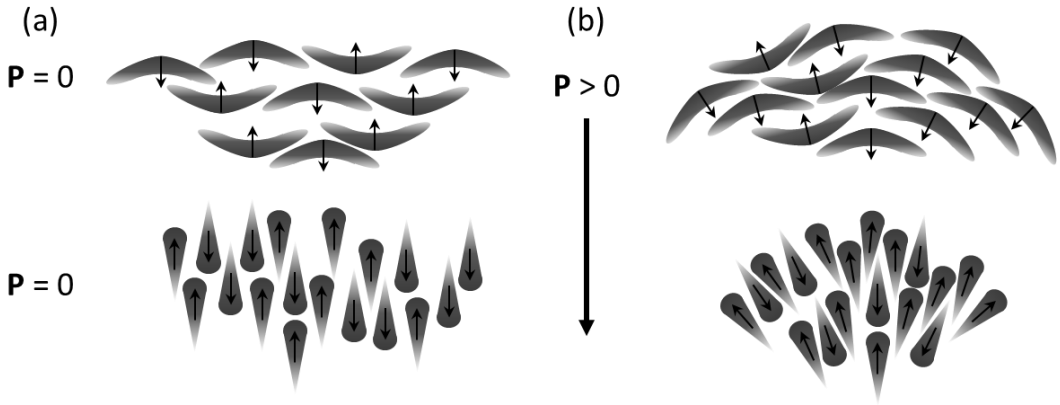

Figure 3.2. The flexoelectric polarisation. The schematic shows "pear" and "banana" shaped molecules (a) with no net polarisation and (b) constrained to bend and splay geometries, respectively, which result in the generation of a net flexoelectric polarisation.

When considering the free energy of the system, a term needs to be included to describe the coupling between the flexoelectric polarisation and an applied field that takes the form $f_{\text{flexo}}(\hat{\mathbf{n}}) = -\mathbf{P}_{\text{f}} \cdot \mathbf{E}$**.** The free energy due to the flexoelectric effect is therefore given by [92]

$$f_{\text{flexo}}(\hat{\mathbf{n}}) = -\mathbf{P}_{\text{f}} \cdot \mathbf{E} = -[e_1 \hat{\mathbf{n}}(\nabla \cdot \hat{\mathbf{n}}) + e_3(\nabla \times \hat{\mathbf{n}}) \times \hat{\mathbf{n}}] \cdot \mathbf{E} \qquad (3.2)$$

The full expression for the bulk free energy density of an LC in an external field **E** becomes

$$f_{\text{bulk}}(\hat{\mathbf{n}}) = f_{\text{elastic}}(\hat{\mathbf{n}}) + f_{\text{dielectric}}(\hat{\mathbf{n}}) + f_{\text{flexo}}(\hat{\mathbf{n}}) \qquad (3.3)$$

$$= \frac{1}{2}\{k_1[\nabla \cdot \hat{\mathbf{n}}]^2 + k_2[\hat{\mathbf{n}} \cdot (\nabla \times \hat{\mathbf{n}}) + q]^2 + k_3[\hat{\mathbf{n}} \times (\nabla \times \hat{\mathbf{n}})]^2\} - \frac{1}{2}\varepsilon_0 \varepsilon_\perp E^2$$
$$- \frac{1}{2}\varepsilon_0 \Delta\varepsilon(\hat{\mathbf{n}} \cdot \mathbf{E})^2 - [e_1 \hat{\mathbf{n}}(\nabla \cdot \hat{\mathbf{n}}) + e_3(\nabla \times \hat{\mathbf{n}}) \times \hat{\mathbf{n}}]$$

In chiral nematic LCs, the coupling between electric fields and flexoelectricity can lead to a macroscopic rotation of the optic axis, which may be as fast as 100 μs for short pitch (<300 nm) chiral nematic LCs [93-95]. This electro-optic behaviour is typically referred to as the flexoelectro-optic effect and is observed when an electric field is applied orthogonal to the helical axis of the chiral nematic LC. The rotation of the optic axis is about the electric field direction which is shown in **Figure 3.3**. The most commonly studied configuration involves a Uniform Lying Helix (ULH) alignment of the chiral nematic LC whereby the helical axis is aligned parallel to the device substrates [93-103], as shown in **Figure 3.4**.

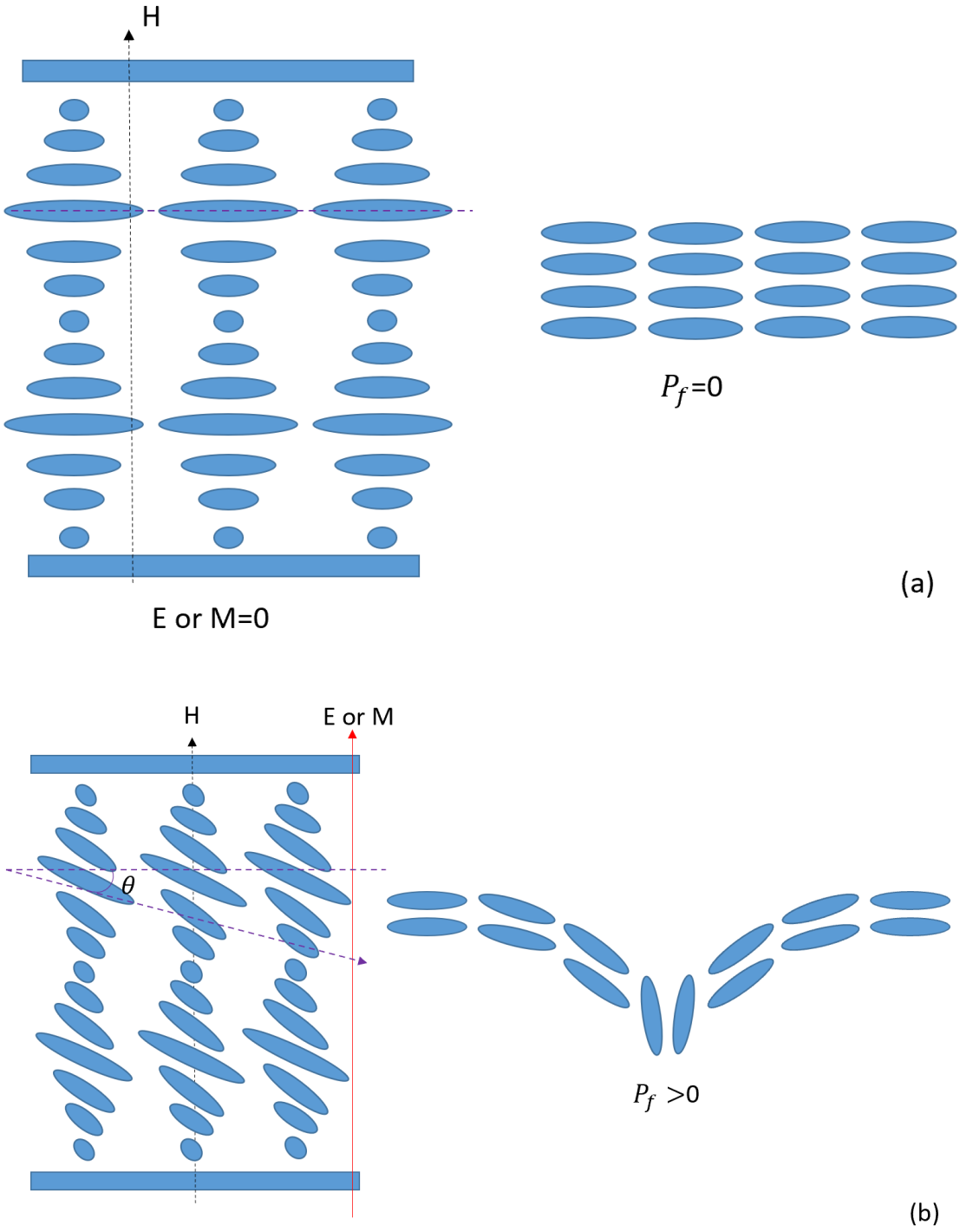

Figure 3.3. The flexoelectric effect in chiral nematic LCs. (a) Left: the helical structure in the absence of an applied electric field. Right: Bouligand plane reveals no splay or bend distortion. (b) Left: The flexoelectric tilt of a chiral nematic LC under the application of an electric field perpendicular to the helical axis. Right: Bouligand plane of the director tilted with respect to the helix reveals the splay-bend distortion that induces the flexoelectric polarisation.

3.3 ULH Alignment

The ULH configuration has attracted lots of attention for short pitch (<500 nm) chiral nematic LCs as it provides a route towards fast in-plane switching for display technology [92, 93, 98]. Unfortunately, the ULH structure is intrinsically unstable as it is not a minimum energy state and is incompatible with planar and homeotropic alignments. Hence, in order to generate ULH configuration, large periodic distortions or defect lines are necessary to be introduced close to the surface [92, 93] which are normally generated by an electric field. Hence, it is impossible for negative dielectric anisotropy materials to form a ULH structure.

For positive dielectric anisotropy materials, the ULH configuration can be created by cooling down the sample from the isotropic phase while applying an electric field, but the ULH alignment generated by this method is quite poor. When the electric field is removed, the system will relax back to the lower energy Grandjean state where the helical axis is perpendicular to the confining surfaces. There have been many attempts to stabilise the ULH structure by using specially engineered devices or polymerisation [92,93,104]. However, both methods still require an electric field for the initial alignment. In addition, the switching angle is confined by the polymer network. For most applications, an appropriate concentration of polymer is essential for generating a stable ULH alignment so that suitable switching angles can be achieved at the same time [92, 93].

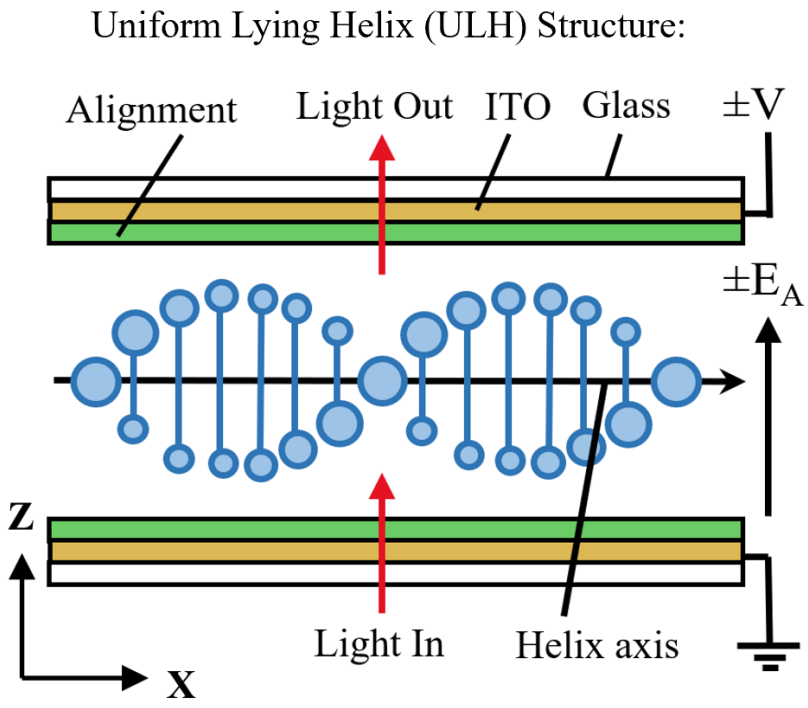

Figure 3.4. The geometry of a chiral nematic LC in the ULH alignment. The helical axis is along the *x*-axis and parallel to the substrate. The ULH is formed by applying an electric field.

3.4 Flexoelectro-optic effect

To understand the flexoelectro-optic behaviour, it is necessary to consider the total flexoelastic energy density for a chiral nematic LC, which can be expressed as a sum of the Frank elastic energy terms and the terms that describe the coupling between the flexoelectric polarisation and the electric field, which is applied perpendicular to the helical axis [96-98]. When the applied electric field E_x is perpendicular to the plane of the director in a nematic LC results in coupling to the difference between the flexoelectric coefficients (e_1 - e_3). The tilt angle, ϕ, defines the orientation of the director field in the yz-plane. Applying the electric field along the *y*-axis induces a twist, θ, in the xz-plane

$$\hat{\mathbf{n}} = \begin{pmatrix} n_x \\ n_y \\ n_z \end{pmatrix} = \begin{pmatrix} \cos\theta \\ 0 \\ \sin\theta \end{pmatrix} \tag{3.4}$$

Under the application of an electric field along the *y*-axis, E_y, the components of the director field along the *x, y* and *z*- axes can be written in spherical polar coordinates as

$$\hat{\mathbf{n}} = \begin{pmatrix} n_x \\ n_y \\ n_z \end{pmatrix} = \begin{pmatrix} \cos\theta \\ \sin\theta\cos\phi \\ \sin\theta\sin\phi \end{pmatrix} \tag{3.5}$$

where $\theta = qz$, The gradient operator can be written as

$$\nabla = \begin{pmatrix} 0 \\ 0 \\ \partial/\partial z \end{pmatrix} \tag{3.6}$$

Once the director field has been defined in this way, then the free-energies due to elastic and flexoelectric contributions can be derived. Through substituting (3.5) and (3.6) into expression (3.2), the flexoelectric free energy density can be written as

$$e_1[\hat{\mathbf{n}}(\nabla\cdot\hat{\mathbf{n}})] = e_1 q \sin\phi\cos^2\theta \tag{3.7}$$

$$e_3[(\nabla\times\hat{\mathbf{n}})\times\hat{\mathbf{n}}] = -qe_3\sin\phi\sin^2\theta \tag{3.8}$$

Hence, the free energy due to flexoelectricity is given by,

$$f_{\text{flexo}}(\hat{\mathbf{n}}) = -\boldsymbol{P}_f\cdot\boldsymbol{E} = -E_x q[e_1\sin\phi\cos^2\theta - e_3\sin\phi\sin^2\theta] \tag{3.9}$$

The free elastic energy components are given by (assuming that there is no dielectric anisotropy):

$$\tfrac{1}{2}k_1[\nabla\cdot\hat{\mathbf{n}}]^2 = \tfrac{1}{2}q^2k_1[\sin^2\phi\cos^2\theta] \tag{3.10}$$

$$\tfrac{1}{2}k_2[\hat{\mathbf{n}}\cdot(\boldsymbol{\nabla}\times\hat{\mathbf{n}}) + q_0]^2 = \tfrac{1}{2}k_2[{q_0}^2\cos^2\phi - 2qq_0\cos\phi + {q_0}^2] \tag{3.11}$$

$$\tfrac{1}{2}k_3[\hat{\mathbf{n}}\times(\nabla\times\hat{\mathbf{n}})]^2 = \tfrac{1}{2}k_3[\sin^2\theta\sin^2\phi\, q^2] \tag{3.12}$$

The total free elastic energy is therefore written as

$$f_{\text{elastic}}(\hat{\mathbf{n}}) = \frac{1}{2}k_1 \sin^2\phi \cos^2\theta\, q^2 + \frac{1}{2}k_2[\cos^2\phi\, {q_0}^2 - 2qq_0\cos\phi + {q_0}^2] + \frac{1}{2}k_3 \sin^2\theta \sin^2\phi\, q^2 \quad (3.13)$$

Averaging the energies in (3.10) and (3.13) over the length of one whole pitch by integrating with respect to z gives ($\int_0^P \cos^2\theta\, dz = \int_0^P \sin^2\theta\, dz = P/2$):

$$\frac{1}{P}\int_0^P f_{\text{flexo}}(\hat{\mathbf{n}}) \cdot dz = -\frac{1}{2}E_x(e_1 - e_3)\sin\phi\, q \quad (3.14)$$

$$\frac{1}{P}\int_0^P f_{\text{elastic}}(\hat{\mathbf{n}}) \cdot dz = \frac{k_1}{4}\sin^2\phi\, q^2 + \frac{k_2}{2}[q_0 - q\cos\phi]^2 + \frac{k_3}{4}\sin^2\phi\, q^2 \quad (3.15)$$

Hence, in equilibrium, the average free energy density is

$$\frac{\sin^2\phi q^2}{4}(k_1 + k_3) + \frac{k_2}{2}[q_0 - q\cos\phi]^2 - \frac{E_x}{2}(e_1 - e_3)\sin\phi\, q = 0 \quad (3.16)$$

Minimising Eq. 3.16 with respect to ϕ we get,

$$\sin\phi\left[\frac{(k_1 - 2k_2 + k_3)}{2k_2}\right] + \tan\phi - \frac{E_x(e_1 - e_3)}{2k_2 q_0} = 0 \quad (3.17)$$

For small tilt angles, the relationship between k_2, k_1 and k_3 can be approximated to $2k_2 = k_1 + k_3$, hence, (3.16) becomes [93-95]

$$\tan\phi = \left(\frac{e_1 - e_3}{k_1 + k_3}\right)\frac{\mathrm{E}}{q} \quad (3.18)$$

where

$$q = \frac{q_0}{\cos\phi} \quad (3.19)$$

In this case ϕ is the flexoelectric tilt angle, k_1 and k_3 are the splay and bend elastic coefficients of the LC, respectively, q_0 is the natural wavenumber ($q_0 = \frac{2\pi}{P_0}$ where P_0

is the natural pitch), q is the actual (field-dependent) wavenumber, and E is the applied electric field [93].

Equation (3.18) is often quoted as the relationship for the flexoelectro-optic tilt angle in terms of the flexoelastic ratio, $\frac{e_1 - e_3}{k_1 + k_3}$, which is considered to be an important parameter as it represents a *figure-of-merit* in terms of the performance of the device. The tilt angle, ϕ, changes sign on reversal of the applied electric field and for small tilt angles ($\tan\phi \approx \phi$) its magnitude increases linearly with the applied field. By virtue of this linear dependence, the flexoelastic ratio is commonly determined by measuring the electro-optic tilt angle, ϕ, over a range of applied electric field amplitudes and then extracting the gradient (in accordance with Equation (3.18)). Importantly, it can also be seen from Equation (3.19) that as the tilt angle increases, the field-induced wavenumber, q, of the helix increases corresponding to a decrease in the helical pitch. Therefore, this model is only relevant when the pitch is free to change (short pitch) on the application of an electric field.

Chiral nematic LCs with short pitch allows fast changes in the optical state leading to microsecond response times given by

$$\tau = \frac{\gamma q^2}{k_1 + k_3}, \tag{3.20}$$

where γ is the rotational viscosity [104]. The response time of conventional nematic LCDs is limited by the material viscosity (which causes different 'on' and 'off' state times). The ULH response time in Equation 3.20 is the characteristic time it takes for ϕ to relax to its equilibrium value in both directions ('on' and 'off' time). In addition,

from Equation 3.20, it can be found that the response time is independent of the device thickness, which is not the case for the characteristic timescale of an anti-parallel planar aligned nematic LC (Fréedericksz) cell. Instead, it is governed by the pitch of the chiral nematic. This is the reason why the flexoelectro-optic effect has attracted lots of attention as it has the potential to reduce the response times from milliseconds down to sub-milliseconds for next-generation displays and optoelectronic devices.

Even though it is possible for the pitch to change, it is quite common for the pitch to be fixed in practice. For example, a polymer network may be included to 'lock-in' a chosen alignment and prevent the helix from unwinding under high electric field amplitudes. In addition, for the ULH alignment, surface interactions, imperfections in the alignment, and trapped defects also tend to inhibit changes in the pitch when an electric field is applied. Therefore, it is perhaps more realistic to consider the case where the pitch is fixed by boundary conditions. To deal with a fixed pitch, a different model was proposed by Lee *et al* [23]. by constraining the wavevector to be $q = q_0$ when minimising the flexoelastic energy when subjected to an electric field to give the result [100, 105, 106]

$$\tan\phi = \frac{(e_1 - e_3)E}{2qk_2} - \frac{(k_1 - 2k_2 + k_3)sin\phi}{2k_2} \tag{3.21}$$

where k_2 is the twist elastic coefficient. Equations (3.18) and (3.21) are identical provided that $k_1 + k_3 = 2k_2$ or when the tilt angle is small so that $\sin\phi \approx \tan\phi \approx \phi$. However, for a given value $e_1 - e_3$, for typical monomesogenic nematic mixtures, the two characteristic parameter combinations are given in Equations (3.18) and (3.21)

can differ by around 15%-20%. The two parameter combinations can differ substantially if $2k_2$ differs substantially from $k_1 + k_3$. However, for certain potentially useful cases the two sets of parameters are similar.

For example, k_1 is typically around twice k_2. Therefore, for a material with a low value of k_3, which may be the case for certain bent-core or bimesogenic materials, $k_1 + k_3$ may be similar to $2k_2$ and the two parameters combinations would be similar.

One reason why the simple free pitch formula is commonly used even in cases where the helix pitch is not clearly free to vary is its simplicity. The formula for fixed pitch cannot be conveniently solved to determine ϕ as a function of the applied field. However, some progress can be made if we consider the series expansions for sine and tan.

Substituting series expansions for sine and tan into Equation (3.21) and expanding up to quintic terms we can write

$$\left[\phi - \frac{\phi^3}{6} + \frac{\phi^5}{120}\right]\left[\frac{k_1 - 2k_2 + k_3}{2k_2}\right] + \left[\phi + \frac{\phi^3}{3} + \frac{2\phi^5}{15}\right] = \frac{(e_1 - e_3)E}{2qk_2} \tag{3.22}$$

which can be rearranged to give

$$\phi(k_1 + k_3) + \phi^3\left[\frac{-k_1 + 6k_2 - k_3}{6}\right] + \phi^5\left[\frac{k_1 + 30k_2 + k_3}{120}\right] = \frac{(e_1 - e_3)E}{q} \tag{3.23}$$

Whether or not this can be used depends on how quickly the terms in the series converge. For example, if we consider the nematic LC, E7, and the tilt angle ϕ is 45°, then at this point, $\phi = 0.785$, $\phi^3 = 0.484$ and $\phi^5 = 0.299$. For E7, k_1, k_2 and k_3 are 11 pN, 6.5

pN and 11 pN, respectively. Hence the coefficients in the series expansion for ϕ, ϕ^3 and ϕ^5 are 28 pN, 1.83 pN and 1.86 pN, respectively. In comparison with the leading linear term, the cubic term is 4% and the quintic term is 2.5% of the leading term. In this case, higher order terms are substantially smaller.

For most LC materials, the quintic term value is quite small. Hence, Equation (3.23) can be simplified to:

$$\phi(k_1 + k_3) + \phi^3 \left[\frac{-k_1+6k_2-k_3}{6}\right] = \frac{(e_1-e_3)E}{q} \tag{3.24}$$

This can be rearranged to give an analytic solution for ϕ

$$\phi = \frac{\sqrt[3]{\sqrt{3}\sqrt{4a^3b^3+27b^4c^2}+9b^2c}}{\sqrt[3]{2}\,3^{\frac{2}{3}}\,b} - \frac{\sqrt[3]{\frac{2}{3}}a}{\sqrt[3]{\sqrt{3}\sqrt{4a^3b^3+27b^4c^2}+9b^2c}} \tag{3.25}$$

where

$$a = k_1 + k_3$$

$$b = \frac{-k_1 + 6k_2 - k_3}{6}$$

$$c = \frac{(e_1 - e_3)E}{q}$$

Here we show plots of (for E7 elastic parameters) the cubic expansion, the linear approximation, the tan/sin and tan ϕ (**Figure 3.5**). As can be seen in Figure 3.5, for a small electric field, the tilt angle values obtained from all the equations are

approximately the same. However, these values are quite different when a large electric field is applied on the device, especially for the tan approximation where the ϕ value is significantly smaller than values calculated by other equations. Hence, it is important to choose the appropriate Equation for large tilt angle calculation.

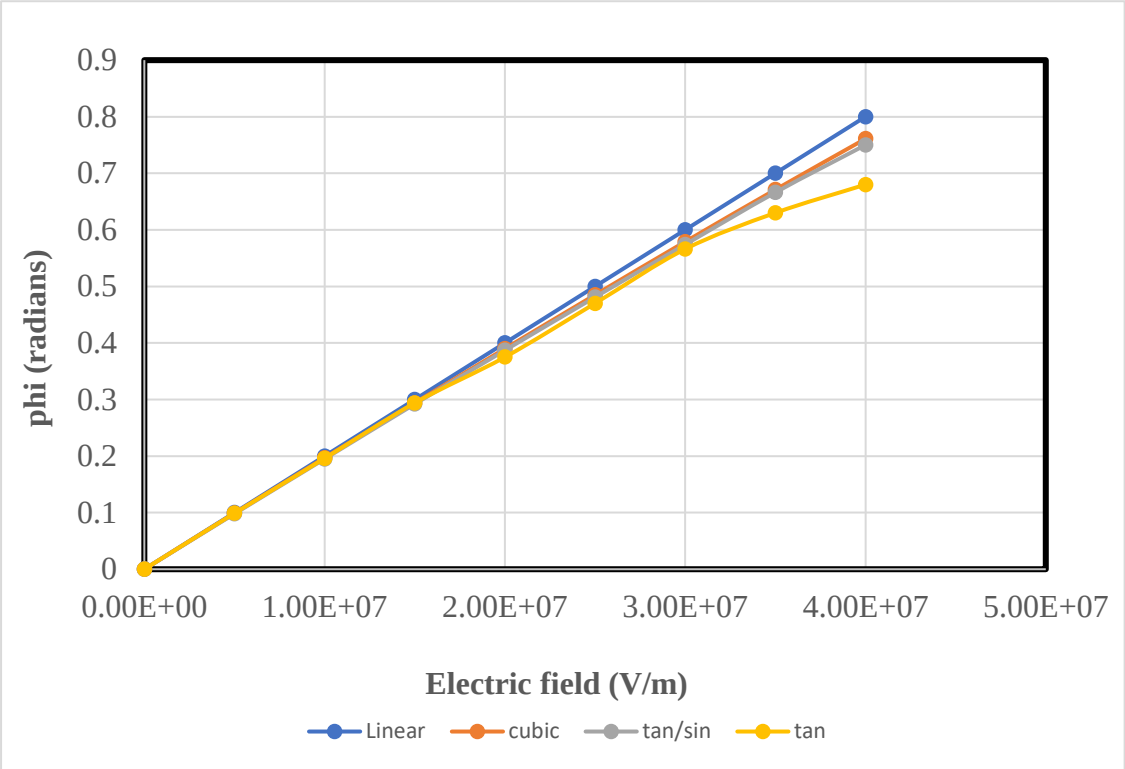

Figure 3.5. Tilt angles are calculated with different approximations. The blue line is based on a linear approximation of equation 3.23, the orange line is based on cubic approximation as shown in equation 3.24, the grey line is based on equation 3.21 and the yellow line is based on equation 3.18.

3.5 Experimental results

To investigate the above difference experimentally, it would be useful to observe the behaviour of a large switching angle material under applied electric fields. This can be most easily done by forming a ULH alignment and then observing the electric field

dependent transmission behaviour of the device placed between crossed polarisers. The configuration of the experimental setup is shown in **Figure 3.6**.

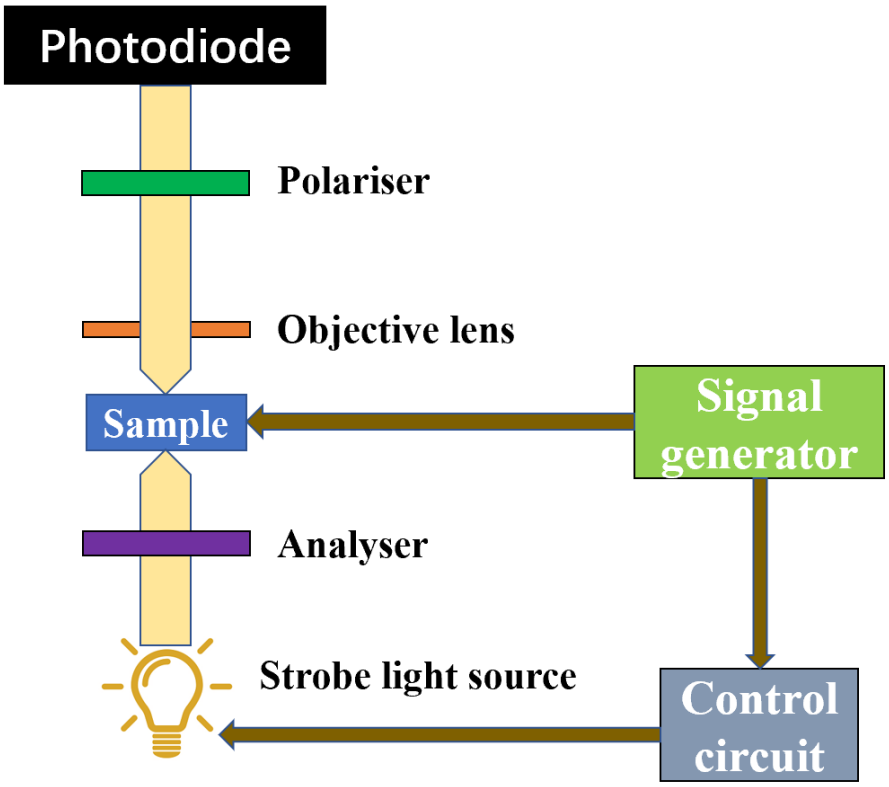

Figure 3.6. Experimental setup used for characterising the large tilt angle material. The sample is observed by using a photodiode installed on the polarization microscope. The light source of the microscope is replaced by a strobe light source so that the flexoelectro-optic switching can be seen. The strobe light source and sample are driven by signals generated by the signal generator. In the microscope, the polariser and analyser are set to be perpendicular to each other.

Before filling the mixture, the thickness of the empty cell was first determined by measuring the white-light transmission spectrum on a UV-Vis spectrometer (Agilent 8454). Thickness measurement is usually measured by measuring the interaction of the film with light. When light enters an empty cell, both the top and bottom surfaces of the

cell will partially reflect light. The total amount of reflected light is dependent upon the sum of these two reflections which can be constructively (add together) or destructively (subtract) depending upon their phase relationship. This phenomenon results from the wave-like nature of light, with the phase relationship determined by the difference in optical path lengths of the two reflections. The cell thickness can then be determined from the resulting interference pattern, assuming that the refractive index and angle of incidence are both known. Alternatively, the refractive index can also be obtained if the film thickness is known. The equation for determining the cell thickness is

$$d = \frac{m}{2N\sqrt{n^2 - \sin\theta^2}} \tag{3.26}$$

where d is film thickness, m is the number of fringes in the wavenumber region used, n is the refractive index, θ is the angle of incident and N is the wavenumber region used. In this experiment, the cell thickness measurement is conducted using an ultraviolet visible (UV-Vis) spectrophotometer shown in **Figure 3.7**. UV-Vis Spectroscopy (or Spectrophotometry) is widely used to determine how much light of a given wavelength passes through a sample and how much is absorbed.

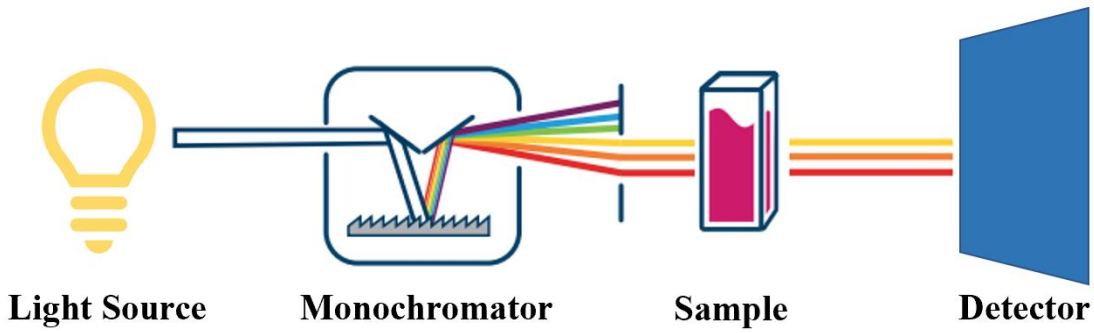

Figure 3.7 A schematic illustration of a UV-vis spectrometer.

A typical cell thickness measurement can be seen in **Figure 3.8.** Peaks in the figure are caused by the interference between the top and bottom substrate of the cell. By counting the number of the peaks in the image, the value of *m* can be determined (there are 13 peaks in the figure, hence the value of *m* is 13). In this experiment, the thickness of the cell is measured to be 4.93 μm.

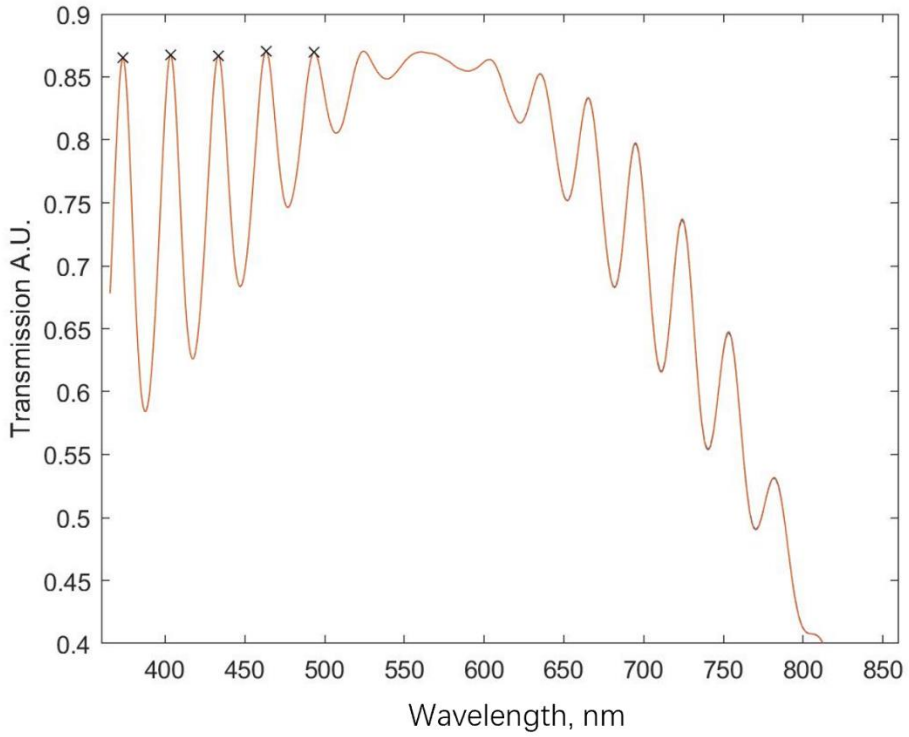

Figure 3.8 Interference fringes recorded between 350 and 860 nm using the UV-vis spectrometer.

After the cell thickness measurement, the empty cell is filled with LC mixture as shown in **Figure 3.9**. The LC mixture used in the device contained the bimesogen (dimer) CBC7CB [4′,4′-(heptane-1,7-diyl)bis(([1′,1″-biphenyl]-4″-carbo-nitrile))] dispersed with 3 wt% of the high twisting power chiral dopant, R5011 (Merck Ltd). The LC mixture was found to exhibit a right-handed, chiral nematic phase between 102 °C and

118 °C (on heating). This mixture was also found to possess a pitch of ~230 nm, which was determined from a combination of the reflection band and the refractive indices through the relation. All subsequent experiments were performed at a temperature of 108℃ in the chiral nematic phase. The device was placed on a polarisation microscope where the transmission axes of the analyser and polariser were perpendicular to one another.

To obtain a ULH configuration, the cell was first heated to 120 °C (above the clearing temperature) and then cooled down in the presence of a 1 kHz, ±20 V square-wave signal (applied to the cell electrodes). A small shear-flow was also induced within the device to promote the formation of a ULH configuration. The reason why a square wave is used in this experiment is to avoid using a DC signal. The performance of the device is observed and measured by using the CCD camera and a photodiode which are attached to the microscope. In order to directly observe the electro-optic behaviour of the device under different applied electric fields, a home-made strobe light source (a stroboscopic light is a device used to produce regular flashes of light), as shown in **Figure 3.10**, is used to replace the original microscope light source so that only the switched state can be captured.

The orange curve in **Figure 3.11** represents the signal to drive the strobe light source. By synchronising the strobe light source (orange curve) with the electric field (blue curve) and adjusting the duty cycle of the light source to make sure that the “on” state of the strobe is within the interesting period, the performance of the device for specific

switching angles can be observed and recorded by a camera. All subsequent measurements were carried out with the device in the chiral nematic phase at a temperature of 106 °C. At this temperature, the switching time (10–90% response time) of the device was found to be approximately 120 μs.

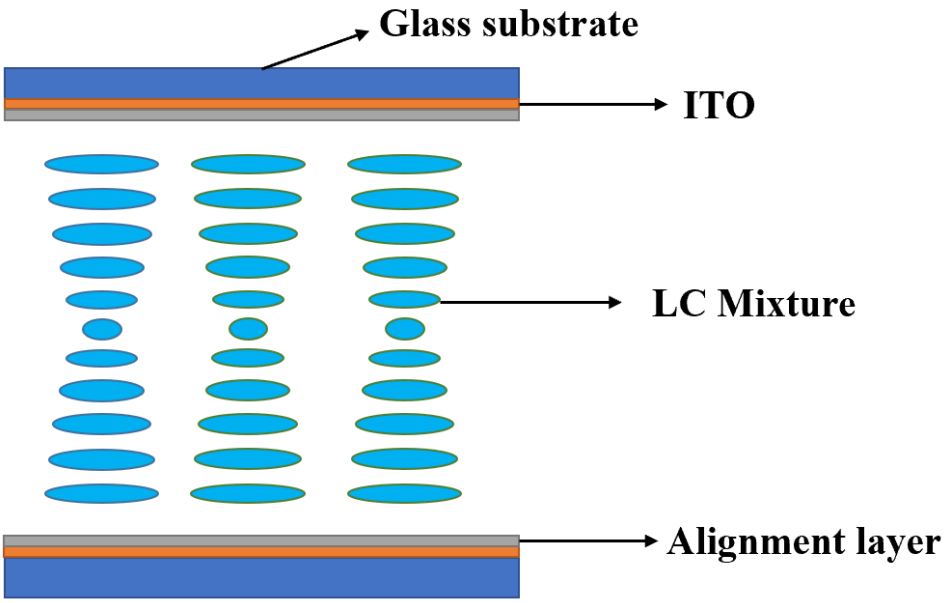

Figure 3.9 Instec cell with 4.93 μm cell gap.

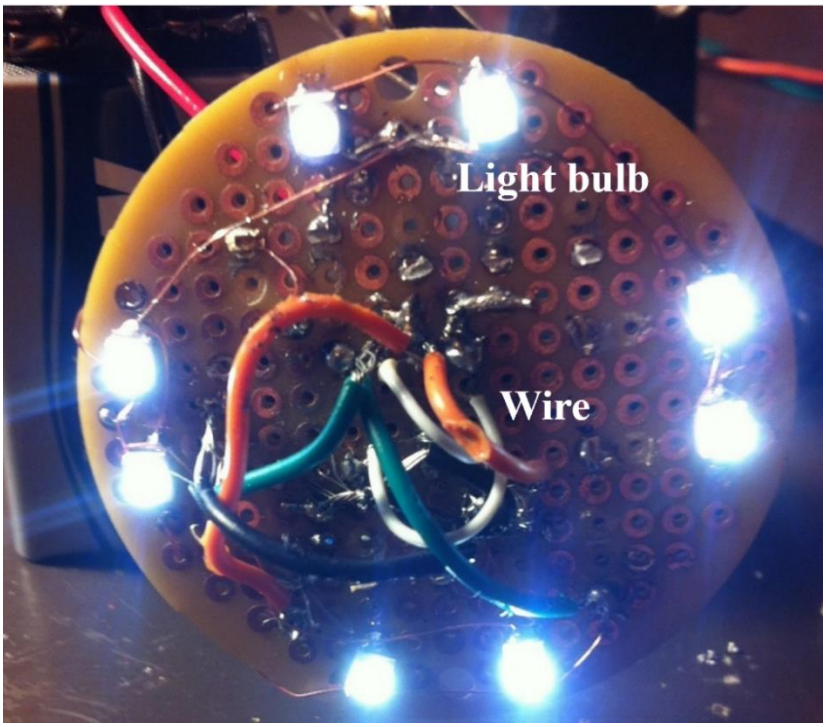

Figure 3.10 Homemade stroboscopic light source.

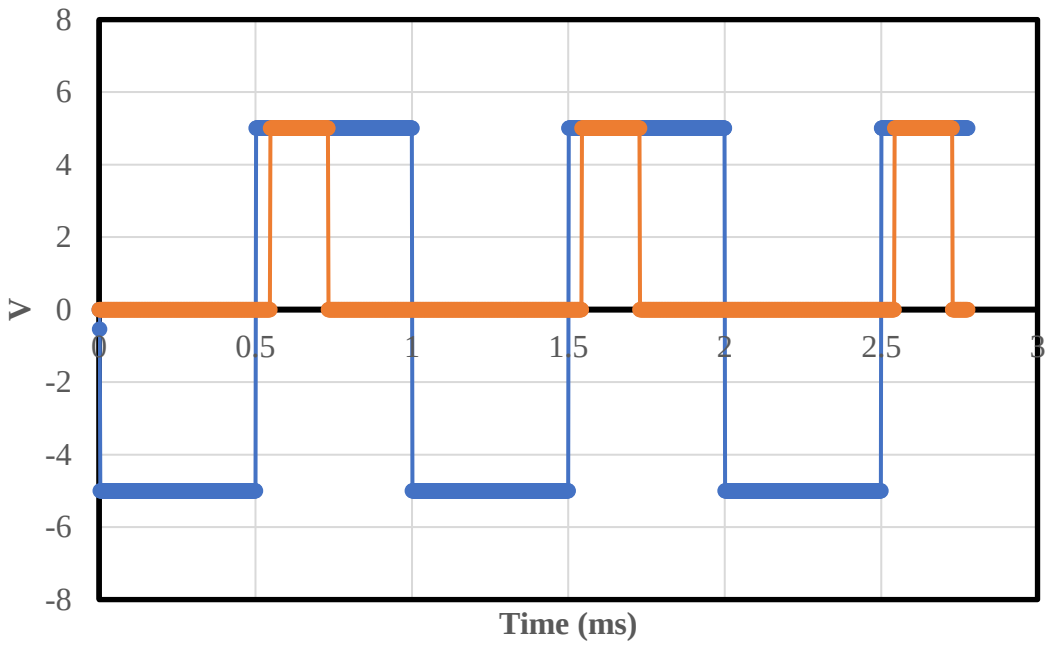

Figure 3.11. Signal for driving the chiral nematic LC sample (blue line) and stroboscopic light source (orange line).

As discussed, the flexoelastic ratio in Equation (3.18), which is determined using an unconstrained pitch model, may not be suitable for characterising most devices, especially those that exhibit large tilt angles (where Equations (3.18) and (3.21) can significantly diverge as shown in Section 3.4) [99, 105]. If we consider the case when the tilt angle, ϕ, of the optic axis is 45° then Equation (3.18) can be re-written to give the flexoelastic ratio as:

$$\frac{(e_1-e_3)}{(k_1+k_3)} = \frac{q_0}{E}\Big|_{\phi=45^\circ} \tag{3.27}$$

Equation (3.27) shows that determining the electric field amplitude at which the tilt angle is ϕ = 45° directly yields the flexoelastic ratio, provided that the pitch of the chiral nematic LC is known. Alternatively, Equation (3.21) under the same conditions (i.e. ϕ = 45°) becomes

$$\frac{\sqrt{2}(e_1-e_3)}{(k_1+2(\sqrt{2}-1)k_2+k_3)} = \frac{q_0}{E}\Big|_{\phi=45^\circ} \tag{3.28}$$

From Equation (3.28), we can see that a new flexoelastic ratio has been introduced and is given by $\frac{\sqrt{2}(e_1-e_3)}{(k_1+2(\sqrt{2}-1)k_2+k_3)}$. This new flexoelastic ratio is more appropriate for characterising and optimising materials that exhibit large tilt angles in devices for which the helical pitch is constrained. Comparing the two flexoelastic ratios, we see that they are identical provided that $k_1 + k_3 = 2k_2$. However, for the same flexoelectric coefficients, the two ratios can differ substantially if the sum $k_1 + k_3$ is different from $2k_2$.

In order to investigate the behaviour further we now consider the response of a ULH device to an applied electric field in the form of a square wave. The induced

flexoelectric tilt angle can be studied through simulations [107], and exemplar results are shown in **Figure 3.12** for the case where the values of the elastic coefficients, k_1, k_2, k_3, are the same as those of the nematic LC mixture, E7, at a temperature of 20°C [108]. The transmission through a birefringent layer placed between crossed polarisers is given by

$$\mathrm{T} = \sin^2(2\chi)\sin^2(\frac{\pi\Delta n d}{\lambda}) \tag{3.29}$$

where χ is the tile angle, Δn is the birefringence, d is the distance between the device substrates and λ is the wavelength of incident light. The figure shows three separate plots for values of $(e_1 - e_3)E$ that have been adjusted to give tilt angles of ±10°, ±22.5° and ±45°. The corresponding optical transmissions are shown in **Figure 3.13**, where the flexoelectro-optic LC device is placed between crossed polarisers such that the helix axis is at 22.5° to the input polarisation, and the maximum transmission is normalised to unity. In **Figure 3.12**, we can see that the flexoelectro-optic tilt angle results in a change in the transmission around an equilibrium level of T = 0.5. Interestingly, according to the transmission plots in **Figure 3.13**, it can also be seen that when the electric field amplitude is sufficient to induce a tilt in the angle of the optic axis of ±45°, the transmissions for the two switched states are equivalent to one another, with both transmissions reaching T = 0.5. This too is reflected in Equation (3.29) because when χ =22.5+45° = 67.5° and χ = 22.5-45° = -22.5°, then 2χ =135° and 2χ = -45°, respectively, which are 180° apart. Consequently, the values of $\sin^2(2\chi)$ are the same for both cases.

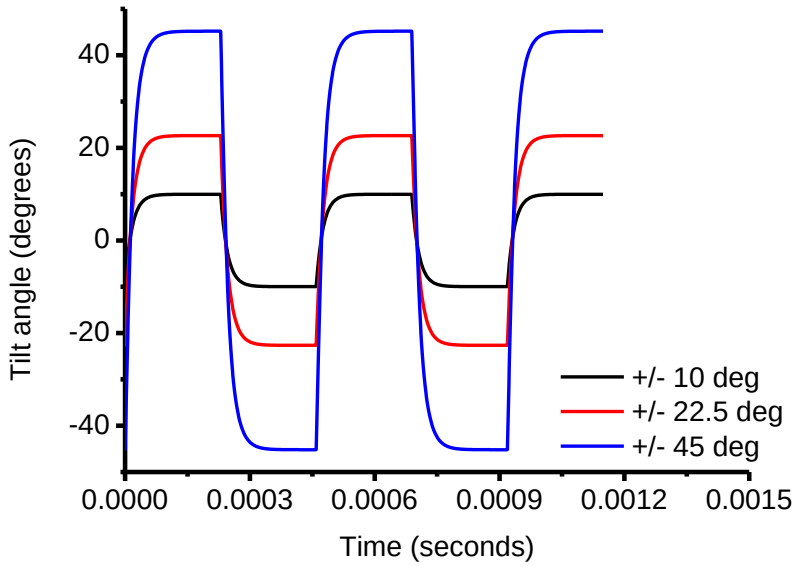

Figure 3.12. Simulations of the tilt angle of the optic axis as a function of time for values of $(e_1 - e_3)E$ set to give tilt angles, ϕ, of ±10°, ±22.5° and ±45°.

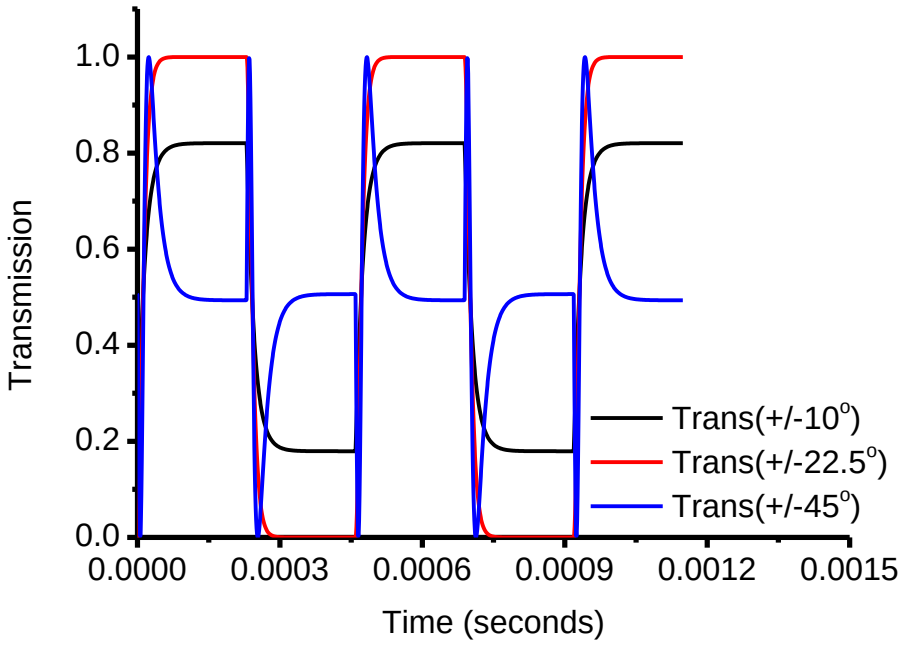

Figure 3.13. Simulations of the normalised transmission at a fixed wavelength of light as a function of time for tilt angles, ϕ, of ±10°, ±22.5° and ±45° with the helix axis aligned at 45° to the input polarisation.

Figure 3.14 shows transmission plots for flexoelectro-optic switching when ϕ = ±45° and when the device is aligned such that the helical axis is at three different,

arbitrary orientations (A, B, C) in the plane of the device. In each case, it is shown that for the $\phi = \pm 45°$ switched states they approach the same transmission level after some initial response. Furthermore, we can see from **Figures 3.13** and **3.14** that when the tilt angle is at ±45°, the transmission levels corresponding to these states will always tend to the same value irrespective of the orientation of the helical axis with respect to the input polarisation.

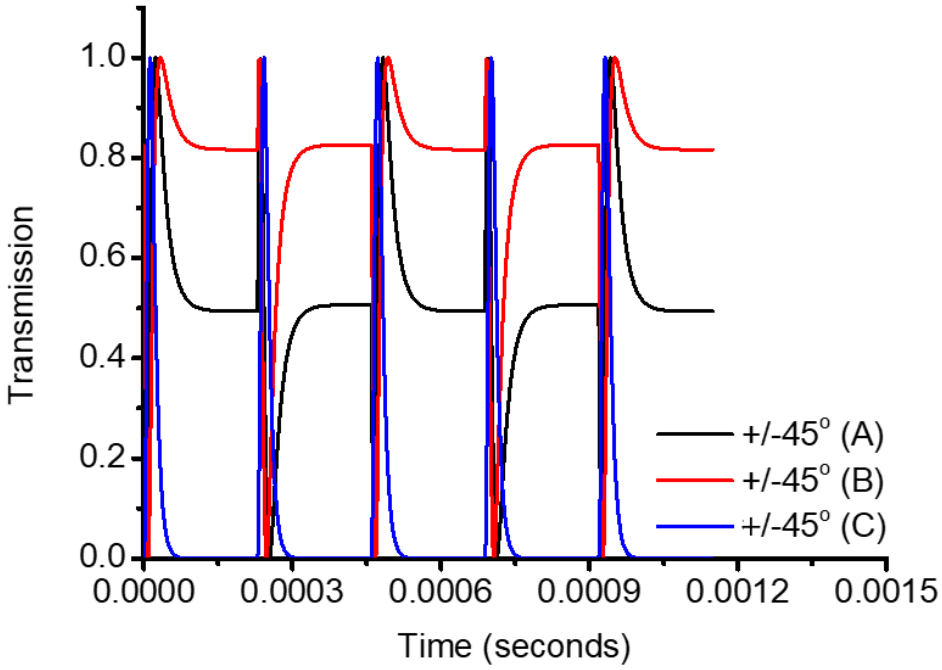

Figure 3.14 Simulation of transmission plots as a function of time for the case when $\phi = \pm 45°$ for three arbitrary orientations (A, B, and C) of the mean optic axis in the plane of the device.

The equivalence in the transmission plots for the case when $\phi = \pm 45°$ as seen in the simulations presented in **Figure 3.14** is interesting to investigate experimentally. For a flexoelectro-optic device aligned in the ULH configuration, adjusting the amplitude of an applied square wave electric field until the transmission of the device placed between crossed polarisers for the positive and negative polarities are the same allows for the

direct determination of the electric field amplitude required for a tilt angle of ±45°. This observation does not require: 1) any knowledge of the precise orientation of the helix axis, 2) any prior knowledge of the birefringence of the device under study, and 3) the measured transmission does not need to be normalised. Provided that the pitch of the helix is known, observation of the point at which the transmissions for positive and negative polarity electric fields are equal leads to the direct determination of the combination of coefficients in Equation 3.28, which is the more appropriate flexoelastic ratio for large switching angle materials.

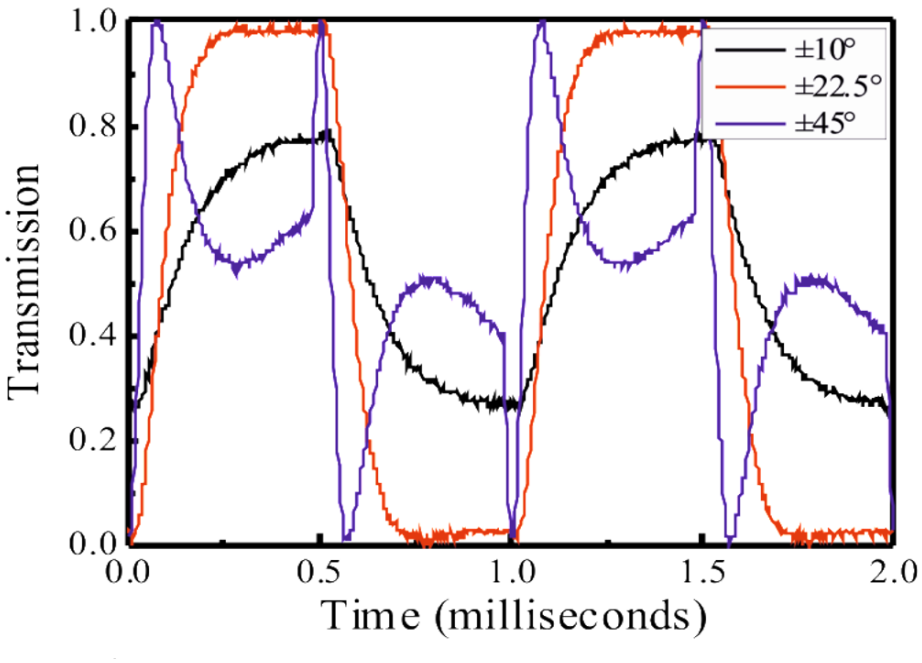

Figure 3.15. Experimental results of the normalised transmission of white light through the flexoelectro-optic device between crossed polarisers as a function of time for flexoelectro-optic tilt angles, ϕ, of approximately ±10°, ±22.5° and ±45°. Results are presented for a chiral nematic mixture consisting of CBC7CB and 3 wt% chiral dopant (R5011, Merck) in a 5 μm-thick planar-aligned device.

Figure 3.15 shows the experimentally-measured transmission of light as a function of time for the LC device placed between the crossed polarisers of an optical polarising

microscope with the helical axis oriented at 22.5° with respect to the polariser axis. The applied signal was a square wave with frequency 1 kHz and the electric field amplitudes required were found to be ±1.3 $V\mu m^{-1}$, ±3.1 $V\mu m^{-1}$ and ±6.12 $V\mu m^{-1}$ to give tilt angles of approximately ±10°, ±22.5° and ±45°, respectively. Some relaxation in the tilt angle over the duration of one polarity of the applied electric field is noticeable, especially for the case of the ±45°. It is believed that this behaviour is due to the presence of ions in the LC material used in the experiment.

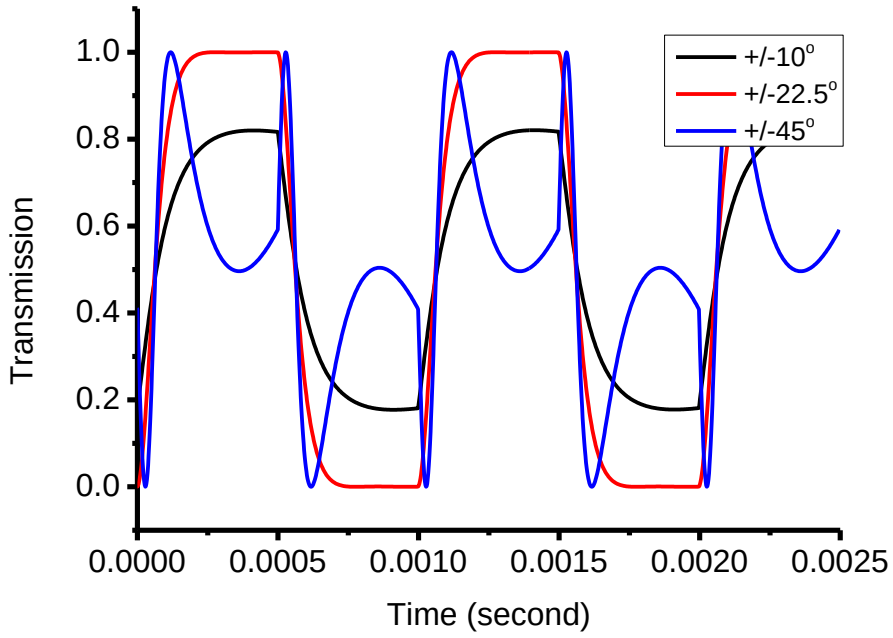

Figure 3.16 Theoretical results of the transmission as a function of time for tilt angles of approximately ϕ = ±10°, ±22.5° and ±45° with the inclusion of a voltage-dependent decay term that has been added to the internal electric field.

The relaxation behaviour seen in **Figure 3.15** was not reproduced in the model used to obtain the theoretical results shown in **Figure 3.13**. However, if a voltage-dependent decay term is added to the internal electric field to represent the effect of the movement and internal field-screening effect of ions within the LC device, it is then

possible to model more realistically the experimental results, as shown in **Figure 3.16**. The parameters used in the inset have been adjusted to ensure that the model better represents the experimental situation.

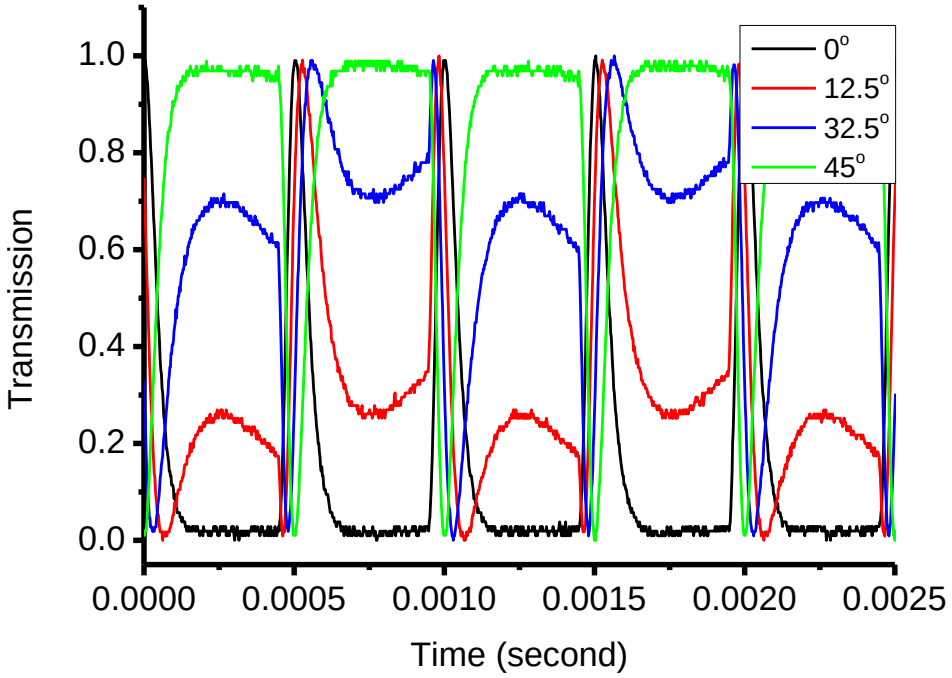

Figure 3.17 Experimental results of the transmission as a function of time for the ϕ = ±45° switched states for a range of orientations of the helical axis (mean optic axis).

Even though the relaxation in the tilt angle caused by the ionic content inevitably influences the resulting flexoelectro-optic behaviour, the ϕ = ±45° switching point is still apparent in **Figures 3.15** and **3.16** in both the experimental and the theoretical results, respectively. The expected equivalence in the transmission levels for the ϕ = ±45° switched states for all orientations of the helical axis (shown in the model in **Figure 3.14**) can also be investigated experimentally. **Figure 3.17** shows the transmission data obtained for a range of device orientations. It is evident that, in each

case, the response to the positive and negative electric field polarities are equivalent, as expected. This point is relatively easy and convenient to identify as it does not require any calibration/normalisation of the transmission measurement, as explained previously, and does not require precise knowledge of the device orientation. For the device used here, this point was found to occur at an applied voltage of ±30.7 V, which is equivalent to an electric field strength of ±6.12 $V\mu m^{-1}$.

The behaviour observed in **Figure 3.15** is also illustrated in the sequence of optical polarising microscope images of the responses to the positive and negative electric field polarities of the square wave as its amplitude is increased. These results are shown in **Figure 3.18**, where the device is oriented with the helical axis at 22.5° to the polariser axis and the images are obtained stroboscopically, with the illumination synchronised with either the positive or negative switching voltage. The sequence starts from the un-switched (0V) state and is followed by a series of pairs of images for the responses to both positive and negative voltage polarities, where the tilt angles correspond to $\phi \approx$ ±10°, ±22.5°, ±39°, and ±45°.

In **Figure 3.18(a)**, for the un-switched (0V) state, the pair of images are of course identical to each other as no electric field is applied to the sample. As the voltage is increased, differences between the positive and negative switched states appear in the pairs of images. The contrast between the images for the positive and negative electric field polarities increases with the amplitude as the tilt angle of the optic axis increases,

and becomes largest when $\phi = \pm 22.5°$ (**Figure 3.18(c)**), which corresponds to maximum intensity modulation. However, a further increase in the field amplitude, and consequently the tilt angle, results in a decrease in the contrast between the pairs of images (**Figure 3.18(d)**). At the point where the electric field amplitude is such that the tilt angle reaches $\phi = \pm 45°$, the contrast in the images between the positive and negative polarity electric fields vanishes and the two images are again identical (**Figure 3.18(e)**). This is exactly as expected from the transmission data presented in **Figure 3.15**, because the transmission through the positive and negative switched states are equivalent to one another when $\phi = \pm 45°$.

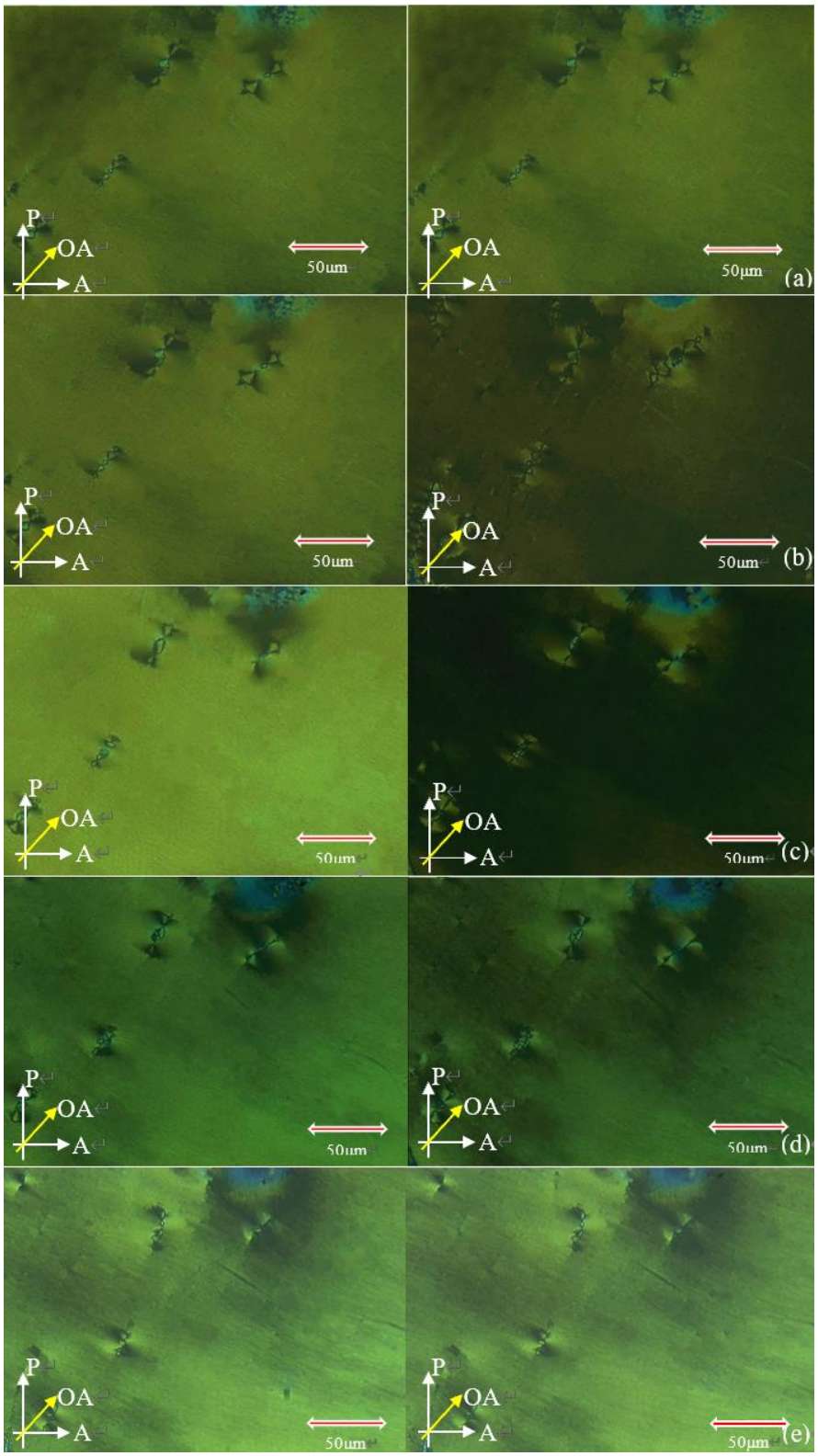

Figure 3.18 Microscope images for the positive and negative electric field polarities for (a) the unswitched (0V) state, and with tilt angles of (approximately) (b) ±10°, (c) ±22.5° degrees, (d) ±39°, and (e) ±45°. The changes in brightness are caused by the different electric field amplitudes. P, A and OA represent the orientations of the transmission axes of the polariser, analyser and helix axis, respectively.

For the LC mixture used in this study, the pitch was found to be of the order of 230 nm [90, 108]. Using Equation 3.21 along with the value of the electric field amplitude required to obtain a tilt angle of ϕ = ±45°, the new large tilt angle flexoelastic ratio is then determined to be,

$$\frac{\sqrt{2}(e_1-e_3)}{\{K_1+2(\sqrt{2}-1)K_2+K_3\}} = 4.13\ V^{-1}. \quad (3.29)$$

This value for the ratio can be compared to the result obtained for small tilt angles, where a tilt angle of ϕ = ±10° is observed at an applied voltage of ±6.5 V (equivalent to an electric field strength of ±1.3Vμm^{-1}), leading to a value for the more commonly-applied, unconstrained-pitch flexoelastic ratio (Equation (3.18)) of

$$\frac{e_1-e_3}{K_1+K_3} = 3.64\ V^{-1}. \quad (3.30)$$

As demonstrated, the new flexoelastic ratio given by Equation 3.29, with a value here of $4.13\ V^{-1}$, is the more useful characteristic for large tilt-angle flexoelectro-optic switching and that the conventional flexoelastic ratio described by Equation (3.30) is only suitable for describing small tilt angle flexoelectro-optic switching.

3.6 Conclusion

In summary, we propose that the flexoelastic ratio, which is commonly used to characterise the electro-optic behaviour of chiral nematic liquid crystal (LC) devices that exhibit flexoelectro-optic switching, can be given by the combination of coefficients in Equation 3.29, which is regarded as a more appropriate expression for the characterisation of liquid crystalline devices that exhibit a large tilt-angle of the optical axis in flexoelectro-optic switching. Moreover, a simple method for determining

this ratio has been proposed by simply recording the electric field amplitude at the point whereby the transmission properties become equivalent [109] allowing for a rapid, and precise measurement of the flexoelectro-optic performance of chiral nematic LC devices. This method is quite important as we are going to use it to characterise phase modulators shown in chapters 4-6.

CHAPTER 4 Fast Response Analogue Phase-Only Modulator

4.1 Introduction

In the previous chapter, a rapid and precise method has been proposed for determining when the tilt angle reaches $\pm\pi/4$ by simply recording the electric field amplitude at the point whereby the transmission properties become equivalent. In this chapter, using chiral nematic LCs that exhibit a flexoelectro-optic tilt angle of $\pm\pi/4$, an analogue phase modulator with $>2\pi$ phase range is demonstrated with a 1 kHz switching frequency.

The chiral nematic LC mixture consists of the bimesogen CB7CB doped with a high twisting power chiral dopant (R5011, Merck), aligned in the uniform lying helix mode. The mixture exhibits $>\pm\pi/4$ rotation of the optic axis for a drive voltage of ±21.5 V (E = ±4.5 V μm^{-1}). The rotation of the optic axis is converted into a phase modulation with the aid of a reflective device configuration incorporating a ≈5 μm LC cell, a polariser, two quarter-wave plates, and a mirror. The residual amplitude modulation is found to be <23%. In addition, experiments have been carried out whereby the mirror is replaced with a chiral nematic reflector, which is found to be very tolerant to imperfections in the chiral nematic reflector provided that the flexoelectro-optic LC layer fulfils the half-wave condition. Encouragingly, the modulation in the phase, which operates at kHz frame rates, is accompanied by even lower amplitude modulation. The phase modulator configuration demonstrated in this chapter is particularly promising for the development of next-generation LC on silicon spatial

light modulators (SLM).

4.2 Application of SLMs

As mentioned in Chapter 2, SLMs have been used in various applications, among which are microscopy [110-116], telecommunication [117-123] and holography [124-134]. For application in microscopy, LCOS SLMs were used in building a phase contrast microscope [113,135,136] where phase contrast, dark field images and differential interference contrast can be generated by addressing different phase patterns to the SLM located in the Fourier plane. In addition, Auksorius et al. [137] has proposed to use phase SLMs in the super-resolution microscopy where phase SLMs have been used in generating and controlling the point spread function of a stimulated emission depletion (STED) beam. Compared with the standard confocal technique, this new configuration showed correction of aberrations and rapid switching between different modes of STED imaging which results in significant improvement in resolution. The compensation of aberrations caused by the introduction of phase SLMs is especially important which enhance the stability of the system [137,139,140].

Another attractive application for SLM is telecommunication, Frumker and Silberberg [119] have demonstrated amplitude and phase shaping of femtosecond laser pulse using an LCOS phase modulator. In the system, a grating is used to split the femtosecond pulses into a spectrum and each wavelength component is focused onto the SLM in a single direction with the help of a cylindrical Fourier lens. The amplitude and phase modulation are generated by writing corresponding gratings. In addition to

telecommunication, Meeser et al. [125] and their team have used an SLM to develop a holographic sensor that is able to adapt the reference wave for objects in different positions. The accurate phase distribution in the CCD plane and rapid switching between Fresnel and Fourier holograms are all realised by using an SLM. Light Blue Optics developed a full colour 2D holographic projection unit by using SLMs based on ferroelectric effect [131]. The fast response ferroelectric SLMs enable a good quality of reconstruction and low speckle noise [71]. The availability of SLMs has helped researchers to explore a wide range of potential applications. High-resolution devices were made possible, but for phase modulators, a high frame rate with analogue phase modulation is still a challenge. In this work, a fast response analogue phase modulator has been developed, which will be explained in the following sections [73,74,138].

4.3 Phase modulation simulation

LC SLMs are attractive optical components to manipulate an optical phase over a two-dimensional area because they can be relatively low in cost and offer a high spatial resolution [52, 141]. SLMs are typically used in a reflective configuration, the reflector is divided up into an array of pixels, each independently electrically controlled via a silicon backplane. As a result, there is an increasing need for providing a sub-millisecond analogue 2π phase modulation. However, as mentioned in Chapter 2, current SLMs based on nematic LC or ferroelectric LC cannot satisfy this need [68-72]. Hence, this thesis presents the development of a new phase modulation configuration

based on the flexoelectro-optic effect, which is able to meet this requirement [138].

In the previous chapter, we have investigated the electro-optic behaviour in a material that shows a large tilt angle of the optic axis when subjected to an electric field [109]. The behaviour of this electro-optic effect (referred to as the flexoelectro-optic effect) is illustrated in **Figure 4.1**, where the applied signal presented in **Figure 4.1**(a) leads to the tilt angle response shown in **Figure 4.1**(b).

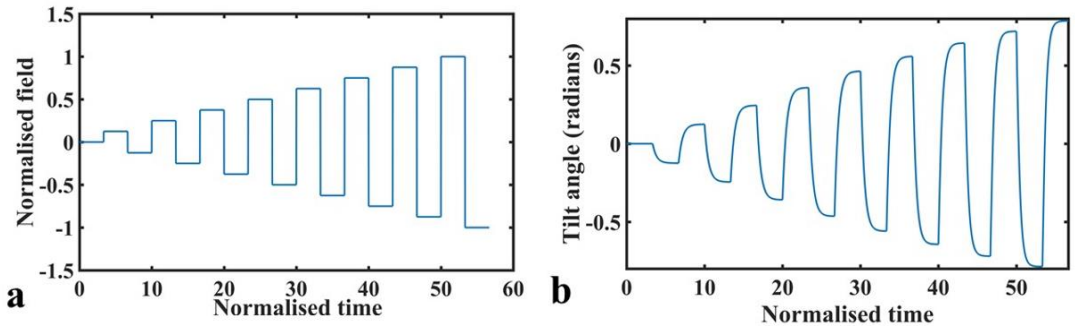

Figure 4.1 Results of the flexoelectro-optic effect (**a**) An exemplar case of an electric field applied to a ULH-aligned flexoelectro-optic device. The electric field and time are normalised to be dimensionless quantities. (**b**) The resulting tilt angle (in radians) as a function of time.

LC phase modulators based on the flexoelectro-optic effect in chiral nematic LCs in the ULH mode have been proposed previously and demonstrated to give a phase modulation range of 0.71π at 500 Hz and 0.52π at 1 kHz [142]. While fast, the low phase modulation range will be insufficient for many applications. The lack of suitable technology for stable, fast, analogue phase-only SLMs is a severe limitation for dynamic optical systems. Here, a solution to this problem is presented and a new ULH device configuration is presented that allows a full 2π analogue phase modulation range,

fast switching speeds, no unwanted residual amplitude modulation, and a thin device for good spatial resolution.

To enhance the phase modulation performance of flexoelectro-optic LC phase modulators, three different configurations have been investigated which are shown in **Figure 4.2**. The basic configuration (I) has a ULH LC layer in a reflective configuration. This is similar to that employed by Chen *et al.* [142], but with an additional polarizer at the front to preserve the polarization state. Configuration (II) is similar to configuration (I), except that there is an additional quarter-wave plate after the polarizer, and the LC layer has a retardance of $\lambda/4$. Configuration (III) has, in addition, a second quarter-wave plate between the LC and the reflector and, in this case, the LC retardance is set to $\lambda/2$ which is similar to that of Stockley *et al.* [143].

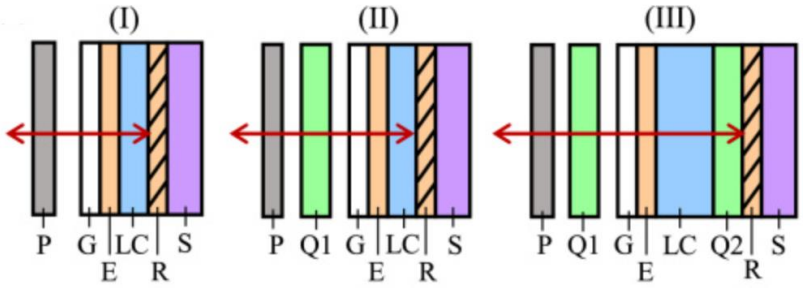

Figure 4.2 Three device configurations (I)–(III) of the optical phase modulator. P, polarizer; G, glass; E, transparent electrode; LC, liquid crystal; R, reflective electrode; S, silicon backplane; Q1, Q2, quarter-wave plates. The alignment layers on each side of the LC are omitted for clarity. The LC retardance is as follows: (I) 0.25–0.5λ (II) 0.25λ and (III) 0.5λ.

In order to understand the phase performance of each configuration, the three configurations are first simulated by using Jones Calculus in Matlab. In the Jones

matrices, the LC may be modelled as a waveplate with an optic axis in a plane normal to the incident beam, whereby this angle changes with the amplitude of the applied field (and, hence, voltage). Expressions for the output optical field, $\boldsymbol{E_{out}}$, for three configurations are given by:

$$(III)\ E_{out} = \boldsymbol{PD}(-\varphi, \delta)\{\boldsymbol{M}\}\boldsymbol{D}(\varphi, \delta)\boldsymbol{P}E_{in} \quad (4.1)$$

$$(II)\ E_{out} = \boldsymbol{PQ_1}\left(-\frac{\pi}{4}\right)\boldsymbol{D}(-\varphi, \delta)\{\boldsymbol{M}\}\boldsymbol{D}(\varphi, \delta)\boldsymbol{Q_1}\left(\frac{\pi}{4}\right)\boldsymbol{P}E_{in} \quad (4.2)$$

$$(III)\ E_{out} = \boldsymbol{PQ_1}\left(-\frac{\pi}{4}\right)\boldsymbol{D}(-\varphi, \delta)\left\{\boldsymbol{Q_2}\left(-\frac{\pi}{4}\right)\boldsymbol{MQ_2}\left(\frac{\pi}{4}\right)\right\}\boldsymbol{D}(\varphi, \delta)\boldsymbol{Q_1}\left(\frac{\pi}{4}\right)\boldsymbol{P}E_{in} \quad (4.3)$$

Taking Eq. (4.3) as an example, reading this equation from right-to-left, the input light $\boldsymbol{E_{in}}$ is first passed through the vertical linear polariser represented by matrix $\boldsymbol{P}$. The quarter-wave plate, the axis of which is at 45° to the vertical, is represented by a matrix $\boldsymbol{Q_1}\left(\frac{\pi}{4}\right)$. $\boldsymbol{D}(\varphi, \delta)$ is then the Jones matrix of an LC device having retardance δ at an orientation of angle φ to the horizontal [144]. The term in curly-brackets is the Jones matrices for mirror $\boldsymbol{M}$ and the second quarter-wave plate, $\boldsymbol{Q_2}\left(\frac{\pi}{4}\right)$.

Note that in the terms after the mirror (terms to the left of $\boldsymbol{M}$ in Equation (4.3)), the orientation angles of the waveplates are reversed because these angles are measured from the horizontal and the light is now propagating in the opposite direction. The terms to the left of the curly brackets represent the light passing back through the LC device, quarter-wave plate, and vertical linear polariser after being reflected from the mirror. Multiplying out the terms in Equation (4.3), and assuming that all components are ideal (with the LC device forming a perfect half-wave plate) and that the input and output

light is vertically polarised, leads to the simple but informative result that:

$$E_{out} = E_{in} e^{+4i\varphi} \tag{4.4}$$

The Matlab simulation code for configuration (III) is shown in **Figure 4.3**. Assuming that all the components are ideal and thus every optical component can be represented by Jones matrices. The horizontal and vertical linear polarizer can be represented by [1,0;0,0] and [0,0;0,1], as shown in Line 10,11 in **Figure 4.3**. The matrices for the quarter waveplate in the transmission path and reflected path are similar except the second and third term in the matrix of the transmission path (1-j) is replaced with –(1-j) in the reflection path. As mentioned above, in order to simulate the phase performance of the LC device, the LC device is treated as a quarter or half waveplate (Jlc=[exp(j*delta/2),0;0,exp(-j*delta/2)]) and the rotation of the optical axis due to the flexoelectro-optic effect is represented by the rotation matrix (line 18,19). In this case, the retardance of the LC device is 0.5λ, which means that the LC device is regarded as a half waveplate where the retardance in the Matlab code is set to 0.5 and delta is 2*π*retard = π. Using Jones matrices, the phase and amplitude performance of three different configurations can be successfully simulated, as shown in **Figure 4.4**.

```
retard=0.5 %setting the retardance of the LC device
j=1i;
delta=2*pi*retard; % Phase different after a half waveplate
Ein= [0;1]; % Input light
Jmirror= [1,0;0, -1]; % Mirror
Jquarter=[1+j,1-j;1-j,1+j] *exp(j*pi/4)/2; % Quarter waveplate on the transmission path
Jquarter_r= [1+j, -(1-j); -(1-j),1+j] *exp(j*pi/4)/2; % Quarter waveplate on the reflection path
Jh= [1,0;0,0]; % Horizontal Polariser
Jv= [0,0;0,1]; % Vertical Polariser
theta_array= [-pi/4: pi/1000: pi/4]; % Tilt angle array
for n=1: length(theta_array),
    theta=theta_array(n);
    Rn=[cos(theta), -sin(theta); sin(theta), cos(theta)]; % Rotation matrix
    Rp=[cos(theta), sin(theta); -sin(theta), cos(theta)]; % Rotation matrix
    Jlc=[exp(j*delta/2),0;0, exp(-j*delta/2)]; % LC device
    Jsys = Jv*Jquarter_r*Rp*Jlc*Rn*Jquarter_r*Jmirror*Jquarter*Rn*Jlc*Rp*Jquarter*Jv;
    % Result of system Jone matrix
    Eout=Jsys*Ein;
    phase= (angle (Eout));
    mag=abs (Eout);
end
```

Figure 4.3 Matlab code for simulating the amplitude and phase performance of the three device configurations presented in Figure 4.2. In the simulations, the optical losses due to the scattering in the LC and nonideality in the optical components are ignored.

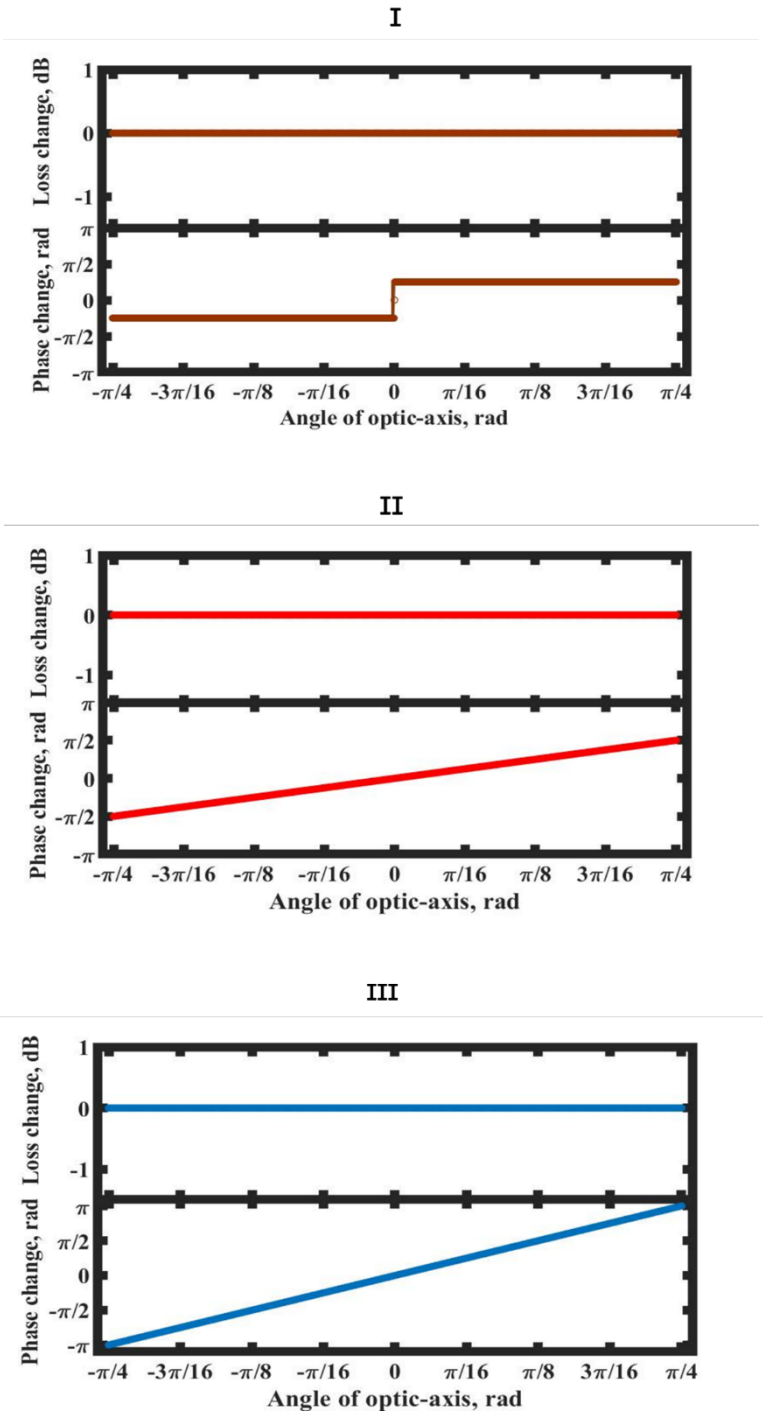

Figure 4.4 Simulation results of the three different optical phase modulation configurations presented in Figure 4.2. For each plot, the upper part shows the intensity change while the lower part illustrates the phase change as a function of the absolute angle of the optic-axis of the ULH-aligned flexoelectro-optic device relative to the horizontal. The LC device is regarded as a quarter (I), half-waveplate (II), and half waveplate (III). The optical losses due to the nonideality in the LC and optical components are ignored.

From **Figure 4.4**, it can be seen that for the ideal case, all of the configurations are lossless (the intensity is unity, indicating that all of the incident light is returned and therefore the amplitude of the reflected light is constant regardless of the angle of the optic-axis). For an angle ϕ that is within the range of $\pm\pi/4$ (i.e., a tilt angle of the optic axis in the ULH device of ±45°, with a total switching angle range of 90°), a phase modulation range of 2π can only be obtained from configuration (III) (configuration (I) only gives binary phase modulation and configuration (II) produce a π phase modulation for ±45° switching angle), which means that configuration (III) has the potential to enable a full 2π analogue phase range at switching speeds of >1 kHz. Hence, in the following, this combination is chosen for the development of a new LC phase modulator.

4.4 Michelson Interferometer

A bench-top implementation of configuration (III) with a bimesogen-based chiral nematic LC was constructed, and its phase response was measured using a Michelson interferometer, shown in **Figure 4.5**. The LC mixture used in the flexoelectro-optic device contained the bimesogen (dimer) CBC7CB [4′,4′-(heptane-1,7-diyl)bis(([1′,1″-biphenyl]-4″-carbo-nitrile))] dispersed with 3 wt% of the high twisting power chiral dopant, BDH1281 (Merck Ltd). The mixture was then filled into a nominally 5 μm-thick Instec cell that contained antiparallel rubbed polyimide alignment layers and indium tin oxide electrodes. The thickness of the empty cell was determined to be 4.73 μm by measuring the white-light transmission spectrum on a UV-Vis spectrometer

(Agilent 8454).

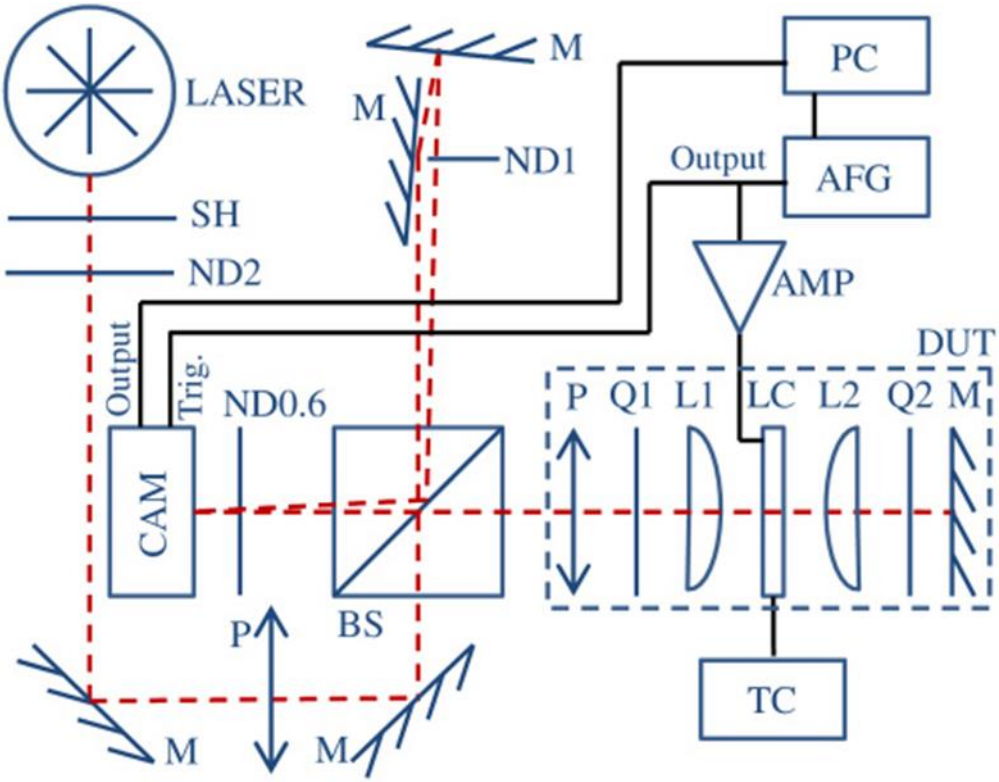

Figure 4.5 Experimental arrangement to measure the phase of the proof-of-concept LC optical phase modulator: SH, shutter; NDx, neutral density filter of optical density *x*; PC, personal computer; AFG, arbitrary function generator; AMP, amplifier; TC, temperature controller; CAM, camera; DUT, device under test; P, polarizer; Q1; Q2, quarter-wave plates; L1; L2, lenses; M, mirror; BS, non-polarizing beam splitter.

As described in Chapter 3, the LC mixture was found to exhibit a chiral nematic phase between 102 °C and 118 °C (on heating). To obtain a ULH configuration, the cell was first heated to 120 °C (above the clearing temperature) and then cooled down in the presence of a 1 kHz, ±20 V square-wave signal (applied to the cell electrodes) which is generated by a combination of arbitrary function generator (Wavetek 395) and voltage amplifier (FLC Electronics F10AD) to meet the voltage requirement. The ULH structure is then checked with optical polarisation microscope (Olympus BX51) to find out whether a suitable ULH alignment has been formed. The OPM images in **Figure**

4.6 show the bright (45°) and dark (0°) states of the ULH device. The images were taken once the device had been cooled to 108 °C whilst under the application of the external electric field. A fairly uniform ULH alignment can be seen on a local scale and defects are visible across larger regions of the device due to the spacer bead and discontinuous in the helical axis. However, good contrast can still be seen between the bright and dark states.

Under the ULH structure, taking the ordinary and extraordinary refractive indices for the nematic LC, CBC7CB, at a wavelength of 633 nm and using a standard expression for the effective optical anisotropy of a ULH structure [101,102], the retardance for the device used here was estimated to be 0.51λ. Since the retardance of the LC device is approximately 0.5λ, we consider it to behave as a near-ideal half-wave plate, which reverses the hand of circularly polarised light passing through it. All subsequent measurements were carried out with the device in the chiral nematic phase at a temperature of 106 °C. At this temperature, the switching time (10–90% response time) of the device was found to be approximately 120 μs.

The light source used in this setup was a continuous wave Helium-Neon (He-Ne) laser (Uniphase 1125P) that generates light at a wavelength of 632.8 nm. As illustrated in **Figure 4.5**), the input light is arranged to be vertically polarized and then passes via the aid of mirrors through a non-polarising beam-splitter (Newport 05BC16NP). One of the output beams (the signal beam) passes through the ULH flexoelectro-optic device and is reflected by the mirror through the same system. The other output beam (the reference beam) is directed by two mirrors to reflect the light with a small angle offset

so as to generate clear interference fringes. The flexoelectro-optic-based phase modulator is also shown in **Figure 4.5**. The polarizer and quarter-wave plates were placed on rotation mounts. Q1 was then rotated to obtain the right circular polarization, which was confirmed using a polarization analyzer (Schäfter + Kirchhoff SK010PA-VIS). Lenses L1 and L2 (respectively, Thorlabs LA1131A and LA1608) were used to focus the beam through the LC cell, mounted on a hot stage (Linkam LTS350 with TP93 controller).

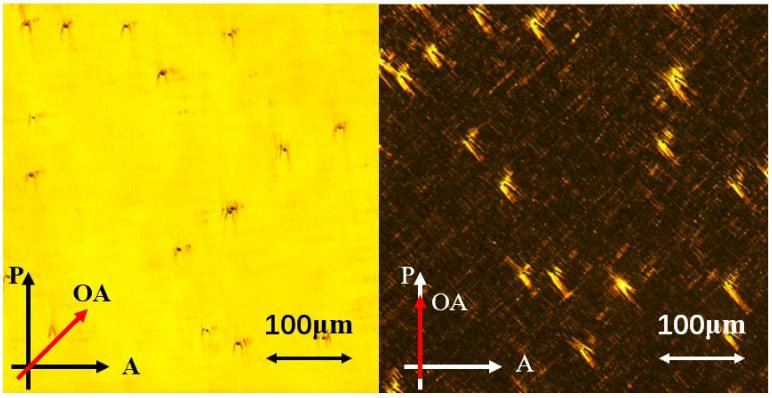

Figure 4.6. Optical polarisation microscope images showing the bright (left) and dark (right) states of a ULH texture. Defects shown in the image are mainly caused by the spacer bead and discontinuous in the helical axis. A fairly uniform ULH alignment can be seen locally, with good contrast between the bright and dark states. The direction of the polarizer and analyser are indicated by the white and black arrows for different images and the optical axis is represented by the red colour arrow.

The fringes were captured using a collection lens to directly image onto a CCD camera (Thorlabs DCU224C, 1280 × 1024, 8-bit colour). The arbitrary function generator (Wavetek 395) is used to trigger the acquisition of images from the CCD camera. For all measurements, the device drive signal was a 1 kHz square-wave with a controllable amplitude level, and the camera was triggered on one half-cycle of the square-wave in order to record the instantaneous fringe intensity pattern at any desired

drive voltage level. In addition, the CCD camera was set to record a 100 μs exposure towards the end of a half-cycle of the square-wave.

4.5 Phase Modulation Results

Figure 4.7 shows the interference fringes recorded on the camera in response to different applied peak voltage levels up to ±21.5 V (E = ±4.5 V μm^{-1}). It can be seen that the fringes move relative to the reference line as the voltage is increased, all the way to the point that the next fringe reaches the line, demonstrating a 2π phase range. The 8-bit spatial data recorded from the camera were fitted to an interference pattern from two Gaussian beam profiles to determine the amplitude and relative phase at each voltage level. **Figure 4.8**(a) shows the optical transmission of the LC through crossed polarizers for an exemplar case of an applied 1 kHz square wave at ±11 V. The change in the tilt angle at this drive voltage is approximately ±π/8 rad, and it can be seen that the device permits 1 kHz switching. **Figure 4.8**(b) shows typical fitted data extracted from the fringe intensity data shown in **Figure 4.7**.

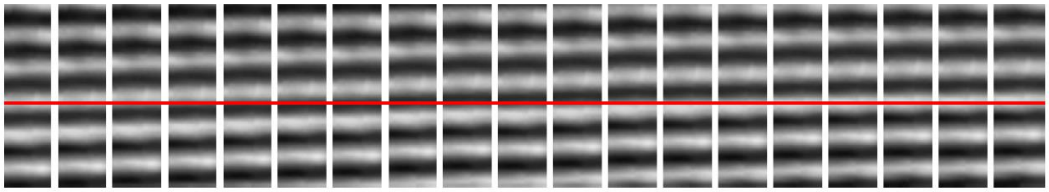

Figure 4.7 Experimentally captured interference fringes for different voltages applied to the LC optical phase modulator. A 1 kHz amplitude signal was applied to the LC and the camera was triggered on one half-cycle of the square wave to record the instantaneous fringe intensity pattern at each voltage level. The red line provides a reference phase.

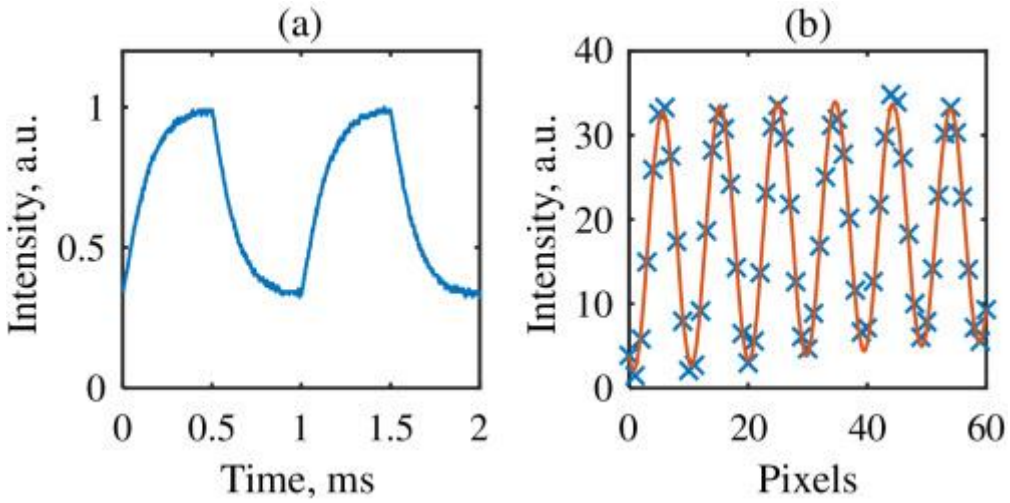

Figure 4.8 Experimentally measured data: (a) optical transmission of LC through crossed polarizers (with no other components) under an applied 1 kHz square-wave drive of ±11 V. The device optic axis at zero electric fields was at an orientation of π/8 from the transmission axis of one of the polarizers. (b) (× blue) fringe data recorded from the camera, (— red) fit to fringe data.

Figure 4.9 shows the phase shift and amplitude variation for the bench-top phase modulator as a function of the applied voltage. The tilt angles were measured against the voltage for the LC mixture by using a time-resolved technique [145] and is shown as an inset in **Figure 4.9**, with >π/4 angle change. From the figure, it can be found that the phase range exceeds 2π and the relationship between voltage and phase change is approximately linear, as expected from **Figure 4.4**. Compared with a standard nematic LC phase modulator, which is also able to provide multi-level phase modulation, the linear property is quite favourable as it means the characterisation of a phase modulator based on flexoelectro-optic effect will be much easier. In addition, it has been noticed that the amplitude variation is also low at less than 23% which might be caused by noise from the experimental measurement system and nonideality in the optical components and LC cell. For noises that come from the environment, it is impossible to get rid of

them. However, it is possible to improve the setup to make the system less sensitive to the nonideality in the LC phase modulation element. The method replaces the mirror and the second quarter waveplate with a chiral reflector which will be explained in the next section.

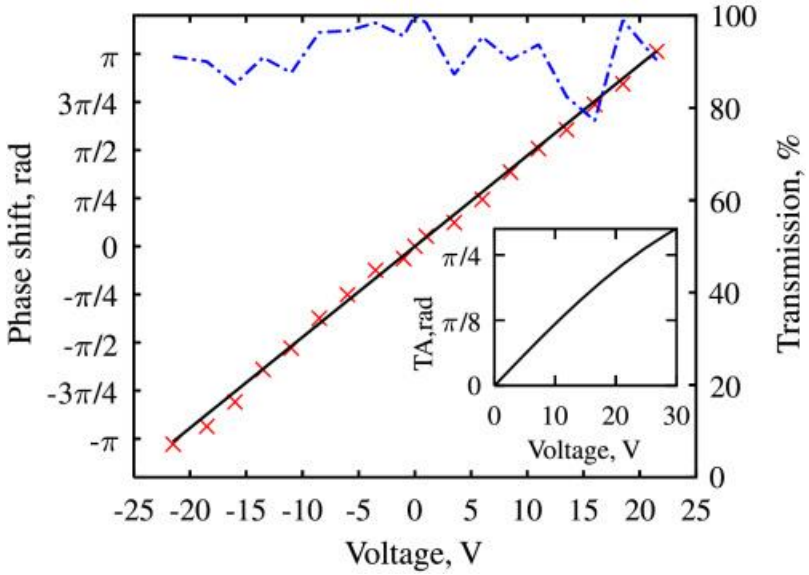

Figure 4.9 Experimentally extracted phase (left axis) and transmission (right axis) for the LC optical phase modulator. (× red) phase, (– · blue) amplitude. Inset: tilt angle of the optic axis (TA) versus voltage for the LC mixture (without any additional components).

4.6 Simulations of a phase modulator with a chiral reflector

The Jones Matrix method [40] has also been used to model the optical behaviour of a chiral reflector-based phase modulator so as to make comparisons with the previous arrangement [138]. The configuration of the device (See **Figure 4.10**) is quite similar to the previous configuration which also consists of a vertical polariser, a quarter-wave plate and the flexoelectro-optic chiral nematic LC device, which aligned in the ULH geometry and, ideally, corresponds to a half-wave plate in terms of thickness. However, in this case, the light is reflected from a chiral nematic reflector instead of the

combination of quarter waveplate and mirror.

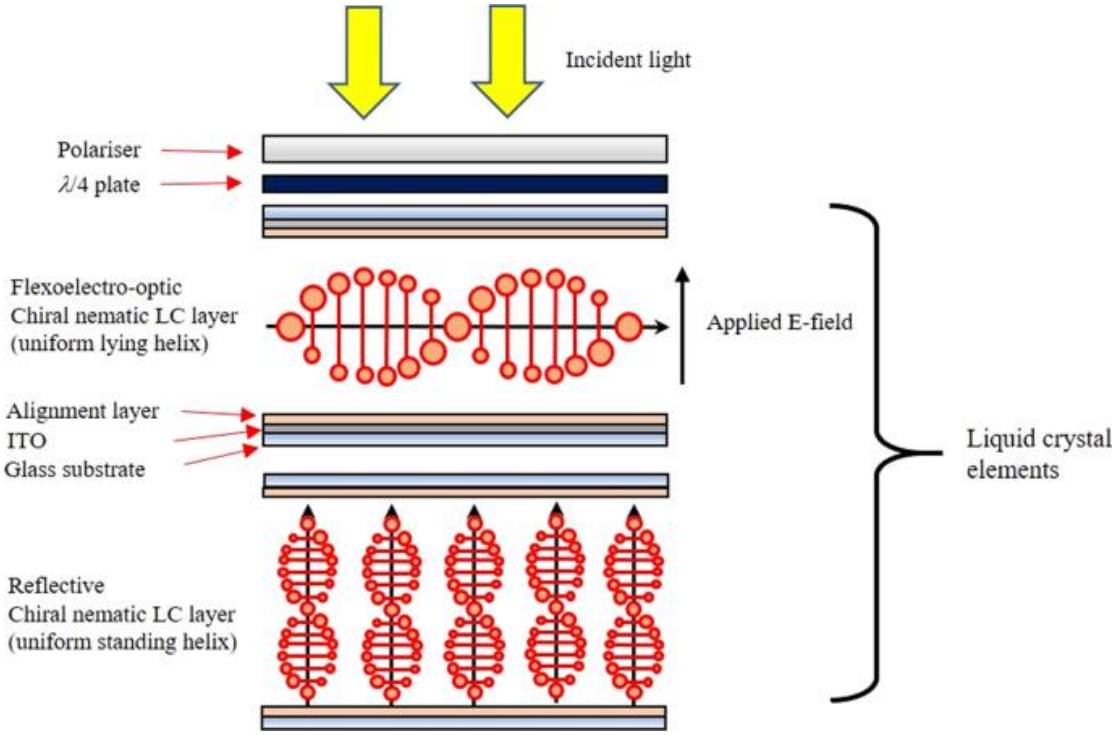

Figure 4.10 Illustration of the low-loss LC phase modulator comprising a flexoelectro-optic chiral nematic LC cell in the uniform lying helix configuration and a reflective chiral nematic LC glass cell in the uniform standing helix alignment.

The incident polariser, quarter-wave plate and LC device still can be modelled using the previous way. On the other hand, the chiral nematic reflector is less commonly modelled using the Jones Matrix technique. Here this element is modelled by combining the well-established Jones Matrices of three standard optical components – a quarter-wave plate, a linear polariser and a mirror. This is equivalent to a chiral nematic reflector because the quarter-wave plate converts the incident circular polarisation of each handedness into two linear polarisation states, the linear polariser then rejects one of these states and the transmitted linear component is subsequently reflected by the mirror. It then passes back through the linear polariser, and then through

the quarter-wave plate which converts it back to the circular polarisation of one handedness only. The net effect is a component that reflects circularly polarised light of one handedness and rejects the other. Bringing all of the components together we can then get the optical output field for this new configuration, $\boldsymbol{E_{out}}$ as

$$E_{out} = \boldsymbol{PQ_1}\left(-\frac{\pi}{4}\right)\boldsymbol{D}(-\varphi,\delta)\left\{\boldsymbol{Q_2}\left(-\frac{\pi}{4}\right)\boldsymbol{PMPQ_2}\left(\frac{\pi}{4}\right)\right\}\boldsymbol{D}(\varphi,\delta)\boldsymbol{Q_1}\left(\frac{\pi}{4}\right)\boldsymbol{P}E_{in} \tag{4.5}$$

```
retard=0.5 %setting the retardance of the LC device
j=1i;
delta=2*pi*retard; % Phase different after a half waveplate
Ein= [0;1]; % Input light
Jmirror= [1,0;0, -1]; % Mirror
Jquarter=[1+j,1-j;1-j,1+j] *exp(j*pi/4)/2; % Quarter waveplate on the transmission path
Jquarter_r= [1+j, -(1-j); -(1-j),1+j] *exp(j*pi/4)/2; % Quarter waveplate on the reflection path
Jh= [1,0;0,0]; % Horizontal Polariser
Jv= [0,0;0,1]; % Vertical Polariser
theta_array= [-pi/4: pi/1000: pi/4]; % Tilt angle array
for n=1: length(theta_array),
    theta=theta_array(n);
    Rn=[cos(theta), -sin(theta); sin(theta), cos(theta)]; % Rotation matrix
    Rp=[cos(theta), sin(theta); -sin(theta), cos(theta)]; % Rotation matrix
    Jlc=[exp(j*delta/2),0;0, exp(-j*delta/2)]; % LC device
    Jsys = Jv*Jquarter_r*Rp*Jlc*Rn*Jquarter_r*Jv*Jmirror*Jv*Jquarter*Rn*Jlc*Rp*Jquarter*Jv;
    % Result of system Jone matrix
    Eout=Jsys*Ein;
    phase= (angle (Eout));
    mag=abs (Eout);
end
```

Figure 4.11 Matlab code for simulating the chiral reflector-based phase modulator.

Equation (4.7) is quite similar to Equation (4.5) except the term in curly-brackets here represents the chiral nematic reflector which includes $\boldsymbol{M}$: Jones matrix of a mirror, $\boldsymbol{Q_2}\left(\frac{\pi}{4}\right)$**:** quarter-wave plate and $\boldsymbol{P}$: polariser. The Matlab code for this system is shown in the following **Figure 4.11**, it has been noticed that this time there is a vertical polariser J_v between the $J_{quarter}$ and J_{mirror}.

Figure 4.12 shows the performance of the ideal and non-ideal optical phase modulator. In this case, we mainly consider the non-ideal properties caused by two components, the LC cell and the chiral nematic reflector. In this simulation, when the LC layer is ideal, the retardance of the device is set to be 0.5λ (i.e. a half-wave plate). As explained previously, this is expected to lead to pure phase modulation of light propagating through the device. The non-ideal case is considered to be a possible error in the thickness of the ULH LC layer and is represented by setting the LC device retardance to be 0.4λ (i.e., it deviates from the half-wave condition). To represent an imperfection in the chiral nematic reflector, we "modify" the quarter-wave plate which is adjusted to have a retardance of 0.2λ (instead of the ideal quarter-wave condition (i.e., 0.25λ), and its orientation is adjusted to be at an angle of π/5 from the vertical (instead of the ideal π/4). The net result is that the reflected light from the chiral nematic "reflector" becomes slightly elliptical.

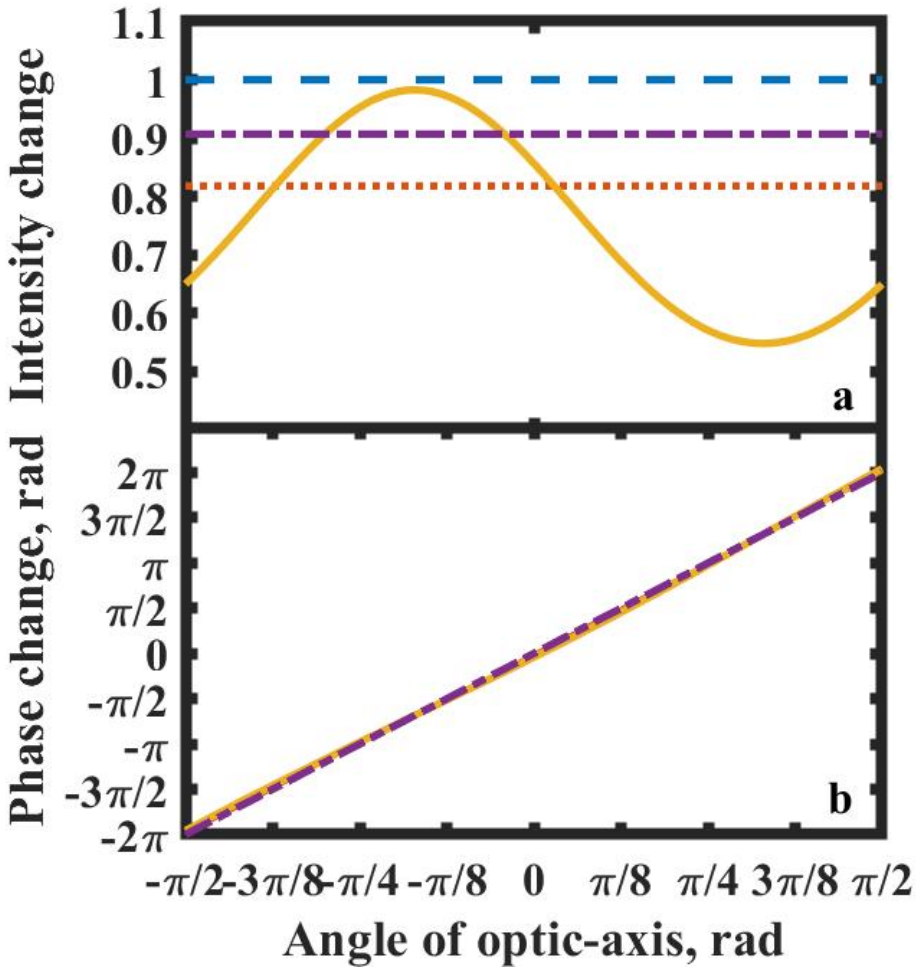

Figure 4.12. Simulations of ideal and non-ideal optical phase modulators based on the chiral nematic reflector configuration. (**a**) intensity and (**b**) phase change are shown as a function of the absolute angle of the optic-axis of the ULH-aligned flexoelectro-optic device relative to the horizontal. The four plots shown in each case are as follows: the ideal case with LC retardance of 0.5λ and ideal chiral nematic reflector (blue line dashed line); imperfect reflector and ideal LC retardance (purple dashed line); non-ideal LC retardance of 0.4λ and ideal chiral nematic reflector (red dotted line); non-ideal LC retardance of 0.4λ and imperfect reflector (yellow line).

It is worth commenting on some interesting effects seen in **Figure 4.12**. Firstly, as expected, for the ideal configuration consisting of both an ideal retardance and reflector, we have full 2π phase modulation for an optic-axis tilt angle range of $\pi/2$ of the

flexoelectro-optic device (a phase modulation range of $\pm 4\pi$ for the optic-axis tilt range of $\pm\pi/2$). Additionally, similar to the previous simulation results, for the ideal case, the system is lossless. From the figure, it can also be seen that a full 2π phase modulation range can always be realised even when one or both components is/are not ideal. Furthermore, from the intensity plots it can be seen that even if one or the other of the components are individually not perfect, the intensity change is still zero (as indicated by the red dashed and purple dashed plots in the figure). Thus, although there is now a loss in the system, the variation in loss for both cases is zero, indicating no modulation in the intensity. Consequently, pure phase modulation is again obtained, which is essential for many technological applications.

Substantial intensity changes (loss variation) only happens when both components are not ideal (as indicated by the yellow curve). The intensity now varies between a maximum of unity and a minimum of around 0.5 (an amplitude minimum of $\sqrt{0.5}$) for the illustrative case considered here. Hence, to minimise the intensity modulation, the required condition is that one of the components (but not both) should be "ideal". This is an encouraging result since in practice it can be difficult to ensure that the ULH device forms an exact half-wave plate, whereas it might be possible to engineer a chiral nematic LC reflector such that the polarisation of the reflected light is close to ideal circular polarisation (by ensuring that the device is operating in the middle of the reflection band), thus providing greater flexibility and tolerance in the construction of the device.

4.7 Experimental results of the phase modulator with chiral reflector

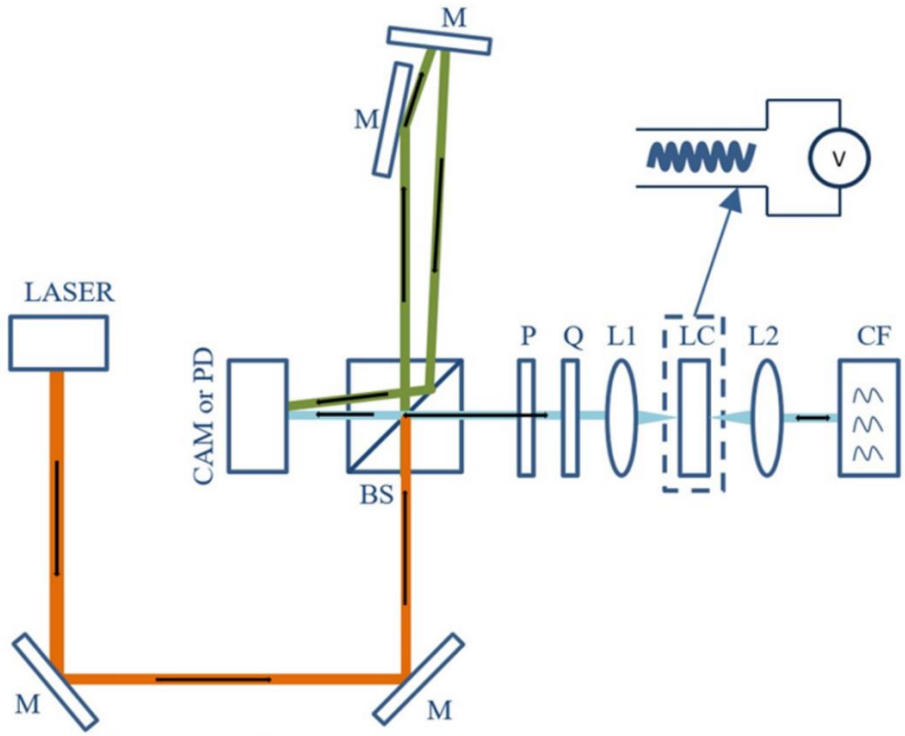

Figure 4.13 Experimental arrangement to measure the phase and intensity response of the LC optical phase modulator. (M, mirror; BS, beam-splitter; P, polariser; Q quarter-wave plate; L1, L2, lenses; LC, modulation device; CF, chiral reflector; CAM, CCD camera; PD, photodiode.) The device is placed in one arm of a Michelson interferometer. Light is focused through the device to ensure that it passes through a mono-domain of ULH alignment. An extra mirror was introduced into the reference arm so that the light from both arms will intersect to generate clear fringes. The reflecting component in the device arm is formed from a chiral nematic LC reflector to reproduce the system outlined in the text. To measure the intensity, the CCD is replaced with a photodiode, together with a pin-hole to ensure that only the signal beam is admitted. The modulation device is a ULH flexoelectro-optic chiral nematic LC as shown.

The implementation of the chiral nematic reflector-based phase modulator is shown in **Figure 4.13**, which is quite similar to the previous configuration except that the mirror and quarter waveplate is replaced by a chiral reflector. The chiral nematic reflector, in this experiment, is made by mixing the nematic LC, HTW114200-100,

(Fusol) with 22.2 wt% of the left-handed chiral dopant, S811 (Merck). This mixture was then filled into a cell and was found to form a Grandjean texture (whereby the helix axis is aligned parallel to the normal of the glass substrates) on a polarising optical microscope. Measurements on a UV-Vis spectrometer confirmed that the centre of the reflection band was close to the wavelength of the He-Ne laser (632.8 nm) as shown in **Figure 4.14**.

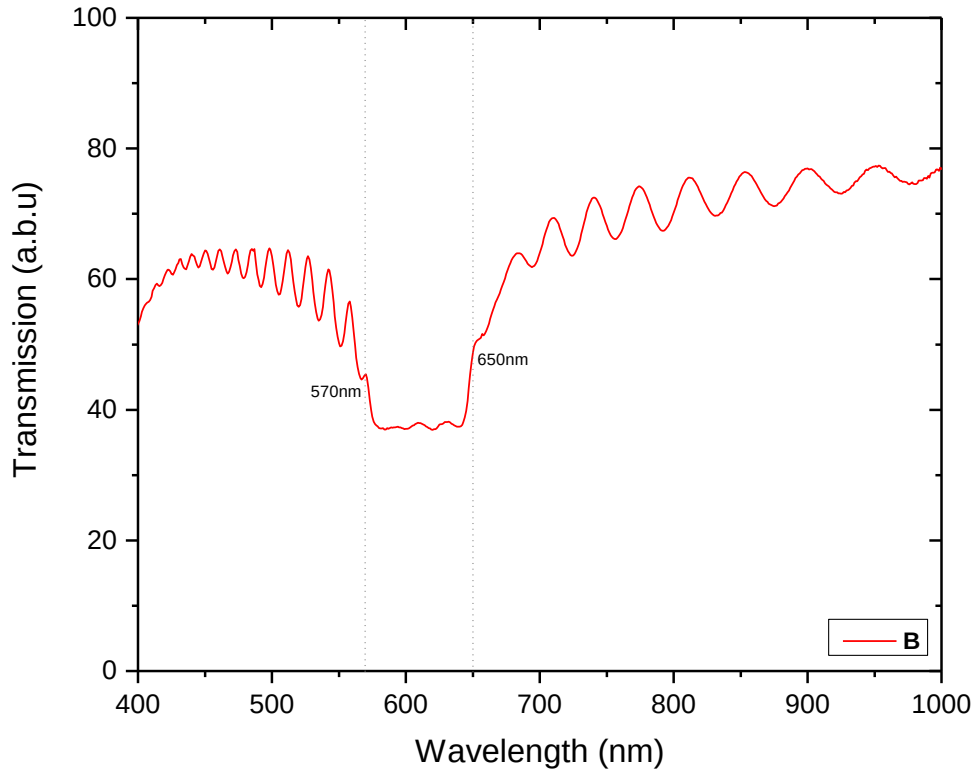

Figure 4.14. The transmission spectrum of a chiral nematic LC, E7+S811. The thickness of the device is 4.93 μm and the cell is measured at room temperature. The bandgap is between 575nm and 650nm.

Figure 4.15 shows the experimental results for the optical phase shift and intensity variation of the new configuration. The applied voltage was varied up to ±21 V, at which point the phase range was found to be almost 2π (actually measured to be 361.4°). The phase change as a function of voltage follows an almost linear behaviour, as expected

from the model results shown in **Figure 4.4**. The slight nonlinearities seen in the optical phase behaviour have two origins: (i) the flexoelectro-optic tilt angle in the ULH device is not precisely linear with voltage; (ii) small drifts in environmental temperature and corresponding air currents (caused principally by the hot-stage stabilising the device temperature) lead to small drift errors in the fringe phase. It can also be seen in the inset shown in **Figure 4.15** that there is very little modulation in the intensity (and hence the amplitude) of the light. So, as anticipated this device configuration with a chiral nematic reflector operates well as a pure phase modulation system. The small changes in intensity that are observed are likely to be due to the electric field-dependence of the birefringence of the chiral nematic LC in the ULH alignment.

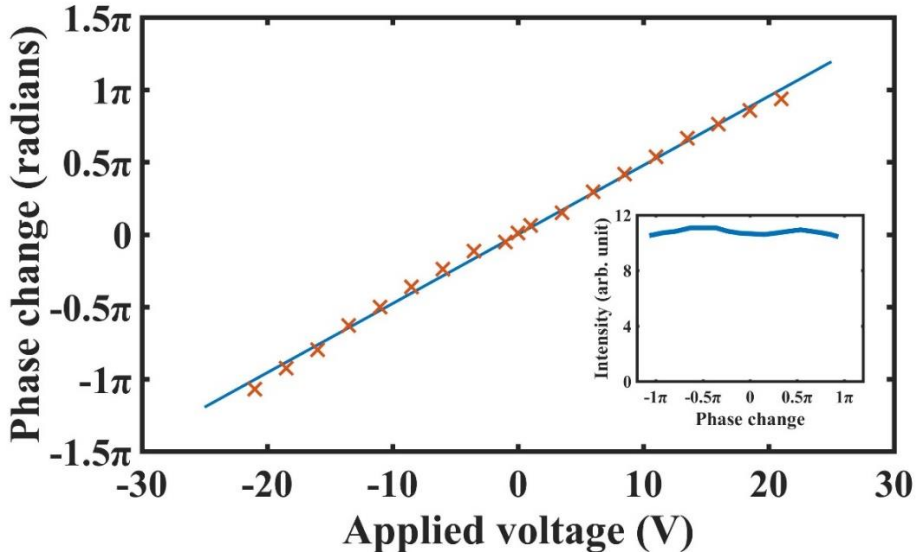

Figure 4.15 Experimentally determined phase and intensity for the LC optical phase modulator presented in this work (measured using the system presented in Figure 4.14 with a CCD camera and photodiode). The main plot shows the optical phase shift as a function of voltage. The lower right inset shows the intensity variation as a function of the measured optical phase angle. The variation in intensity is seen to be minimal. The unit used in the inset is the arbitrary unit, the actual efficiency of this configuration is about 44.8%.

4.8 Conclusion

In summary, this chapter has demonstrated a new LC optical phase modulator based on the flexoelectro-optic behaviour of a ULH-aligned chiral nematic LC. This configuration has substantial potential in spatial light modulator technology which can exhibit full 2π phase modulation with sub-millisecond response time by applying a 4 V/μm electric field at a temperature of 106°C. In addition, through this research, it has been shown that an ideal chiral nematic reflector can be used to replace the mirror and quarter waveplate combination to ensure that the system is less sensitive to the nonideality in the LC phase modulation element. Based on this reflective mode phase modulator, in the next chapter, a new phase modulator in a transmissive configuration is presented, which can be used in applications where a reflective mode is not desirable. While a 4V/μm electric field and an operating temperature of 106°C are still not yet suitable for commercial SLM devices, these limitations can be addressed through the development and refinement of the liquid crystalline materials and mixtures to obtain larger e/K ratios and larger Δn.

Chapter 5 Transmissive liquid crystal optical phase modulator with 2π phase modulation and 1 kHz switching

5.1 Introduction

Following the demonstration of a reflective-mode phase modulator in the previous chapter, the purpose of this chapter is to demonstrate an analogue phase modulator in a transmissive configuration using the flexoelectro-optic effect in short-pitch chiral nematic liquid crystal (LC) devices. Two different modes are considered, both of which generate full 2π phase modulation at 1 kHz switching frequency. The first configuration that is considered consists of a half-wave plate placed between two flexoelectro-optic LC devices subjected to electric fields that are applied in phase. Secondly, we demonstrate that a similar phase modulation response can be observed by removing the half-wave plate and subjecting the two flexoelectro-optic LC devices to electric fields whereby the polarities are out of phase. Both configurations demonstrated herein are promising for developing next-generation LC spatial light modulators, particularly when reflective geometries are challenging or impractical.

5.2 Comparison of transmissive and reflective spatial light modulators

As mentioned in the previous chapter, LC SLMs have been widely used in various optical manipulation applications. The devices come in different pixel formats but basically can be divided into two types: reflective and transmissive mode [146-157]

(**Figure 5.1**). Due to the pixelated nature of the LC SLMs, light that enters an LC SLM and hits these dead areas (the non-functional areas between pixels) are not modulated by the SLM which leads to a zero-order diffracted beam [147, 148]. The ratio of the intensity of the zero-order diffracted light to the intensity of the total incident light is called the zero-order diffraction efficiency, which is an essential parameter for characterising the LC SLMs. Usually, low zero-order diffraction is desirable as zero-order diffraction will distort the light profile and undermine the reconstruction quality.

Assuming that the SLM is flat, for a reflective mode LC SLM, the zero-order diffraction efficiency can be approximated by multiplying the square of the fill factor (the ratio of the size of the dead area to the pixel area) with the reflectivity of the backplane. The zero-order diffraction efficiency for a transmissive LC SLM, on the other hand, is equal to the fill factor squared times the transmission of the SLM. Typically, the zero-order diffraction efficiency of reflective SLMs is higher than that of transmissive SLMs [148]. However, in reality, the overall efficiency of transmissive SLMs is lower than that of reflective SLMs due to the presence of electronics in the backplane that blocks the light, which reduces the system's overall efficiency. In addition, for the same applied voltage, pre-tilt angle and LC material, the thickness of the device for a transmissive SLM is two times higher than that of a reflective SLM. Hence, the response time of a reflective phase modulator is about four times faster than that of a transmissive modulator [149]. Despite the slow response time and system efficiency of transmissive devices, transmissive LC SLMs normally have advantages such as small size, low weight and simple to fabricate [149-151,157] due to the fact

they are in the transmissive configuration which is quite useful, especially when the reflective configuration is challenging.

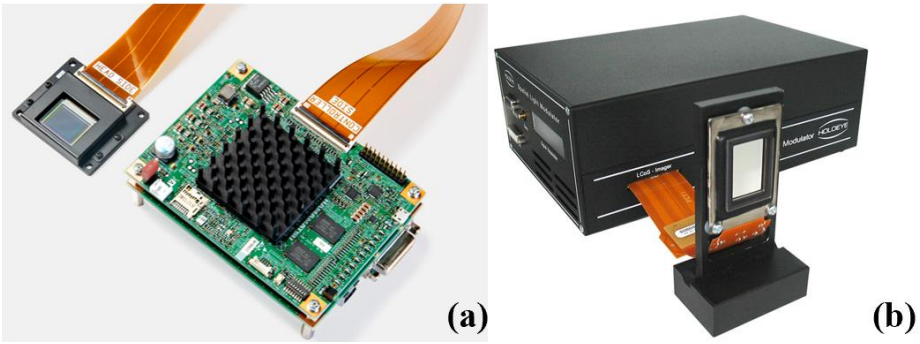

Figure 5.1 Different types of phase modulators. (a) Reflective phase modulator (b) Transmissive phase modulator.

In the previous chapter, a reflective phase modulator based upon the flexoelectro-optic effect in chiral nematic LCs has been demonstrated that exhibits a complete 2π phase range and a fast switching frame rate of 1 kHz and low residual amplitude modulation and drive voltage [73,138]. As a reminder, the concept is based on the effect of passing circularly polarised light through a rotatable half waveplate. In practice, this can be realised using our proposed technology by passing linearly polarised light through a chiral nematic LC, aligned in the uniform lying helix (ULH) geometry, placed between a pair of quarter-wave plates. The range of phase modulation available, θ_p, depends on the angle through which the optic axis of the LC layer can be rotated electrically and is found to be equal to twice the switching angle. Accordingly, flexoelectro-optic devices that can exhibit ±45° degree switching result in phase modulation of ±π/2 (i.e. a $\theta_p = \pi$ phase range).

In the work presented in this chapter, two different transmissive phase modulation schemes are presented that could be used to generate a 2π phase range with kHz frame rates by placing two flexoelectro-optic LC devices in series. The first configuration consists of a half waveplate that is placed in between two LC devices that are switched in the same direction by applying the same bipolar electric field to both devices. The second configuration demonstrated comprises two flexoelectro-optic LC devices for which the optic axes are switched in the opposite direction to one another by applying electric fields to each layer that are of the opposite polarity.

5.3 Simulation results of the transmissive phase modulator

Jones calculus [39, 40] has also been used in this work to model the optical behaviour of the two different configurations of transmissive phase modulators. A schematic of the primary device configuration is shown in **Figure 5.2**. The incident light is converted into circularly polarised light through the combination of a polariser and a quarter-wave plate, which then passes through a flexoelectro-optic chiral nematic LC device that is aligned in the ULH geometry. The thickness of the LC layer was chosen to provide a half-wave retardance at the wavelength of interest (i.e. $\lambda = 633$ nm). Finally, the transmitted light then passes through a second-quarter waveplate. Assuming that all the components are ideal, the phase modulation that could be achieved using this configuration ranges from 0 to π, depending upon the tilt of the optic axis and the magnitude of the applied electric field.

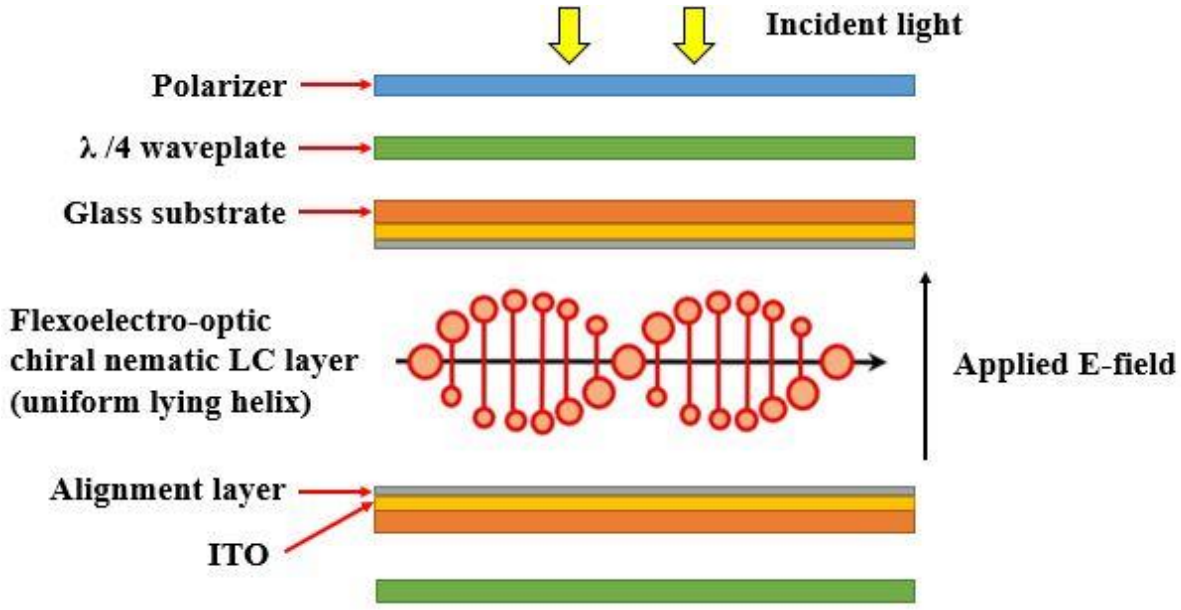

Figure 5.2 Illustration of the LC phase modulator configuration containing a linear polariser, flexoelectro-optic chiral nematic LC layer in the ULH mode (an electrically tunable half-wave plate) and two quarter-wave plates. The optic axis of the LC layer is parallel to the substrates (horizontal).

In this experiment, the linear polariser, quarter-wave plate and the LC device can be modelled using the concepts mentioned in the previous chapter. The optical field at the output of the device, $\boldsymbol{E_{out}}$ for the basic configuration (i.e. polariser, quarter-waveplate, LC layer, quarter-wave plate), is given by

$$E_{\text{out}} = \mathbf{Q}_2\left(\frac{\pi}{4}\right)\mathbf{D}(\varphi)\mathbf{Q}_1\left(\frac{\pi}{4}\right)\mathbf{P}E_{\text{in}} \tag{5.1}$$

where $\mathbf{D}(\varphi)$ is the Jones matrix of an LC layer with a retardance, δ, and an optic axis that is oriented at an angle, φ, to the horizontal in the plane of the device. $\mathbf{Q_1}\left(\frac{\pi}{4}\right)$ and $\boldsymbol{Q}_2\left(\frac{\pi}{4}\right)$ are the Jones Matrices for quarter-wave plates at π/4 to the vertical direction in the lab frame, $\boldsymbol{E}_{\text{in}}$ is the Jones vector for linearly (vertical) polarised light at the input and **P** is a vertically aligned linear polariser. Multiplying out the terms in Equation 5.1,

assuming that all components are ideal (with the LC layer forming a perfect half-wave plate), leads to

$$E_{\text{out}} = E_{\text{in}} e^{\pm 2i\varphi} \tag{5.2}$$

which demonstrates the dependence of the phase on the switching angle of the optic axis of the LC layer.

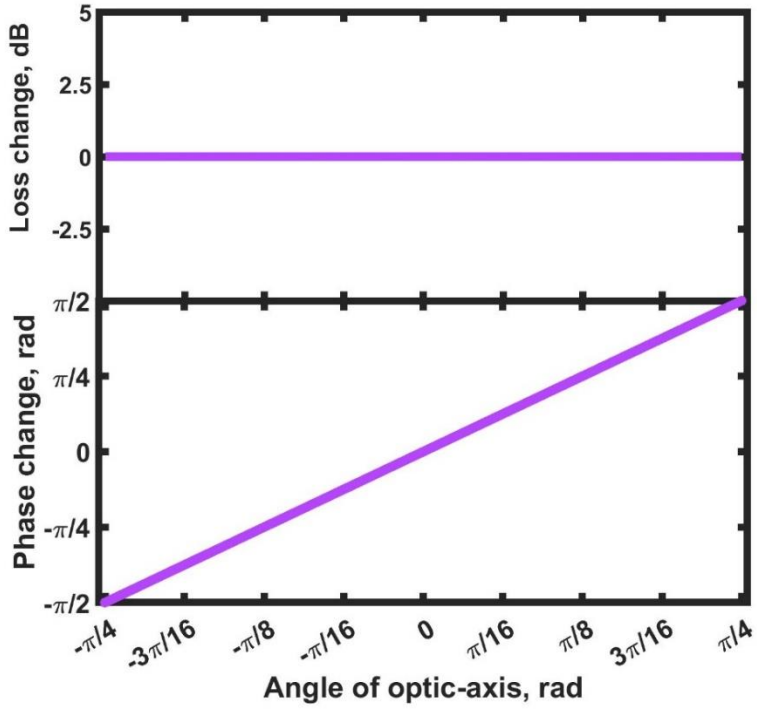

Figure 5.3 Simulation results for the single transmissive device (consisting of a single LC layer) are shown in Figure 5.2. When all of the components in the system are assumed to be ideal, the single device configuration is limited to a π phase range for a switching angle of ±π/4. No amplitude variation is observed when all the components in each system are considered to be ideal.

Figure 5.3 (which has been generated using Matlab) shows the performance of the "basic" phase modulator. In this simulation, the LC cell and the quarter waveplate are assumed ideal i.e. the retardance of the LC device is set to be 0.5λ (i.e. a half-wave

plate) and the retardance of the quarter waveplate is 0.25λ. This is expected to lead to pure phase modulation of light propagating through the device. As mentioned above, if every component in the system is ideal, the system will generate a π phase change and there is no amplitude modulation.

Figures 5.4(a) and (b) show the configurations of the two transmissive phase modulators based on the fundamental device configuration shown in Figure 5.2. Both systems include two LC devices, two quarter-wave plates and a polariser, but as mentioned previously a half waveplate is placed in between the two LC cells in Configuration I (Figure 5.4(a)) and the electric field applied to the two LC layers are in the same direction. For Configuration II, the need for an additional half-waveplate is negated as the electric fields are applied in opposite directions. The optical output fields, $\boldsymbol{E_{\mathrm{out}}}$ for the two different transmissive phase modulator configurations are given by

$$E_{\mathrm{out}} = \mathbf{Q}_2\left(\frac{\pi}{4}\right)\mathbf{D}(\varphi)\boldsymbol{H}_1\left(\frac{\pi}{2}\right)\mathbf{D}(\varphi)\mathbf{Q}_1\left(\frac{\pi}{4}\right)\mathbf{P}E_{\mathrm{in}} \tag{5.3}$$

$$E_{\mathrm{out}} = \mathbf{Q}_2\left(\frac{\pi}{4}\right)\mathbf{D}(-\varphi)\mathbf{D}(\varphi)\mathbf{Q_1}\left(\frac{\pi}{4}\right)\mathbf{P}E_{\mathrm{in}} \tag{5.4}$$

Note that in Equation (5.4) the angles of the optic axis in the LC layers are of opposite signs because the electric fields are of the opposite polarity and there is no half-waveplate in the middle of the two LC devices. Multiplying out the terms in Equations (5.3) and (5.4) and (assuming that all components are ideal) leads to the result

$$E_{\mathrm{out}} = E_{\mathrm{in}}e^{+4i\varphi} \tag{5.5}$$

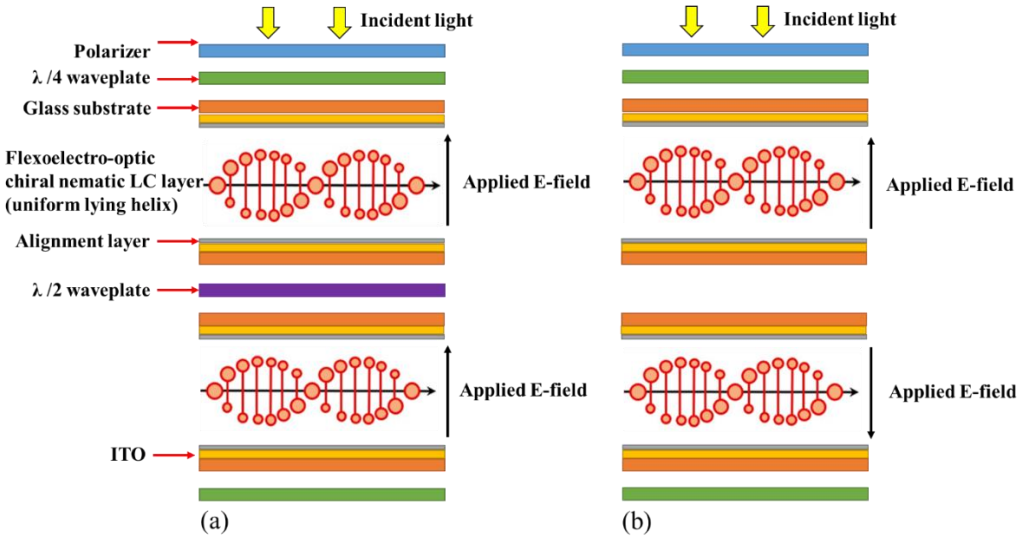

Figure 5.4 Illustration of the two configurations of transmissive LC phase modulators considered in this work. (a) Configuration I comprises two flexoelectro-optic chiral nematic LC cells in the ULH geometry, two quarter-wave plates, a half-wave plate and electric fields applied to both LC cells that are in-phase. (b) Configuration II consists of two flexoelectro-optic chiral nematic LC cells in the ULH geometry and two quarter-wave plates. The electric fields on both LC cells are of the opposite polarity.

From Equation (5.5) it can be seen that a switching angle of φ will result in a 4φ phase modulation. For this study, the switching angle of our LC layer is within the range of 90° (i.e. a tilt angle of the optic axis in the ULH device of ±45°), hence a phase modulation of $\pm\pi$ can be obtained (i.e. a 2π phase range).

Figure 5.5 illustrates the results from simulations based on Equations (5.3) and (5.4). For the simulations, the LC and quarter-wave plates are assumed to be ideal (e.g., the LC behaves as an ideal half-wave plate). When all the components are ideal, Configurations I and II lead to a phase modulation that is a multiple of four of the switching angle of the flexoelectro-optic LC layers as expected which means Configurations I and II generate a 2π phase range for a switching angle of ±45°. As shown, no amplitude variation is observed when all the components in each system are

considered to be ideal.

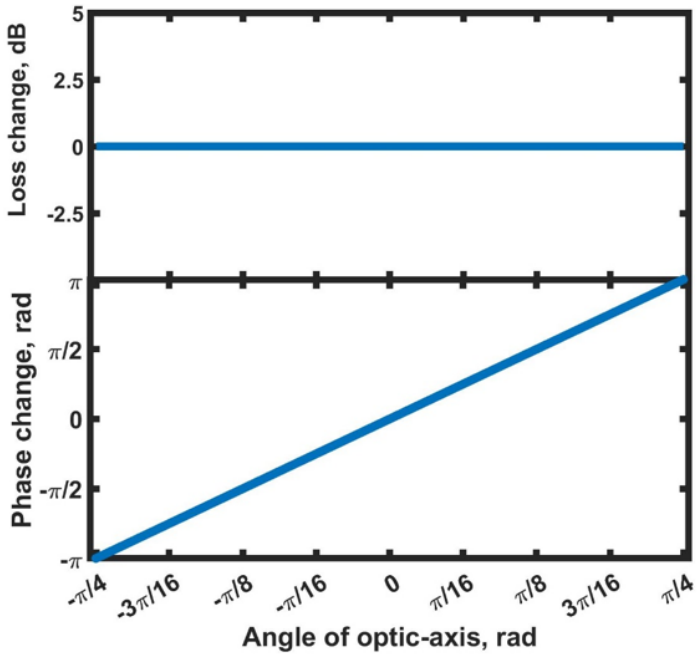

(a)

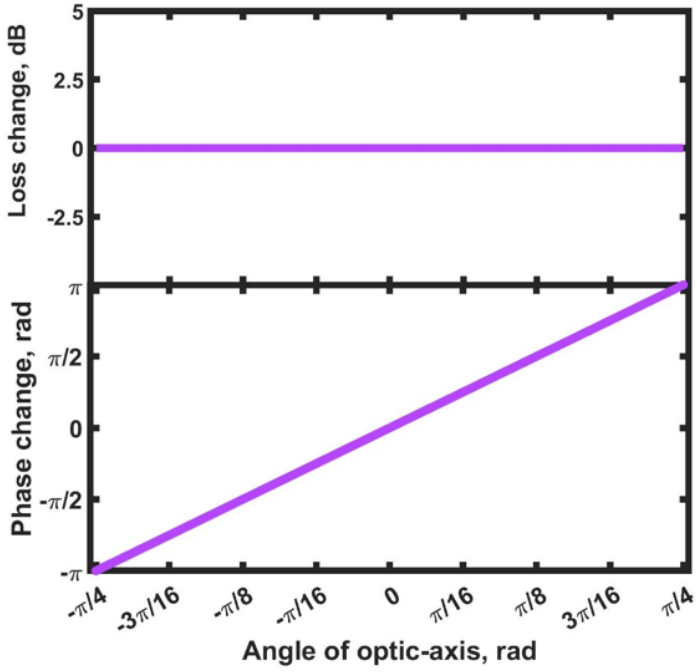

(b)

Figure 5.5 Results from simulations using Equation (5.3) and Equation (5.4). (a) is the result from Configuration I and (b) is the result from Configuration II**.** Both the loss change and the phase change are presented as a function of the tilt angle of the optic axis of the flexoelectro-optic LC layers.

5.4 Experimental results for transmissive phase modulators

The device configurations in **Figures 5.2** and **5.4** were investigated experimentally using a Michelson interferometer arranged as shown in **Figure 5.6**. In this case, the device under test (DUT) corresponds to either the basic single flexoelectro-optic device configuration or Configurations I or II. Light from a helium-neon laser at 632.8 nm (Uniphase 1125P) was passed through a linear polariser (vertical in the lab frame) to a 50:50 non-polarising beam splitter (Newport 05BC16NP) in order to divide the beam into separate arms. For the first arm, 50% of the light was directed to a mirror before it was incident on the second beam splitter (BS2, Thorlabs CM13) where it combined with the light that had propagated through the second arm of the interferometer (which contained one of the LC phase modulator configurations). After passing through the first beamsplitter (BS1), the light propagating along the second arm of the interferometer passed through a quarter waveplate, which generated either left or right circularly polarised light, before entering the chiral nematic LC layer. The LC layer was pre-aligned in the ULH geometry and exhibited flexoelectro-optic switching when subjected to an electric field that was oriented orthogonal to the helix axis. The thickness of the LC layer was set as close as possible to that corresponding to a half waveplate condition.

The LC mixture used in this study is similar to the material used in the reflective phase modulator. The mixture consists of the bimesogen (dimer) CBC7CB dispersed with 3 wt% of the high twisting power chiral dopant, BDH1281 (Merck KGaA). The chiral nematic mixture was filled into a nominally 5 μm-thick Instec cell with antiparallel rubbed polyimide alignment layers and indium tin oxide electrodes. The

LC mixture was found to exhibit a right-handed chiral nematic phase between 106°C and 113°C (on heating). At this temperature, the device is placed under the microscope to check the flexoelectro-optic effect as shown in **Figure 5.7**. A fairly uniform ULH alignment can be observed on a local scale and defects in the Figure are mainly caused by spacer beads. Good contrast can be found between the bright and dark states which indicates a strong flexoelectro-optic effect. In addition, at this temperature, the switching time (10-90% response time) of the device was found to be ≈160 μs.

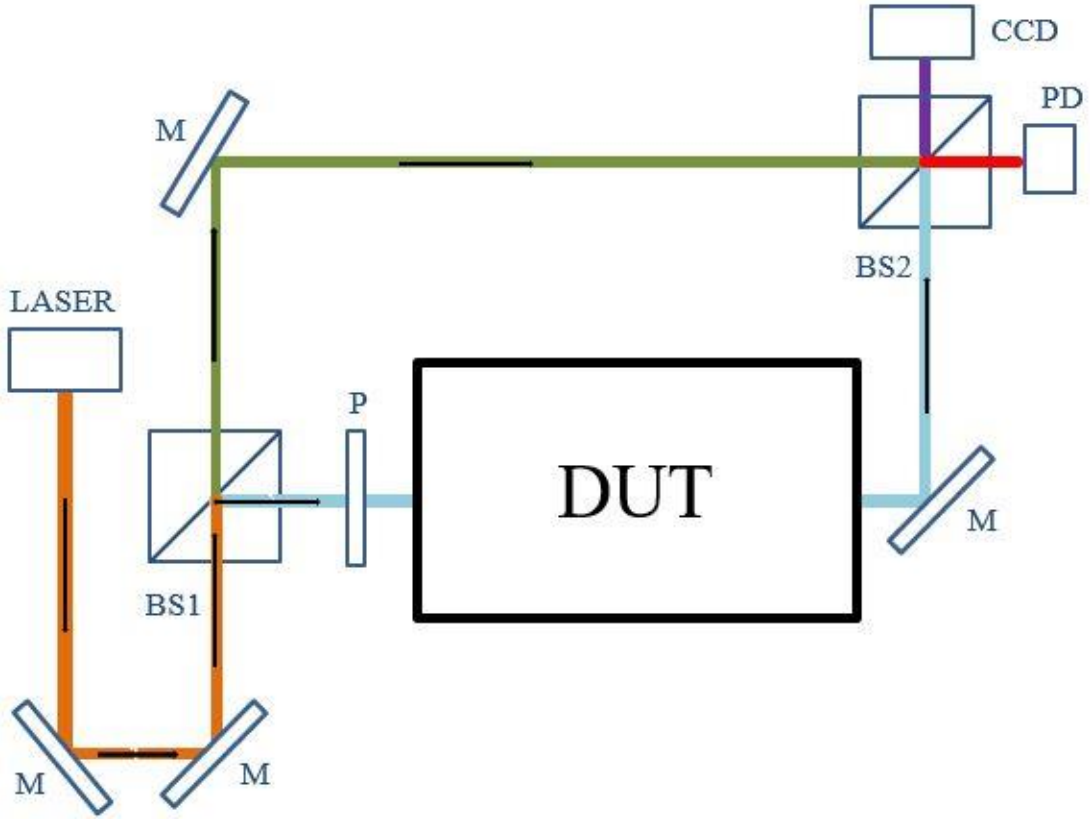

Figure 5.6 The Michelson interferometer used to measure each device under test (DUT), which represents either the basic single LC device (Figure 5.2) or the two LC device configurations (Figure 5.4). The remaining components are M, mirror; BS1, BS2, beam-splitters; CCD camera; PD, photodiode.

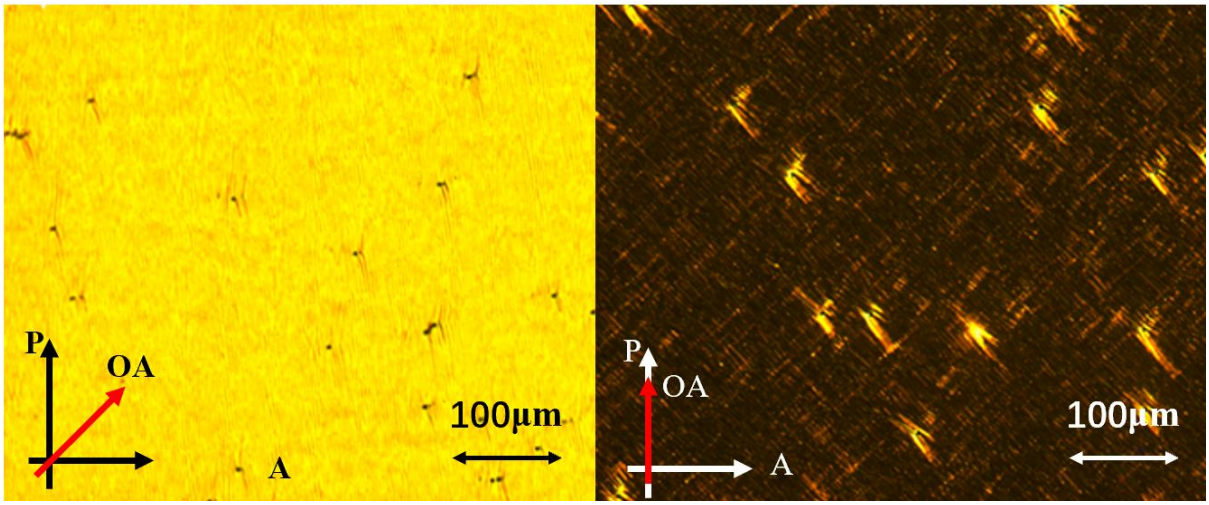

Figure 5.7. shows the polarizing optical microscope images of the bright (left) and dark (right) state of the chiral nematic LC device used to illustrate the flexoelectro-optic effect. The device is under the ULH structure by applying a 1 kHz square-wave at 106°C. The device consists of 3 wt% chiral dopant (BDH1281) in the nematic host CB7CB. The thickness of the device was 4.82 µm. The discontinuities in the structure are due to the presence of spacer beads. A fairly uniform ULH alignment can be seen locally, with good contrast between the bright and dark states. The direction of the polarizer and analyser are indicated by the white and black arrows for different images and the optical axis is represented by the red colour arrow.

Each LC device was mounted on a temperature-controlled hot stage and an electric field was applied using an arbitrary function generator (Wavetek 395) and a voltage amplifier (FLC Electronics F10AD). The configurations for each DUT are shown explicitly in **Figure 5.8**. In all three cases, the outer components of the DUT are the quarter-wave plates. For the basic, single flexoelectro-optic device (**Figure 5.8**(a)), a pair of focal lenses (L1 and L2) were used to ensure that the light only passed through a mono-domain region of the LC device (which were typically 50-100 μm^2 in size). **Figure 5.8**(b) shows the arrangement for experimentally testing Configuration I (**Figure 5.4**(a)), which is similar to the basic configuration except with the addition of

the extra LC device and half-wave plate (H), which are introduced into the modulation arm to produce a 0-2π phase modulation range in accordance with the results obtained from simulations. In this case, instead of using just a pair of lenses, an additional lens (L3) is added between the two LC devices to form a three lens (2f-f-2f) system so that the light can be appropriately focused onto mono-domain regions within the two LC layers. Similarly, **Figure 5.8**(c) shows the arrangement for testing Configuration II (**Figure 5.4**(b)). Here the electric field applied to the second LC layer is of the opposite polarity to the electric field applied to the first LC layer, which negates the use of the half-wave plate (H).

After passing through the DUT, light from both arms of the interferometer is combined at the beam splitter to generate an interference pattern. The phase and amplitude response were subsequently recorded by a CCD camera (Thorlabs DCU224C, 1280 × 1024, 8-bit colour) and a photodiode, respectively. The drive signal for the LC device was set as a 1 kHz square-wave with a controllable amplitude level, and the camera was set to an exposure time of 100 μs so as to record the change observed in the interference fringes when the amplitude of the electric field applied across the LC device was altered.

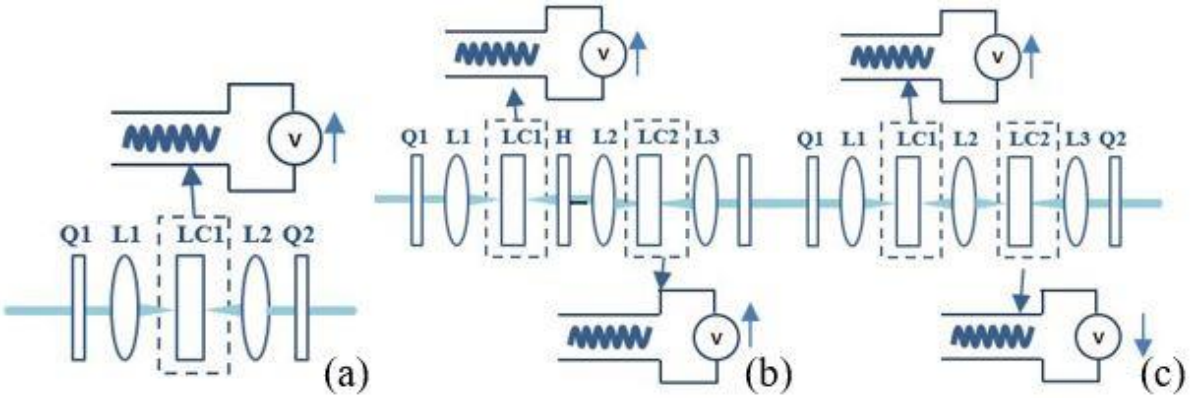

Figure 5.8 Experimental arrangement of the three different DUT inserted in the Michelson interferometer presented in Figure 5.6. (a) basic configuration with one LC layer, (b) Configuration I and (c) Configuration II. (H, half-wave plate; Q1, Q2 quarter-wave plates; L1, L2, L3 - lenses; LC1, LC2, LC – phase modulation devices).

Images of the interference fringes recorded by the CCD camera of the interferometer for the basic configuration, Configuration I and Configuration II, are shown in **Figure 5.9**. **Figure 5.9**(a) shows five different images of the interference fringes, each representing a phase modulation state corresponding to a specific voltage applied to the single LC layer. For this configuration, the shift in the fringes corresponding to a π phase change is found to occur for $\pm$34V (6.9 V/μm). Alternatively, for Configuration I and II, shown in **Figures 5.9**(b) and **5.9**(c), respectively, a 2π phase shift is observed for an applied voltage of $\pm$34V.

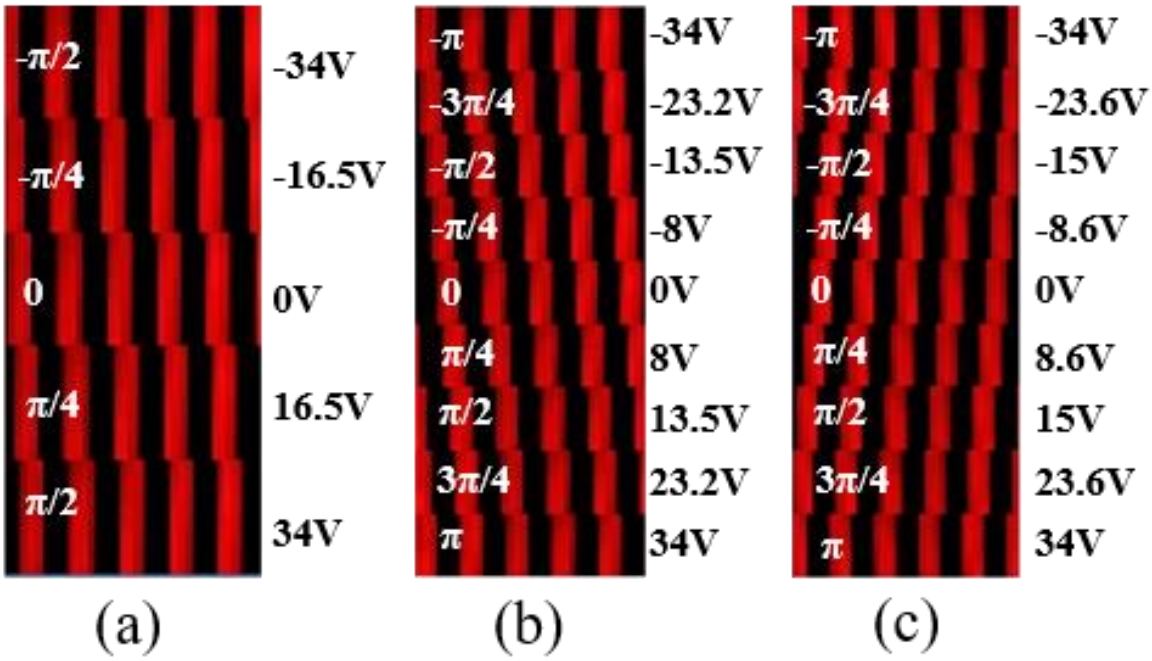

Figure 5.9 Images recorded on the CCD of the Michelson interferometer for the basic device and the two configurations I and II. (a) Results for the basic, single LC device configuration. Nine images for (b) Configuration I and (c) Configuration II. These are shown for modulated phase angles at π/4 intervals.

Figure 5.10 shows the results for the optical phase modulation of three configurations as a function of the voltage applied to the LC layer(s). These are found to be in good agreement with the simulations in **Figure 5.3** and **Figure 5.5** in that both Configurations I and II exhibit full 2π phase modulation whereas the basic single LC device shows a phase modulation that is about π for a switching angle of 90°. In order to show that some of the configurations can provide greater than 2π (6.3 rads) phase range, the applied voltage was varied up to ±37.5 V (7.6 V/μm) and the range was found to be almost 2.2π (6.9 rads). From the figure, it can be seen that in all cases the phase change as a function of voltage appears to follow a roughly linear behaviour across the

voltage range considered here, which again is in good agreement with the simulation results shown in **Figure 5.3** and **Figure 5.5**. It should be noted that the intensity variation measured by the photodiode was found to be very small in each case.

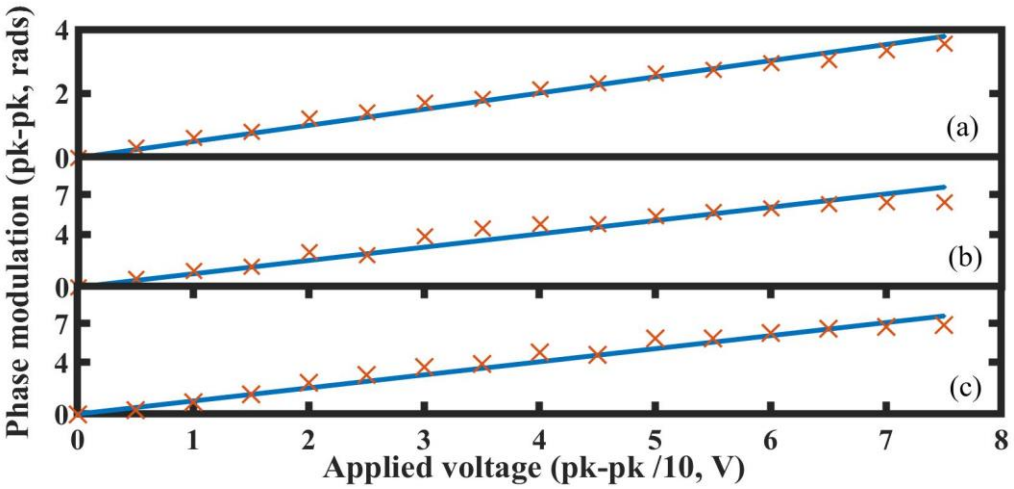

Figure 5.10 Phase modulation extracted from the interference fringes plotted as a function of the applied voltage for (a) the basic (single LC layer) configuration, (b) Configuration I and (c) Configuration II. Lines of best fit to the experimental data (shown in blue) are also presented.

For the basic configuration (**Figure 5.10**(a)), the slight deviation from the linear dependence seen in the optical phase behaviour is believed to come from: (i) the flexoelectro-optic tilt angle in the ULH device not being perfectly linear with applied voltage; and (ii) small drifts in the environmental temperature and corresponding air currents (caused principally by the hot-stage stabilising the device temperature) leading to small drift errors in the phase extracted from the fringes. For the other two configurations, it can be observed that the deviation from linear dependence is slightly larger than that recorded for the basic configuration: this is because two LC layers are used which increases the drift errors described previously. Compared with the results

presented in the previous chapter, which achieve a 2π phase modulation with a reflective geometry, the transmissive configurations presented here exhibit a greater deviation from linear dependence. It is expected that the drift caused by the environment is small compared with the nonlinearities introduced by the LC layers.

5.5 Conclusion

In summary, three different transmissive mode LC optical phase modulators have been presented based on the flexoelectro-optic effect of a chiral nematic LC aligned in the ULH geometry. A basic configuration consisting of a single LC layer between quarter-wave retarders is found to exhibit a phase modulation π corresponding to a $\pm 45°$ switching angle of the flexoelectro-optic effect. To achieve full 2π modulation in transmission with flexoelectro-optic devices that exhibit a switching angle of $\pm 45°$, an additional LC layer is required. It has been shown that this can be achieved by either adding a half-wave plate in between two LC layers when the electric field applied to the two layers is the same or by applying electric fields of opposite polarity, avoiding the need for an additional half-wave plate.

Both configurations are investigated using simulations involving Jones matrices and are consistent with our experimental results when the chiral nematic LC layers exhibit $\pm 45°$ switching angles. This is achieved using LC layers consisting of the bimesogen CBC7CB doped with 3 wt% chiral dopant and subjected to an applied electric field of 6 V/μm at a temperature of 106 °C. These configurations have potential

in terms of the development of spatial light modulator technology, enabling full 2π phase modulation with low-intensity modulation to be achieved when transmissive devices and geometries are required.

Even though the transmissive configuration is desirable in some applications, the system still contains numerous components, which increases the footprint of the modulator. Therefore, in the next chapter, an integrated phase modulator will be presented.

Chapter 6 A compact full 2π flexoelectro-optic liquid crystal phase modulator

6.1 Introduction

In Chapter 4, it has been shown that the flexoelectro-optic effect can be used to achieve full 2π phase modulation when chiral nematic LCs with large tilt angles (>45°) of the optic axis are combined with a $\lambda/4$ waveplate and a reflector that both preserves the handedness of circularly polarized light and creates a double-pass geometry; this reflector can either be a combination of a $\lambda/4$ waveplate and a mirror or a chiral nematic reflector [73, 138]. The previous chapter, Chapter 5, has demonstrated an analogue phase modulator in a transmissive configuration using the flexoelectro-optic effect. The transmissive phase modulator can be set in two different configurations. The first configuration that was considered consisted of a half-wave plate that is placed between two flexoelectro-optic LC devices that are subjected to electric fields that are applied in phase. The phase modulation for the second one can be obtained by removing the half-wave plate and subjecting the two flexoelectro-optic LC devices to electric fields whereby the polarities are out of phase [160].

For both reflective and transmissive phase modulators presented in the preceding chapters, achieving full 2π phase modulation experimentally has been made possible by the development of large tilt-angle LC compounds such as 4′,4′-(heptane-1,7-diyl)bis(([1′,1″-biphenyl]-4″-carbo-nitrile)) (CB7CB), which exhibits switching angles in excess of ±45° when it is doped with a small concentration of high twisting power

chiral dopant [73,100,104,109,139,159,160]. Even though the phase modulators can generate 2π phase modulation with sub-millisecond response time, there are still several drawbacks with those configurations such as high operating temperature and unstable LC alignment [73,138]. Besides, one of the essential disadvantages is that numerous optical components were required for building the phase modulator, which makes the current arrangement impractical for many device applications as the overall thickness is rather large and bulky. For example, for the reflective phase modulator in Chapter 4, an LC cell with a nominal gap of 5 μm was used as the tunable π/2 waveplate and standard bench-top optical components in the form of π/4 waveplates and mirrors were needed to build the phase modulation system. Furthermore, the numerous free-space components result in multiple interfaces and therefore unwanted reflection losses. Consequently, before this technology can be deployed into real systems, the optical components need to be integrated into a compact package so that the overall device thickness is comparable with existing SLM devices.

This chapter presents the first integrated LC phase modulator that combines a flexoelectro-optic LC layer that behaves as a switchable $\lambda/2$ waveplate with a polymerized reactive mesogen layer, which acts as a $\lambda/4$ waveplate, and a mirrored substrate that creates a double-pass geometry. For a flexoelectro-optic LC layer that exhibits switching angles of ±45º at a voltage of ±85 V we observe full 2π phase modulation when driven by a 1 kHz waveform. Finally, experimental results are compared with modelling using Jones calculus of the amplitude and phase variation when the LC and the polymer layer deviate from their desired waveplate conditions.

The reduction of the individual components into a single device represents an important step forward in terms of development towards the realization of a flexoelectro-optic optical phase modulator, which is particularly significant for applications where size and cost are critical factors such as in LiDAR for the Space [84,85,162-164] and Automotive industries [84, 85,165-169].

6.2 Device fabrication

The concept and basic structure of the integrated device that was fabricated and studied in this work are illustrated in **Figure 6.1.** Briefly, the device consists of a 100-nm thick silver layer that is coated onto a glass substrate, a reactive mesogen polymer film (PF) that acts as a $\lambda/4$ polymer retarder, a tunable $\lambda/2$ flexoelectro-optic LC layer that is sandwiched between alignment layers, and a top glass substrate that is coated with the transparent conductor, ITO. The total thickness of the device was not precisely measured, but the thickness of the region where the device shows the appropriate phase modulation has been estimated from the results presented in this chapter. The silver layer on the bottom substrate has two functions in the device: 1) it acts as a reflector for the incoming light so as to increase the modulation depth by creating a double-pass through the LC layer, and 2) it acts as the bottom electrode, which together with the top ITO electrode, facilitates the application of an electric field across the chiral nematic LC layer so as to initiate flexoelectro-optic switching.

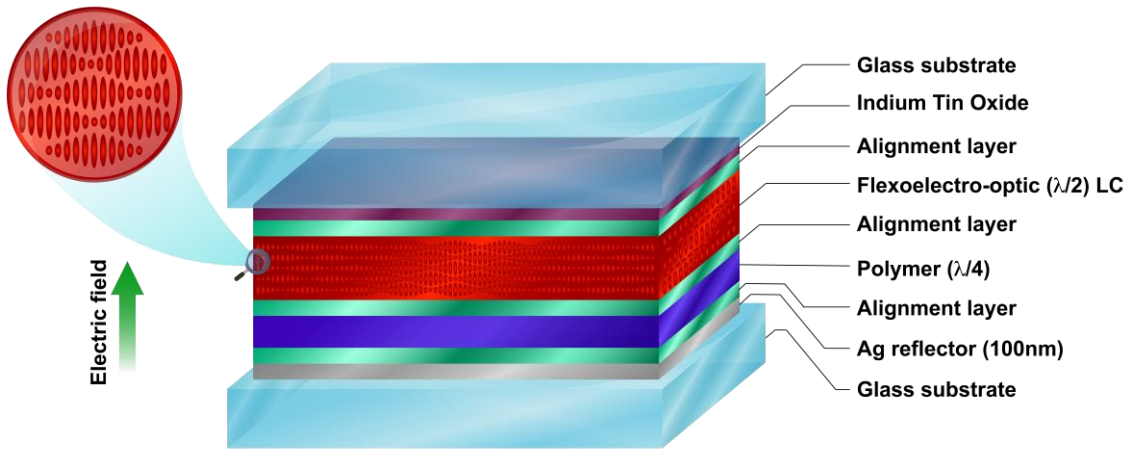

Figure 6.1 Device architecture of the 'integrated' flexoelectro-optic LC modulator.

One experimental challenge that is encountered when fabricating the device presented in Figure 6.1 is the necessity for the polymer and LC layers to form $\lambda/4$ and $\lambda/2$ waveplates, respectively, at the desired wavelength. In turn, this requires precise control of the thickness of the layers, which is non-trivial. To relax the constraints on the thickness, the polymer and LC layers were fabricated so that the thickness of each layer varied across the cell: in other words, each layer formed a wedge shape. The subsequent orientations of the wedged polymer and LC layers were orthogonal to each other, allowing us to find a region where the polymer and LC layers function as a $\lambda/4$ waveplate and a $\lambda/2$ waveplate, respectively.

In addition, several issues have been encountered when fabricating the polymer layer that functions as a $\lambda/4$ waveplate. The initial idea is to develop a free-standing film that can be transferred onto the silver film at a later stage. For the polymer film, the alignment is created by using mechanical rubbing. Although precise alignment can be obtained by using this method, a problem is encountered when we separate the cell.

It is impossible to get a complete film using this method as it is very thin and fragile, which is easy to break during the cell separation process (**Figure 6.2**). A complete polymer film is important for this experiment because a region that functions as a $\lambda/4$ waveplate must be found. A damaged polymer film may result in the loss of a region that works as a $\lambda/4$ waveplate. Besides, it was not easy to attach the free-standing film directly onto the silver surface and the film could be easily broken during the process. Hence, in order to maintain the completeness of the polymer film, an alternative plan was developed to separate the cell but keep the film attached to the silvered side. To achieve this, the material for making the alignment layer had to be chosen carefully. The original plan was to use PVA to form the alignment layer, but this was unsuitable as the film may remain on either substrate. Alternatively, the sulphuric azo-dye (SD1), which is a photoalignment material, is easy to dissolve into water whereas polyvinyl alcohol (PVA) is not readily soluble into water. By using the different water solubility, in principle, the cell will automatically separate by placing it into the water and the polymer film will stay at the substrate where the PVA is used as an alignment material (**Figure 6.3**). After several attempts, a complete polymer film was prepared as shown in **Figure 6.4**.

The next step was to ensure that the polymer film sticks to the substrate where the silver has been deposited. This was challenging because the reactive mesogen will normally first polymerize at the substrate that faces the UV source, which in this case is the substrate without the silver layer. It has been found that in order to ensure that the polymer film will stick to the substrate where the silver has been coated, the intensity

of the UV light had to be carefully controlled so that UV light passed through the polymer film to ensure that the polymerization process takes place on both sides. During the experiment, it was found that to ensure the polymer film adhered to the silver layer, the UV light intensity had to be greater than 20 mW/cm^2 and the distance between the device and the UV source was smaller than 5 cm. Using this approach, a complete and uniform polymer film was successfully generated, which is shown in the following sections.

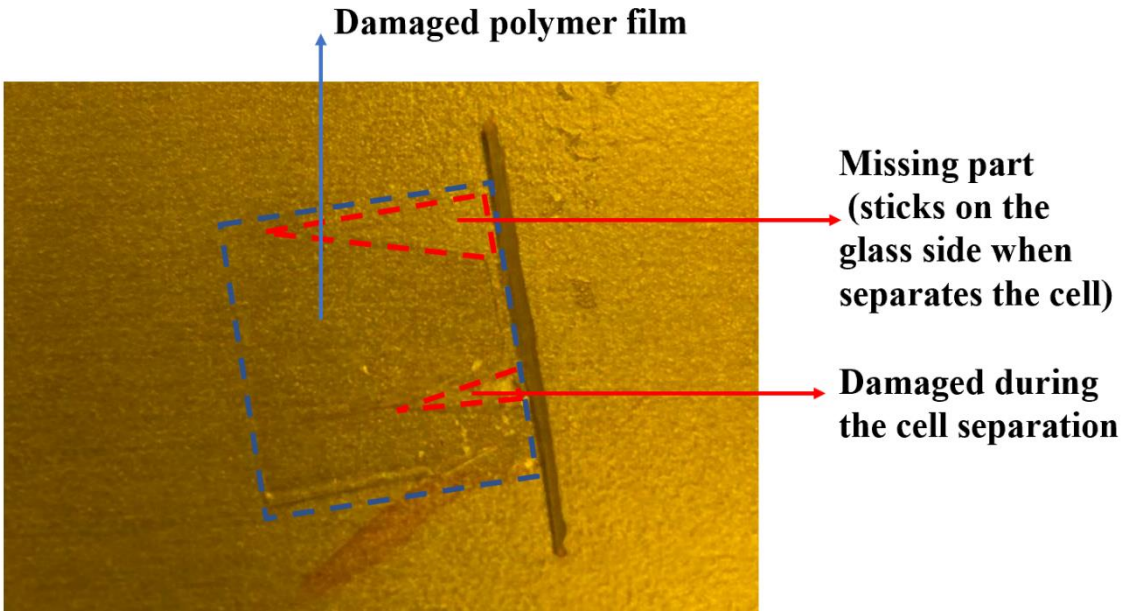

Figure 6.2 An example photograph of the polymer film that was damaged during the cell separation process. The alignment of the LC polymer is achieved by PVA. During the cell separation, some parts of the polymer film stick onto the glass substrate and some parts are damaged due to the film being quite fragile. The mixture used for making the polymer film is RM257+IRG819. The thickness of the homemade cell is controlled by using 6 μm spacer beads on one side of the glass substrate and no spacer beads on the other side. In order to form the polymer film, the cell was exposed to a polarized UV light source (λ = 365 nm, power density = 10 mW/cm^2) for 40 minutes.

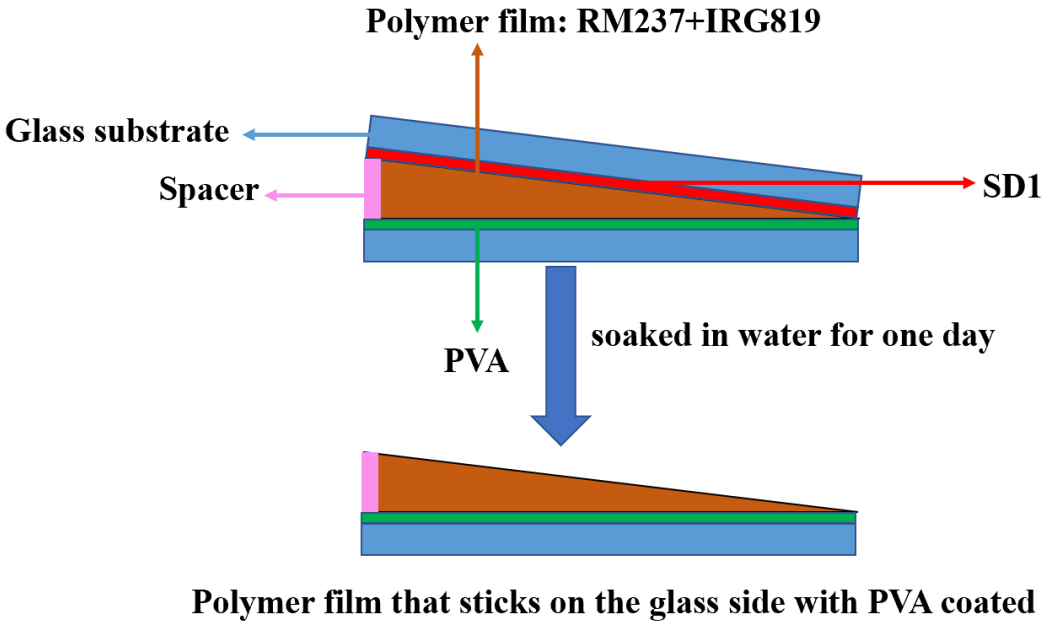

Figure 6.3. Schematic illustrating the process for making the polymer film. In order to ensure the completeness of the polymer film, the alignment layer for one substrate is SD1 and for the one is PVA. Due to their different water solubility, a complete polymer film can be easily obtained which will stick on the substrate that has been coated with PVA.

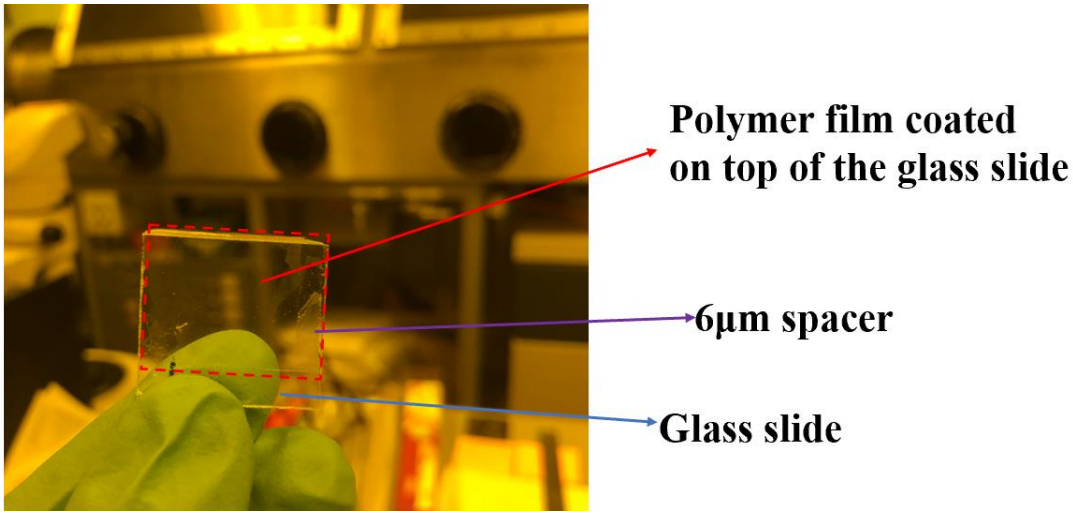

Figure 6.4 Glass substrate with a polymer film coated which works as a $\lambda/4$ waveplate, the film is attached to the substrate where the PVA and SD1 were used as the alignment material. The mixture used for making the polymer film is RM257+IRG819. The thickness of the homemade cell is controlled by using 6 μm spacer beads on one side of the glass substrate and no spacer beads on the other side. In order to form the polymer film, the cell was exposed to a polarized UV light source (λ = 365 nm, power density = 10 $\mathrm{mW/cm^2}$) for 40 minutes.

The procedures employed to fabricate the device are presented schematically in **Figure 6.5**. To begin with, a glass substrate (1 mm-thick) was first cleaned using acetone and a UV Ozone Cleaner (Ossila Corp.) (**Step 1**), which was then coated with a silver film that was approximately 100 nm-thick using thermal evaporation (Syskey Technology Corp.) (**Step 2**). Thermal evaporation is a well-known method for coating a thin layer of material onto the substrate. This method is particularly useful for materials with a low melting temperature [167-173]. In this method, the material, which is normally in powder form or as a solid ball (in my case), is first placed on a resistive coil or a charge holding boat (in my case).

In order to support the evaporation of the metal and protect it from oxidization, the system is then set to a high vacuum (normally below 10^{-5} Pa) by using a pump to exhaust the air. After that, the resistive coil or charge boat is exposed to a large current to reach the melting temperature. The high temperature and vacuum environment facilitate the movement of the vapour particles to the rotating substrate (which is held by the substrate holder) where these vapours again change to a solid-state. A schematic of the thermal evaporation system and thermal evaporator utilized in this experiment is shown in **Figure 6.6**. In this experiment, the silver was in the form of a solid ball and the system temperature was set to 1000℃ in order to melt the silver. The thermal evaporator was situated in a glove box (MBERAUN Labstar) and subjected to a nitrogen atmosphere and an internal pressure of 2×10^{-6} Torr. The deposition was performed at a rate of 0.1 nm/s, which was monitored using a quartz-oscillation thickness monitor. The silver was deposited through a shadow mask resulting in an

active area of approximately 21 mm × 23 mm (**Step 3**).

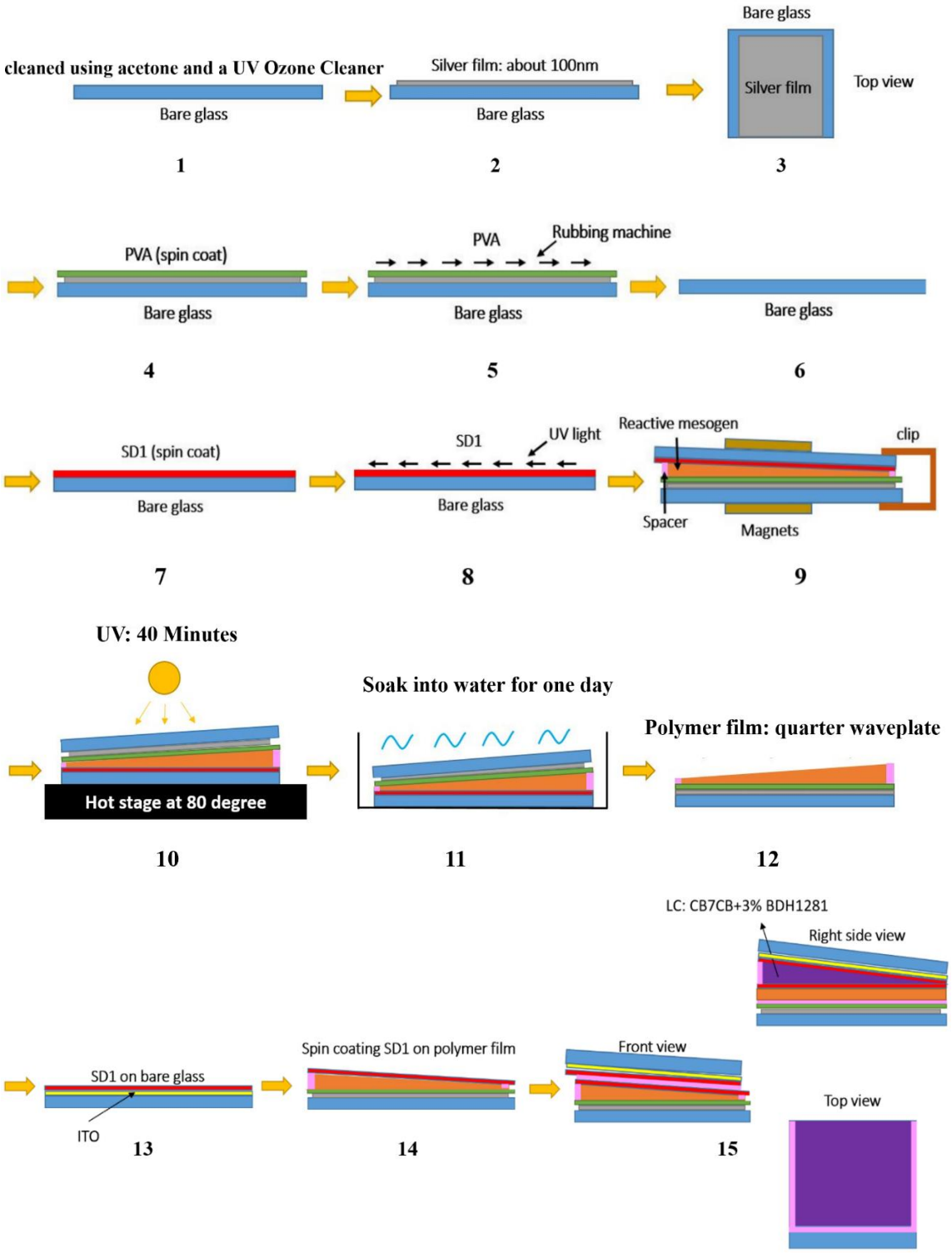

Figure 6.5. Schematic illustrating all steps in the procedure for fabricating the integrated device and the formation of wedge-shaped geometries for the polymer retarder (orange layer) and flexoelectro-optic LC (purple layer) layers to achieve $\lambda/4$ and $\lambda/2$ waveplate behaviour, respectively.

After deposition of the silver coating, a thin poly-vinyl alcohol (PVA) layer was deposited on top of the silver film using a spin-coating process at a rate of 1000 rpm for 2 minutes (**Step 4**) before being mechanically rubbed with a rubbing machine to form the first of two uniaxial alignment layers for the polymer $\lambda/4$ retarder (**Step 5**). For the other alignment layer, a second glass substrate was prepared which was also cleaned using acetone and a UV Ozone Cleaner (**Step 6**) and a thin film of the azobenzene-based photoalignment material, SD1 [164-176], was deposited onto the bare glass substrate using spin-coating (2000 rpm, 1 minute) (**Step 7**). As mentioned in Chapter 2, in order to generate alignment on the SD layer, the SD1 coated substrate is required to be exposed to a polarized UV light source (λ = 365 nm, power density = 5 mW/cm^2 and the curing time was 10 mins) which will generate alignment that is perpendicular to the direction of the polarization of the UV light (**Step 8**).

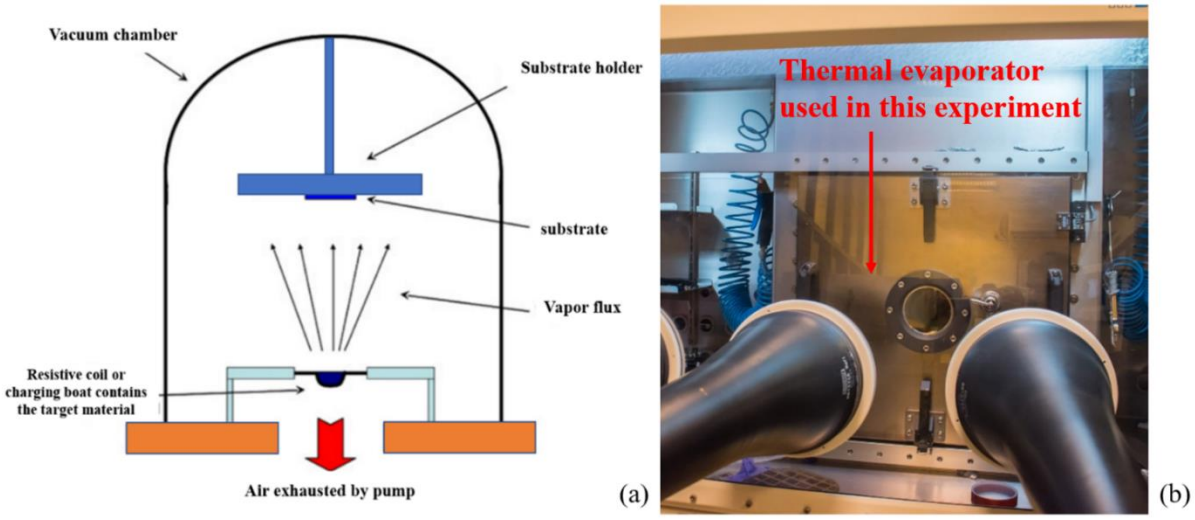

Figure 6.6. (a) A schematic of the thermal evaporation system and (b) thermal evaporator used in this experiment.

The two substrates were then assembled to form a wedge-cell by using 6 μm spacer

beads on one side of the glass substrate and no spacer beads on the other side. For the $\lambda/4$ polymer retarder, we opted for a reactive mesogen (RM) LC mixture (98 wt% RM257 and 2wt% IRG819), which was capillary filled into the glass cell (**Step 9**) before being placed on a hot-stage that was set to a temperature of 80 °C. Following this, the sample was exposed to UV light for 40 minutes at a power density of 100 $\mathrm{mW/cm^2}$ to cross-link the RM layer (**Step 10**); this power density and duration of exposure was chosen as it was found that in this case the RM film would grow primarily on top of the PVA layer, allowing the cell to be readily delaminated. The device was then soaked in water for one day to dissolve the SD1 layer (**Step 11**) so that the upper substrate could be removed, leaving a reflective substrate coated with a $\lambda/4$ waveplate (**Step 12**). The finished coated substrate is shown in **Figure 6.7**.

In order to investigate whether a wedge has been formed, the substrate was placed on an optical polarising microscope in the reflective configuration. As can be seen from **Figure 6.8 (a)-(d)**, a continuous colour change have been observed by using the microscope when moving the sample from top to bottom which proves the thickness of the polymer film varies from position to position (for the same material, different thicknesses of polymer film will exhibit different colours under the illumination of the white light source). In addition, from **Figure 6.8 (e)** and **(f)**, a good dark state can also be observed when the substrate was rotated by a 45°. The nice contrast between the bright (**Figure 6.8 (e)**) and dark states (**Figure 6.8 (f)**) indicate the good alignment of the LC polymer. From the above observations, it can be concluded that a wedge geometry has been successfully developed.

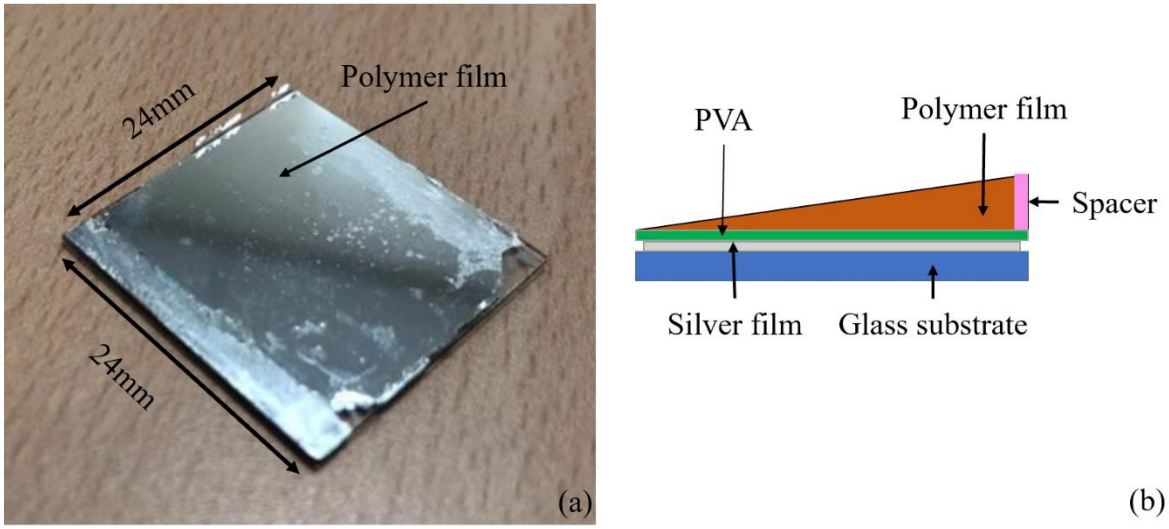

Figure 6.7 (a) Glass substrate with a polymer film coated which functions as a $\lambda/4$ waveplate. The size of the glass substrate is 24mm × 24mm. The grey layer represents the silver film. The structure of the device is shown in (b) which contains a glass substrate, a silver film, a layer of PVA and polymer film and spacer.

An ITO glass substrate with a photo-aligned SD1 film was prepared (**Step 13**), while a layer of SD1 was also coated on the top of the polymer film on the mirrored substrate to promote the alignment of the chiral nematic LC (**Step 14**). During the process, it was found that the SD1 does not easily spread on top of the polymer film. In order to improve its wettability for SD1, the top surface of the polymer film was treated in a UV Ozone Cleaner (Ossila E511) for 5 min, which ensured that the SD1 could be coated onto it. The two substrates (the mirrored substrate with the RM layer and the SD1-coated ITO substrate) were then assembled to form a cell with a wedge geometry in two orthogonal directions: one axis consisted of a wedge in the polymer layer (y-axis) and the glass substrates were assembled in such a way as to form a wedge along the x-axis. Once constructed, the cell was then filled with the chiral nematic LC mixture, CBC7CB + 3wt% BDH1281 (high twisting power chiral dopant supplied from Merck Ltd.) to form the integrated device (**Step 15**). The LC mixture was found to exhibit a

right-handed chiral nematic phase between 106 and 113 °C (on heating). The pitch (p) of the mixture was found to be approximately $p \approx 210$ nm, which was estimated from the spectral position of the reflection band, measured using a UV–vis spectrometer (Agilent 8454), and the refractive indices quoted in Ref. 89 at the measurement temperature. The quality of the ULH texture was investigated using polarizing optical microscopy and was found to be similar to that reported in previously published work [73,138,160]. The complete integrated device is shown in **Figure 6.9**.

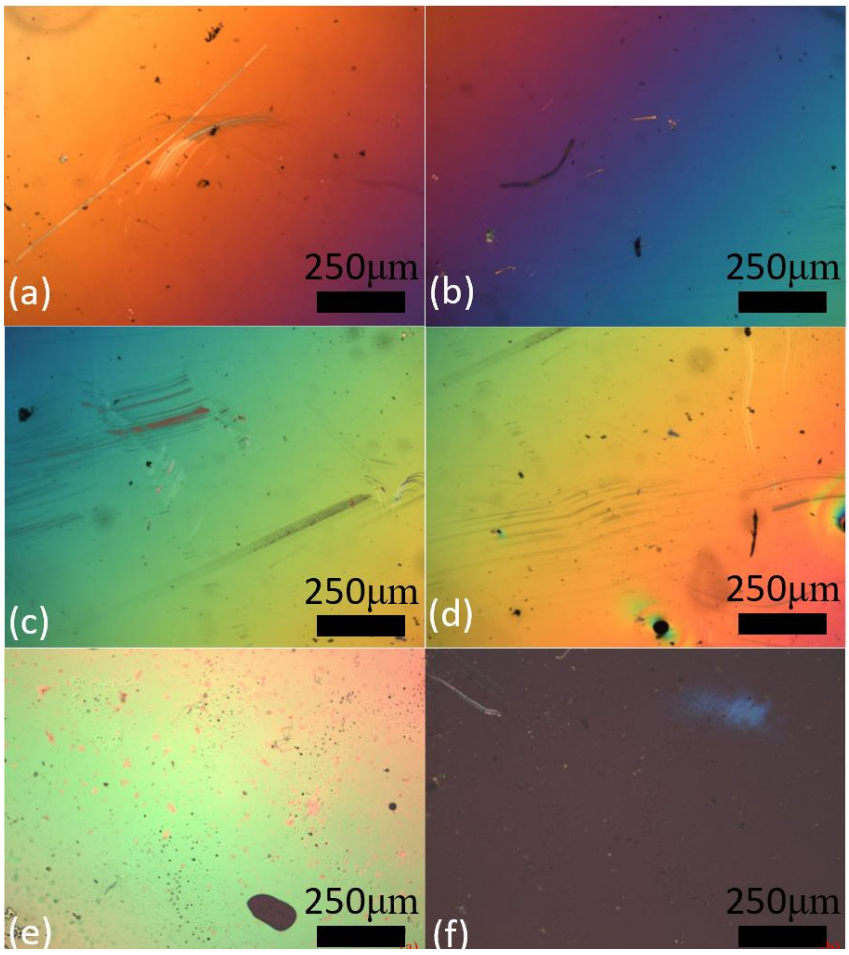

Figure 6.8 Substrate in Figure 6.7 was observed on an optical polarizing microscope that was set to a reflective configuration. Due to the existence of silver film (underneath the polymer film), the film cannot be observed in transmission. The mixture used for making the polymer film was RM257+IRG819. (a)-(d) shows the microscope images of different positions of the polymer film (top to bottom). The continuous colour change indicates a wedge has been formed. (e) bright state and (f) dark state of the polymer film. The black holes in each image are cracks on the polymer film.

After filling with the chiral nematic LC mixture, CB7CB, the device was inspected on a polarising optical microscope in reflection mode. At this stage, the LC layer was aligned in the ULH geometry by cooling from the isotropic phase in the presence of an electric field (≈2 V/µm) and, where necessary, mechanically rubbing the device with a blunt instrument to promote the lying helix alignment. Once the ULH alignment had

been obtained, the device was subjected to an applied electric field to confirm flexoelectro-optic switching using a combination of a waveform generator (Tektronix AFG 3022), a fast Si photodiode, and an oscilloscope (Tektronix TBS1154).

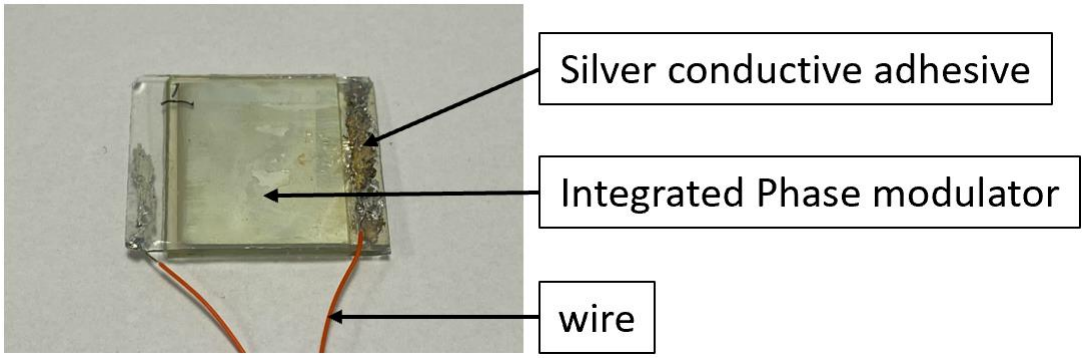

Figure 6.9. Integrated phase modulator device containing a silver film, a layer of $\lambda/4$ polymer retarder and a tunable $\lambda/2$ flexoelectro-optic LC layer. The thickness of the silver film is about 100 nm. The polymer and LC layers were fabricated so that the thickness of each layer varied across the cell which allowed us to find a region where the polymer and LC layers function as a $\lambda/4$ waveplate and a $\lambda/2$ waveplate, respectively.

6.3 Measurements of the Phase Modulation

After fabrication, as in the previous chapters, the phase modulator device was placed in a Michelson interferometer to measure the optical phase shift as shown in **Figure 6.10**. The setup is similar to the setup in chapter 4 except the LC device, quarter waveplate and mirror are replaced by an integrated device and the driving voltage is ±85V.

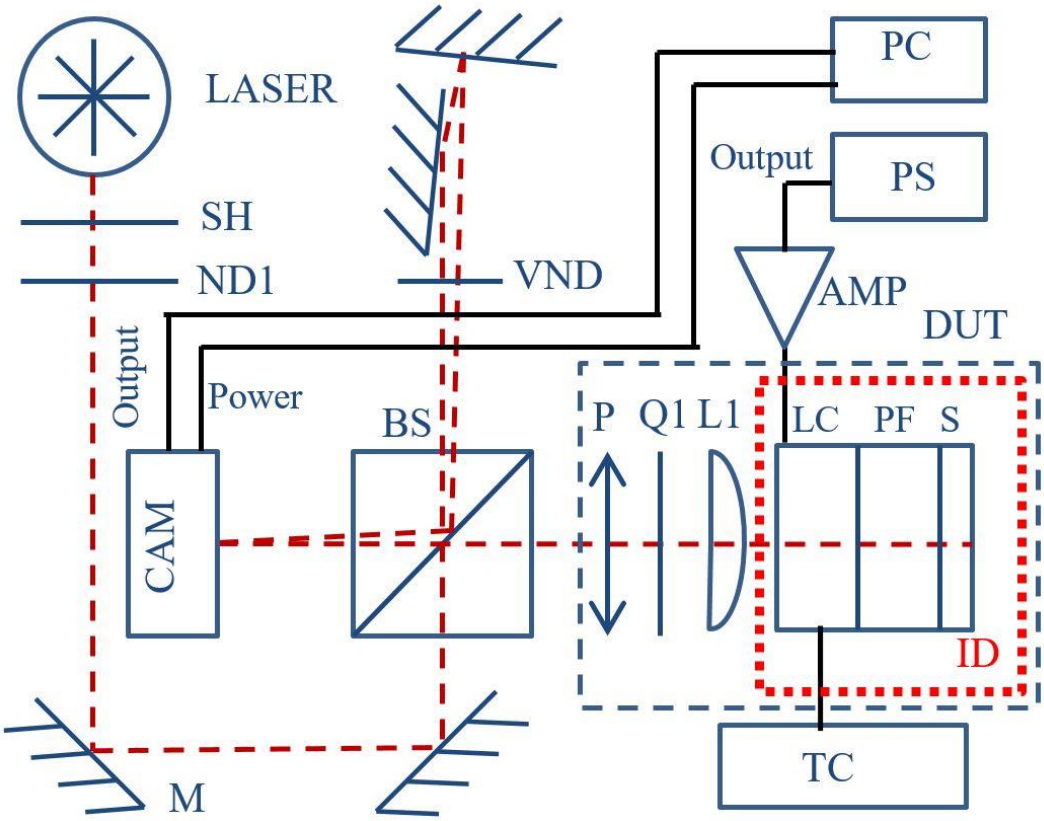

Figure 6.10. Michelson interferometer arrangement to measure the phase and intensity response of the integrated LC optical phase modulator: (SH) shutter; (NDX) neutral density filter of optical density X; (VND) variable neutral density filter; (PC) personal computer; (PS) power supply; (AMP) voltage amplifier; (TC) temperature controller; (CAM) CCD camera; (DUT) device under test; (P) linear polarizer; (Q1) $\lambda/4$ waveplate; (L1) lens; (LC) liquid crystal layer; (PF) reactive mesogen polymer film; (S) silvered substrate; (M) mirror; (BS) non-polarizing beam splitter. The components highlighted by the red-dashed line represent the integrated device (ID).

6.4 Experimental results for the integrated phase modulator

The purpose of the wedge-shaped design of the RM polymer layer and the LC layer was to enable us to obtain the correct thicknesses required for these layers to function as a $\lambda/4$ waveplate and $\lambda/2$ waveplate, respectively. However, due to the wedge cell configuration, there are many different thickness combinations of the RM polymer film and LC layer. Deviation from the desired waveplate conditions results in both phase error and variation in the amplitude loss. To explore the effect of thickness variation,

the light was passed through a region of the device in which neither the thickness of the RM polymer layer nor the LC layer corresponds to their correct values for achieving a $\lambda/4$ and $\lambda/2$ waveplate, respectively. **Figure 6.11** presents experimental results of the measured phase and normalised amplitude loss variation from this region of the device where the waveplate conditions are not satisfied, which were determined from the interference fringe images using MATLAB®.

The simulation of the integrated device is quite similar to that presented in previous chapters except that the flexoelectro-optic LC layer was modelled as a random wave-plate instead of a half waveplate and the second quarter waveplate is also set to a random waveplate. The optical field at the output, E_{out}, of the integrated system including the linear polarizer and quarter-wave plate shown in the experimental set-up in Figure 6.10, is given by

$$E_{\text{out}} = \mathbf{P}\mathbf{Q}_1\left(-\frac{\pi}{4}\right)\mathbf{D}(-\varphi,\delta)\mathbf{R}_2(-\theta)\mathbf{M}\mathbf{R}_2(\theta)\mathbf{D}(\varphi,\delta)\mathbf{Q}_1\left(\frac{\pi}{4}\right)\mathbf{P}E_{\text{in}} \qquad (6.1)$$

where $\boldsymbol{E}_{\mathbf{in}}$ is the Jones vector for a vertically polarized light at the input, **P** is a vertically aligned linear polarizer, $\mathbf{Q_1}\left(\frac{\boldsymbol{\pi}}{\mathbf{4}}\right)$ is the Jones matrix for a $\lambda/4$ waveplate at $\pi/4$ to the vertical, $\mathbf{D}(\varphi)$ is the Jones matrix of the flexoelectro-optic LC layer with a retardance, δ, and optic axis that is oriented at an angle, φ, to the vertical axis and $\mathbf{Q}_2(\theta)$ is the Jones matrix for the RM polymer layer, which has a retardance of ξ to allow deviation from the optimum $\lambda/4$ waveplate condition, and **M** is the Jones matrix for a mirror. Note that in the terms after the mirror (i.e., terms to the left of **M** in Equation (6.1)) the orientation angles of the waveplates are reversed because the system has a mirror symmetry configuration, and the light is now propagating in the opposite direction.

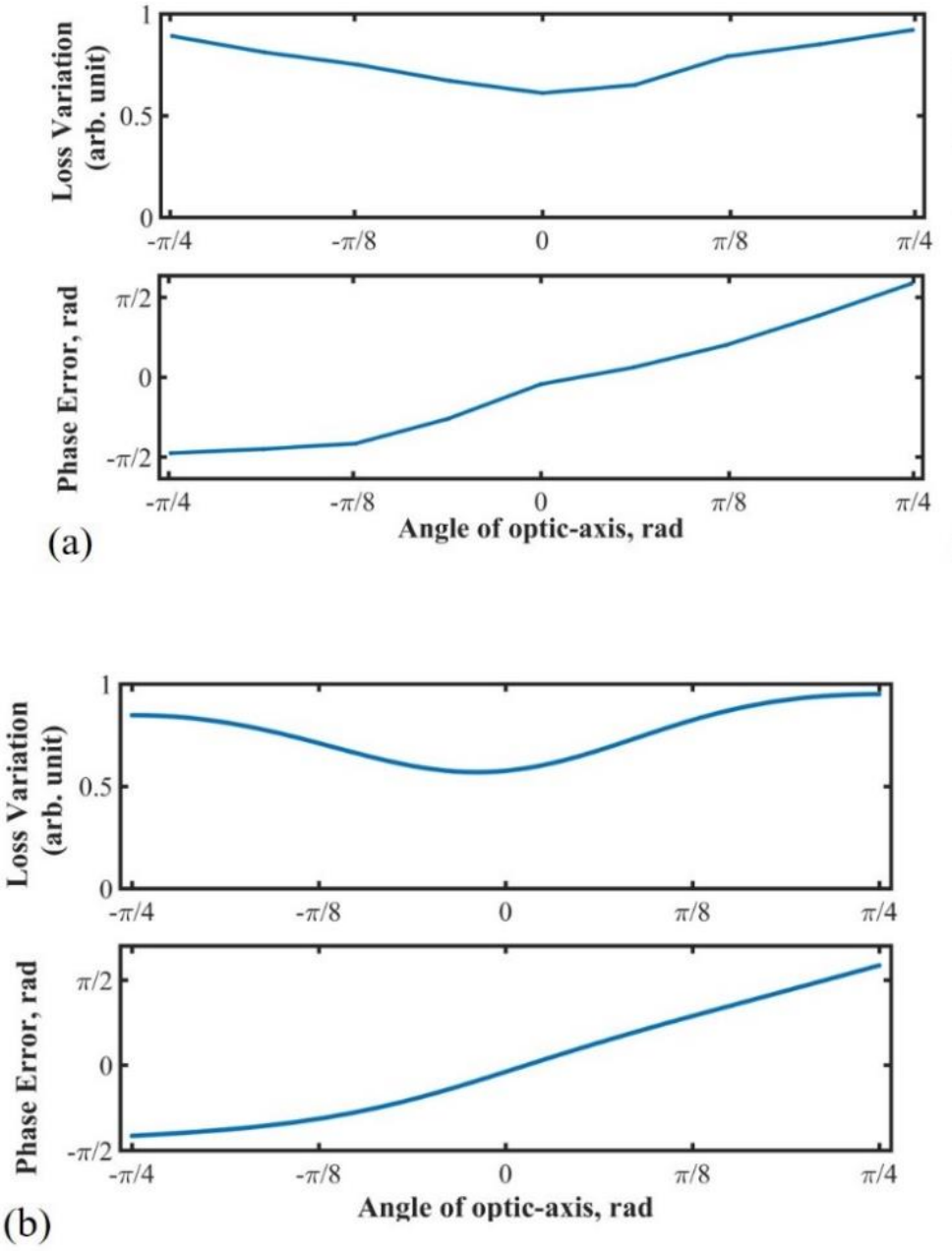

Figure 6.11 Experimental (a) and modelling (b) results for the amplitude loss variation and the phase error as a function of the absolute angle of the optic-axis of the flexoelectro-optic device relative to the vertical axis. These results are an example case of when the RM polymer film was not a precise $\lambda/4$ waveplate and the switchable LC layer does not fulfil the condition of a $\lambda/2$ waveplate.

In this example of a non-optimal region of the device, we see that there is almost a 50% variation in the amplitude across the full range of switching angles (±45º). Figure

6.11(b) shows simulated results from Equation (6.1), with the retardance of the RM polymer layer set to $\xi = 0.38$ waves and the retardance of the LC layer set to δ=0.8 waves. With these values of ξ and δ, both the simulated phase and loss variation show close correlation with the experimental data. Although there is a significant deviation from the ideal values of $\xi = 0.25$ waves and $\delta = 0.5$ waves, the device still functions as a phase modulator, but at the expense of unwanted amplitude modulation and a reduction in linearity of the phase response.

Figure 6.12 shows experimental results for light passing through an optimal area of the integrated device, where the thickness of the LC layer is close to that required for a $\lambda/2$ waveplate (nominally 5 μm) and the thickness of the RM polymer film is close to that required for a $\lambda/4$ waveplate (7 μm). Example images of the interference fringes captured on the CCD can be seen in the inset. In this exemplar case, the phase range was found to be almost 2π when the applied peak-to-peak voltage reached $170V_{pp}$ (±85V). The response time was not directly measured for this integrated device (it was faster than the frame-rate of the CCD camera). However, from the measurement of the switching times for the same mixture in a commercially-available glass test cell (Instec, 5 μm-thickness), the response time was estimated to be around 500 μs. Here the voltage required to achieve 2π is found to be substantially larger than that observed in Chapters 4 (it should be noted that even though the voltage is relatively large, for this switching range the ULH helix does not unwind, and therefore the changes in the birefringence are small). The primary reason for this is that the thickness of the device is considerably greater than that employed in previous studies as the electric field was applied not just

across the LC layer but also the $\lambda/4$ polymer retarder and the numerous alignment layers. To confirm that this was the case, the LC mixture was also filled into a commercially available glass cell (5 µm-thickness, Instec). In this case, a driving voltage of ±34 V was required to achieve ±45° switching. The results in the figure also show that the dependence of the phase modulation on the applied voltage follows an almost linear behaviour. Deviation from linearity is observed and is believed to be the combined result of a flexoelectro-optic tilt angle that is not linear with voltage at high amplitudes and small drifts in environmental temperature, which lead to measurement error. Nevertheless, the results show that by combining an RM polymer layer with a chiral nematic layer operated in a flexoelectro-optic mode it is possible to achieve full 2π modulation of the optical phase when subjected to 1 kHz switching frequencies.

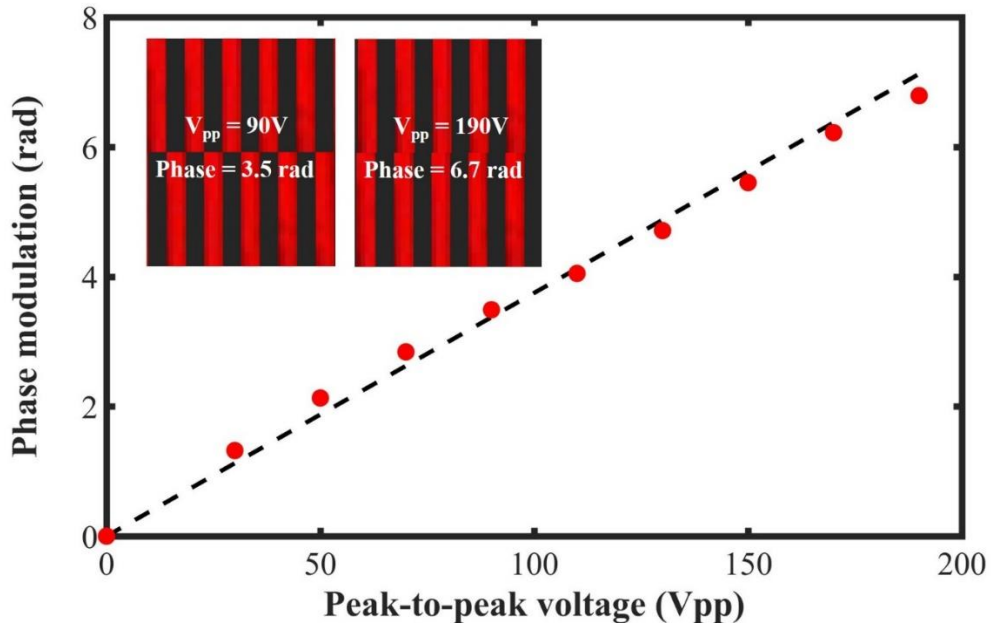

Figure 6.12. Experimentally determined phase for the integrated LC optical phase modulator presented in this work (measured using the system presented in Figure 6.9). The main plot shows the optical phase shift as a function of the applied peak-to-peak voltage (V_{pp}). The red solid data points represent experimental measurements where the RM polymer and LC layers function as $\lambda/4$ and $\lambda/2$ waveplates, respectively and

the dashed line is a line of best fit. The inset contains an upper fringe pattern and a lower fringe pattern. Each fringe pattern corresponds to a specific voltage level and the phase difference can be obtained by comparing the position of upper and lower fringe patterns.

There are important key characteristics of the phase modulator which we can comment on. One is the optical efficiency of the device, which was found to be around 20% to 40%, depending upon the ULH alignment quality. The relatively low efficiency is due to scattering from non-uniformities in the lying helix alignment of the LC phase modulation layer, but it is anticipated that the maximum efficiency could be significantly improved through the use of high-quality ULH alignments such as those formed using solvent-assisted processes [177]. Additionally, we can consider the Figure-of-Merit (*FoM*) for the modulator, as introduced by Khoo and Wu [67]. For nematic-based devices this parameter can be defined as:

$$FoM = \frac{K_{11}(\Delta n)^2}{\gamma_1} \tag{6.2}$$

where K_{11} is the LC splay elastic constant, Δn is the optical anisotropy and γ_1 is the rotational viscosity. Unfortunately, this definition does not relate directly to the electro-optic effect that we employ in this study. However, if we note that the switching time of a nematic layer of thickness d can be characterized as:

$$\tau = \frac{\gamma_1 d^2}{K_{11}\pi^2} \tag{6.3}$$

then we can re-write the *FoM* as:

$$FoM = \frac{1}{\tau} \cdot \frac{(\Delta n \cdot d)^2}{\pi^2} \tag{6.4}$$

For our device $\Delta n \cdot d$ is close to a half-wave at λ = 632.8nm. The switching time varies with voltage, but is typically around 0.5ms. Putting these values into Eq. (4) leads to an *FoM* of 20 $\mu m^2/s$, which is very encouraging. By way of comparison, for a standard nematic material, such as the eutectic mixture, E7, the *FoM* is found to be approximately 4 $\mu m^2/s$. However, care must be taken when making such a comparison because the electro-optic mechanisms used are fundamentally different in the two cases. For example, in the nematic case the "switch-on" time is controlled by $\gamma_1/(\Delta\varepsilon E^2)$, where $\Delta\varepsilon$ is the dielectric anisotropy and E is the applied electric field, whereas the "switch-off" time is controlled by $\gamma_1 d^2/K_{11}$ [178], so the switch-on time is field dependent and the switch-off time is device thickness dependent. In contrast, for flexoelectro-optic switching, the response time is controlled by $\gamma_1 p^2/(K_{11} + K_{33})$, where p is the helix pitch and K_{33} is the bend elastic constant, so the switching time is independent of the electric field, but strongly dependent on the helical pitch of the material. Nevertheless, in both cases, Equation 6.4 illustrated that the *FoM* depends on the ratio of the square of the required retardation to the switching time, and in that sense, comparing the metrics is useful.

There are two key operational bandwidths which can be considered in this experiment. One is the optical spectral bandwidth over which the device can be operated, the other is the electro-optic switching speed bandwidth. The device is normally designed to operate at a specific wavelength (in our case λ = 633 nm) where the LC layer with appropriate thickness will work as a half-waveplate and the RM layer in front of the mirror is a quarter-wave thick. Variation in the wavelength (over a

spectral bandwidth) will effectively result in errors in the phase modulation and variation in the intensity when switching. The effect of this can be seen in **Figure 6.11**. This is shown here as "non-ideal" conditions in the layer thicknesses, but is equivalent to changing the wavelength to around 400 nm. As noted, the electro-optic switching speed for the material used in this study was around 500 μs, leading to a 1kHz bandwidth (assuming an equal duty-cycle switching waveform).

6.5 Conclusion

This work has successfully demonstrated an integrated LC optical phase modulator based on the flexoelectro-optic effect of a chiral nematic LC aligned in the ULH mode which exhibits a 2π phase range with a frame rate of 1 kHz with the assistance of an additional $\lambda/4$ waveplate placed before the integrated device, which comprises an LC layer consisting of chiral nematic LC and a birefringent polymer film. Although the precise thickness of the whole device was not determined, the approximate thickness of the "working" region can be estimated from the driving voltages. As noted above, a driving voltage of ±34 V is required to achieve ±45º switching across a 5 μm thick layer of material. Therefore, our required driving voltage of ±85 V for the integrated device suggests an overall thickness for the LC layer and waveplate of around 12.5 μm. The operating condition for this device is currently ±85 V at a temperature of 108 °C but could be reduced with further material optimisation, such as the mixtures presented in the work of Varanytsia and Chien. Additionally, the device we developed shows a response time that is quite fast for analogue phase

modulation, with potential operational speeds of more than 1kHz. This integrated device has substantial potential in spatial light modulator technology, enabling full 2π phase modulation with low-intensity modulation to be achieved. Development into a pixelated spatial light modulator would have a range of applications in optical wave-front engineering and optical light-beam steering in areas such as optical communications. In Chapter 7, a new beam steering system is presented which can be used in the visible light communication. The original plan was to combine the new flexoelectro-optic LC phase modulator with polarisation gratings to make a new beam steering system. Unfortunately, this work had to be substantially delayed due to the COVID pandemic, which will be discussed further in Chapter 8.

Chapter 7: Beam-steering with Polarization Gratings and LC Phase Shifters

7.1 Introduction

As mentioned in Chapter 2, precisely positioning a laser beam or light ray is crucial for many technological applications, including optical communications [76], VR/AR displays [77], LiDAR [78], microscopy [79] and laser micro-machining [80]. Currently, there are a number of beam steering methods that have been demonstrated [81-85, 179-196]. In this chapter, a new beam steering system is presented by combining polarization gratings with LC devices (with potential for combination with the flexoelectro-optic phase modulator) which is shown to have a great potential in an optical communication system.

7.2 Light diffraction and diffraction Gratings

Diffraction refers to the phenomenon when light waves encounter an obstacle or opening that is physically similar to or smaller than the wavelength of light. The light tends to bend around and spread out [197,198]. In classical physics, the diffraction of light can be understood by using the Huygens–Fresnel principle and the superposition of waves. Using this approach, the propagation of light can be approximated by considering every position on the wavefront as a point source of a spherical wave. The final wave is then the sum of these point sources [198]. As mentioned in chapter 4, the

phase difference between two waves determines their relationship (whether they are added together or cancel each other out). Hence, the final diffraction pattern consists of a series of maxima and minima, typically depending on the phase relationship between different point sources. Light diffraction has been used in various applications [193,199], and one of the most critical applications of this is diffraction gratings.

Diffraction gratings are an optical component that contains a periodic structure. These have been widely used in the spectral analysis of light. Their unique spectral properties rely on the fact that light with different wavelengths impinging on the periodic structure will be reflected or transmitted at different angles. The angles of light propagation can be determined by a simple expression which is termed as the grating equation (7.1), which is related to the wavelength of the incident light, λ, the incident angle, θ_i, and the groove spacing d [200-202]:

$$\sin\theta_d = -\sin\theta_i + \frac{m\lambda}{d} \tag{7.1}$$

where θ_d represent the angle of the diffracted light and m is an integer that describes the diffraction order. From the equation, it can be found that when the value of the diffraction order m is zero, the incident beam will be reflected by the diffraction grating as the diffraction angle θ_d is equal to θ_i. The diffraction grating works as a mirror (reflection) and does not exhibit any spectral properties. However, when the diffraction order $m \neq 0$, the diffraction properties appear and light with different wavelengths will be distinguished due to the different diffraction angles. The value of m can be positive or negative, hence the diffraction order can also be positive or negative. By convention,

the diffraction order is positive when the diffracted ray is on the left side of the position of the zero-order and is negative when it falls to the right side of the zero-order. For monochromatic light, the diffraction pattern will generate an energy distribution that occurs at angles corresponding to the diffraction order, as shown in **Figure 7.1**. If the light is polychromatic, light with a specific wavelength will produce a distribution according to equation (7.1).

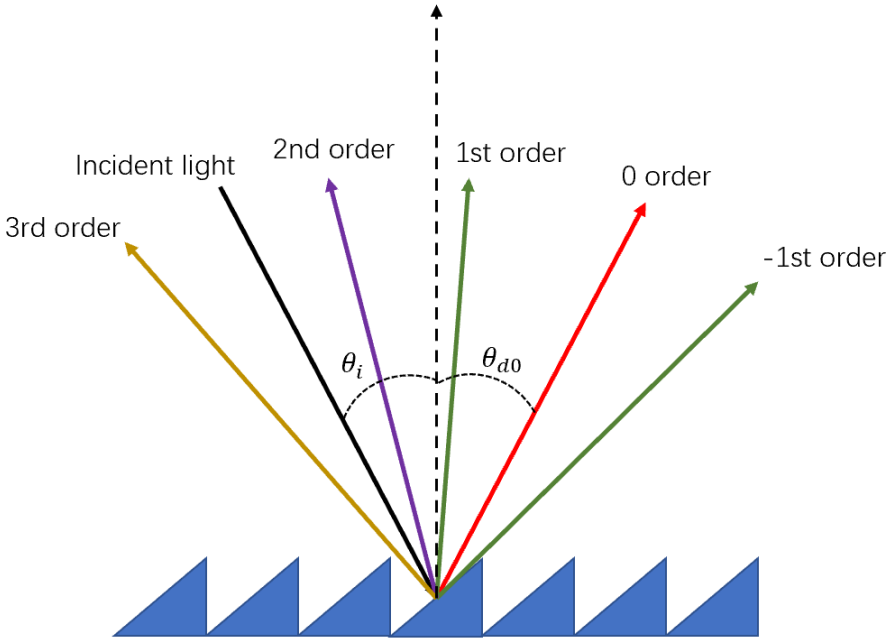

Figure 7.1 Output beams of possible diffraction orders at a diffraction grating.

Many properties have been used to characterise diffraction gratings [200-203]. One of the essential traits of the diffraction grating is groove density, which measures the number of groves contained per unit length. The groove density determines the angular position of different diffraction orders and is limited by the current fabrication method.

Diffraction efficiency is another property that will be considered. It is the fraction of incident light that enters a certain diffraction order. For some applications, such as a pulse compressor, it is desirable to concentrate incident light into a single order, such as the first order, rather than distribute it across higher orders or the zero order. In addition, polarisation dependence also influences the performance of the diffraction grating, especially for a reflective diffraction grating. The polarisation of input light can affect the diffraction efficiency of some orders [200].

7.3 Polarisation gratings

LC gratings have attracted a lot of attention as they can modulate unpolarised light with high contrast and are easily integrated with other projection equipment [204-208]. However, LC gratings currently cannot achieve high diffraction efficiency (small grating period) due to the existence of random disclinations and domain boundary lines [204]. Some research groups have tried to use different methods to address these issues, but it is still challenging to fabricate a grating period of the order of 10s of μm owing to the binary nature of the LC gratings [209].

A polarisation grating is a type of diffraction grating that can periodically modulate the state of polarisation of incident light. For this grating, incident light with different circular polarisations will be diffracted to different orders, especially for the first order. A very thin grating can obtain an approximately 100% diffraction efficiency [210].

Several research groups [211-214] recognised this advantage and have used LC materials to generate the diffraction grating. It has been found that LC-based polarisation gratings have significantly high diffraction efficiency, which has overcome the main problem of normal gratings.

Compared with traditional gratings such as Wollaston grating, which operate on linear eigenpolarisations, LC-based polarisation gratings are based on circular eigenpolarization [215]. Normally, this type of grating contains a thin layer of LC polymer aligned to form a continuous, in-plane, bend-splay pattern (as shown in **Figure 7.2**). This pattern is generated using photoalignment where the LC polymer material is coated on a clean substrate and then aligned by a UV polarisation hologram. For unpolarised light, it will be diffracted evenly between the positive and negative first orders while circularly polarised light is diffracted entirely to one order with the polarisation state being changed to its opposite state (as shown in Figure 7.2). The first order diffraction efficiency for the structure illustrated in **Figure 7.3** is [210]:

$$m_{\pm 1} = \frac{1 \pm V}{2} \sin^2\left(\frac{\pi \Delta n d}{\lambda}\right) \qquad (7.2)$$

where V is the normalised Stokes vector component of the incident light related to its fraction of elliptical polarisation, d is the thickness of the film, Δn is the birefringence and λ is the wavelength of the incident light. The zero-order efficiency always equals 1-$m_{-1} - m_1$. From equation (7.2), it can be found that in order to get a 100% diffraction efficiency, $\frac{\pi \Delta n d}{\lambda}$ should be equal to $\frac{\lambda}{2}$ (i.e., a half waveplate). However, due to the

fabrication process and power loss inside the film, the diffraction efficiency cannot reach 100%.

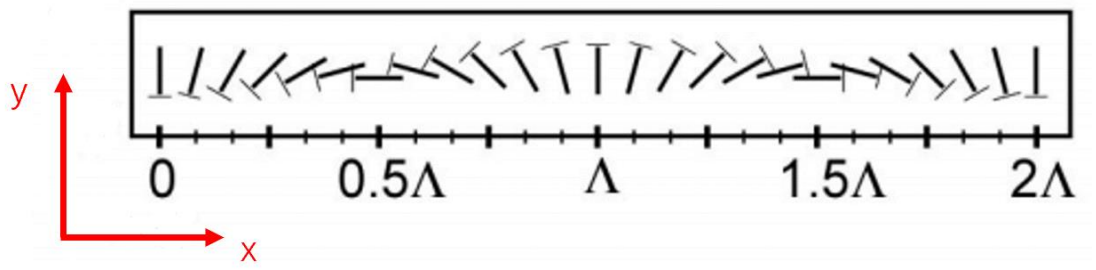

Figure 7.2 Basic geometry of the liquid crystal polarisation grating.

Recently, there has been considerable interest in the use of polarisation gratings (typical elements include lenses, gratings and deflectors) in combination with variable retarders to engineer new photonics technologies [212, 214, 216-218]. In the previous chapters, a new optical phase-shifting technique that involves combining switchable flexoelectro-optic LC layers, aligned in the so-called uniform lying helix configuration, with quarter-wave plates has been shown to achieve sub-millisecond 2π phase modulation [72,138,160,161]. This new technology could also potentially be configured as a dynamic switch to control the polarisation state. By combining commercial off-the-shelf polarisation-gratings with this LC technology, a new optical beam-steering device could be developed that has substantial potential in optical communications and holographic projection.

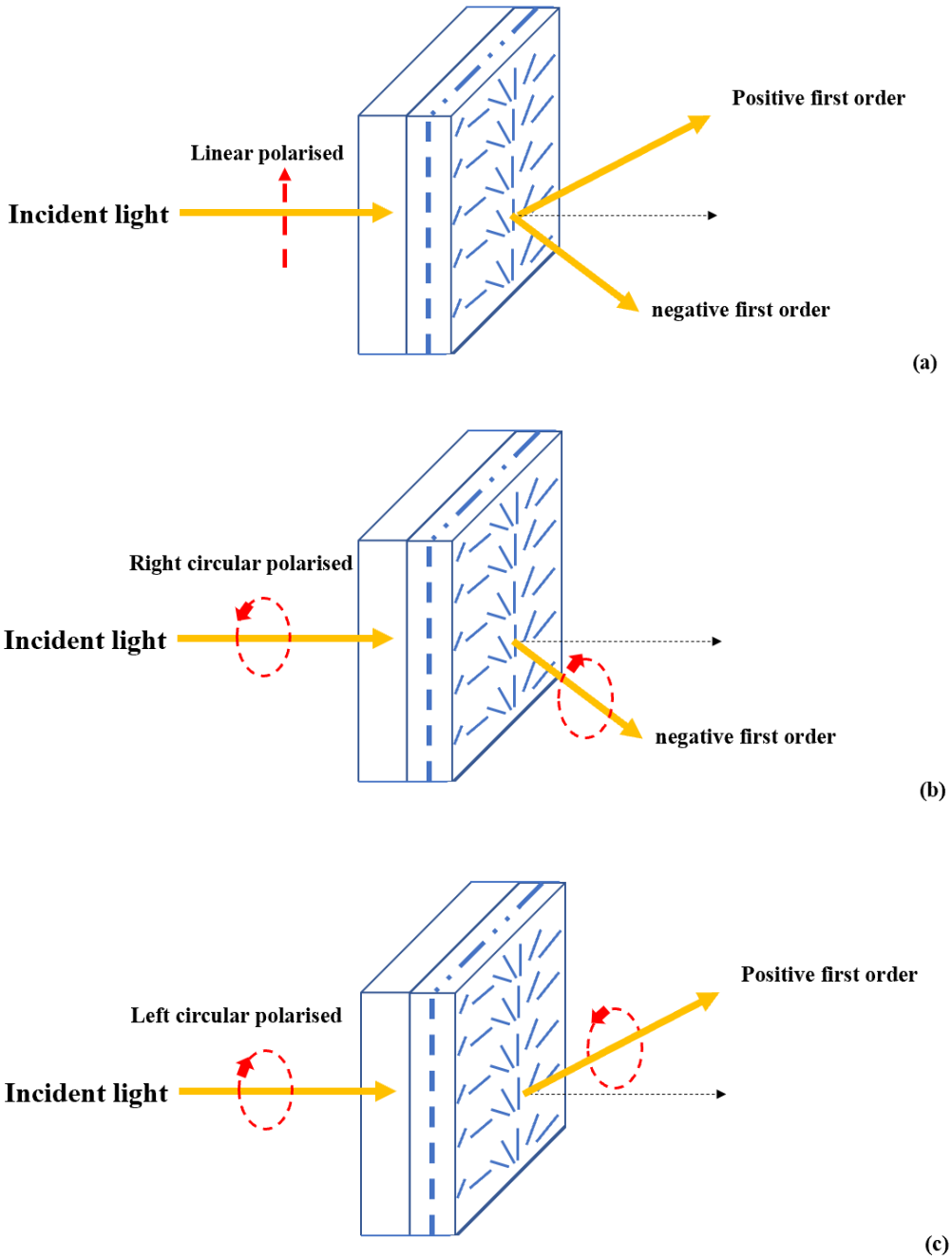

Figure 7.3 LC polarisation grating: (a) linear polarised light splits equally into the two first orders. (b) right and (c) left circularly polarised light to diffract fully into only one of the first orders.

7.4 Experimental characterisation of LC polarisation grating

In order to first test the idea of combining polarisation gratings with variable retarders,

commercially-available polarisation gratings were obtained from Edmund Optics (16-590) and have been examined on an optical polarising microscope. An example microscope image of the polarisation grating is shown in Figure 7.4.

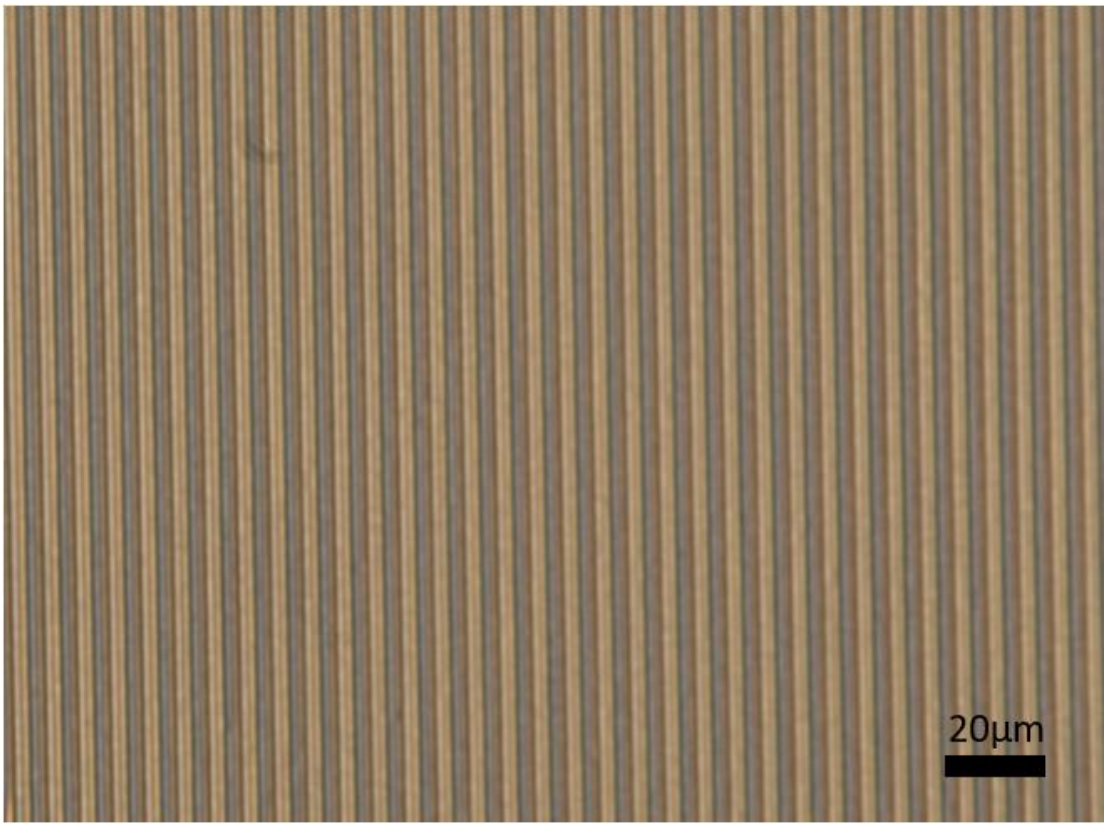

Figure 7.4. Polarisation Grating used in this study was observed on a polarising optical microscope. According to the measurement from the microscope image, the grating size is about 3.3 µm, which is in good agreement with the specification provided in the datasheet (3.5 µm).

The first step of the experiment was to characterise the polarisation grating. As mentioned previously, the diffraction angle, efficiency, and output light polarisation are important properties that need to be determined for diffraction gratings. In order to measure these parameters, we have constructed the experiment as shown in **Figure 7.5**. The polarisation grating was tested with a 546 nm green laser. After the laser, a vertical polariser (P) ensures the polarisation of the light is linearly polarised. The light then

passes through a pinhole (PH) and polarisation grating (PG), whereupon light is diffracted resulting in output with multiple orders. The pinhole was included to reduce the reflected light coming back from the polarisation grating. The intensity of the output light was recorded using a photodiode and the diffraction angles were determined geometrically with the aid of a ruler.

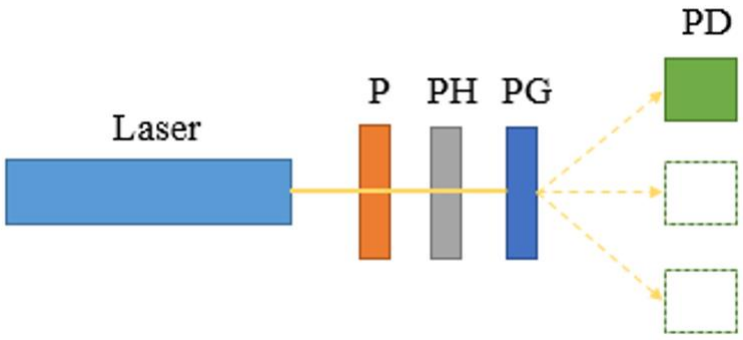

Figure 7.5 Experimental setup used to measure the properties of the polarisation grating. P is a polariser, PH is a pinhole, PG is the polarisation grating and PD is a photodiode.

Diffraction angle

In this experiment, 20 points on the polarisation gratings have been measured and it has been found that the diffraction angle varies from 10.4° to 11.2° (in the datasheet, the diffraction angle was quoted to be larger than 9°, so our results are consistent with the information provided by the manufacturers). However, the variation in the diffraction angle observed for the different points across the grating is relatively small and may result from errors in the measurement.

Output polarisation

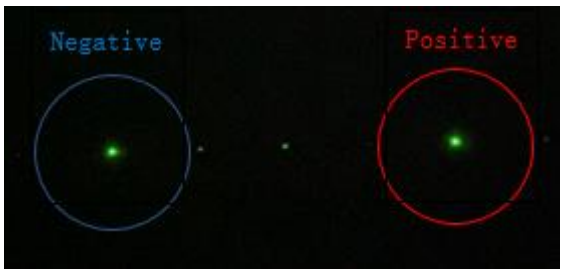

Figure 7.6. Output when linear polarised input light is fed into the PG.

Polarisation gratings are used to selectively diffract light based on the polarisation state, with the angle of diffraction dependent on the grating film design. Linear polarised light is diffracted evenly between the positive and negative first orders while circularly polarised light is diffracted entirely to one order whilst changing to its opposite polarisation state. In this experiment, the input light is linearly polarised, and thus most of the light will diffract into the positive and negative first orders, as shown in **Figure 7.6**. In this experiment, the intensities (as recorded by the photodiode) for the negative and positive first orders were 4.22V and 4.5V, respectively. In principle, equal amounts of light should be diverted to the negative and positive first orders. However, from our measurement, we find a slight discrepancy. The small difference in intensity between the negative and positive first orders could be the result of one or a number of factors:

1. The polarisation grating is designed for 540 nm. However, the wavelength of our laser is 546 nm.
2. The linear polarised light that we use is not ideal, which could cause uneven light distribution.
3. The polarisation grating is not as perfect as we expected.

The polarisation state for the negative and positive first orders was measured using a polariser and chiral reflector. A chiral reflector is a chiral nematic LC cell that only reflects the circular polarisation of one handedness. The chiral reflector that we have used consists of a right-handed helix reflecting light with a right circular polarisation. Using this chiral reflector, we found that the positive first order has a left-handed polarisation whereas the negative first order is right-handed, which means the polarisation grating works as a half waveplate. The polarisation states of both of the first orders were found to be quite close to circular polarised light, as shown in **Figure 7.7**.

Efficiency

The polarisation efficiency was measured by using a photodiode to record the intensity of the output light. In this case, we have also measured 20 different points on the polarisation grating and the efficiencies were found to vary from approximately 95% to 96% (which means 96% of the input light was diffracted into the first orders). This is also consistent with the datasheet specification as these gratings are designed for high transmission and greater than 97% diffraction efficiency, resulting in a maximum of 4% of light leakage into the zero-order.

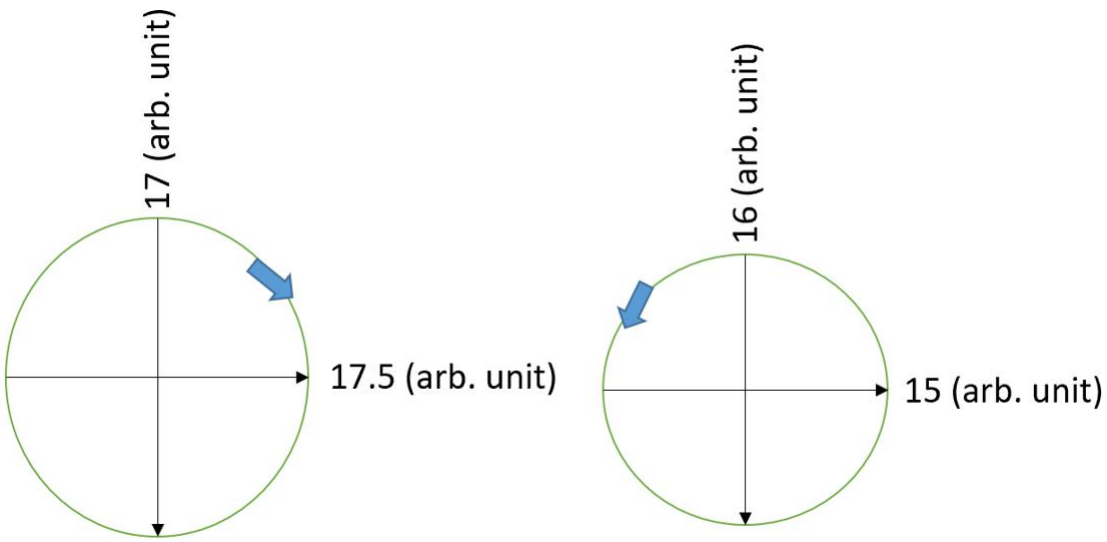

Figure 7.7 Measurement of the polarisation of the first orders. The polarisation states for negative and positive first orders were elliptical with opposite handedness (the state of the negative first order is right elliptical and the state of the positive first order is left elliptical). The ratio of height to width for the negative first order was 17:17.5 and the ratio of height to width for the positive first order was 16:15.

Circularly polarised input light

After testing the system with linearly polarised input light, we decided to characterise the performance of the polarisation grating for circularly polarised input light. Circularly polarised input light was generated by adding a nematic LC cell. By controlling the voltage applied to the nematic LC, we are able to make the LC behave as a quarter waveplate, which will change the input linearly polarised light to circularly polarised light. In order to determine the voltage required to make the LC device function as a quarter waveplate, we have set up the experiment as shown in **Figure 7.8**.

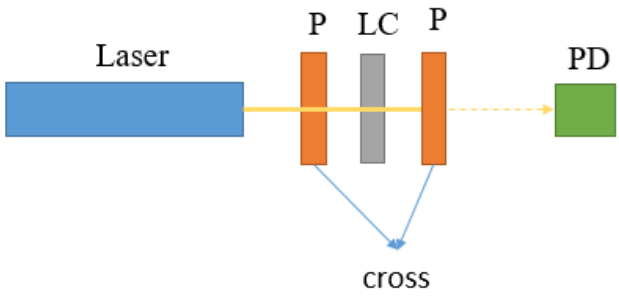

Figure 7.8 Experimental setup used to measure the output light for different voltages applied to the LC device (anti-parallel, planar-aligned nematic LC cell). The two polarisers were set so that the transmission axes were crossed (i.e., were perpendicular to one another) and the LC device was rotated to obtain the maximum transmission. This was achieved by aligning the optic axis of the LC device without an applied voltage at an angle of 45º to the transmission axes of the two polarisers. The intensity of the output light was recorded by the photodiode connected to an oscilloscope. P: Polariser, LC: Liquid crystal device, PD: Photodiode.

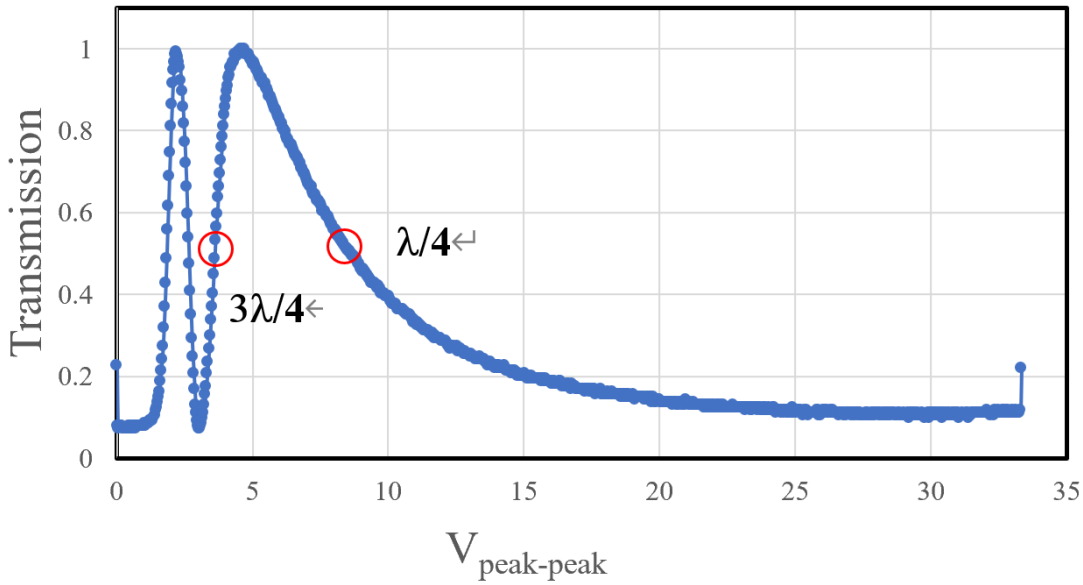

Figure 7.9 Transmission as a function of applied voltage for an anti-parallel rubbed planar aligned nematic LC device at room temperature. The thickness of the device was 4.97 μm.

Figure 7.9 shows the results for the transmission of the 546 nm laser light through a planar aligned nematic LC device placed between linear polarisers with the

transmission axes crossed. The ramp signal, which was applied to the device, was generated using a 0.1 Hz ramp signal to modulate a 1 kHz square wave. The LC device can be made to function as a λ/4 waveplate and in this case the input light will change to circularly polarised light and only half of the light will pass through the second polariser. Hence, the LC device will work as a λ/4 waveplate or 3λ/4 waveplate when the transmission is 0.5 and we can use that level of transmission to find the corresponding voltages, as can be seen in the Figure. In this case, the LC material we used was the nematic LC, E7, and the device can be made to behave as a 3λ/4 waveplate or a λ/4 waveplate at voltages of approximately 3.7V and 8V, respectively.

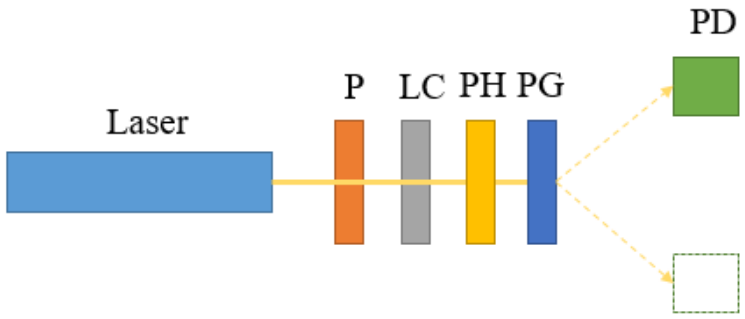

Figure 7.10 Experimental setup for circularly polarised input light. P: Polariser, LC: Liquid crystal device, PD: Photodiode, PG: Polarisation grating PH: Pin hole.

Figure 7.10 shows the experimental setup for measuring the output light with circularly polarised input light. A circularly polarised light incident on the grating was generated by using a combination of a vertical polariser and the nematic LC device, operating at the correct voltage so that the latter functions as a λ/4 waveplate. The pinhole in the system helps to reduce the interference from reflections that arise from the free-space optical system.

As suggested in the datasheet, circularly polarised light is diffracted entirely into one order with the polarisation state being changed. In our experiment:

1. when the input light is left circular polarised, about 95% of the input light will enter the negative first order while 5% will feed into the zeroth and positive first order. The polarisation state of the output light was found to be close to a circular polarisation with a 4º offset, which is shown in **Figure 7.11**(a).
2. When the input light was quite circularly polarised, about 92% of the light was diffracted to the positive first order. The remaining contribution was diffracted into the zeroth and negative first orders. Similar to the previous situation, the output light was found to be slightly elliptical with a 4º offset (Figure 7.11(b))

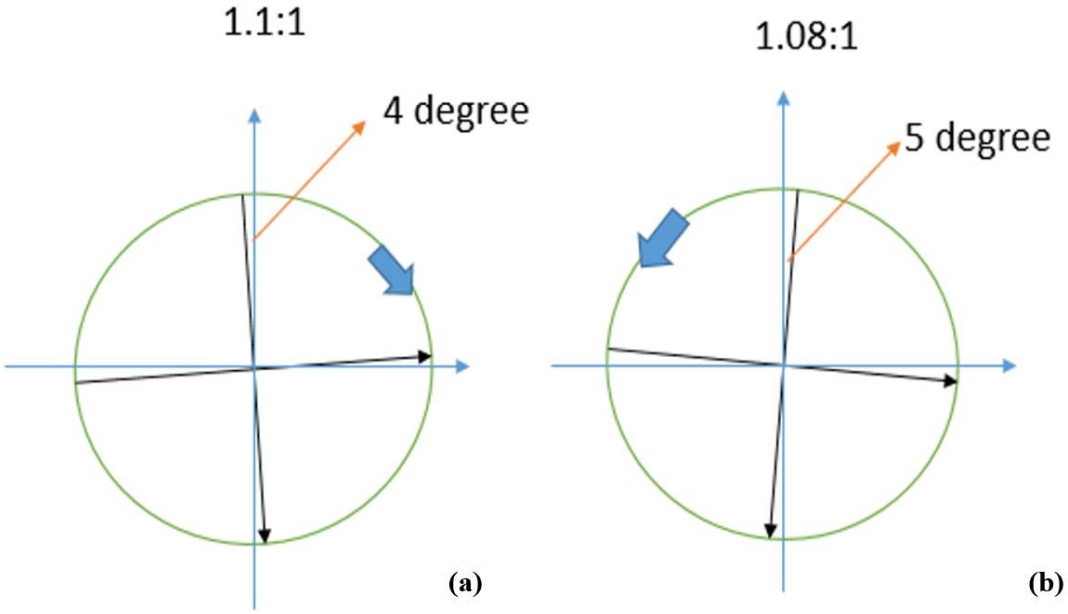

Figure 7.11: a) The polarisation state of the negative first order when the input light was left circularly polarised. The ratio of height to width was found to be 1.1:1. b) The polarisation state of the positive first order when the input light was right circularly polarised. The ratio of height to width was found to be 1.08:1.

In addition to the above measurement, the output intensity for the two first orders

has also been recorded by applying a ramp signal to the LC device as shown in **Figure 7.12** and **Figure 7.13**. From **Figures 7.11** to **7.13**, it can be seen that when the LC device behaves as a λ/4 waveplate (8V), we see that the transmission in **Figures 7.12** and **7.13** reach their minimum and maximum values, respectively. On the other hand, when the LC device was set to function as a 3λ/4 waveplate, the transmission in **Figure 7.12** is seen to reach a maximum value while the transmission value in **Figure 7.13** is close to zero. These results are consistent with what we have observed in that for different handedness of circularly polarised light, the light will diffract into either the negative or positive first order.

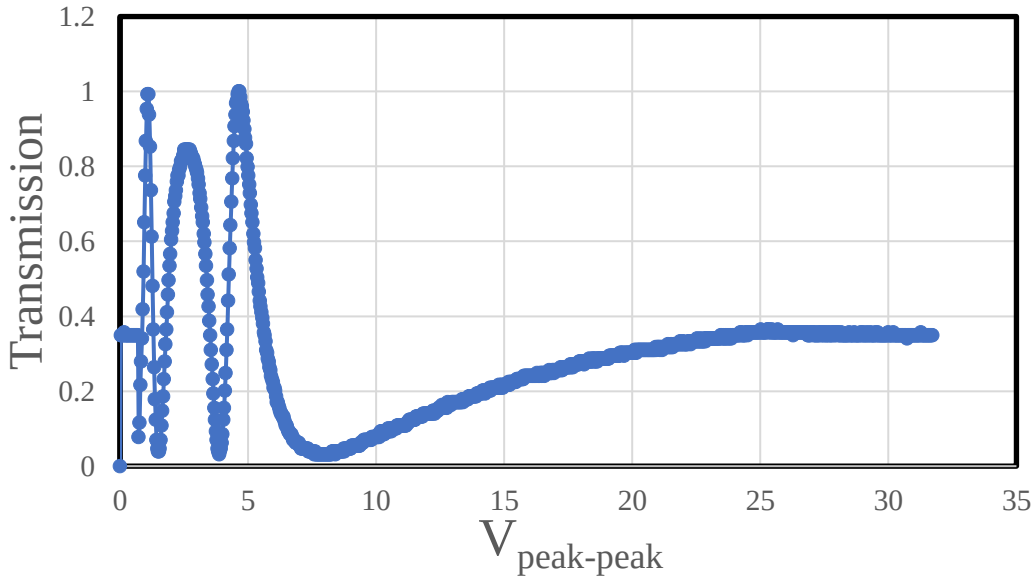

Figure 7.12 Transmission recorded for the negative first order when the nematic LC device was subjected to the ramp signal described in the text.

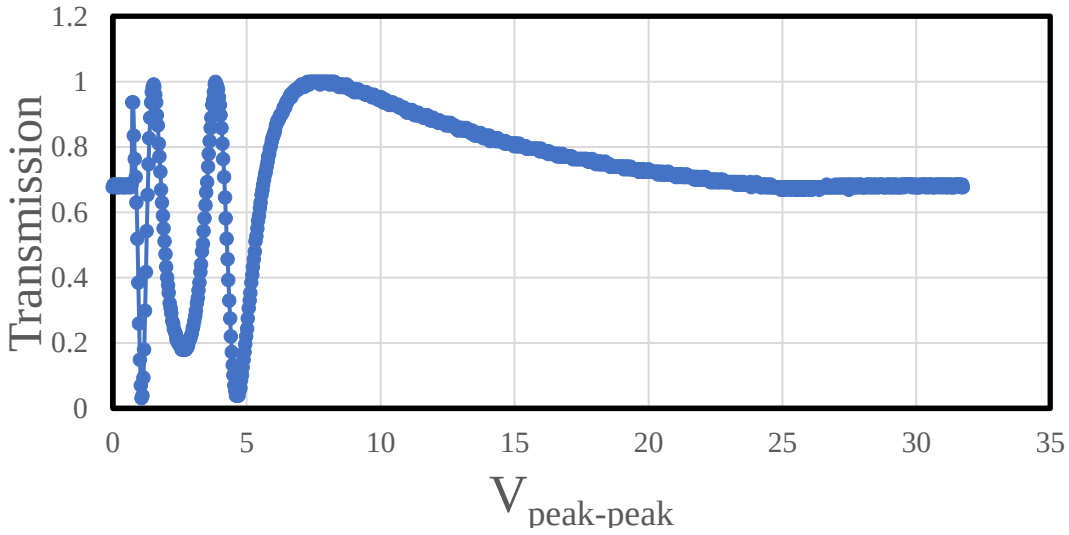

Figure 7.13 Transmission recorded for the positive first order when the nematic LC device was driven by the ramp signal described in the text.

The light passing through the PG was then measured for different incident angles to the grating. Two different methods were considered: the first one was to add a mirror to generate different incident angles. The second method explored in this study involved altering the orientation of the polarisation grating (as shown in **Figure 7.14**). For each way, two configurations with four different angles were tested. The behaviour of the output light using the first method was found to yield somewhat odd results. This might be due to reflections from the mirror altering the polarisation state of the input light.

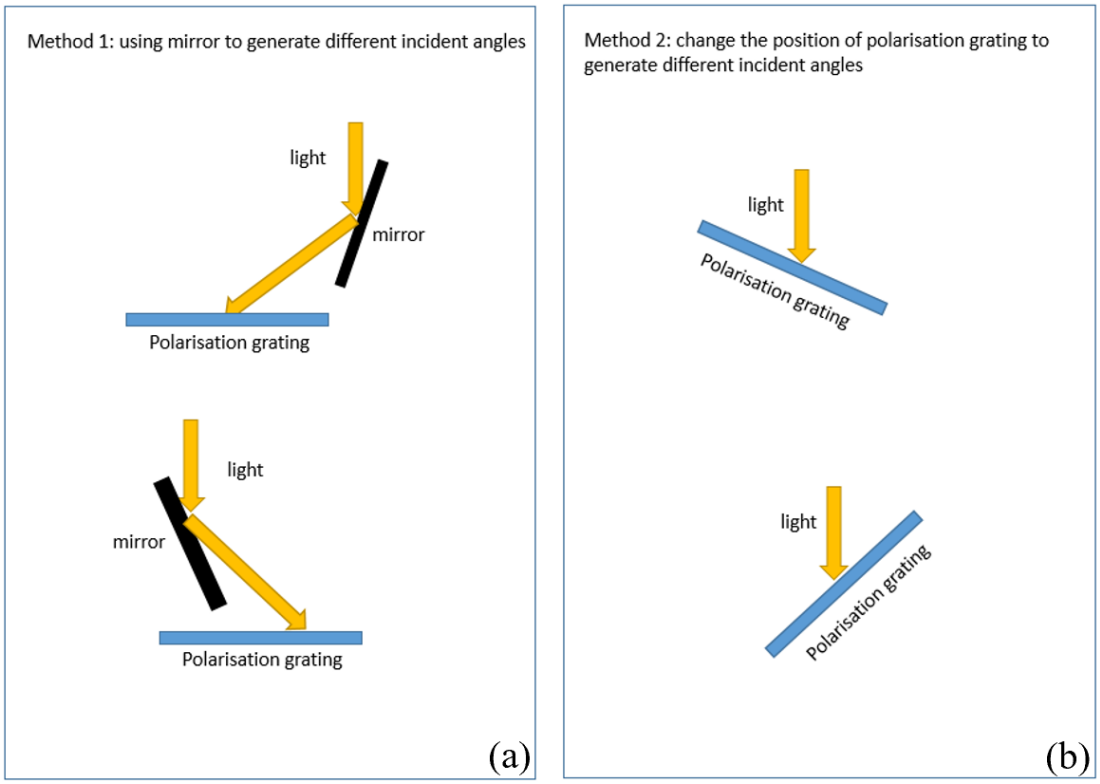

Figure 7.14 Methods for measuring the dependence on the incident angle. (a) Light is reflected by a mirror to generate different incident angles. (b) Different incident angle is generated by rotating the polarisation grating.

On the other hand, the results obtained using the second method were as follows: With linearly polarised input light and an incident angle of 90º, the diffraction angle was found to be 11.2º with about 50.5% of the output light going to the positive first order and 49.4% output of the light going to the negative first order. The handedness of the polarisation state in the zeroth order could not be measured accurately since the intensity of the light was too small. However, the light in the positive and negative first orders tended towards a circular polarisation (**Figure 7.15**).

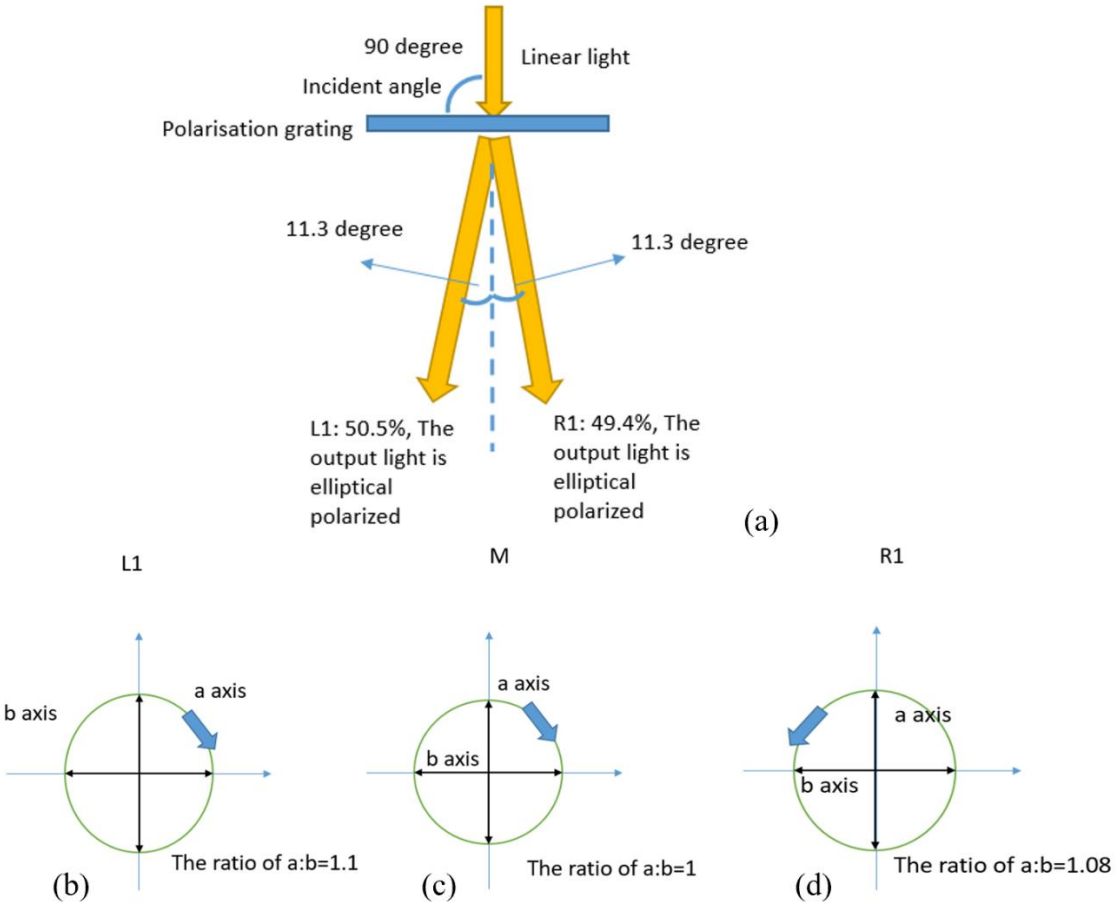

Figure 7.15 (a) Output from the polarisation grating when the light was incident at an angle of 90º (relative to the plane of the grating). The polarisation of the input light is linear polarised. L1, M and R1 show the output light measured from the (a) negative first order, (b) zero-order and (c) positive first order. The ratios of height to width for L1, M and R1 are approximately (a) 1.1:1, (b) 1:1 and (c) 1.08:1.

It was found that even when the incident light was perpendicular to the polarisation grating (the incident angle was 90º to the plane of the grating), the output light in the first order was not perfectly circularly polarised. Possible reasons why this might be the case are as follows:

1. The polarisation grating is designed for 540 nm whereas the wavelength of our laser is 546 nm which also introduce errors in the system.

2. The input light might not be a perfect linear polarisation, or for circularly polarised input light, the LC device might not function as a perfect quarter waveplate.

Besides a 90º incident angle, we have also considered the behaviour of the polarisation grating for other incident angles: 60º, 45º and 30º, the results of which are presented in **Figure 7.16**, **Figure 7.17**, and **Figure 7.18**, respectively.

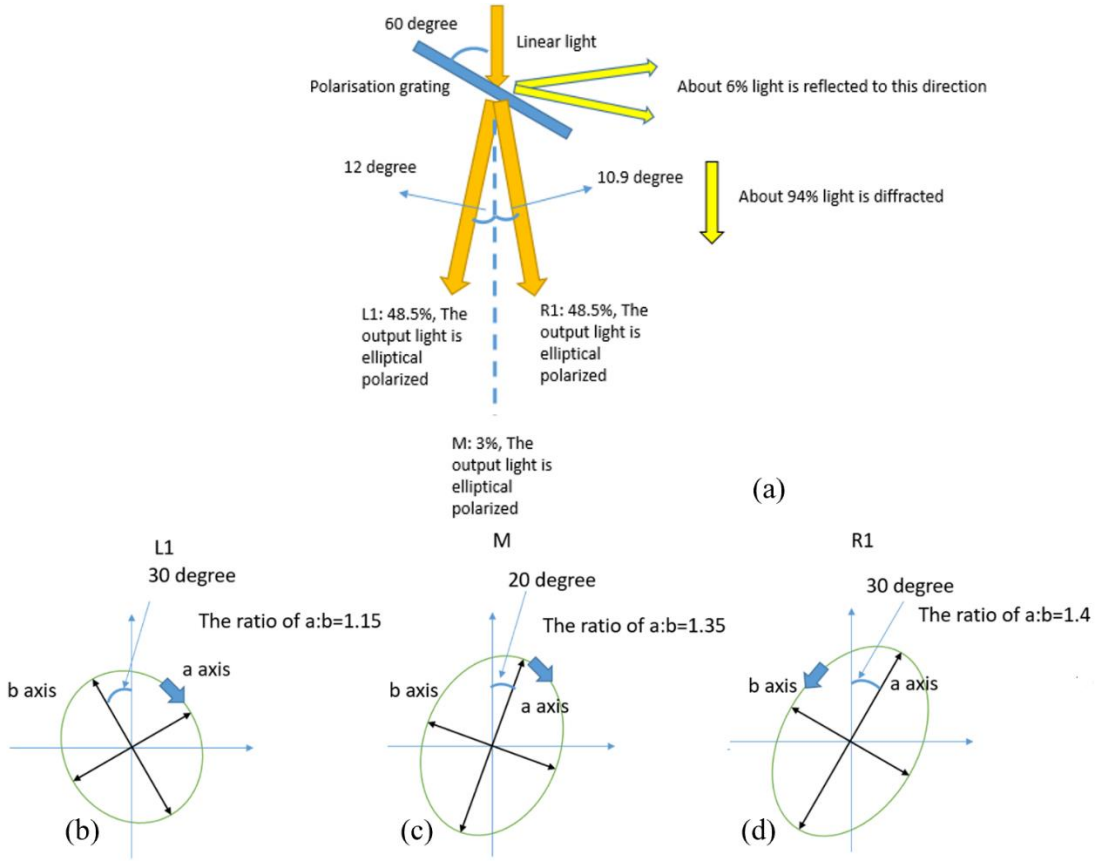

Figure 7.16 (a) Output from the polarisation grating when the light was incident at an angle of 60º (relative to the plane of the grating). The polarisation of the input light is linear polarised. L1, M and R1 show the output light measured from the (a) negative first order, (b) zero-order and (c) positive first order. The ratios of height to width for L1, M and R1 are approximately (a) 1.15:1, (b) 1.35:1 and (c) 1.4:1.

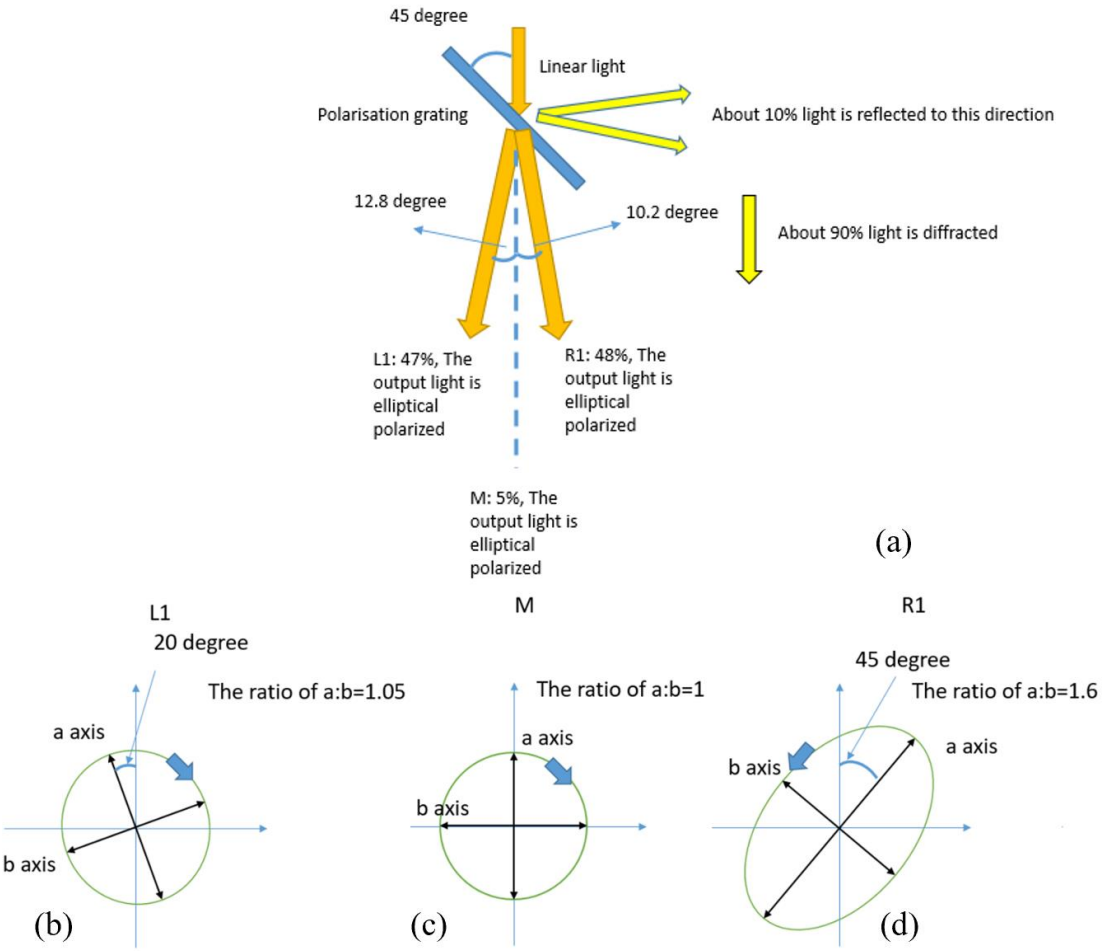

Figure 7.17 (a) Output measurement with linear polarisation at an incident angle of 45º. The polarisation of the input light is linear polarised. L1, M and R1 show the output light measured from the (b) negative first order, (c) zero-order and (d) positive first order. The ratios of height to width for L1, M and R1 are approximately (b) 1.05:1, (c) 1:1 and (d) 1.7:1.

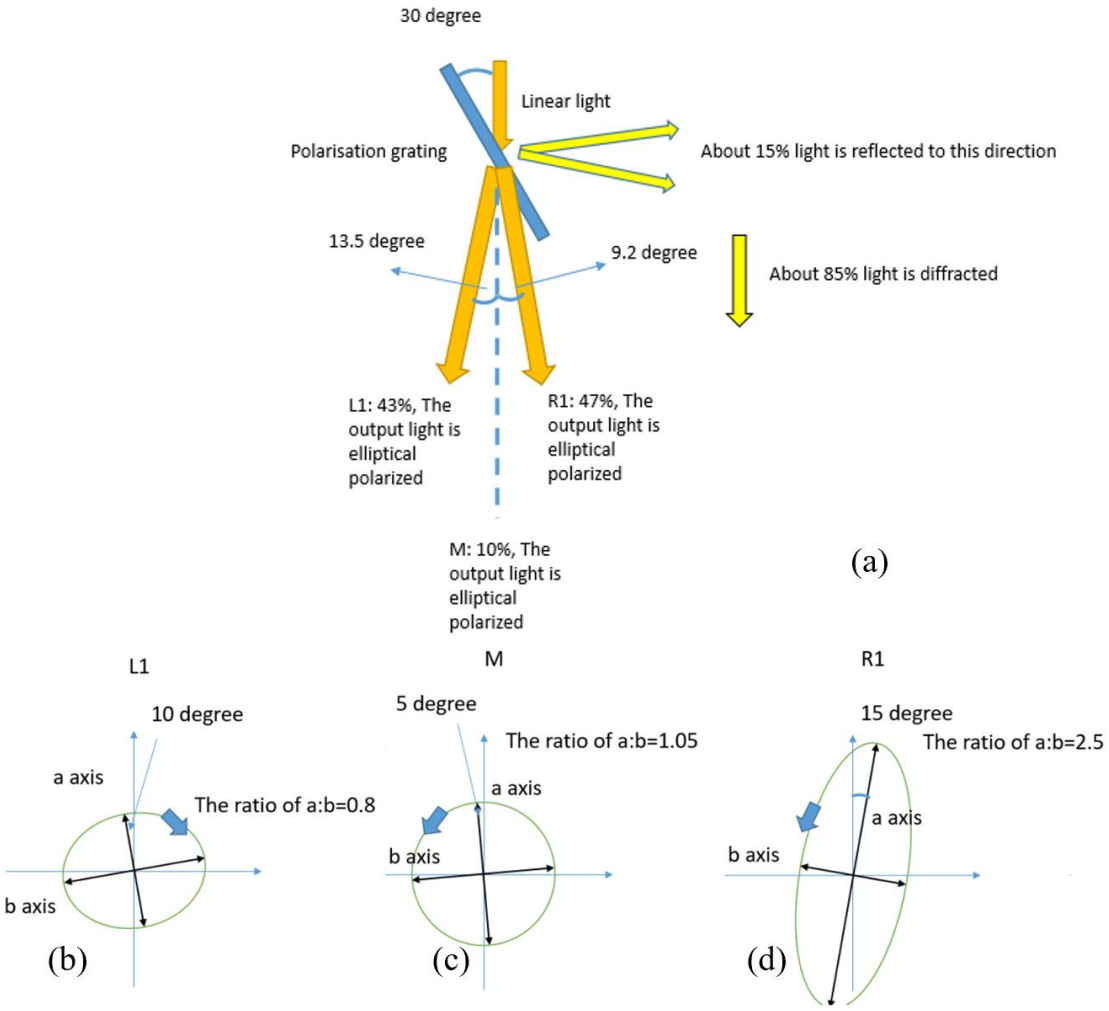

Figure 7.18 (a) Output measurement for linearly polarised light incident at 30º to the polarisation grating. The polarisation of the input light is linear polarised. L1, M and R1 show the output light measured from the (b) negative first order, (c) zero-order and (d) positive first order. The ratios of height to width for L1, M and R1 are approximately (b) 0.8:1, (c) 1.05:1 and (d) 2.5:1.

From these collective figures, it can be seen that the diffraction angle for the left first order increases (the diffraction angle for the right first order decreases) when the incident angle (the angle between the input light and polarisation grating) decreases. This is because a greater proportion of the light goes into the zeroth order and is reflected when the incident angle changes from 90º to 30º. On the other hand, the output polarisation tends to become more elliptical as the incident angle decreases for the

polarisation state. Thus, the handedness for the left and the right first order is maintained but the handedness for the zeroth order appears to change from left to right when the incident angle is smaller than 45°.

After measuring the behaviour for different incident angles, experiments were then carried out to measure the output after passing through two polarisation gratings. The output pattern after the two polarisation gratings, which are oriented perpendicular to each other, is shown in **Figure 7.19**. If we insert two LC devices into the system, then we can control the direction of the output (direct the output light to one of the four spots) by controlling the voltage applied to the LC devices (by changing the polarisation of the light after the LC cell to be either left or right circularly polarised).

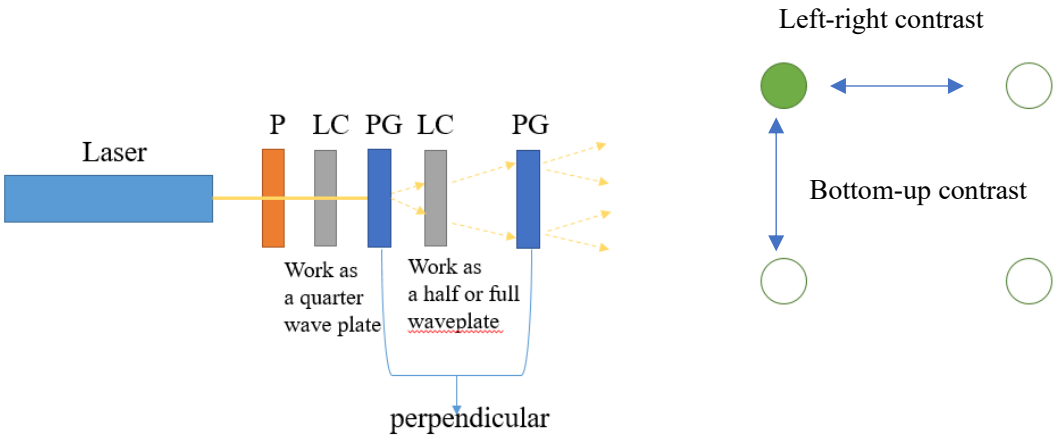

Figure 7.19 Experimental setup used to direct the output light to four different spatial positions. P: Polariser, LC: Liquid crystal device, PD: Photodiode, PG: Polarisation grating.

7.5 Simulation results of two LC devices and polarisation gratings

As in previous chapters, Jones matrices have been used to simulate the performance of the system. With Jones matrices, the polarisation grating can be modelled as a half

waveplate with an optic axis in a plane normal to the incident beam, whereby the angle of the optical axis changes with the position on the polarisation grating. Two LC devices are model as a quarter waveplate (the one after the linear polariser) and a half or full waveplate (the one after the second polarisation grating). The input optical field E_{in}, in this case, can be a linear input or circular input. Hence, a variable is required to be included in the expression of E_{in} so that the polarisation of the input light can be adjusted. The expression for the optical output field, E_{out}, after the first polarisation grating is given by

$$E_{out} = \boldsymbol{D}(\varphi, \delta)\boldsymbol{Q_1}\left(\frac{\pi}{4}\right)\boldsymbol{P}E_{in} \tag{7.3}$$

where $\boldsymbol{Q_1}\left(\frac{\pi}{4}\right)$ is the Jones matrix for the quarter-waveplate, $\boldsymbol{P}$ is Jones matrix for a linear polariser and $\mathbf{D}(\varphi, \delta)$ is the Jones matrix of the polarisation grating with a retardance, δ, and optic axis of the LC molecules oriented at an angle, φ, to the vertical axis. In order to obtain an intensity profile, the optical output field, E_{out}, needs to be Fourier transformed and the final intensity distribution can be obtained from the multiplication of the absolute value of the *x* and *y* components for E_{out}. The Matlab code for getting is E_{out} is shown in **Figure 7.20**.

It can be seen that an ideal LC polarisation grating can be obtained by setting *s* (the symmetry property of the polarisation grating, 0.5 means that the polarisation grating is fully symmetric) to 0.5 (assuming a perfect period structure) and setting *f* equal to π (a perfect half waveplate). The rotation of the optical axis of the polarisation grating is achieved using the rotation matrix, as shown in lines 34 and 35. Results obtained from this Matlab code are illustrated in **Figure 7.21**, where linear polarised light will only

diffract to the first diffraction order when the polarisation state is ideal.

```
clear all;

% symmetry point....
s=0.5; % this is the symmetry point....
% s=0.5 makes "ideal" strcuture, s<>0.5 breaks the symmetry....

% input polarisation state...
phase=0; % this is phase shift between x & y components, 0=linear, pi/2=circular, etc.
Ein = [1;exp(i*phase)]; % this is the input polarisation state... In "jones" notation, so [1;1] is linear at
45 degrees

% grating retardation....
phi=pi; % set to pi for 1/2-wave retardance (ideal case)

count_j=0; % a handy counter for indexing vectors as the model runs....

% loop to run along grating diffraction direction, perpendicular to lines
% variable "orient" goes from 0 to 1 along one-period of the grating
for orient=0:1/128:(1-1/128); % run orientation loop along grating
count_j=count_j+1; % increment counter as loop runs (y-direction)

% A is orientation of optic axis in polarisation grating
% control symmetry of structure....
if(orient<=s);
   A=pi*(orient/s);
else
   A=pi+pi*(orient-s)/(1-s);
end

% set up Jones matrix for grating wave plate at local angle A:
%A=pi/4; % this is the orientation angle of the waveplate if fixed
RM1 = [cos(A) -sin(A); sin(A) cos(A)]; % rotation matrix
MRM1 = [cos(-A) -sin(-A); sin(-A) cos(-A)]; % invesrse rotation matrix
WP1 = [1 0; 0 exp(i*phi)]; % unrotated waveplate matrix
WP1 = MRM1*WP1*RM1; % create jones matrix of waveplate at angle "A"

Eout = WP1*Ein; % calc local Eout

% set up Eout as function of position along the grating
Eout_x(count_j)=Eout(1); % select complex x-comp of E_out
Eout_y(count_j)=Eout(2); % select complex y-comp of E_out

end % end of grating loop

far_field_x=fft(Eout_x); % fourier transform for far-field of x-comp
far_field_y=fft(Eout_y); % fourier transform for far-field of y-comp
far_field_x=fftshift(far_field_x); % re-centre far-field of x-comp
far_field_y=fftshift(far_field_y); % re-centre far-field of y-comp

% get intensities - guesstimate for normalisation????
intensity=abs(far_field_x.*far_field_x)/(count_j*count_j)+abs(far_field_y.*far_field_y)/(count_j*cou
nt_j);

intensity=intensity'; %transpose intensity....
orders=intensity(60:70); % extract -5th to +5th orders
bar(orders); %bar chart of extracted orders
```

Figure 7.20 Matlab code for determining the optical output field after the first polarisation grating.

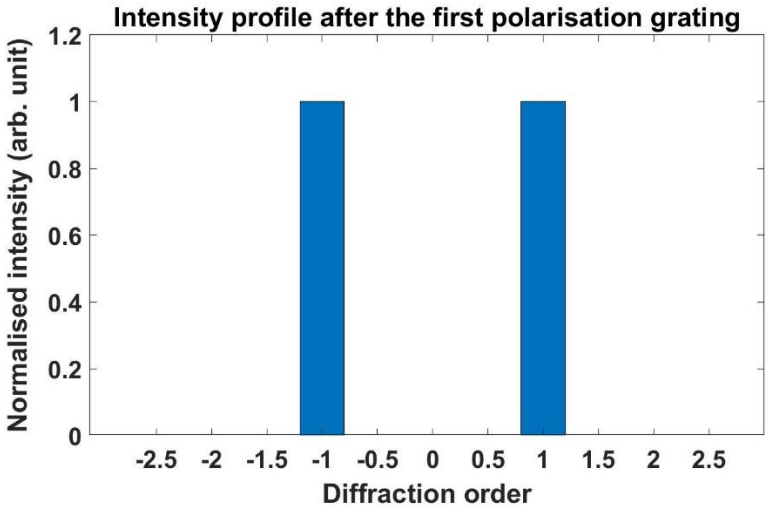

Figure 7.21 Simulation results of the intensity profile after the first polarisation grating. The polarisation grating is set as ideal, and the incident light is linearly polarised.

Diffracted light after the first polarisation grating will pass through a half or full waveplate where the polarisation will be maintained or change to the opposite state. Following this, light will be diffracted by the second polarisation grating which is perpendicular to the previous grating. The final output field, E_{fout}, becomes

$$E_{fout} = \boldsymbol{D}(\varphi, \delta)\boldsymbol{W}(\theta)E_{out} \tag{7.4}$$

where $\boldsymbol{W}(\theta)$ is the Jones matrix for the second LC-based waveplate which can be a half or full waveplate. The Matlab code for Equation (7.4) is quite similar to the previous simulation code except the waveplate is a half or full. In the simulation, the half or full waveplate and the second polarisation grating are all assumed to be ideal.

The intensity profiles for all combinations are shown in **Figure 7.22**. From the Figure, it can be found that columns appear in different positions for different conditions, which means that light can be directed to four different spatial positions by using different waveplates and two polarisation gratings. This simulation result is quite important as we can use two polarisation gratings and different waveplates to develop

a beam steering system which can direct light into four spatial directions.

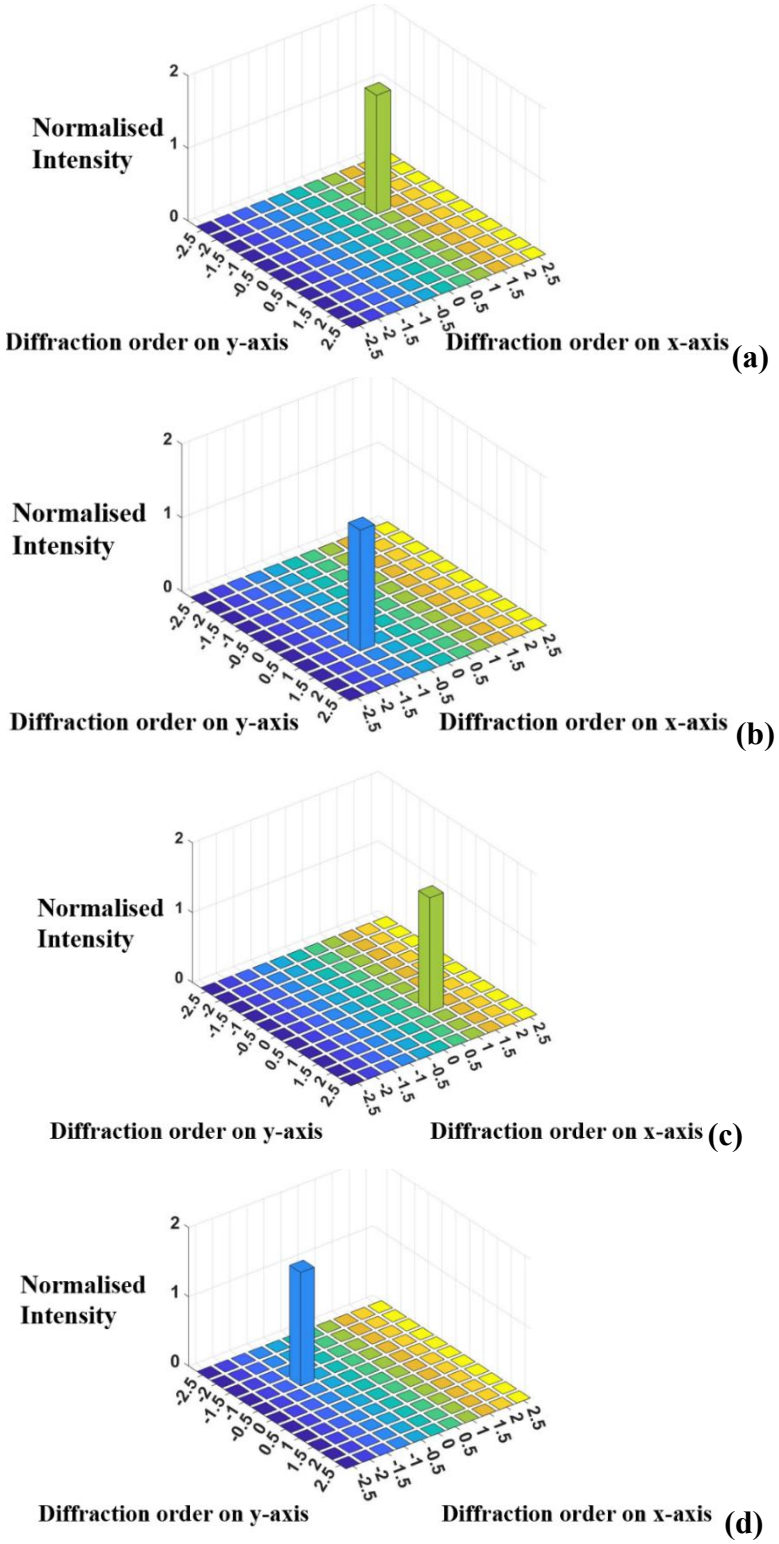

Figure 7.22 Simulation results of intensity profile generated by two polarisation gratings and two waveplates. (a) and (b): Quarter waveplate + full waveplate. (c) and (d) Quarter waveplate + half waveplate. Light after quarter waveplate in (a) and (d) is left circularly polarised, in (b) and (c) it is right circularly polarised. In the system, all components are assumed to be ideal.

7.6 Experimental results

The experiment results for the system in **Figure 7.19** are shown in **Figure 7.23**. For position 1, light after the quarter waveplate is left circular polarised and hence directed to the left. Then light changes to right circularly polarised after the first polarisation grating and its polarisation state is maintained after the full waveplate. The polarisation of the output light changes to left circularly polarised. Position 3 is similar to position 1 except the full waveplate becomes a half waveplate and the polarisation of the final output light is right circular polarised. For positions 2 and 4, light after the quarter waveplate is right circular polarised and thus the light will be directed to the right. The final position of the output light depends on whether the second waveplate is a full or half-wave.

In order to control the output light to switch between the four different spatial locations, it is important to control the first LC device to be a quarter waveplate and the second LC device to be either a half or full waveplate. We have found that the LC device works as either a half or full-wave plate when the voltage is 2.77V or 2.17V, respectively. However, we found that the output only showed good contrast for the left-right positions during the experiment. The bottom-up contrast is low, which is not desirable. This happens because the left-right contrast is controlled by the first polarisation grating whereas the bottom-up contrast is controlled by the second polarisation grating. The polarisation of the input light for the first polarisation grating can be precisely controlled by using the first LC device. However, for the second polarisation grating, the input light polarisation state is not perfectly circular polarised.

There are three possible reasons for this:

1. As shown in the previous results, the output light from the polarisation grating is not perfectly circular polarised due to the nonideality of the polarisation grating.
2. There is an incident angle between the input light and the second LC device that also causes errors in the system.
3. As the previous results show, if the incident angle between the polarisation grating and input light is not 90º, the output polarisation will be elliptical with an offset angle.

In order to reduce the influence of these factors, the second LC cell was replaced with a nematic pi cell so that the incident angle would then not have a significant impact on the output. After several attempts, we have found that, in order to get a good contrast along both orientations, we need four different voltages (two sets of voltage: 2.03V, 2.58V and 2.33V, 3.02V) to control the second LC device to make it behave as either a full or half waveplate for the two different input light polarisations.

In order to better understand the results, the second polarisation grating has been removed and the voltage required to make the output light after the second polarisation grating be circularly polarised light was determined. Surprisingly, it was found that the voltages required to make the second LC device behave as either a half or full waveplate were found to be 2.17V and 2.79V, respectively, which are approximately half of the two sets of voltages ($2.17V \approx \frac{2.03V+2.33V}{2}, 2.79V \approx \frac{2.58V+3.02V}{2}$).

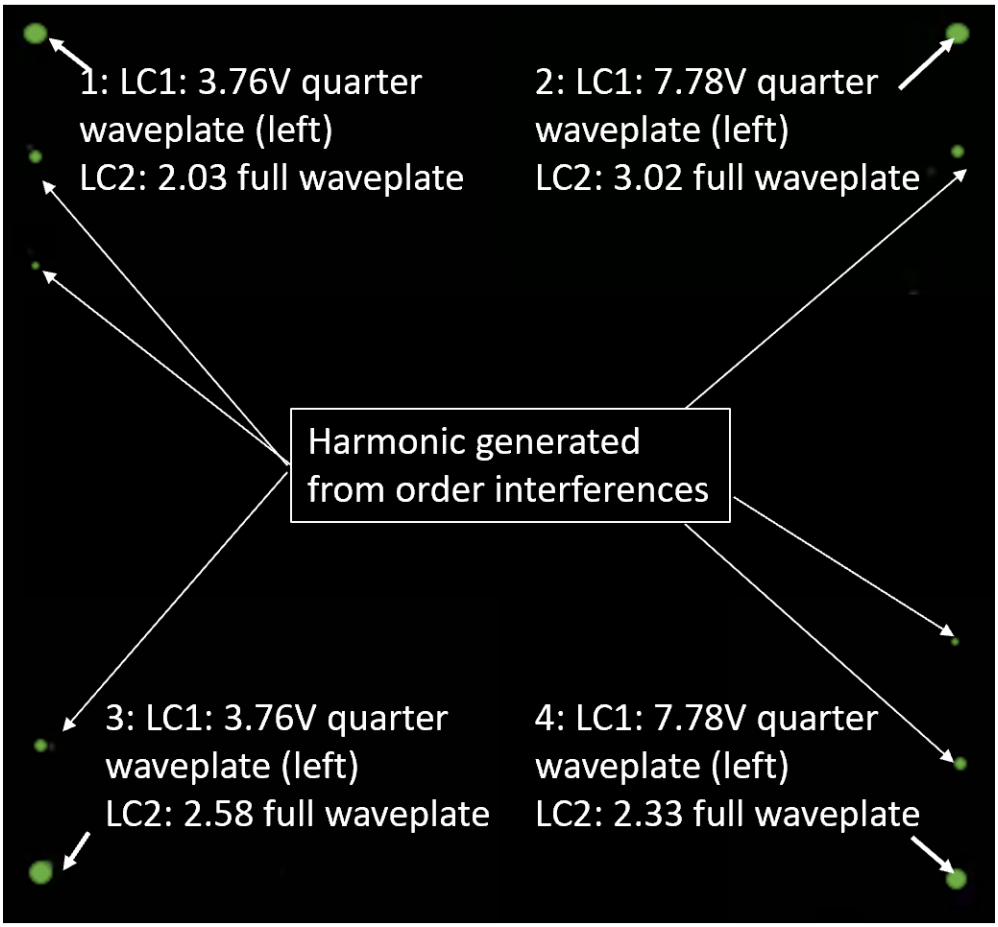

Figure 7.23 Experimental results of the optical output light intensity after the second polarisation grating. **1**. Light after the quarter waveplate is left circularly polarised and the second waveplate is a full waveplate. The final output polarisation is left circular polarised. **2**. Light after the quarter waveplate is right circularly polarised and the second waveplate is a half waveplate. The final output polarisation is left circularly polarised. **3**. Light after Quarter waveplate is left circularly polarised and the second waveplate is a half waveplate. The final output polarisation is right circularly polarised. **4**. Light after the quarter waveplate is right circularly polarised and the second waveplate is a full waveplate. The final output polarisation is right circularly polarised. By changing the voltage on each LC-based waveplate, the polarisation after the LC waveplate can be altered which will diffract the light to four different spatial positions. In addition, due to the imperfections in the polarisation gratings, higher harmonics exist in the image.

After verifying that light can be directed to four different spatial positions by using the previous setup, this system was tested to see if it could be used in an optical

communication testbed (visible light communication). The first aim of the experiment is to test whether our reflected path can be made to be parallel with the input path. First we have built the system as shown in **Figure 7.24**. For all the following experiments, the mirror is placed at a position that is substantially far away from the beam steering system. In all cases, the laser source was immediately followed by a neutral density filter in order to reduce the beam to be equivalent to a Class 2.

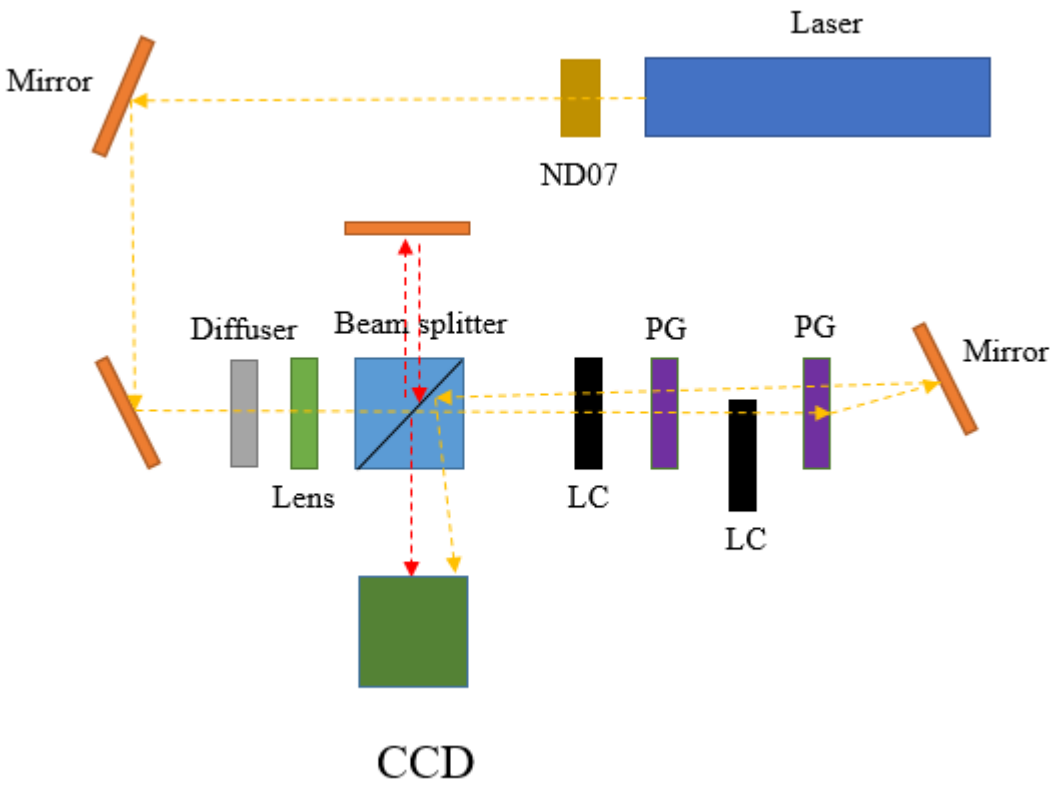

Figure 7.24 System to test reflected light path (LC: liquid crystal, PG: polarisation grating, ND: ND filter, CCD: CCD camera).

Figure 7.25 illustrates one situation whereby the light is transmitted and reflected between the beam steering system. The mirror is placed at the position which is substantially far away from the beam steering system.

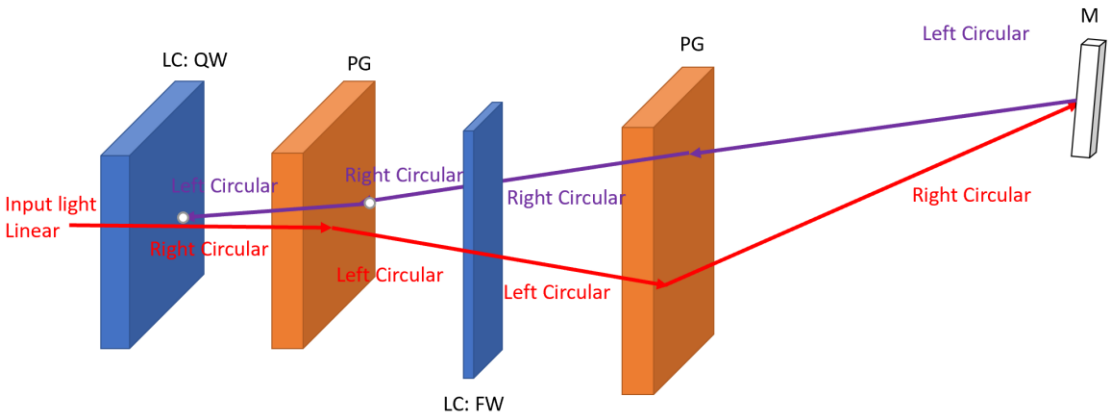

Figure 7.25 illustrates one situation whereby the light is transmitted and reflected between the beam steering system, the thickness of the LC device is approximately 5μm and through controlling the voltage on the LC device, we can make the LC device work as a quarter waveplate, a half waveplate or a full waveplate. The return light from the mirror is near parallel to the input light because the mirror is a substantial distance away.

As shown in **Figure 7.25**, when input light passes through the first LC device, which works as a quarter waveplate, the polarisation of the input light changes from linearly polarised light to right circular polarised light. Hence, light after the first polarisation grating will diffract to the right and change to left circular polarisation. The second LC device works as a full waveplate so that light propagating through it will not change its polarisation. When left circularly polarised light enters the second polarisation grating, it diffracts to the upper position where the polarisation state changes to right circularly polarised light. Light is then reflected by the mirror and its polarisation becomes left circular. Since the reflected light is left circularly polarised, the light will then be deflected downwards upon passing through the second polarisation grating (as shown in **Figure 7.26**). The reflected light will not pass through the second LC device, hence the polarisation will not be altered and light will be directed to the right and pass through the first polarisation grating. In theory, the final

reflected light will propagate parallel to the input light in the horizontal plane but not in the vertical plane. (As the propagating direction of the reflected light is from right to left, the light entering the first polarisation grating is not perpendicular to the substrate of the polarisation grating as shown in **Figure 7.27**).

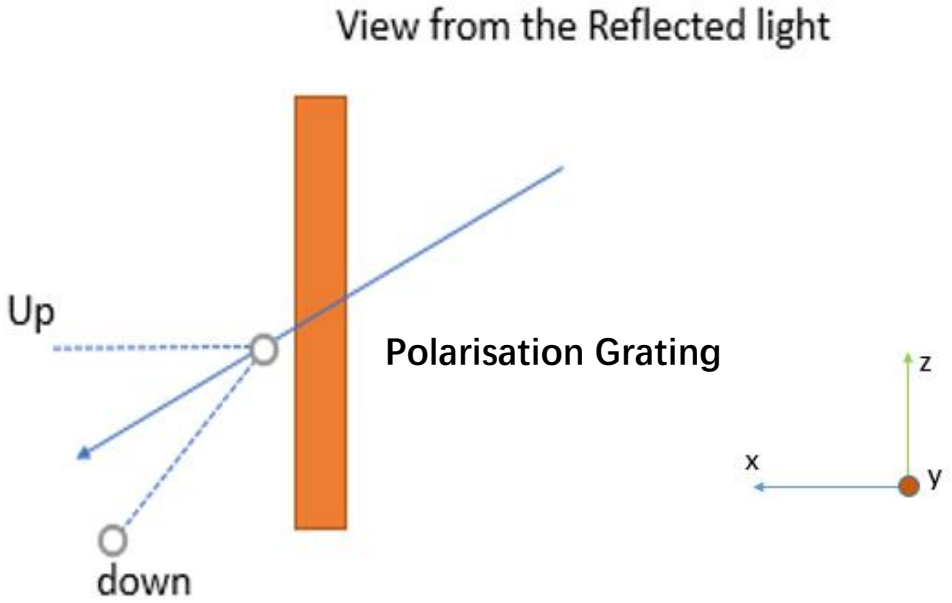

Figure 7.26 Reflected light path to the second polarisation grating

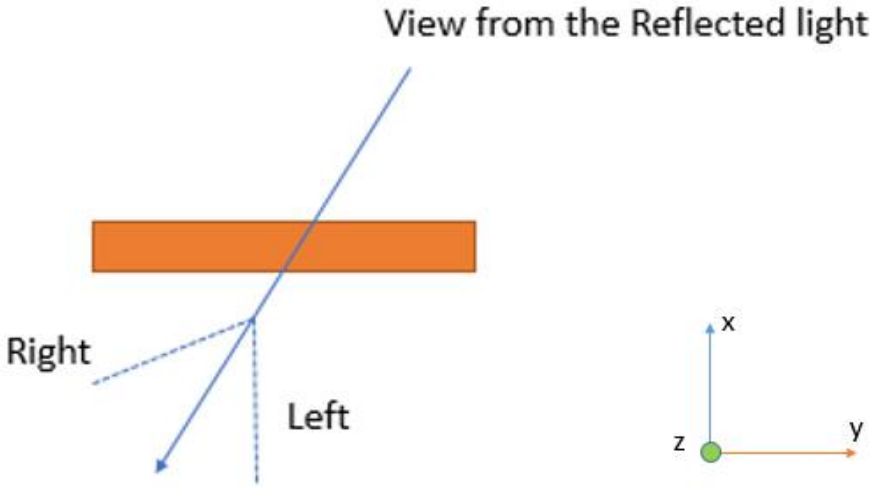

Figure 7.27 Reflected light path to the first polarisation grating.

Hence the reflected light path will propagate parallel to the input path in the

horizontal plane but is at an angle to the vertical plane. The experiment setup and results are presented in **Figure 7.28** and **Figure 7.29**, respectively.

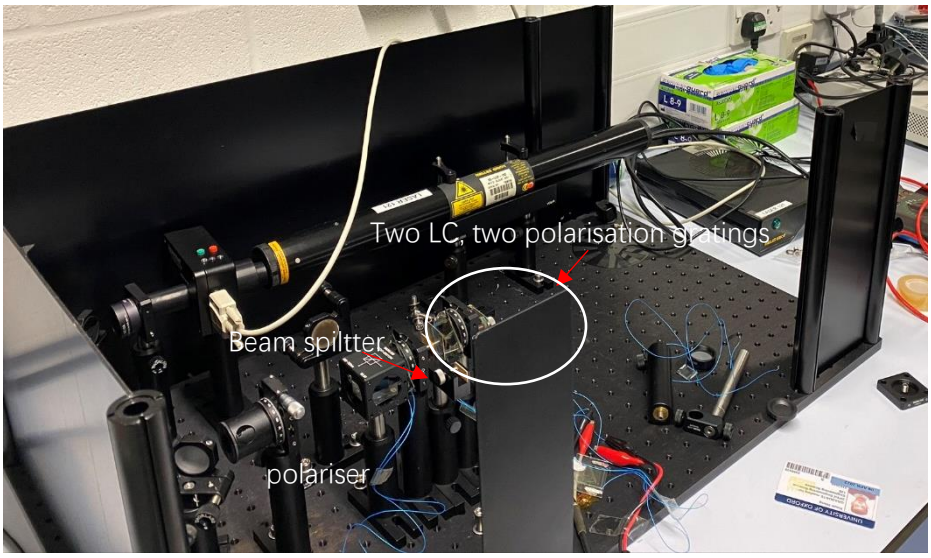

Figure 7.28 The experimental setup for testing whether the light can be reflected back along the same path.

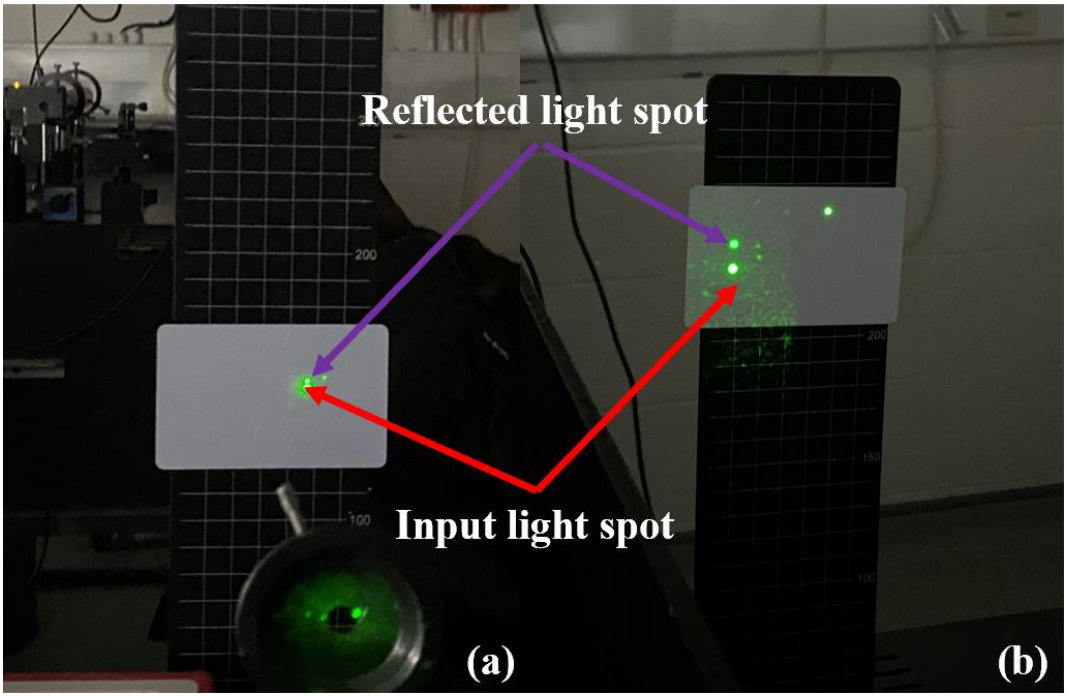

Figure 7.29 Experimental results for the input light spot and reflected light spot with different measurement distances. For (a) and (b), the distances between the white display card and the beam splitter are 1 m and 15 cm, respectively. The input spot looks weaker because we have placed an ND filter in the reference beam to reduce the intensity so that the input spot will not look too bright in the image. From the Figures, it was found that the vertical distance between the input and reflected spot increases as the measurement distance increases. This proves that the input and reflected light are parallel in the horizontal direction but not in the vertical direction.

The experiment results shown in **Figure 7.29** demonstrate that the reflected light path is parallel to the input light in the vertical plane but they are not parallel in the horizontal plane, as we expected. In order to make the input light path and reflected light path parallel to each other, we have added an LC device (LC 3) to the reflected path between the second polarisation grating and the mirror. This LC device will function as a half waveplate to make the polarisation of the reflected light the same as the polarisation of the input light. This configuration and experimental setup is shown in **Figure 7.30** and **Figure 7.31**, respectively.

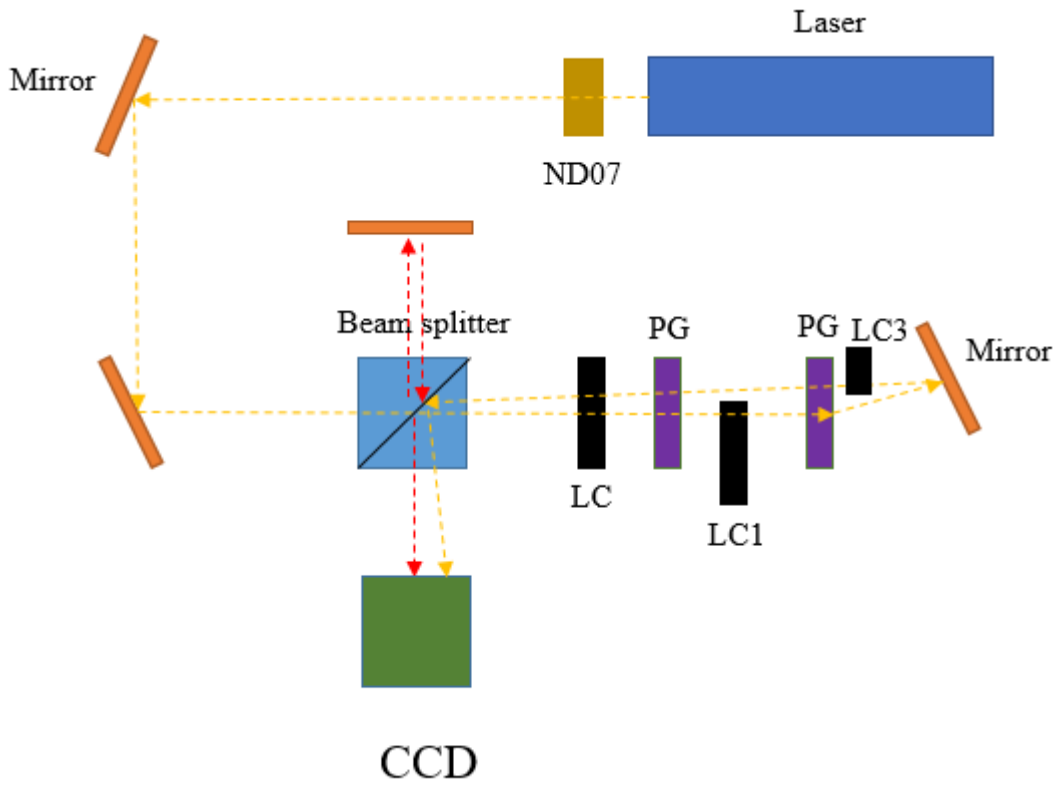

Figure 7.30 Configuration of the experiment when an extra LC device is added in the reflected path.

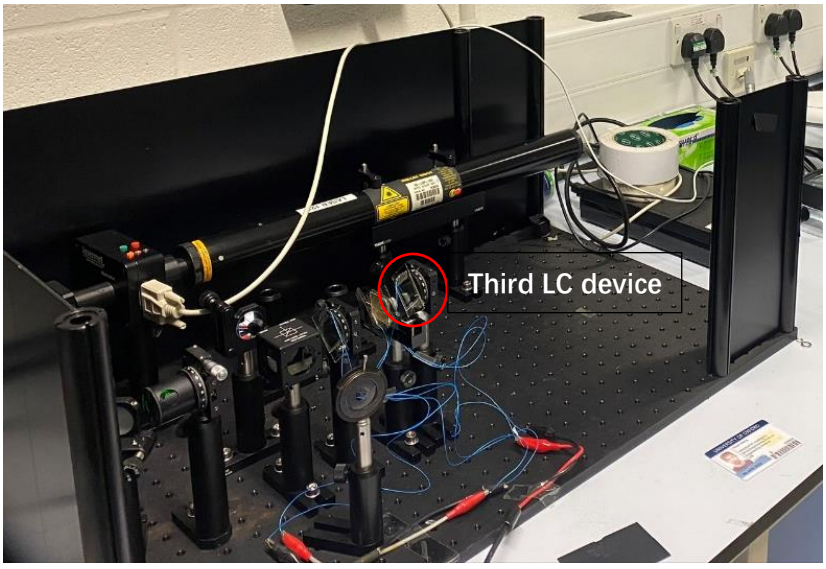

Figure 7.31 Revised experiment setup.

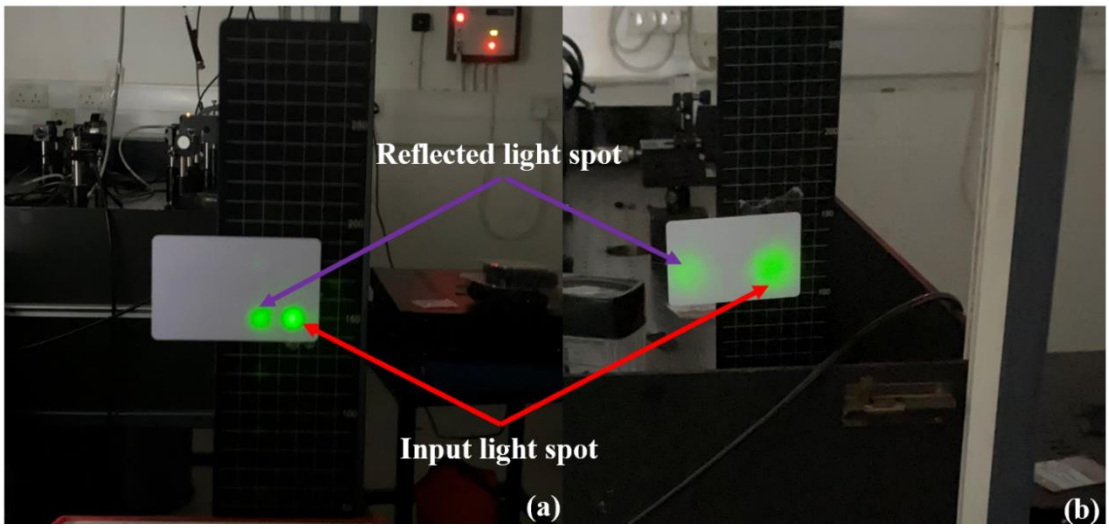

Figure 7.32 Experimental results obtained with an additional LC device between the mirror and the second polarisation grating. For (a) and (b), the distances between the white card display card and the beam splitter are 15 cm and 1 m, respectively. From the Figures, we can see that the horizontal distance between the input and reflected spot increases as the measurement distance increases but the vertical position does not change as the measurement distance increase. This proves that the input and reflected light are parallel in the vertical direction but not in the horizontal direction.

Figure 7.32 shows the experimental results obtained from the setup illustrated in **Figure 7.31**. The experiment results indicate that the reflected light path is parallel to that of the input light in the vertical plane but not parallel in the horizontal plane. To make sure the reflected light path is parallel to the input light path in both the vertical and horizontal planes, we need to do the following:

1. The polarisation of the reflected light from the mirror needs to be the same as the polarisation of the input light to the mirror.
2. The polarisation of the reflected light that enters the first polarisation grating needs to be different from the polarisation of the input light into the first polarisation grating (as shown in Figure 7.33).

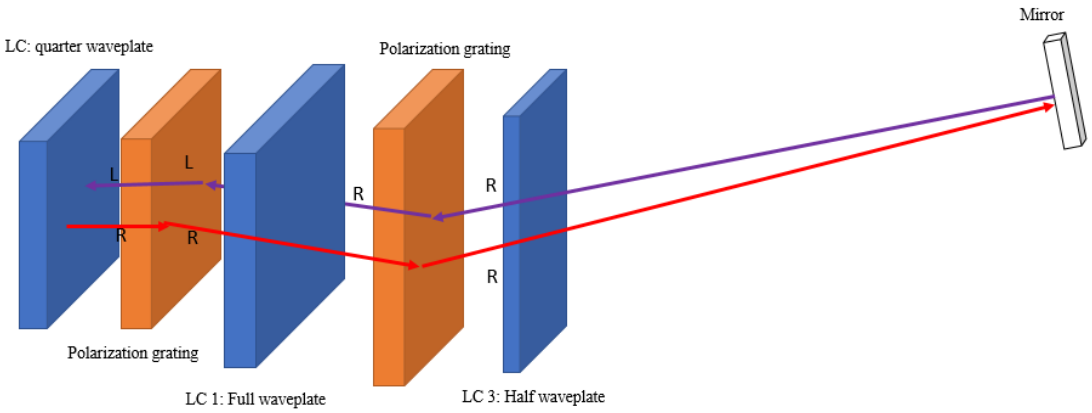

Figure 7.33 Polarisation of the input and reflected light to ensure the input and reflected light paths are parallel. The return light from the mirror is near parallel to the input light because the mirror is a substantial distance away.

In order to meet these conditions, we have added another LC device (LC 2) into the system as illustrated in **Figure 7.33**. Now there are two LC devices between the two polarisation gratings. Depending on the position we want the light to be directed to, the function of the two LC devices will be different.

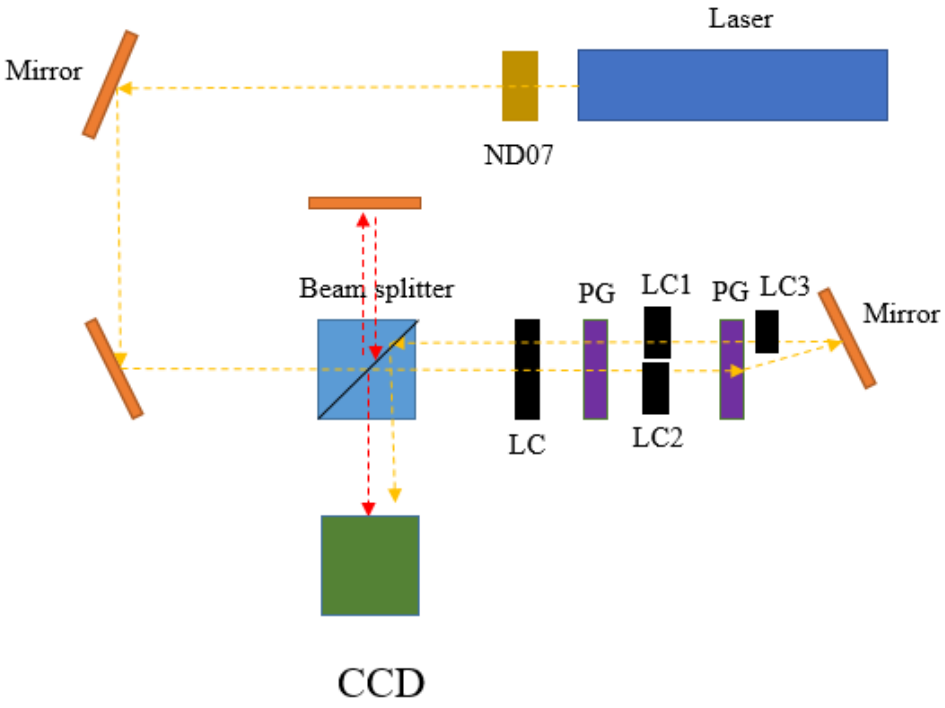

Figure 7.34 Configuration of the experimental setup.

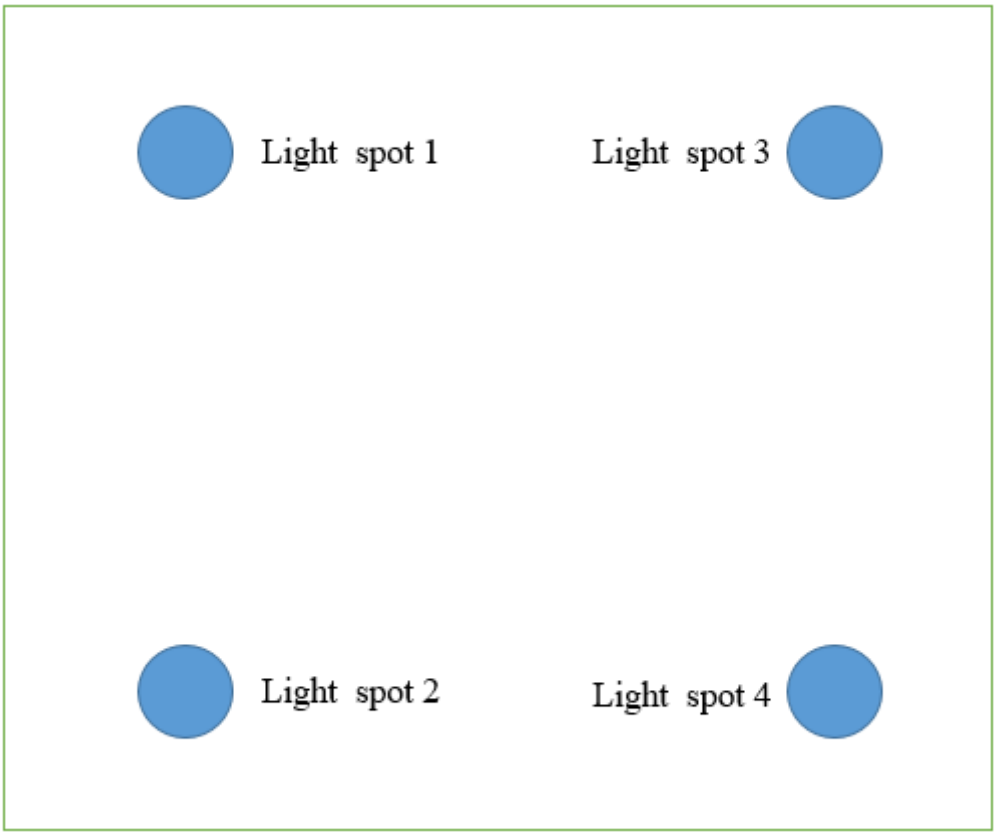

Figure 7.35 Locations of the laser spots after passing through the setup.

For the beam steering, when the input light to the two polarisation gratings is right circular polarised, the light will diffract to the right for the first polarisation grating and then upwards for the second polarisation grating (light spot 3 in Figure 7.35). In this case, the two LC devices between the two polarisation gratings will be set to function as a full waveplate (on the input path, LC 1) and half waveplate (on the reflected path, LC2). For light spots 1 and 4, both LC 1 and LC 2 are set to a half waveplate condition. The situation for light spot 2 is the same as light spot 4. By adding an extra LC device between the two polarisation gratings, we can ensure the input and reflected light paths are parallel in both the horizontal and vertical planes. The result of adding an extra LC device is shown in **Figure 7.36.**

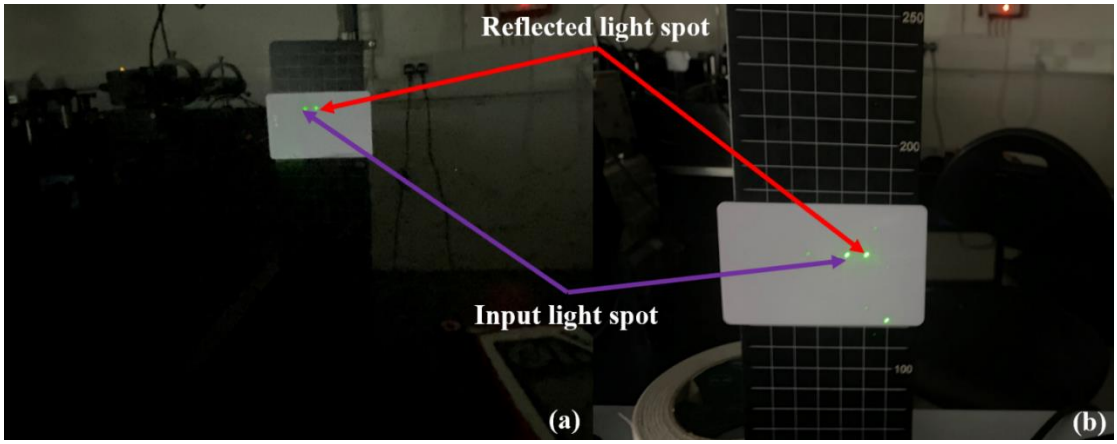

Figure 7.36 Experiment result of adding an extra LC device between two polarisation gratings. For (a) and (b), the distances between the white display card and the beam splitter are 1 m and 15 cm, respectively. From the Figures, we find that both the horizontal and vertical distance between the input and reflected spot do not change as the measurement distance increases. This proves that the input and reflected light are parallel in both the vertical and horizontal directions.

For optical communication systems, the beam radius is normally quite large. In order to simulate the performance of the system with a large beam spot, a diffuser was added into the system as shown in **Figure 7.37**.

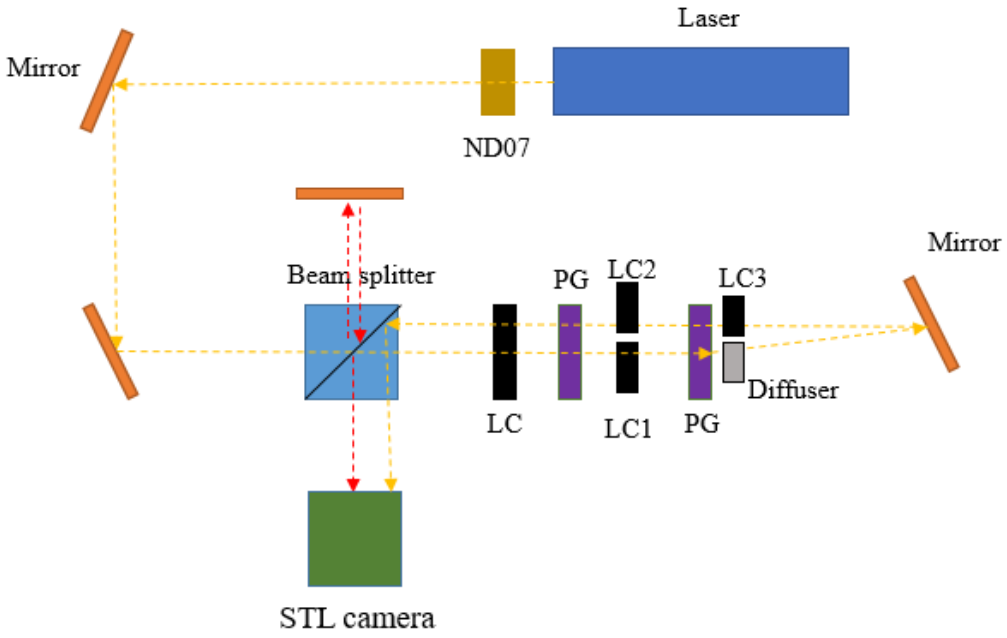

Figure 7.37 Revised experiment setup by adding a diffuser into the system.

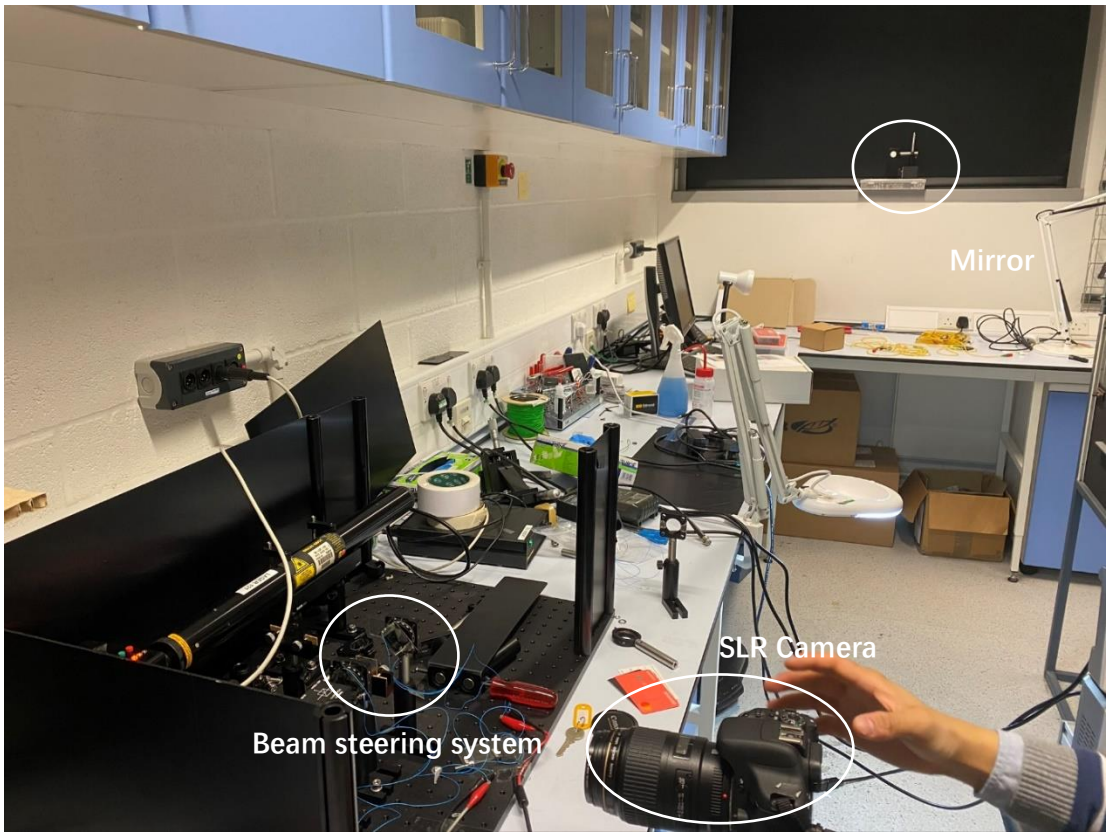

Figure 7.38 The actual experiment setup, the distance between the mirror and our beam steering system is about 3 m and the reflected light is recorded by a digital SLR camera.

During the experiment, we found that the reflected light was too weak to be seen by the naked eye after the addition of a diffuser. Therefore, we used a digital SLR camera to observe the reflected light. The images from the camera are presented in **Figure 7.39**. From these images, we can verify that system still works for a long distance even when we add a diffuser into the system.

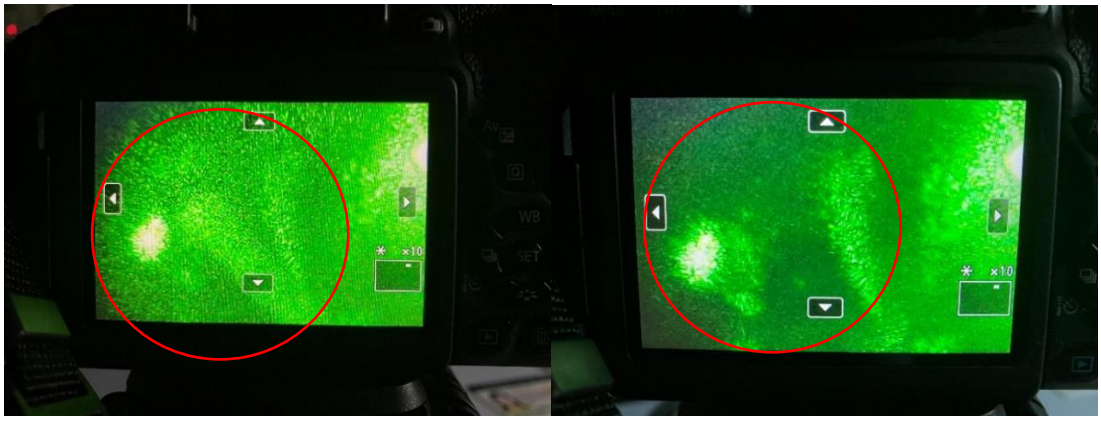

Figure 7.39 Experiment results by using a digital SLR camera to observe the reflected light. Both images are magnified by 10 times to see the difference. The region inside the red circle shows the reflected light. The second image is taken by blocking the reflected light. Comparing these two images, we can identify the reflected light.

In addition to the above results, we have also added a chopper into the system to simulate the communication system. **Figure 7.40** shows the experimental setup of the beam steering system when a chopper was added.

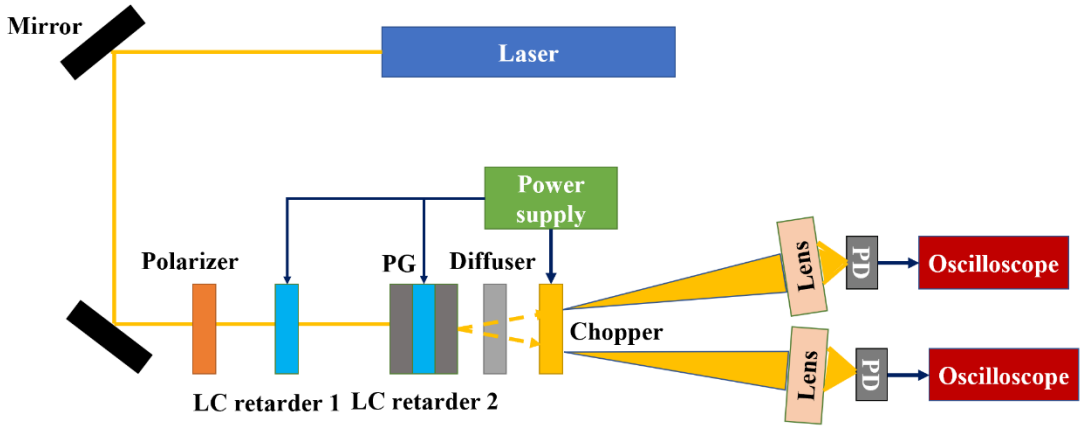

Figure 7.40 Experiment setup to simulate the communication system. A chopper is added after the diffuser and the frequency of the chopper is set to 203 Hz. The light is diffused by the diffuser and directed to two different positions through controlling the voltage on the LC retarder 1 and LC retarder 2. Due to the existence of the diffuser, the signal that reaches the photodiode will be very weak. Hence, a lens has been added before the photodiode to ensure enough signal will be collected by the photodiode. PG: polarisation grating, PD: photodiode.

As mentioned, the reflected light is too weak and cannot be measured by our photodiodes, hence we have replaced the mirror with a photodiode to show the performance of our system with a pulse signal. Due to the existence of the diffuser, the signal that reaches the photodiode will be very weak. We have added a lens before the photodiode to measure the signal to ensure we can successfully record the signal. In this experiment, due to the space limitations, we can only measure the two upper signals over a relatively long distance, the two lower signals are physically blocked by the bench.

Figure 7.41 shows the response recorded on an oscilloscope, channel 1 (yellow curve) shows the signal measured by photodiode 1 and channel 2 (blue curve) shows the result measured by photodiode 2. The frequency of the chopper was set to be 203 Hz and the oscilloscope was set to AC mode so that only the pulse signal was recorded. By changing the voltage applied to LC 1, we can direct light to either photodiode 1 or photodiode 2. When the input light enters photodiode 1, a pulse signal will appear on channel 1 ($\pm$10mV) while channel 2 is just noise (as shown in the first image). When we change the voltage applied to LC 1, which causes light to go to photodiode 2, channel 2 ($\pm$10mV) will display a signal while channel 1 just shows noise. Through this method, we have successfully demonstrated that the beam steering system can work with a pulse signal and that we alter the voltage amplitude in order to direct light to different spatial positions.

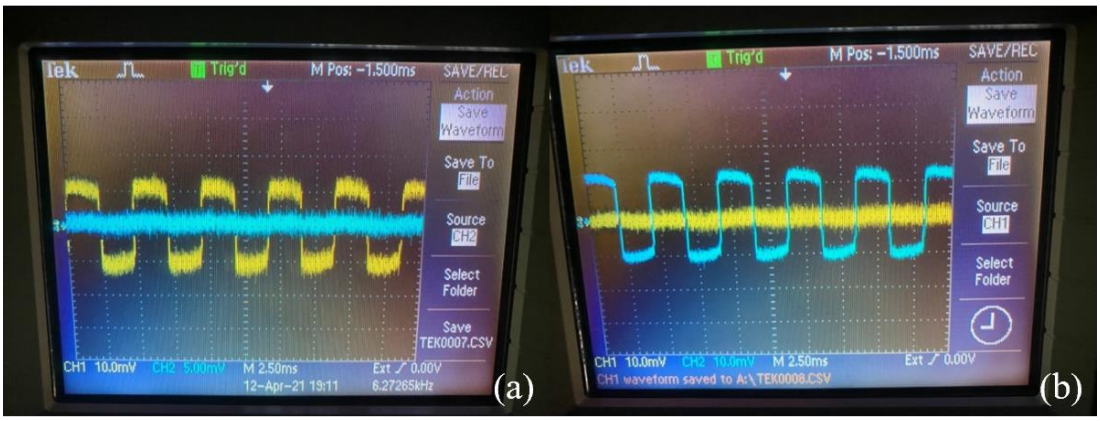

Figure 7.41 Measurements from the two photodiodes. By changing the voltage applied to the LC device between the two polarisation gratings in the input path, we can change the input light to switch from one photodiode to another photodiode.

7.7 Conclusion

In this work, we have developed a beam steering system by combing polarisation gratings with an LC-based tuneable waveplate. This beam steering system can diffract light to four different spatial positions by controlling the voltage applied to the LC device in order to change the behaviour of the waveplate. In addition, it has also been demonstrated that light can be reflected back along the same path by adding two extra LC devices (functioning as half waveplates) into the system. This beam steering system has substantial potential in visible light communications, enabling a high efficiency optical communication system to be achieved. Future work would involve testing the system in a real communication system and also combining this with the phase modulation technology developed in the previous chapters with polarisation gratings to make an integrated beam steering system. Originally, the pi-cell work had been intended as a proof of concept before the implementation of the phase modulation system. Unfortunately, this work was impacted by the COVID pandemic. Hence the

original plan will be demonstrated in Chapter 8: Future work.

Chapter 8 Conclusions and Future work

8.1 Concluding Remarks

This thesis has shown a novel phase modulator that can provide full 2π phase modulation with the sub-millisecond response. In order to thoroughly carry out this study, the flexoelectro-optic behaviour of chiral nematic liquid crystal (LC) devices has been characterised by using a flexoelastic ratio which can be determined by recording the amplitude of the electric field when the transmission properties become equivalent. This rapid characterisation method helps us to develop a phase modulator based on the reflective configuration where phase modulation is generated by combing the LC device with a quarter waveplate and reflector. The reflector can be a combination of a mirror and a quarter waveplate or a chiral reflector that is more robust than the previous configuration. Besides, a transmissive phase modulator has been developed which is more useful when the reflective configuration is not desirable. A further study on the phase modulator led us to generate an integrated device that has the potential to combine with polarisation gratings to make an integrated beam steering system. The following sections draw conclusions for each chapter and future directions of the work presented

8.1.1 LC Phase modulator

Liquid crystal (LC) phase modulators have widely used as a standard class of instruments for the control of light. Through the field driven control of their internal anisotropic medium, these devices can manipulate the phase, amplitude and

polarization of incident beams according to user's requirements. In order to satisfy the needs of various applications [219-221], LC phase modulators should exhibit a large phase change ($\geq 2\pi$), fast response time (~ 1 ms), and a low operating voltage ($\leq$15 V). Although reseachers has proposed many approaches to fulfil those requirements, these device attributes are intrinsically tied and optimization of one performance metric often leads to the detriment of others. In this thesis, we have presented a phase modulator which can exhibits 2π phase modulation with sub millisecond response time at 4V/μm. Chapter 3 describes a rapid and simple method to characterise the flexoelectro-optic behaviour of chiral nematic liquid crystal (LC) devices that exhibit a large tilt-angle. This method leads us to develop a phase modulator which can be reflective (chapter 4) and transmissive configuration (chapter 5). For the reflective LC phase modulator, the system contains a LC device, a quarter waveplate and a reflector. The reflector can be a combination of mirror and quarter waveplate or a chiral reflector which can enhance the tolerance of the system. In order to provide full 2π phase modulation, in addition to a LC device and a quarter waveplate, the transmissive configuration also involves an additional LC layer and a half waveplate or an additional LC layer with the opposite electric field applied. Furthermore, an integrated LC optical phase modulator based on the reflective mode phase modulator has been successfully demonstrated (chapter 6) which combines a birefringent polymer film (worked as a $\lambda/4$ waveplate), a chiral nematic layer and silver film (worked as a mirror) into one cell. This phase modulators is believed to have substantial potential in developing into a pixelated spatial light modulator that would be used in a range of applications such as microscopy, optical

telecommunication and holography.

8.1.2 Optical Beam Steering System

In chapter 7, a beam steering system is demonstrated by combing polarisation gratings with two LC-based tuneable waveplates. Light can be directed into four different directions by controlling the voltage on the LC-based tuneable waveplates to make them work as a quarter waveplate and a half waveplate or a full waveplate. Besides, we have also shown that diffracted light can be reflected back along the same path by adding two extra LC devices (functioning as half waveplates) into the system. This beam steering system has substantial potential in visible light communication, enabling a high efficiency optical communication system to be achieved. In the future, the pi-cell work will be replaced with phase modulator developed in chapter 6 and test in a real communication system.

8.2 Future work

8.2.1 Phase modulator

As mentioned in the previous chapter, an analogue phase-only modulator has been demonstrated which can achieve full 2π phase modulation with sub-millisecond. In this configuration, the phase modulation is based on the flexoelectro-optic effect under ULH structure. The rotation of optical axis is generated by applying 4 V/μm electric field at a temperature of 106°C. Although this configuration has substantial potential in spatial light modulator technology, several issues are still existed which limit the development of this phase modulator configuration, such as high operating temperature and unstable LC alignment.

A possible topic for future work is to directly address these issues. For example, for high operating temperatures, even though we can reduce the working temperature by mixing the LC dimer CB7CB with a room temperature nematic LC mixture such as, E7, this method also reduces the flexoelectro-optic effect, which means that a higher driving voltage is required in order to obtain ±45° switching angles. A high working voltage is not desirable for SLM fabrication. In collaboration with the University of Hull, the research group has started to develop new materials that can exhibit switching angles in excess of ±45° with sub-millisecond switching time.

For example, the compound CB9OCB shows a tilt angle of ±45° with sub-millisecond switching time with a nematic LC phase at 70℃ which is much lower than that of the material used in this thesis. Nevertheless, 70 ℃ is still too high for commercial usage. In addition to the high operating temperatures, the unstable ULH

alignment is also an important issue which forbids further development. As mentioned in Chapters 4 and 6, the ULH alignment is not stable in the absence of an electric field or polymer stabilization. Therefore, a continuous electric field is necessary for maintaining this structure, which is not desirable for the fabrication of SLM technologies.

In order to solve this problem, the method used in Ref. 88 to develop a surface polymer network so as to stabilize the ULH structure could be considered. Using a surface polymer network, the reduction in the flexoelectro-optic effect caused by the polymer network can be minimised so that a high driving voltage can be avoided. Towards this end, a small amount of reactive mesogen RM257 (Merck) and photoinitiator IRG819 (Merck) were chosen to be doped into a chiral nematic mixture for polymer stabilization of the non-permanent ULH alignment. The cell contained two substrates where one of the substrates has two regions: one region was coated with ITO whereas the other one was not coated with ITO. After applying an electric field, the mixture in the ITO-coated region forms a ULH alignment while the mixture in the non-ITO-coated region only forms a Uniform Standing Helix (USH) alignment.

The sample was then exposed to UV light to form a surface localized polymer network that stabilizes the ULH and USH alignments (**Figure 8.1**). During the photo-polymerization process, an electric field is required to maintain the ULH structure. **Figure 8.2** shows the sample after the photopolymerization process, the sample was kept at 108℃ but the electric field was removed. It can be found that the left region and right region show different colours, which is the result of the different alignments of

the helical structure.

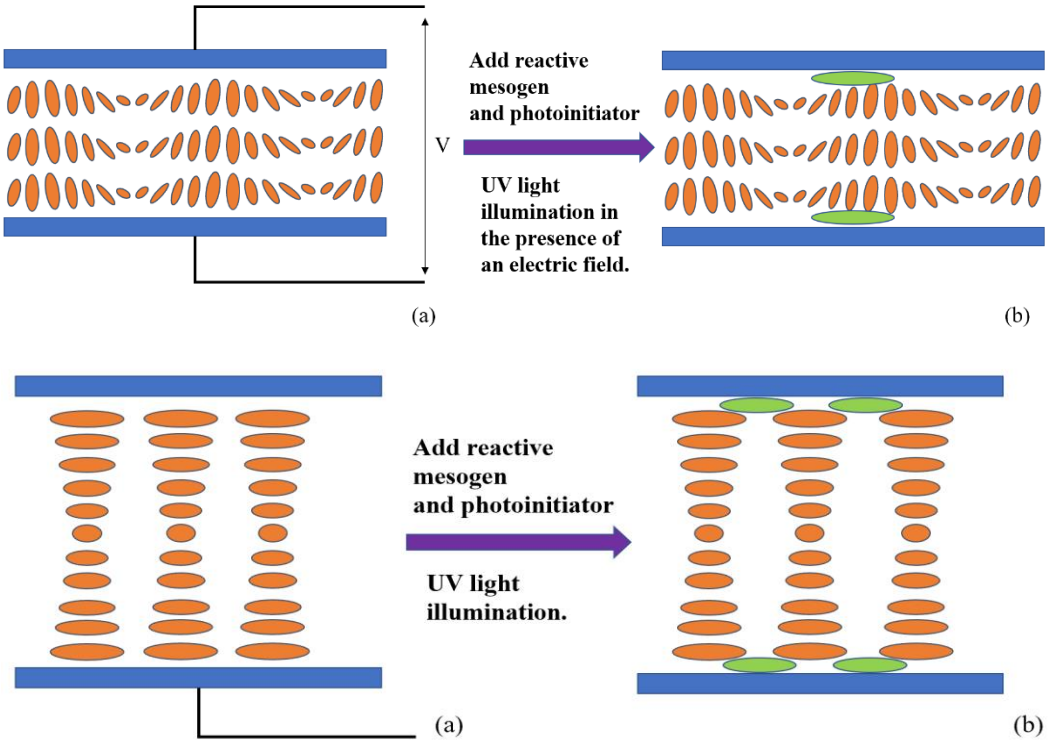

Figure 8.1 (a) unstable ULH alignment with an external electric field, and (b) the polymer-stabilized ULH alignment. Orange ellipses represent the LC molecules and green ellipses represent the surface-localized polymer network. (c) stable USH alignment without an external electric field and (d) the polymer-stabilized USH CLC texture. Blue ellipses represent the LC molecules and brown ellipses represent surface localized polymer.

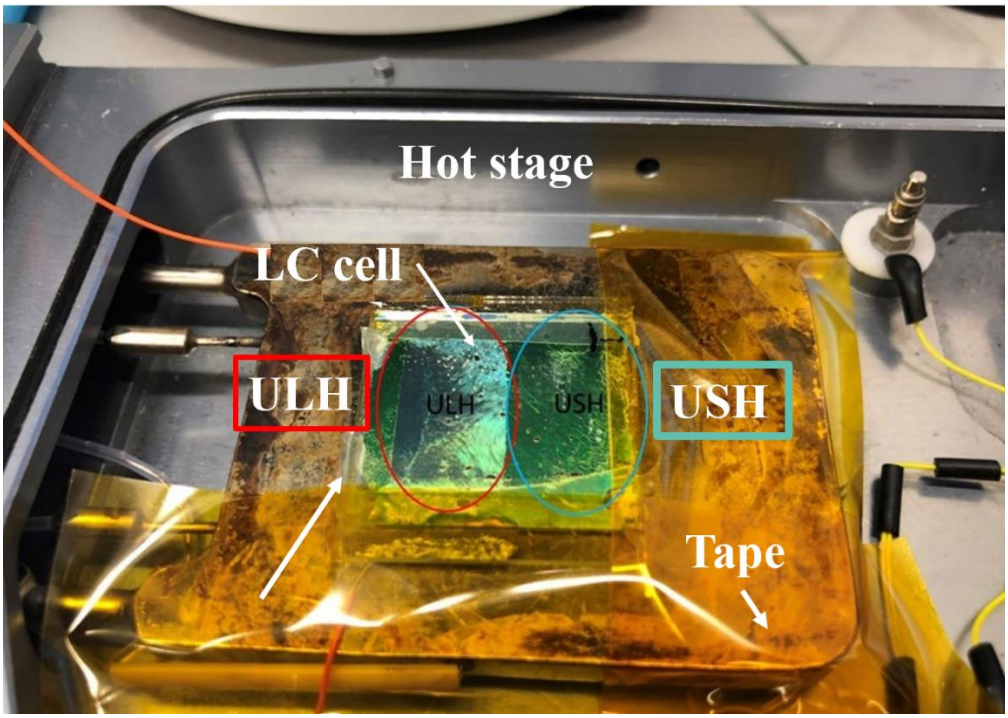

Figure 8.2. Sample after the photopolymerization process without the application of an external electric field. The left region forms a ULH structure and the right region forms USH structure.

As mentioned in Chapter 4, an ideal chiral nematic reflector can replace the mirror and quarter waveplate combination to ensure that the system is less sensitive to the nonideality in the LC phase modulation element. When we try to make the integrated device, the LC, quarter waveplate and mirror configuration are chosen to reduce the difficulties of developing the integrated device. However, the LC, quarter waveplate and chiral reflector configuration are preferable in the future as they can lead to a more robust integrated phase modulator.

In addition to the above work, several directions need to be investigated:

1. Single-pixel LC devices can be fabricated using off-the-shelf glass cells. The cells consist of two glass substrates which are each coated with ITO and

alignment layers. They adhere to each other (with the alignment layer on the inside), separated by spacers to give cell gaps ranging from 2 to 50 μm. The two substrates are typically offset so that the ITO electrodes on each side are exposed, such that they can be electrically contacted. The cells are relatively inexpensive and give thicknesses within a reasonably narrow tolerance. However, unfortunately, cells with patterned electrodes are not commercially available and a single cell device used in this thesis is not suitable for a commercial SLM. In the future, it would be better to test this phase modulator configuration using multipixels. Hence, it is important to find a way to generate a multipixel device. Currently, there are several technologies available for upgrading one pixel device to multipixels device and one of the technologies has been widely used is photolithography which can create extremely small patterns (down to a few tens of nm in size) on thin film or the bulk of a substrate. In addition, this method can provide precise control of the shape and size of the objects it creates and can create patterns over an entire surface cost-effectively. Through using this method, we can generate small electrodes on an integrated phase modulator to upscale it from one pixel device to multipixels device. In addition, recently, our lab has developed a new fabrication concept using a femtosecond laser to pattern an ITO coated glass substrate. Which can obtain high precision removal of the ITO from a glass substrate, whilst ensuring there was no electrical conductivity across the gaps. Using this technique, a 4-pixel electrode was fabricated by inscribing two lines across a glass substrate coated

in 10 nm ITO. This technique is also a option for us to choose to fabricate multipixels devices.

2. It is important to measure the actual phase response of the full SLM (including the additional polariser, quarter-wave plates, and reflector). In a practical device, the additional components will deviate from the ideal, resulting in imperfections in the phase response of the device and causing residual amplitude modulation. Previously, SLM phase modulators have been measured using an interferometer to measure the interference fringes between the reflected beam and a reference beam using a camera. However, this data gives very limited resolution and it is very prone to environmental drift in the optical path lengths which means it cannot give time-resolved data and the measurement is time-consuming. Besides, this method can only be used for single cell phase response measurement, which is not desirable as commercial SLMs normally have multiple pixels. Hence, it would be advantageous to design a new experimental system to measure the phase response as a function of time for these fast-switching SLMs.
3. The fabrication of a full SLM is a major undertaking as it requires a full custom Liquid Crystal on Silicon process. This process requires a silicon wafer fabrication run to produce a custom silicon substrate incorporating CMOS electronics. Therefore, an industrial partner with existing capability in this area is needed to transition from low pixel count prototypes to high pixel count devices suitable for the actual application. Several SLM manufacturers who

could potentially fabricate the devices were identified (Meadowlark Boulder, Holoeye and Hamamatsu Shizuoka)

4. One of the key challenges in the fabrication of the SLM is the accurate control of the thickness of quarterwave plate between the LC material and the rear reflecting electrode on the CMOS silicon substrate. In the integrated device, the polymer and LC layers were fabricated so that each layer formed a wedge shape. However, this method cannot be used in a commercial SLM as the active region is not big which is not cost effectively. In order to solve this problem, we will actively engage with SLM fabrication companies such as Meadowlark and Holoeye Photonics AG.

8.2.2 Optical beam steering device

As mentioned in Chapter 7, we have developed a new beam steering system by combining polarization gratings with nematic LC devices, which has great potential in an optical communication system. The original idea is to combine the polarisation grating with our phase modulator to build the beam steering system. Unfortunately, this work was substantially delayed due to the COVID. For future work, the first step will be to replace the nematic pi-cells (LC1, LC2 and LC3) used in this thesis (shown in **Figure 8.3**) with our phase modulator to see whether the system can still work as expected.

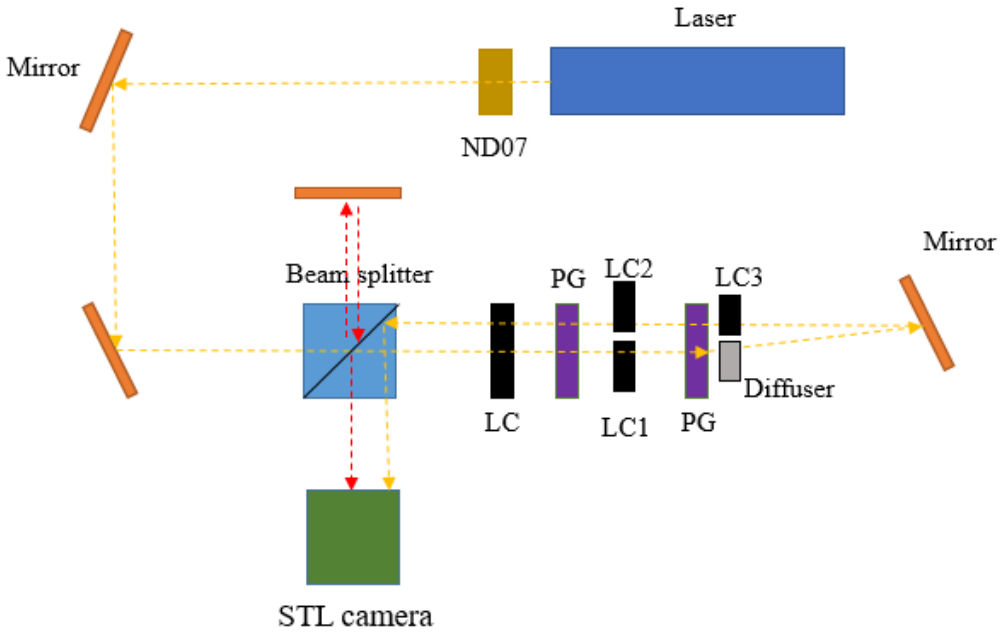

Figure 8.3. Beam System that developed in the previous chapter (LC: liquid crystal, PG: polarisation grating, ND: ND filter, CCD: CCD camera).

If the system can function as expected, then the system will be tested by replacing the He-Ne laser with a real communication laser and the CCD camera will be replaced with a high-resolution photodiode to test whether the light can be reflected back. The success of this experiment will lead us to the final step: to test the system in a real environment with a visible light communication system, as shown in **Figure 8.4**.

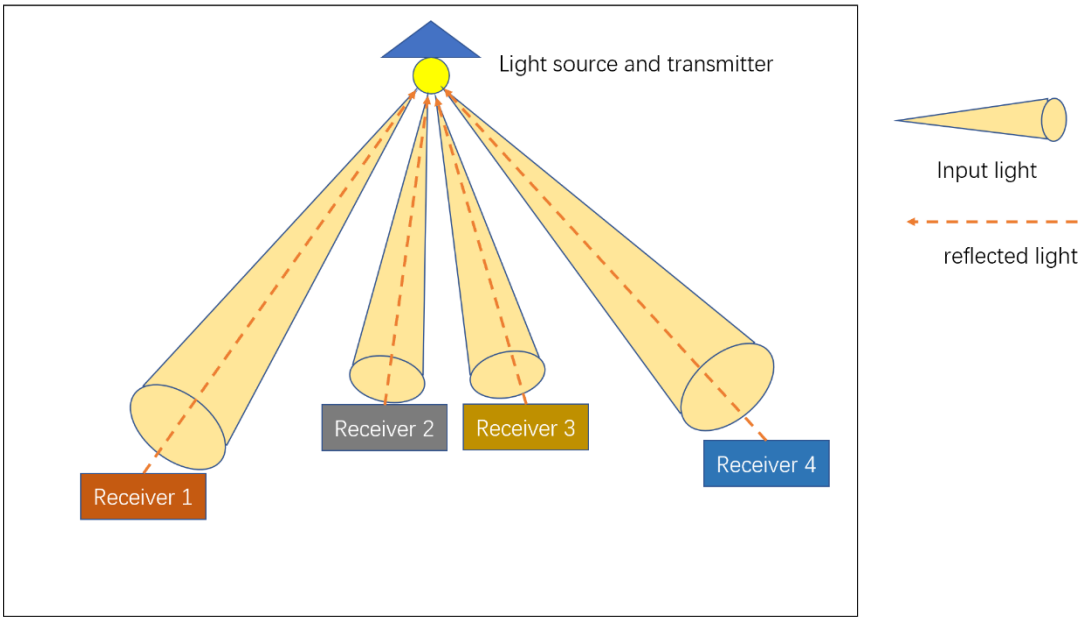

Figure 8.4. A proposed configuration to test our beam steering system.

Bibliography

1. Bahk, S., Fess, E., Kruschwitz, B. & Zuegel, J. A high-resolution, adaptive beam-shaping system for high-power lasers. *Optics Express* 18, 9151 (2010).
2. Hu, L. et al. Phase-only liquid crystal spatial light modulator for wavefront correction with high precision. *Optics Express* 12, 6403 (2004).
3. Crossland, W., Wilkinson, T., Manolis, I., Redmond, M. & Davey, A. Telecommunications Applications of LCOS Devices. *Molecular Crystals and Liquid Crystals* 375, 1-13 (2002).
4. Lee, Y. et al. Recent progress in Pancharatnam–Berry phase optical elements and the applications for virtual/augmented realities. *Optical Data Processing and Storage* 3, (2017).
5. Zhan, T., Xiong, J., Zou, J. & Wu, S. Multifocal displays: review and prospect. *PhotoniX* 1, (2020).
6. Hua, H. Enabling Focus Cues in Head-Mounted Displays. *Proceedings of the IEEE* 105, 805-824 (2017).
7. Li, Y. et al. Front-lit LCOS for Wearable Applications. *SID Symposium Digest of Technical Papers* 45, 234-236 (2014).
8. Cuypers, D., De Smet, H. & Van Calster, A. VAN LCOS Microdisplays: A Decade of Technological Evolution. *Journal of Display Technology* 7, 127-134 (2011).

9. Takatoh, K., Harima, A., Kaname, Y., Shinohara, K. & Akimoto, M. Fast-response twisted nematic liquid crystal displays with ultrashort pitch liquid crystalline materials. *Liquid Crystals* 39, 715-720 (2012).
10. Komitov, L., Hegde, G. & Kolev, D. Fast liquid crystal light shutter. *Journal of Physics D: Applied Physics* 44, 442002 (2011).
11. Haas, W., Adams, J. & Flannery, J. New Electro-Optic Effect in a Room-Temperature Nematic Liquid Crystal. *Physical Review Letters* 25, 1326-1327 (1970).
12. Xianyu, H., Gauza, S. & Wu, S. Sub-millisecond response phase modulator using a low crossover frequency dual-frequency liquid crystal. *Liquid Crystals* 35, 1409-1413 (2008).
13. Lin, Y. et al. Polarization-independent liquid crystal phase modulator using a thin polymer-separated double-layered structure. *Optics Express* 13, 8746 (2005).
14. Srivastava, A., Chigrinov, V. & Kwok, H. Ferroelectric liquid crystals: Excellent tool for modern displays and photonics. *Journal of the Society for Information Display* 23, 253-272 (2015).
15. Knust, S., Wahle, M. & Kitzerow, H. Ferroelectric Liquid Crystals in Microcapillaries: Observation of Different Electro-optic Switching Mechanisms. *The Journal of Physical Chemistry B* 121, 5110-5115 (2017).
16. Chen, H., Gou, F. & Wu, S. Submillisecond-response nematic liquid crystals for augmented reality displays. *Optical Materials Express* 7, 195 (2016).

17. Palffy-Muhoray, P. The diverse world of liquid crystals. *Physics Today* 60, 54-60 (2007).
18. Collings, P. & Goodby, J. *Introduction to liquid crystals*. 245-294 (2012).
19. Chandrasekhar, S. Discotic liquid crystals. A brief review. *Liquid Crystals* 14, 3-14 (1993).
20. Bisoyi, H. & Kumar, S. Discotic nematic liquid crystals: science and technology. *Chem. Soc. Rev.* 39, 264-285 (2010).
21. Subramhanyam, H., Prabha, C. & Krishnamurti, D. Optical Anisotropy of Nematic Compounds. *Molecular Crystals and Liquid Crystals* 28, 201-215 (1974).
22. Adamski, P. Polarizability Anisotropy of CB6, CB7, CB8 and OCB8 Liquid Crystal Molecules. *Crystal Research and Technology* 34, 763-768 (1999).
23. Chien, L. *Liquid crystal materials, devices, and applications XI*. 457-560 (SPIE, 2006).
24. Gennes, P. & Prost, J. *The physics of liquid crystals*. 2-104 (Clarendon Press, 1998).
25. Kuczyński, W., Żywucki, B. & Małecki, J. Determination of Orientational Order Parameter in Various Liquid-Crystalline Phases. *Molecular Crystals and Liquid Crystals* 381, 1-19 (2002).
26. Singh, A. & Singh, S. Thermodynamic model for the description of smectic C* and smectic A–smectic C* phase transition properties. *Phase Transitions* 83, 205-222 (2010).

27. Brand, H., Cladis, P. & Pleiner, H. Macroscopic properties of smectic liquid crystals. *The European Physical Journal B* 6, 347-353 (1998).
28. Holmes, M. & Charvolin, J. Smectic-nematic transition in a lyotropic liquid crystal. *The Journal of Physical Chemistry* 88, 810-818 (1984).
29. Cook, M. & Wilson, M. Calculation of helical twisting power for liquid crystal chiral dopants. *The Journal of Chemical Physics* 112, 1560-1564 (2000).
30. Schadt, M. Dielectric Properties of Some Nematic Liquid Crystals with Strong Positive Dielectric Anisotropy. *The Journal of Chemical Physics* 56, 1494-1497 (1972).
31. Kelly, S. & Schad, H. Some Novel Nematic Liquid Crystals of Negative Dielectric Anisotropy. *Molecular Crystals and Liquid Crystals* 110, 239-261 (1984).
32. Klasen, M. et al. Calculation of Optical and Dielectric Anisotropy of Nematic Liquid Crystals. *Japanese Journal of Applied Physics* 37, L945-L948 (1998).
33. Ewald, P. Group velocity and phase velocity in X-ray crystal optics. *Acta Crystallographica* 11, 888-891 (1958).
34. Mitov, M. Cholesteric Liquid Crystals with a Broad Light Reflection Band. *Advanced Materials* 24, 6260-6276 (2012).
35. Adler, J., Atherton, T., Benson, T., Emerson, D. & MacLachlan, S. Energy Minimization for Liquid Crystal Equilibrium with Electric and Flexoelectric Effects. *SIAM Journal on Scientific Computing* 37, S157-S176 (2015).

36. Poon, C. & Fung, B. Orientational ordering of a ferroelectric liquid crystal with high spontaneous polarization. *Liquid Crystals* 5, 1159-1169 (1989).

37. de Gennes, P., Prost, J. & Pelcovits, R. The Physics of Liquid Crystals. *Physics Today* 48, 70-71 (1995).

38. Selinger, J. Interpretation of saddle-splay and the Oseen-Frank free energy in liquid crystals. *Liquid Crystals Reviews* 6, 129-142 (2018).

39. Yamauchi, M. Jones-matrix models for twisted-nematic liquid-crystal devices. *Applied Optics* 44, 4484 (2005).

40. Lu, S. & Chipman, R. Homogeneous and inhomogeneous Jones matrices. *Journal of the Optical Society of America A* 11, 766 (1994).

41. Kahn, F., Taylor, G. & Schonhorn, H. Surface-produced alignment of liquid crystals. *Proceedings of the IEEE* 61, 823-828 (1973).

42. Wu, H. et al. Liquid-crystal alignment of rubbed polyimide films: A microscopic investigation. *Applied Physics B Laser and Optics* 62, 613-618 (1996).

43. Jung, J., Lee, K., Sohn, B., Lee, S. & Ree, M. Novel polypyromellitimides and their liquid crystal aligning properties. *Macromolecular Symposia* 164, 227-238 (2001).

44. Oh-e, M., Yokoyama, H. & Kim, D. Mapping molecular conformation and orientation of polyimide surfaces for homeotropic liquid crystal alignment by nonlinear optical spectroscopy. *Physical Review E* 69, (2004).

45. Wu, W., Wang, C. & Fuh, A. Controlling pre-tilt angles of liquid crystal using mixed polyimide alignment layer. *Optics Express* 16, 17131 (2008).

46. Takatoh, K., Sakamoto, M., Hasegawa, R. & Koden, M. *Alignment Technology and Applications of Liquid Crystal Devices*. (CRC Press, 2005).

47. Hiltrop, K. & Stegemeyer, H. Contact Angles and Alignment of Liquid Crystals on Lecithin Monolayers. *Molecular Crystals and Liquid Crystals* 49, 61-65 (1978).

48. Sinha, G., Wen, B. & Rosenblatt, C. Large, continuously controllable nematic pretilt from vertical orientation. *Applied Physics Letters* 79, 2543-2545 (2001).

49. Shioda, T., Wen, B. & Rosenblatt, C. Continuous nematic anchoring transition due to surface-induced smectic order. *Physical Review E* 67, (2003).

50. Seki, T. New strategies and implications for the photoalignment of liquid crystalline polymers. *Polymer Journal* 46, 751-768 (2014).

51. Chigrinov, V., Kozenkov, V. & Kwok, H. *Photoalignment of liquid crystalline materials*. (Wiley, 2010).

52. Jesacher, A., Maurer, C., Schwaighofer, A., Bernet, S. & Ritsch-Marte, M. Near-perfect hologram reconstruction with a spatial light modulator. *Optics Express*, 16(4), 2597–2603 (2008).

53. Gould, T., Burke, D., Bewersdorf, J. & Booth, M. Adaptive optics enables 3D STED microscopy in aberrating specimens. *Optics Express*, 20(19), 20998–21009 (2012).

54. Jesacher, A. & Booth, M. Parallel direct laser writing in three dimensions with spatially dependent aberration correction. *Optics Express*, 18(20), 21090–21099 (2010).

55. Salter, P. S., Baum, M., Alexeev, I., Schmidt, M. & Booth, M. J. Exploring the depth range for three-dimensional laser machining with aberration correction. *Optics Express*, 22, 17644–17656 (2014).

56. Chan, V. Free-Space Optical Communications. *Journal of Lightwave Technology*, 24(12), 4750–4762 (2006)

57. Knoernschild, C., Kim, T., Maunz, P., Crain, S. & Kim, J. Stable optical phase modulation with micromirrors. *Optics Express*, 20(3), 3261–3267 (2012).

58. Khalil, K. *et al*. In-Line Optical MEMS Phase Modulator and Application in Ring Laser Frequency Modulation. *IEEE J. Sel. Top. Quantum Electron* 52(8), 1–8 (2016).

59. Wu, M., Solgaard, O. & Ford, J. Optical MEMS for Lightwave Communication. *Journal of Lightwave Technology*, 24(12), 4433–4454 (2006).

60. Zhang, Z., You, Z. & Chu, D. Fundamentals of phase-only liquid crystal on silicon (LCOS) devices. *Light Science & Application*, 3(10), e213–e213 (2014).

61. Grigory, L., Stefanie, B., Philip, E., Daniel, H. & Gunther, N. High-resolution LCOS microdisplay with sub-kHz frame rate for high performance, high precision 3D sensor. *Proc. SPIE 10335, Digital Optical Technologies* 2017, 103351B (2017).

62. Xianyu, H., Wu, S. & Lin, C. Dual frequency liquid crystals: a review. *Liquid Crystals* 36, 717-726 (2009).

63. Li, Y. et al. Submillisecond-Response Polymer Network Liquid Crystal Phase Modulators. *Polymers* 12, 2862 (2020).

64. Peng, F., Xu, D., Chen, H. & Wu, S. Low voltage polymer network liquid crystal for infrared spatial light modulators. *Optics Express* 23, 2361 (2015).
65. Chen, H. et al. Pursuing High Quality Phase-Only Liquid Crystal on Silicon (LCoS) Devices. *Applied Sciences* 8, 2323 (2018).
66. Fergason JL. Display devices utilizing liquid crystal light modulation. US Patent US3731986; 1973.
67. Khoo IC, Wu ST. *wang*. Singapore: World Scientific, 1993.
68. Huang, Y., He, Z. & Wu, S. Fast-response liquid crystal phase modulators for augmented reality displays. *Optics Express* 25, 32757 (2017).
69. Lee, Y. et al. Two-photon polymerization enabled multi-layer liquid crystal phase modulator. *Scientific Reports* 7, (2017).
70. Schiekel, M. & Fahrenschon, K. Deformation of Nematic Liquid Crystals with Vertical Orientation in Electrical Fields. *Applied Physics Letters* 19, 391-393 (1971).
71. Kurokawa, T. & Fukushima, S. Ferroelectric liquid crystal spatial light modulators and their applications. *Ferroelectrics* 149, 245-254 (1993).
72. Collings, N. et al. Measurements on ferroelectric liquid-crystal spatial light modulators: contrast ratio and speed. *Applied Optics* 34, 5928 (1995).
73. Wang, X. et al. Fast and low loss flexoelectro-optic liquid crystal phase modulator with a chiral nematic reflector. *Scientific Reports* 9, (2019).
74. Wang, X. et al. A Compact Full 2π Flexoelectro-Optic Liquid Crystal Phase Modulator. *Advanced Materials Technologies* 5, 2000589 (2020).

75. Jovicic, A., Li, J. & Richardson, T. Visible light communication: opportunities, challenges and the path to market. *IEEE Communications Magazine* 51, 26-32 (2013).

76. He, J., Dong, T. & Xu, Y. Review of Photonic Integrated Optical Phased Arrays for Space Optical Communication. *IEEE Access* 8, 188284-188298 (2020).

77. Chen, H., Weng, Y., Xu, D., Tabiryan, N. & Wu, S. Beam steering for virtual/augmented reality displays with a cycloidal diffractive waveplate. *Optics Express* 24, 7287 (2016).

78. Zohrabi, M. et al. Lidar system with nonmechanical electrowetting-based wide-angle beam steering. *Optics Express* 27, 4404 (2019).

79. Palonpon, A. et al. Raman and SERS microscopy for molecular imaging of live cells. *Nature Protocols* 8, 677-692 (2013).

80. Lendraitis, V., Brikas, M., Snitka, V., Mizarienė, V. & Raciukaitis, G. Fabrication of actuator for nanopositioning using laser micro-machining. *Microelectronic Engineering* 83, 1212-1215 (2006).

81. Heck, M. Highly integrated optical phased arrays: photonic integrated circuits for optical beam shaping and beam steering. *Nanophotonics* 6, 93-107 (2017).

82. Watson, E. Analysis of beam steering with decentered microlens arrays. *Optical Engineering* 32, 2665 (1993).

83. McManamon, P. & Ataei, A. Progress and opportunities in optical beam steering. in *SPIE* 10926 (SPIE OPTO, 2019).

84. McManamon, P. A review of non mechanical beam steering options. *Ieeexplore.ieee.org* (2008). at https://ieeexplore.ieee.org/document/4688748

85. Hoy, C. et al. Non-Mechanical Beam Steering with Polarization Gratings: A Review. *Crystals* 11, 361 (2021).

86. Zhan, T. et al. Pancharatnam–Berry optical elements for head-up and near-eye displays [Invited]. *Journal of the Optical Society of America B* 36, D52 (2019).

87. Lin, T. et al. Recent Advances in Photoalignment Liquid Crystal Polarization Gratings and Their Applications. *Crystals* 11, 900 (2021).

88. Dai, H., Liu, K., Wang, X. & Liu, J. Characteristics of LCoS Phase-only spatial light modulator and its applications. *Optics Communications* 238, 269-276 (2004).

89. Babakhanova, G. et al. Elastic and viscous properties of the nematic dimer CB7CB. *Physical Review E* 96, (2017).

90. Meyer, R. Piezoelectric Effects in Liquid Crystals. *Physical Review Letters* 22, 918-921 (1969).

91. Dierking, I. Flexoelectricity in liquid crystals. *Liquid Crystals Today* 22, 48-48 (2013).

92. Patel, J. & Meyer, R. Flexoelectric electro-optics of a cholesteric liquid crystal. *Physical Review Letters* 58, 1538-1540 (1987).

93. Patel, J. & Lee, S. Fast linear electro-optic effect based on cholesteric liquid crystals. *Journal of Applied Physics* 66, 1879-1881 (1989).

94. Lee, S., Patel, J. & Meyer, R. Effect of flexoelectric coupling on helix distortions in cholesteric liquid crystals. *Journal of Applied Physics* 67, 1293-1297 (1990).

95. Rudquist, P., Buivydas, M., Komitov, L. & Lagerwall, S. Linear electro-optic effect based on flexoelectricity in a cholesteric with sign change of dielectric anisotropy. *Journal of Applied Physics* 76, 7778-7783 (1994).

96. Rudquist, P., Carlsson, T., Komitov, L. & Lagerwall, S. The flexoelectro-optic effect in cholesterics. *Liquid Crystals* 22, 445-449 (1997).

97. Rudquist, P., Komitov, L. & Lagerwall, S. Volume-stabilized ULH structure for the flexoelectro-optic effect and the phase-shift effect in cholesterics. *Liquid Crystals* 24, 329-334 (1998).

98. Coles, H., Clarke, M., Morris, S., Broughton, B. & Blatch, A. Strong flexoelectric behavior in bimesogenic liquid crystals. *Journal of Applied Physics* 99, 034104 (2006).

99. Morris, S., Clarke, M., Blatch, A. & Coles, H. Structure-flexoelastic properties of bimesogenic liquid crystals. *Physical Review E* 75, (2007).

100. Varanytsia, A. & Chien, L. Bimesogen-enhanced flexoelectro-optic behavior of polymer stabilized cholesteric liquid crystal. *Journal of Applied Physics* 119, 014502 (2016).

101. Outram, B. & Elston, S. Spontaneous and stable uniform lying helix liquid-crystal alignment. *Journal of Applied Physics* 113, 043103 (2013).

102. Park, K., Baek, J., Lee, Y., Kim, J. & Yu, C. Effects of pretilt angle and anchoring energy on alignment of uniformly lying helix mode. *Liquid Crystals* 43, 1184-1189 (2016).

103. Coles, H., Morris, S., Castles, F., Gardiner, D. & Malik, Q. Ultrafast High Optical Contrast Flexoelectric Displays for Video Frame Rates. *SID Symposium Digest of Technical Papers* 43, 544-547 (2012).

104. Varanytsia, A. & Chien, L. Giant Flexoelectro-optic Effect with Liquid Crystal Dimer CB7CB. *Scientific Reports* 7, (2017).

105. Broughton, B., Clarke, M., Morris, S., Blatch, A. & Coles, H. Effect of polymer concentration on stabilized large-tilt-angle flexoelectro-optic switching. *Journal of Applied Physics* 99, 023511 (2006).

106. Corbett, D. & Elston, S. Modeling the helical flexoelectro-optic effect. *Physical Review E* 84, (2011).

107. Chen, H., Zhu, R., Zhu, J. & Wu, S. A simple method to measure the twist elastic constant of a nematic liquid crystal. *Liquid Crystals* 42, 1738-1742 (2015).

108. de Vries H. Rotatory power and other optical properties of certain liquid crystals. Acta Crystallogr. 1951;4:219–226.

109. Wang, X. et al. Characterization of large tilt-angle flexoelectro-optic switching in chiral nematic liquid crystal devices. *Liquid Crystals* 46, 408-414 (2018).

110. Nikolenko, V., Watson, B.O., Araya, R., Woodruff, A., Peterka, D.S., and Yuste, R., SLM microscopy: scanless two-photon imaging and photostimulation with spatial light modulators. *Front Neural Circuits* 2 (5), 1–14 (2008).

111. Chang, B.-J., Chou, L.-J., Chang, Y.-C., and Chiang, S.-Y., Isotropic image in structured illumination microscopy patterned with a spatial light modulator. *Optics Express* 17, 14710-14714 (2009).

112. Heintzmann, R. Saturated patterned excitation microscopy with two-dimensional excitation patterns., *Micron* 34 (9), 283–291 (2003).

113. Situ, G., Warber, M., Pedrini, G., and Osten, W., Phase contrast enhancement in microscopy using spiral phase filtering. *Optics Communication* 283 (7), 1273–1277 (2010).

114. Rosen, J. and Brooker, G., Non-scanning motionless fluorescence three-dimensional holographic microscopy. *Nature Photonics* 2, 190–195 (2008).

115. Maurer, C., Jesacher, A., Bernet, S., and Ritsch-Marte, M., What spatial light modulators can do for optical microscopy. *Laser & Photonics Review* 5 (1), 81–101 (2011).

116. Brooker, G., Siegel, N., Wang, V., and Rosen, J., Optimal resolution in Fresnel incoherent correlation holographic fluorescence microscopy. *Optics Express* 19, 5047 (2011).

117. Kali, A., Tan, A., Gravey, P., Wolffer, N., Lelah, A., and Pincemin, E., Assessment of LCOS technology for the realization of scalable n×n optical switches. *Proceedings of International Conference on Photonics in Switching* (2003).

118. Roelens, M.A., Bolger, J.A., Williams, D., and Eggleton, B.J., Multi-wavelength synchronous pulse burst generation with a wavelength selective switch. *Optics Express* 16 (14), 10152–10157 (2008).

119. Frumker, E. and Silberberg, Y. Phase and amplitude pulse shaping with two-dimensional phase-only spatial light modulators. *Journal of the Optical Society of America B* 24 (12), 2940–2947 (2007).

120. Bashkansky, M., Park, D., and Fatemi, F.K., Azimuthally and radially polarized light with a nematic SLM. *Optics Express* 18 (1), 212–217 (2010).

121. Vellekoop, I.M. and Mosk, A.P., Focusing coherent light through opaque strongly scattering media. *Optics Letter* 32 (16), 2309–2311 (2007).

122. Kuang, Z., Perrie, W., Liu, D., Edwardson, S., Cheng, J., Dearden, G., and Watkins, K., Diffractive multi-beam surface microprocessing using 10 ps laser pulses. *Applied Surface Science* 255 (22), 9040–9044 (2009).

123. Lima, G., Vargas, A., Neves, L., Guzmán, R. & Saavedra, C. Manipulating spatial qudit states with programmable optical devices. *Optics Express* 17, 10688 (2009).

124. Baumbach, T., Osten, W., von Kopylow, C. & Jüptner, W. Remote metrology by comparative digital holography. *Applied Optics* 45, 925 (2006).

125. Meeser, T., von Kopylow, C., and Falldorf, C. Advanced digital lensless Fourier holography by means of a spatial light modulator. *3DTV-Conference: The True Vision - Capture, Transmission and Display of 3D Video (3DTV-CON)* 79,1–4 (2010).

126. Jenness, N. et al. Three-dimensional parallel holographic micropatterning using a spatial light modulator. *Optics Express* 16, 15942 (2008).

127. Fratz, M., Fischer, P. & Giel, D. Full phase and amplitude control in computer-generated holography. *Optics Letters* 34, 3659 (2009).

128. Cheremkhin, P. et al. Optical reconstruction of digital off-axis Fresnel holograms using phase-only LCOS SLM "HoloEye PLUTO VIS." *Journal of Physics: Conference Series* 536, 012008 (2014).

129. Haist, T., Zwick, S., Warber, M. & Osten, W. Spatial Light Modulators—Versatile Tools for Holography. *Journal of Holography and Speckle* 3, 125-136 (2006).

130. Takeda, M., Wang, W., and Nai, D.N. Coherence holography: a thought on synthesis and analysis of optical coherence fields, *6th International Workshop on Advanced Optical Metrology,* (*Springer*, 2009).

131. Onural, L., Yaraş, F. & Hoonjong Kang. Digital Holographic Three-Dimensional Video Displays. *Proceedings of the IEEE* 99, 576-589 (2011).

132. Buckley, E. Holographic Laser Projection. *Journal of Display Technology* 7, 135-140 (2011).

133. Rosen, J. & Brooker, G. Digital spatially incoherent Fresnel holography. *Optics Letters* 32, 912 (2007).

134. Roh, J. et al. Full-color holographic projection display system featuring an achromatic Fourier filter. *Optics Express* 25, 14774 (2017).

135. Zwick, S., Warber, M., Gorski, W., Haist, T., and Osten, W., Flexible adaptive phase contrast methods using a spatial light modulator. *Proceedings DGAO* A3, (2009)

136. Warber, M., Zwick, S., Hasler, M., Haist, T., and Osten, W., SLM-based phase-contrast filtering for single and multiple image acquisition, *SPIE Proceedings, Optics and Photonics for Information Processing III* 7442, (2009).

137. Auksorius, E. et al. Stimulated emission depletion microscopy with a supercontinuum source and fluorescence lifetime imaging. *Optics Letters* 33, 113 (2008).

138. Fells, J. et al. Flexoelectro-optic liquid crystal analog phase-only modulator with a 2π range and 1kHz switching. *Optics Letters* 43, 4362 (2018).

139. Anderson, J., Aulin, T. & Sundberg, C. *Digital Phase Modulation*. (Springer, 2013).

140. Okunev, Y. *Phase and phase-difference modulation in digital communications*. (Artech House, 1997).

141. Jesacher, A., Maurer, C., Schwaighofer, A., Bernet, S. & Ritsch-Marte, M. Near-perfect hologram reconstruction with a spatial light modulator. *Optics Express* 16, 2597 (2008).

142. Chen, J., Morris, S., Wilkinson, T., Freeman, J. & Coles, H. High speed liquid crystal over silicon display based on the flexoelectro-optic effect. *Optics Express* 17, 7130 (2009).

143. Stockley, J., Sharp, G., Johnson, K. & Serati, S. Analog optical phase modulator based on chiral smectic and polymer cholesteric liquid crystals. *Optics Letters* 20, 2441 (1995).

144. Gil, J. & Bernabeu, E. Depolarization and Polarization Indices of an Optical System. *Optica Acta: International Journal of Optics* 33, 185-189 (1986).

145. Fells, J. et al. Dynamic response of large tilt-angle flexoelectro-optic liquid crystal modulators. *Optics Express* 27, 15184 (2019).

146. Jamie H., Steve S., and Jay S. Comparison of transmissive and reflective spatial light modulators for optical manipulation applications, *Proc. SPIE 5930, Optical Trapping and Optical Micromanipulation II*, 59302D (2005).

147. Itoh, Y., Hamasaki, T. & Sugimoto, M. Occlusion Leak Compensation for Optical See-Through Displays Using a Single-Layer Transmissive Spatial Light Modulator. *IEEE Transactions on Visualization and Computer Graphics* 23, 2463-2473 (2017).

148. Agour, M., Kolenovic, E., Falldorf, C. & von Kopylow, C. Suppression of higher diffraction orders and intensity improvement of optically reconstructed holograms from a spatial light modulator. *Journal of Optics A: Pure and Applied Optics* 11, 105405 (2009).

149. Zou, J. et al. Fast-Response Liquid Crystal for Spatial Light Modulator and LiDAR Applications. *Crystals* 11, 93 (2021).

150. Harvey, J. Analysis and design of wide-angle foveated optical systems based on transmissive liquid crystal spatial light modulators. *Optical Engineering* 48, 043001 (2009).

151. Lin, S., Lin, S. & Yu, J. Study on the light delivery to a transmissive-LCD spatial light modulator used in an LED projector. *Journal of the Society for Information Display* 18, 827 (2010).

152. Villalobos-Mendoza, B., Granados-Agustín, F., Aguirre-Aguirre, D., Izazága-Pérez, R. & Cornejo-Rodríguez, A. Measuring the phase shifts produced by transmissive spatial light modulators. *SPIE Newsroom* (2015).

153. Nys, I., Beeckman, J. & Neyts, K. Fringe-field-induced out-of-plane reorientation in vertically aligned nematic spatial light modulators and its effect on light diffraction. *Liquid Crystals* 1-9 (2021).

154. Dev, K. & Asundi, A. Mueller–Stokes polarimetric characterization of transmissive liquid crystal spatial light modulator. *Optics and Lasers in Engineering* 50, 599-607 (2012).

155. Huang, Y., Wen, C. & Wu, S. Polarization-independent and submillisecond response phase modulators using a 90° twisted dual-frequency liquid crystal. *Applied Physics Letters* 89, 021103 (2006).

156. Fan, Y., Lin, Y., Ren, H., Gauza, S. & Wu, S. Fast-response and scattering-free polymer network liquid crystals for infrared light modulators. *Applied Physics Letters* 84, 1233-1235 (2004).

157. Jamie, H. et. Al, Transmissive spatial light modulators with high figure-of-merit liquid crystals for foveated imaging applications, *Proc. SPIE 6135, Liquid Crystal Materials, Devices, and Applications XI*, 61350C (2006).

158. Varanytsia, A. & Chien, L. Giant Flexoelectro-optic Effect with Liquid Crystal Dimer CB7CB. *Scientific Reports* 7, (2017).

159. Joshi, V. et al. Cholesteric Metronomes with Flexoelectrically Programmable Amplitude. *Advanced Optical Materials* 6, 1800013 (2018).

160. Wang, X. et al. Transmissive flexoelectro-optic liquid crystal optical phase modulator with 2π modulation. *AIP Advances* 10, 055011 (2020).

161. Wang, X. et al. A Compact Full 2π Flexoelectro-Optic Liquid Crystal Phase Modulator. *Advanced Materials Technologies* 5, 2000589 (2020).

162. Geday, M. et al. V-Shape Liquid Crystal-Based Retromodulator Air to Ground Optical Communications. *Molecular Crystals and Liquid Crystals* 494, 213-221 (2008).

163. Geday, M. et al. Development of liquid crystal based adaptive optical elements for space applications. *Procesdings SPIE* 10565, International Conference on Space Optics — ICSO 2010, 105652J (2017).

164. Park, J. et al. All-solid-state spatial light modulator with independent phase and amplitude control for three-dimensional LiDAR applications. *Nature Nanotechnology* 16, 69-76 (2020).

165. Zou, J. et al. Fast-Response Liquid Crystal for Spatial Light Modulator and LiDAR Applications. *Crystals* 11, 93 (2021).

166. Mullins, B., Greenhalgh, P. & Christmas, J. The Holographic Future of Head Up Displays. *SID Symposium Digest of Technical Papers* 48, 886-889 (2017).

167. Skirnewskaja, J., Montelongo, Y., Wilkes, P. & Wilkinson, T. LiDAR-derived digital holograms for automotive head-up displays. *Optics Express* 29, 13681 (2021).

168. Lv, J. et al. Thermal stability of Ag films in air prepared by thermal evaporation. *Applied Surface Science* 253, 7036-7040 (2007).

169. Eccher, J. et al. Thermal Evaporation versus Spin-Coating: Electrical Performance in Columnar Liquid Crystal OLEDs. *ACS Applied Materials & Interfaces* 7, 16374-16381 (2015).

170. Santhosh, T., Bangera, K. & Shivakumar, G. Effect of Ag in CdSe thin films prepared using thermal evaporation. *Semiconductors* 51, 1597-1603 (2017).

171. Pan, Y., Fan, Y. & Niu, J. Optical properties of ultra-thin silver films deposited by thermal evaporation and its application in optical filters. *Infrared Physics & Technology* 104, 103123 (2020).

172. Mattox, D. Physical vapor deposition (PVD) processes. *Metal Finishing* 100, 394-408 (2002).

173. Hao, H., Li, H., Wang, S., Cheng, Z. & Fang, Y. Epitaxial growth of Ag-Cu bimetallic nanoparticles via thermal evaporation deposition. *Applied Surface Science* 505, 143871 (2020).

174. Chigrinov, V., Kwok, H., Takada, H. & Takatsu, H. Photo-aligning by azo-dyes: Physics and applications. *Liquid Crystals Today* 14, 1-15 (2005).

175. Zhang, B., Li, K., Chigrinov, V., Kwok, H. & Huang, H. Application of Photoalignment Technology to Liquid-Crystal-on-Silicon Microdisplays. *Japanese Journal of Applied Physics* 44, 3983-3991 (2005).

176. Tseng, M. et al. Strengthening of liquid crystal photoalignment on azo dye films: passivation by reactive mesogens. *RSC Advances* 6, 48181-48188 (2016).

177. Bolis, S. et al. Solvent-induced self-assembly of uniform lying helix alignment of the cholesteric liquid crystal phase for the flexoelectro-optic effect. *Liquid Crystals* 45, 774-782 (2018).

178. Jakeman, E. & Raynes, E. Electro-optic response times in liquid crystals. *Physics Letters A* 39, 69-70 (1972).

179. Akatay, A. & Urey, H. Design and optimization of microlens array based high resolution beam steering system. *Optics Express* 15, 4523 (2007).

180. Li, Y. Third-order theory of the Risley-prism-based beam steering system. *Applied Optics* 50, 679 (2011).

181. Jofre, M. et al. Fast beam steering with full polarization control using a galvanometric optical scanner and polarization controller. *Optics Express* 20, 12247 (2012).

182. Knoernschild, C., Kim, C., Lu, F. & Kim, J. Multiplexed broadband beam steering system utilizing high speed MEMS mirrors. *Optics Express* 17, 7233 (2009).

183. Alshamrani, N. et al. A Non-Mechanical Multi-Wavelength Integrated Photonic Beam Steering System. *Journal of Lightwave Technology* 39, 4201-4208 (2021).

184. Engström, D., O'Callaghan, M., Walker, C. & Handschy, M. Fast beam steering with a ferroelectric-liquid-crystal optical phased array. *Applied Optics* 48, 1721 (2009).

185. Cheng, Y., Cao, J. & Hao, Q. Optical beam steering using liquid-based devices. *Optics and Lasers in Engineering* 146, 106700 (2021).

186.Niu, Q. & Wang, C. High precision beam steering using a liquid crystal spatial light modulator. *Optical and Quantum Electronics* 51, (2019).

187.Lindle, J. & Watnik, A. Large angle nonmechanical laser beam steering at 4.6 μm using a digital micromirror device. *Optical Engineering* 57, 1 (2018).

188.Frantz, J. et al. Chip-based nonmechanical beam steerer in the midwave infrared. *Journal of the Optical Society of America B* 35, C29 (2018).

189.Lindle, J., Watnik, A. & Cassella, V. Wavelength agile nonmechanical laser beam steering from Fresnel zone plates imprinted on a liquid crystal spatial light modulator. *Optical Engineering* 55, 097103 (2016).

190.McManamon, P. Agile Nonmechanical Beam Steering. *Optics and Photonics News* 17, 24 (2006).

191.Zografopoulos, D. & Kriezis, E. Switchable beam steering with zenithal bistable liquid-crystal blazed gratings. *Optics Letters* 39, 5842 (2014).

192.Serati, S. et al. Large-aperture, wide-angle nonmechanical beam steering using polarization gratings. *Optical Engineering* 56, 031211 (2016).

193.Sarkissian, H. et al. Polarization-controlled switching between diffraction orders in transverse-periodically aligned nematic liquid crystals. *Optics Letters* 31, 2248 (2006).

194.Sun, J., Timurdogan, E., Yaacobi, A., Hosseini, E. & Watts, M. Large-scale nanophotonic phased array. *Nature* 493, 195-199 (2013).

195. Liu, H., Gao, S. & Loh, T. Compact Dual-Band Antenna with Electronic Beam-Steering and Beamforming Capability. *IEEE Antennas and Wireless Propagation Letters* 10, 1349-1352 (2011).

196. Rui, G. & Zhan, Q. Highly sensitive beam steering with plasmonic antenna. *Scientific Reports* 4, (2014).

197. Born, M. & Wolf, E. *Principles of optics. Electromagnetic theory of propagation, interference and diffraction of light. 4.ed*. (Pergamon Press, 1970).

198. Roychoudhuri, C., Kracklauer, A. & Creath, K. *The nature of light*. (CRC Press, 2008).

199. Taghi Tavassoly, M., Moaddel Haghighi, I. & Hassani, K. Application of Fresnel diffraction from a phase step to the measurement of film thickness. *Applied Optics* 48, 5497 (2009).

200. Loewen, E. & Popov, E. *Diffraction gratings and applications*. (M. Dekker, 1997).

201. Wilcox, C. Scattering theory for diffraction gratings. *Mathematical Methods in the Applied Sciences* 6, 158-158 (1984).

202. Zhurikhina, V. Diffusion phase diffraction gratings. *Optics and Spectroscopy* 89, 923-927 (2000).

203. Woods, T., Wrigley, R., Rottman, G. & Haring, R. Scattered-light properties of diffraction gratings. *Applied Optics* 33, 4273 (1994).

204. Zola, R. et al. Dynamic Control of Light Direction Enabled by Stimuli-Responsive Liquid Crystal Gratings. *Advanced Materials* 31, 1806172 (2018).

205. Fan, F., Srivastava, A., Chigrinov, V. & Kwok, H. Switchable liquid crystal grating with sub millisecond response. *Applied Physics Letters* 100, 111105 (2012).

206. Chen, J., Bos, P., Vithana, H. & Johnson, D. An electro-optically controlled liquid crystal diffraction grating. *Applied Physics Letters* 67, 2588-2590 (1995).

207. He, Z., Nose, T. & Sato, S. Diffraction and Polarization Properties of a Liquid Crystal Grating. *Japanese Journal of Applied Physics* 35, 3529-3530 (1996).

208. Honma, M. & Nose, T. Polarization-Independent Liquid Crystal Grating Fabricated by Microrubbing Process. *Japanese Journal of Applied Physics* 42, 6992-6997 (2003).

209. Kim, H., Jang, E., Kim, J., Joo, K. & Lee, S. Dynamic polarization grating based on a dye-doped liquid crystal controllable by a single beam in a homeotropic-planar geometry. *Applied Optics* 51, 8526 (2012).

210. Zuo, K., Shi, Y. & Luo, D. A Review of Two-Dimensional Liquid Crystal Polarization Gratings. *Crystals* 11, 1015 (2021).

211. Packham, C. et al. Polarization Gratings: A Novel Polarimetric Component for Astronomical Instruments. *Publications of the Astronomical Society of the Pacific* 122, 1471-1482 (2010).

212. Chen, W. et al. Linear polarization grating combining a circular polarization grating with a special cycloidal diffractive quarter waveplate. *Optics Express* 27, 33378 (2019).

213. Xiang, X., Kim, J. & Escuti, M. Bragg polarization gratings for wide angular bandwidth and high efficiency at steep deflection angles. *Scientific Reports* 8, (2018).

214. Guo, Q. et al. Fast switching beam steering based on ferroelectric liquid crystal phase shutter and polarisation grating. *Liquid Crystals* 46, 1383-1388 (2019).

215. Kudenov, M., Miskiewicz, M., Sanders, N. & Escuti, M. Achromatic Wollaston prism beam splitter using polarization gratings. *Optics Letters* 41, 4461 (2016).

216. Kawatsuki, N., Hasegawa, T., Ono, H. & Tamoto, T. Formation of Polarization Gratings and Surface Relief Gratings in Photocrosslinkable Polymer Liquid Crystals by Polarization Holography. *Advanced Materials* 15, 991-994 (2003).

217. Weng, Y., Xu, D., Zhang, Y., Li, X. & Wu, S. Polarization volume grating with high efficiency and large diffraction angle. *Optics Express* 24, 17746 (2016).

218. Zhao, Z. et al. High-efficiency large-angle reflective composite polarization grating. *Liquid Crystals* 47, 191-198 (2019).

219. Levenson, M. Wavefront Engineering for Photolithography. *Physics Today* 46, 28-36 (1993).

220. Fourkas, J. Nanoscale Photolithography with Visible Light. *The Journal of Physical Chemistry Letters* 1, 1221-1227 (2010).

221. Seisyan, R. Nanolithography in microelectronics: A review. *Technical Physics* 56, 1061-1073 (2011).